

Structure, Magnetic and Magneto-Optical Properties: A Study of the Interplay of Dopants in Quantum Dots

A Thesis submitted for the degree of

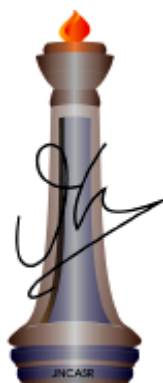
Doctor of Philosophy

As a part of

Ph.D. Programme (Chemical Science)

By

Ms. Mahima Makkar



New Chemistry Unit

Jawaharlal Nehru Centre for Advanced Scientific Research

(A Deemed University)

Bangalore - 560064 (INDIA)

November – 2020



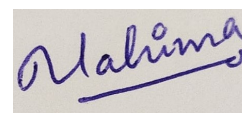
Dedicated to
Gurudevji & Gurumaji

Declaration

I hereby declare that the matter embodied in this thesis entitled “*Structure, Magnetic and Magneto-Optical Properties: A Study of the Interplay of Dopants in Quantum Dots*” is the result of the research carried out by me at the New Chemistry Unit, Jawaharlal Nehru Centre for Advanced Scientific Research, Bangalore, India, under the supervision of Prof. Ranjani Viswanatha and it has not been submitted elsewhere for the award of any degree or diploma.

In keeping with the general practices of reporting scientific observation, due acknowledgements have been made whenever the work described is based on the findings of other investigators. Any omission which might have occurred by oversight or error in judgement is regretted.

Bangalore



.....
Mahima Makkar

Certificate

I hereby certify that the matter embodied in this thesis entitled “*Structure, Magnetic and Magneto-Optical Properties: A Study of the Interplay of Dopants in Quantum Dots*” has been carried out by Ms. Mahima Makkar at the New Chemistry Unit, Jawaharlal Nehru Centre for Advanced Scientific Research, Bangalore, India under my supervision and that has not been submitted elsewhere for the award of any degree or diploma.

Bangalore



Prof. Ranjani Viswanatha

(Research Supervisor)

Acknowledgements

Much of the work presented in this thesis would not have materialized without the support, guidance and companionship that I got from so many people, both in my professional, as well as personal life. *This Ph.D. thesis is the culmination of the efforts of all those who have contributed to this research journey in so many ways.*

I would like to express my sincere gratitude to my research supervisor **Prof. Ranjani Viswanatha** for her guidance and support throughout. Her positive outlook, training and encouragement have been greatly instrumental in my Ph.D. odyssey. I am thankful to her for setting high benchmarks and motivating me to achieve them. I am also grateful for the freedom I got in the lab to work on projects of my interest. *Thank you for making this research journey an indelible learning experience for me!*

I would also like to thank the Chairman of the New Chemistry Unit, **Prof. C. N. R. Rao**, F.R.S., for being a source of constant inspiration. I convey my heartfelt gratitude to him for providing the excellent infrastructure and necessary facilities to carry out the thesis work.

A very special thanks to my **collaborators** around the world. I would like to thank Prof. Giulio Cerullo, Luca Moretti, Margherita Maiuri, Politecnico di Milano, Italy for TA measurements, Prof. Umesh V Waghmare, Lakshay Dheer, Anjali Singh, JNCASR for DFT studies, Dr. Rachel Fainblat and Prof. Gerd Bacher, University of Duisburg Essen, Germany for MCD measurements, Dr. Suvankar Chakraverty and Saveena Goyal, INST, Mohali for magnetic measurements. *I thank you all for the insightful discussions and instrumental collaborations!*

I thank Abhijit Sen, Prem Kumar and Prof. A. Sundaresan, JNCASR for the magnetic measurements. I thank the synchrotron facility at Stanford Synchrotron Radiation Lightsource, SLAC National Accelerator, CA, USA and PETRA III (P64), DESY, Germany for XAFS measurements. I also thank Dr. Wolfgang A. Caliebe, Murzin Vadim and Syed Khalid for assistance in XAFS measurements. I thank the Department of Science and Technology (DST) for financial assistance related to the project.

I am thankful to JNCASR for the Ph.D. fellowship. I would also like to thank DST, International Centre for Materials Science (ICMS), SSL (Sheikh Saqr Laboratory), synchrotron and neutron facility project, DST, JNCASR for funding in different scientific aspects.

I would like to express my sincere gratitude to all the **faculty members of NCU, CPMU, and TSU** for their instructive courses and all the scientific interactions.

My sincere thanks to all the technical staff especially Mr. Kannan, Dr. Jay, Mrs. Usha, Mr. Vasu, Mr. Shiva Kumar, Mr. Anil for their help with various characterization techniques, Mr. Peer, Mr. Mune Gowda, Mr. Dileep for all the audio/visual help. I thank the NCU office (Ms. Mellisa and Mr. Naveen), academic staff, administrative staff, library staff, complab staff, hostel staff, mess workers and security for providing and maintaining various facilities at JNC.

I wish to thank all my school and college teachers and everyone who has helped me shape my research interest. *My special thanks to Prof. A. K. Ganguli, Dr. Sonalika Vaidya, Dr. Kashinath Ojha, at IIT Delhi for introducing me to the field of scientific research.*

I am grateful to my **Lab Family**- Avijit, Murthy, Pradeep, Payel, Saptarshi, Prasenjit, Gautam, Gautam P, Suhas, Subhashri, Adarsh, Sowmeya, Angira, Renu, Kushagra, Amitha for all the help and companionship that I received from them. I thank all the summer students who worked with me for their valuable contribution to the work. *A special thanks to Avijit and Murthy for guiding me during the initial phase of my Ph.D. and for all the insightful discussions we had.*

Feeling like home has nothing to do with geography, it's all about being surrounded by the right people. It is a pleasure to thank all my **friends** at JNC- Disha, Priyank, Vamsee, Suchi, Pahwa, Paramita, Vijaya, Nikita for making the hostel life enjoyable and memorable. A big thanks to Shikha, Kataria, Jayati, Natasha for being there always!

Mom and Dad, thank you for all the support and prayers. I have always felt that you believed in my potential. You raised me to believe that I could do whatever I set my mind to, and without your support, I would likely never have attempted this degree. **Dev bhaiya and Nidhi**

you guys have shown me that any goal can be achieved with hard work. You both have always been my source of inspiration. *Thank you for all the love and support!*

Finally, this Ph.D. and life would have been nothing without you. My sincere gratitude to **SadhGurudevji, Gurumaji, Bhaishreeji and BSLND family** for all the love, support, training and blessings. *Whatever I am is all because of you, Gurudevji. This Ph.D. is a small offering to you.*

Mahima

November 2020

Preface

The interplay between the transition metal dopants and the host in doped semiconductors play an important role in determining their properties and implementing them in technologies. These dopant-host interactions become more significant in the case of quantum dots because of the strong confinement effects and high surface to volume ratio. However, further progress of applications is dependent on the development of reliable doping techniques. In this thesis, entitled “*Structure, Magnetic and Magneto-Optical Properties: A Study of the Interplay of Dopants in Quantum Dots*” we have modeled various synthetic and structural aspects to synthesize singly and dual doped quantum dots and have studied their magnetic and magneto-optical properties. This thesis is divided into seven chapters:

Chapter 1 The first chapter introduces and reviews the field of doping in semiconductor quantum dots. The concept of doping and problems associated with the aggregation of dopants in nanocrystals are discussed together with the recent advances in properties of dilute magnetic semiconductor quantum dots with emphasis on their magnetic and magneto-optical aspects.

Chapter 2 In this chapter we describe briefly the advanced techniques that have been employed to study different nanocrystal systems reported in this thesis, like transient absorption spectroscopy, extended x-ray absorption fine structure, magnetic circular dichroism followed by a discussion on various characterization techniques used to study the doped quantum dots in the thesis.

The research findings of the work are divided into two sections in the thesis. **Section I** discusses the study of surface properties of the undoped nanocrystal host and the spintronic-like properties of singly doped nanocrystals which is divided into chapter 3 and 4 respectively.

Chapter 3 involves the study of vibrational dynamics in CdS nanocrystals using the ultrafast pump-probe technique. The long-lived excited state in CdS nanocrystals sheds light on the defect-free nature of these systems arising from the absence of surface states and are used as an appropriate platform for the study of vibrational dynamics. Transient absorption experiments near-resonance excitation and off-resonance excitation were performed to study the vibrational cooling mechanism in these defect-free CdS nanocrystals. We have utilized this robust system to study the dopant-host interactions within the subsequent chapters.

Chapter 4 focuses on the study of Fe-host interactions in the doped system. Fe doping in semiconductor nanocrystals has largely been treated as uninteresting from the spintronics perspective, due to the absence of an energetically accessible second spin state. In this chapter, we demonstrate that uneven interaction of the two spin states, in a singly doped Fe ion in spatially confined CdS nanocrystals, produces two magnetically inequivalent excitonic states upon mild optical perturbation using ultrafast pump-probe spectroscopy and density functional theoretical analysis. We demonstrate the presence of the Magneto-Optical Stark Effect (MOSE) for the first time by studying the magneto-optical interactions of the dopant states with the host electronic states in Fe doped CdS lattice.

Further, **Section II** talks about dual doping in semiconductor nanocrystals where dual doping can introduce new synergistic properties that are otherwise not present in the individually doped systems. Here, we have discussed the challenges associated with dual doping in quantum dots as it has not been viable to dual dope quantum dots deftly with reproducibility. In chapter 5 we have addressed various synthetic and structural aspects for dual doping followed by studying their magnetic and magneto-optical properties in chapter 6 & 7.

Chapter 5, Part A discusses dual doping as a powerful way to tailor the properties of semiconductor nanocrystals arising out of host-dopant and dopant-dopant interactions. Nevertheless, it has seldom been explored due to a variety of thermodynamic challenges, such as the differential bonding strength and diffusion constant within the host matrix that integrates with the host in dissimilar ways. This chapter discusses the challenges involved in administering them within the constraints of one host. In addition, the various forces in play, such as Kirkendall diffusion, solid- and liquid-state diffusion, hard acid soft base interaction with the host, and the effect of lattice strain due to lattice mismatch, are studied to understand the feasibility of the core to doped transformation. We present experimental evidence that suggests that the Kirkendall effect and lattice strain can initiate the diffusion reactions of binary alloys into the II-VI semiconductor matrix. **Part B** describes that the precise control of crystal orientation, and specifically the exposed surface, is critical for the engineering of heterostructures. We have demonstrated the importance of surface morphology and surface energetics to stabilize the metastable structures of the heterostructures using CoPt as a model system. Different heterostructures are grown ranging from core/shell structure, diffused interface, dumbbell structured dimers, and embedded island structures wherein these hybrids are fabricated via micro/macrolevel facet-selective growth.

Chapter 6. In this chapter, we have synthesized clustered and diffused systems of CoPt in the host CdS matrix to systematically study the effects of clustering on magnetic and magneto-optical properties. Clustering in most cases has been random and irreproducible and the microscopic origin of these effects has so far not been established. In the current study, low magnetic and magneto-optical response has been attributed to the clustering of dopants within the host lattice. After studying the effect of clustering, we have studied the magnetic and magneto-optical of these dual-doped systems. In **Part B**, the role of diamagnetic Pt spacer between the ferromagnetic Co dopants has been studied. Similar-sized diffused nanocrystals of Co doped CdS were considered for the comparative magnetic and magneto-optical study with the Co, Pt co-doped nanocrystals where the magnetic and magneto-optical properties give evidence of magnetic exchange interactions happening in these systems assisted by the local environment.

Chapter 7 This chapter discusses the magnetic properties of CdS nanocrystals simultaneously doped with Fe and Co with varying Fe/Co compositions. The co-doped nanocrystals show magnetic properties that are different from the singly doped counterparts. Interestingly, co-doped samples show that cobalt is able to assist in the magnetic ordering of ferromagnetic iron in CdS nanocrystals at low temperatures as well as at room temperature.

Abbreviations

CB	conduction band
CBM	conduction band minimum
DFT	density functional theory
DMS	dilute magnetic semiconductor
ED	electron diffraction
EDS	energy dispersive x-ray spectroscopy
ES	excited state
EXAFS	extended x-ray absorption fine structure
FC	field cooled
FEG	field emission gun
GS	ground state
HAADF	high-angle annular dark-field
HSAB	hard and soft acids and bases
ICP-OES	inductively coupled plasma-optical emission spectroscopy
ICSD	inorganic crystal structure database
IFT	inverse Fourier transform
LCP	left circularly polarized
LFT	ligand field transition
MAE	magnetic anisotropy energy
MBE	molecular beam epitaxy
MCD	magnetic circular dichroism
MCPL	magnetic circularly polarized photoluminescence
MOSE	magneto-optical Stark effect
NCs	nanocrystals
OA	oleic acid
ODE	1-octadecene
OlAm	oleylamine
OSE	optical Stark effect
PB	photobleaching
PDOS	projected density of states
PL	photoluminescence
PXRD	powder x-ray diffraction
QD	quantum dot
QY	quantum yield
RCP	right circularly polarized
SAED	selected area electron diffraction
SILAR	successive ionic layer adsorption and reaction

SQUID-VSM	superconducting quantum interference device - vibrating sample magnetometer
STEM	scanning transmission electron microscopy
TA	transient absorption
TEM	transmission electron microscopy
TM	transition metal
UV	ultra-violet
VB	valence band
VBM	valence band maximum
XANES	x-ray absorption near edge structure
XAS	x-ray absorption spectroscopy
XRD	x-ray diffraction
ZFC	zero-field cooled

Table of Contents

Declaration.....	iii
Certificate.....	v
Acknowledgements.....	vii
Preface	xi
Abbreviations.....	xv
Chapter 1. Introduction	1
1.1. Summary.....	3
1.2. Challenges in doping quantum dots: Synthesis and characterization	4
1.3. Doping methods.....	7
1.3.1. Extrinsic doping.....	7
Charge injection method.....	8
Ligand modulated quantum dot reduction	9
1.3.2. Intrinsic doping.....	10
Nucleation and growth doping.....	10
Ion diffusion methods	13
Cation exchange.....	14
Diffusion doping.....	14
1.4. Open challenges.....	20
1.5. Dilute magnetic semiconductor quantum dots.....	22
1.6. Properties of DMS QDs.....	26
1.7. Present study	32
Bibliography	35
Chapter 2. Methodology	47
2.1. Summary.....	49
2.2. Experimental techniques.....	49
2.2.1. X-ray absorption fine structure spectroscopy	49
2.2.2. Transient absorption spectroscopy.....	52

2.2.3. Magnetic circular dichroism.....	53
2.2.4. SQUID magnetometer.....	54
2.2.5. X-ray diffraction.....	55
2.2.6. Transmission electron microscopy.....	56
2.2.7. UV-visible absorption.....	57
2.2.8. Inductively coupled plasma optical emission spectrometry.....	58
Bibliography.....	60
Section I. Doping in semiconductor nanocrystals	
Chapter 3. Ultrafast electron-hole relaxation dynamics in CdS nanocrystals	61
3.1. Summary	63
3.2. Introduction	63
3.3. Experimental section	65
3.4. Results and discussion.....	67
3.5. Conclusion.....	74
Bibliography.....	76
Chapter 4. Magneto-optical Stark effect in Fe doped CdS nanocrystals	79
4.1. Summary	81
4.2. Introduction	81
4.3. Experimental/theoretical details	83
4.4. Results and discussion	86
4.5. Conclusion.....	102
Bibliography.....	103
Section II. Dual doping in semiconductor nanocrystals	
Chapter 5. Part A. Dual doping in nanocrystals via Kirkendall diffusion	107
5.1.1. Summary	109
5.1.2. Introduction	109
5.1.3. Experimental section	112
5.1.4. Results and discussion	114
5.1.5. Conclusion.....	122
Bibliography.....	123

Chapter 5. Part B. Heterostructure modeling through crystal facet engineering	129
5.2.1. Summary	131
5.2.2. Introduction	131
5.2.3. Experimental section	133
5.2.4. Results and discussion	136
5.2.5. Conclusion	146
Bibliography	147
Chapter 6. Part A. Probing the effect of clustering of dopants on magnetic and magneto-optical properties of Co, Pt co-doped CdS nanocrystals	151
6.1. Summary	153
6.2. Introduction	153
6.3. Experimental section	155
6.4. Results and discussion	158
6.5. Conclusion	168
Chapter 6. Part B. Effect of Pt co-doping on magnetic and magneto-optical properties of Co, Pt doped CdS nanocrystals	169
6.6. Summary	169
6.7. Results and discussion	169
6.8. Conclusion	175
Bibliography	176
Chapter 7. Magnetism in Fe, Co dual doped CdS nanocrystals	179
7.1. Summary	181
7.2. Introduction	181
7.3. Experimental section	182
7.4. Results and discussion	186
7.5. Conclusion	196
Bibliography	197
Appendix, AWSAR Story, Nature’s play in dual doping of quantum dots ...	201
List of Publications	207

CHAPTER 1

Introduction

The following review articles have been published based on this chapter.

- Recent advances in magnetic ion-doped semiconductor quantum dots.
Curr. Sci. 2017, 112, 1421-1429.
- Frontier challenges in doping quantum dots: Synthesis and characterization.
RSC Adv. 2018, 8, 22103-22112.

1.1 Summary

Impurity doping in semiconductor quantum dots (QDs) has numerous prospects in implementing and altering properties and technologies.¹⁻² In this thesis, we discuss the state of the art doping techniques arising out of the colloidal synthesis methods. We first discuss the advantages and challenges involved in doping followed by various doping techniques including clustering of dopants as well as an expulsion out of the lattice due to self-purification. Some of the techniques are shown to open up a new generation of robust doped semiconductor quantum dots with cluster free doping, which will be suitable for various spin-based solid-state device technologies and overcome the longstanding challenges of controlled impurity doping.³⁻⁴ Further, we discuss the inhibitors like defects, clustering and interfaces followed by current open questions. These include pathways to obtain uniform doping in the required radial position with unprecedented control over dopant concentration and size of the QDs.⁵⁻⁶

Thus, these dilute magnetic semiconductor (DMS) QDs have the potential to be used as basic working components of spin-based electronic devices.⁷⁻⁸ Therefore it is important to study these materials from fundamental and technological viewpoints. Quantum confinement effects are known to enhance exchange interactions in these doped QDs and induce properties that were previously not observed in bulk materials. Properties are known to alter dramatically when dimensions are reduced to nanometre size regime. We further discuss the recent advances in physical (properties) aspects of DMS QDs with emphasis on their magnetic, magneto-optical and magneto-electrical properties arising from the cooperative effects of spin-exchange interactions.

Although doping constitutes an important branch to modulate the properties of II-VI semiconductors, the studies are majorly limited to one type of dopant.⁹⁻¹⁰ However, dual-doping in QDs is an emerging field where synergistic properties can be obtained from the same material that are not present in the individually doped systems. Further optical properties are well explored in singly doped systems¹⁰⁻¹³ and to some extent in dual doped II-VI semiconductors.¹⁴ This is because the optical properties arising out of the dopants can be ascertained to specific features or optical bands. However, magnetic properties are not well explored because of the complications associated with the origin of magnetism if they are from the clustering effect or the dopant host interactions. This is further assisted by the lack of probes to study the origin of magnetism.

1.2 Challenges in doping quantum dots: Synthesis and characterization

Intentional electronic doping into semiconductor QDs has attracted growing interest as impurity ions within the quantum dot lattice can impart desirable properties like optical,^{11, 15-16} magnetic,^{15, 17-20} electrical²¹ and electronic²²⁻²³ properties. Also, doped QDs because of their substantial ensemble Stokes shift avoid self-quenching problems in QDs. These doped dots combine both magnetic and semiconductor properties into a single optoelectronic material making them excellent candidates for solution-processed photovoltaics,²⁴⁻²⁵ photodetectors,²⁶⁻²⁸ light-emitting diodes²⁹⁻³⁰ and spin-photonic applications specifically in this era of miniaturization of devices into nanoscale dimensions. Doping colloidal QDs with aliovalent elements that can act as electron donors or acceptors and is a very promising approach to introduce electrical functionality.³¹⁻³³

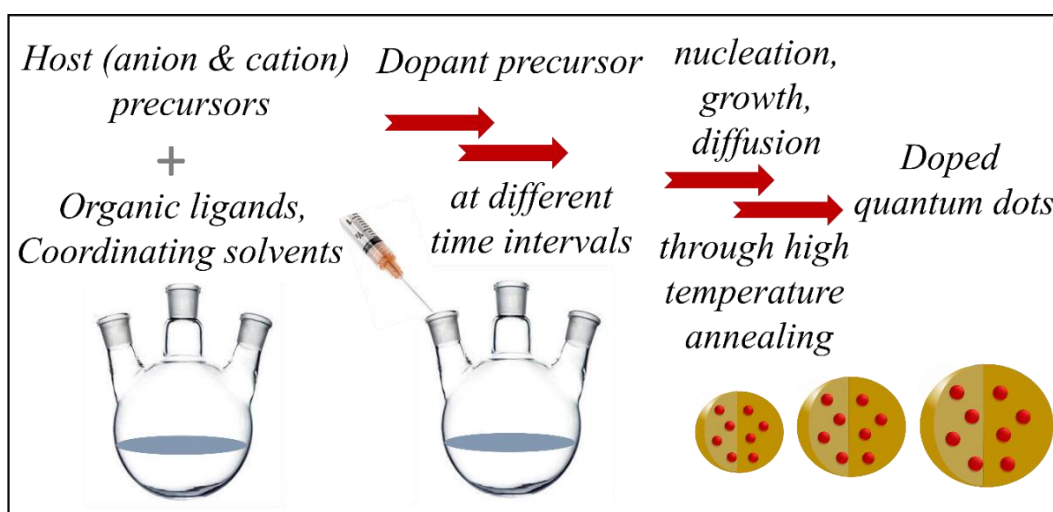


Figure 1.1: General colloidal synthesis schematic of organic ligand capped doped quantum dots.

Some of the sample properties arising from successful incorporation of impurity ions in the semiconductor matrix include giant Zeeman splittings of excitonic excited states introduced by strong dopant-carrier exchange coupling, red-shifted photoluminescence (PL) emission band arising either out of dopant d - d levels or the interaction of the dopant d level with the host and several other applications.³⁴⁻³⁸ The unpaired spins of these open-shell transition metal dopants are magnetically or optically coupled to the free and photogenerated charge carriers wherein the dopant-carrier spatial overlap determines the coupling strength. These sp - d exchange interactions are characteristic features resulting in

magneto-optical and/or magneto-transport properties.³⁹ In fact, the properties and applications have been extensively studied in literature and have also been reviewed in several recent reviews.^{37,40-41} However, further progress of these applications is dependent on the development of reliable methods for effective incorporation of impurities into the semiconductor matrix wherein the dopant ions substitute host atoms in the QDs and are not just adsorbed on the QD surface.

Until recently, these properties have been exploited in devices where doped semiconductors are fabricated using molecular beam epitaxy.⁴² However, the colloidal methods for doping in semiconductor QDs to produce reliable electronic functionalization leading to efficient solid-state devices have attracted significant attention in recent years due to their flexibility in composition, size control and cost-effectiveness.⁴³⁻⁴⁴ Further, with the miniaturization of devices being the order of the day, use of smaller functional materials is important. However, this is riddled with several problems arising due to quantum confinement and have to be overcome to obtain high-quality materials. This has been recognized early on by the community and the synthesis of high-quality functional materials has been extensively studied in the literature. Colloidal synthesis is one of the effective methods to produce highly crystalline QDs. The colloidal synthesis was first reported by Murray, Norris and Bawendi for CdS, CdSe and CdTe QDs.⁴⁵ The high-temperature colloidal synthesis involves pyrolysis of host precursors at high temperatures in the presence of organic ligands followed by nucleation and growth. The high-temperature annealing of QDs facilitates the formation of defect-free dots. Figure 1.1 illustrates a general schematic for the colloidal synthesis of doped QDs wherein dopant precursor can be added at different time intervals, along with the host precursors or at the time of nucleation and growth at appropriate temperatures depending upon the diffusivity of the dopant ions.

In this chapter, we mainly focus on the different concepts adopted for an effective synthesis of doped QDs using the colloidal approach and then explore the properties of these doped QDs.

Early attempts to incorporate dopants within QDs included the stoichiometric addition of the dopant precursor with the host precursor.⁴⁶⁻⁴⁷ In the colloidal synthesis of QDs, the dopant ions were introduced into the semiconductor matrix using metal-organic precursors or metal-salt precursors that is significantly different from doping the bulk counterparts where a pure solid-state reaction at high temperature is used to drive the dopants into the

host matrix. However, it was soon realized that it is not possible to seamlessly include dopant ions within the host lattice even though recently researchers have demonstrated the inclusion of a high percentage of dopants with appropriate controls using stoichiometric addition.⁴⁸ While doping these QDs, only a small fraction of the dopants added is incorporated into the crystal lattice while a large proportion of the dopants remain on the surface or form clusters.⁴⁹⁻⁵⁰ Energetically, it is more favorable to form clusters of dopant ions or segregate into a separate phase or be adsorbed on the host surface. While various characterizations were developed to distinguish between the surface adsorbed ions and those doped into the lattice,⁵¹ the success of this kind of method was limited. Hence it was also important to design clever techniques to stabilize these metastable phases of the dopant ion within the host lattice.

Based on the successes and failures of the stoichiometric addition, researchers were largely driven towards the understanding of the various steps involved in the dopant incorporation and subsequent stabilization of the dopant within the lattice. The current understanding of the mechanism of dopant incorporation within the QDs using colloidal methods is still largely limited. One of the early models based on surface kinetics suggests that doping during the growth of the QDs is controlled by adsorption of impurity ions on the surface of the QD.⁵²

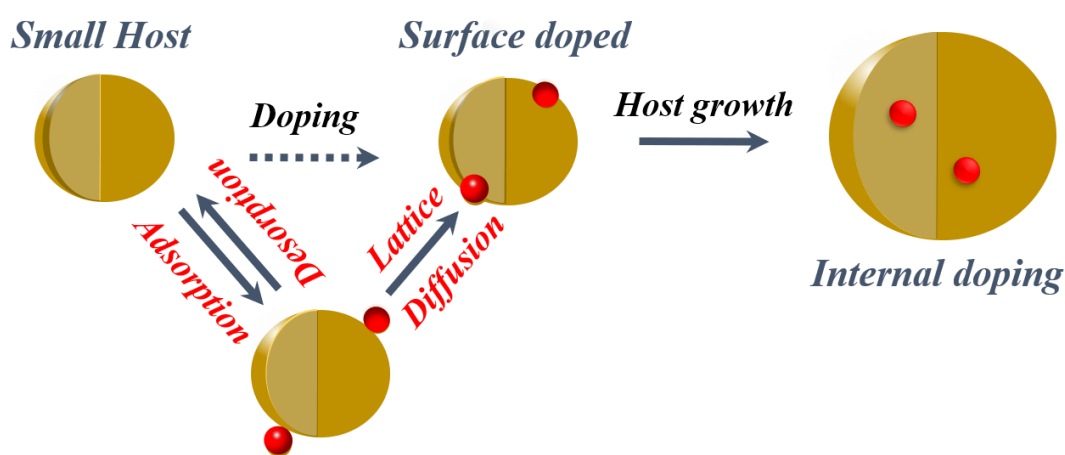


Figure 1.2. Schematic shows the illustration of temperature-dependent dopant lattice diffusion.

Thus, it is expected to be an extrinsic problem and can be controlled by controlling the kinetics of the QDs. However, it has been seen that impurity ions are unstable inside the host thermodynamically due to higher formation energy of defects, indicating the intrinsic

difficulty in doping QDs as exhibited by the self-purification model.⁵³⁻⁵⁵ Thermodynamics suggests that the impurity ion defect formation energy is quite high. However, in solution phase synthesis at low temperatures, kinetics rather than thermodynamics governs the growth of the QDs where the kinetic factors control the dopant incorporation in the host lattice. Recently, Chen et al.⁵⁶ have studied the various elementary processes involved in the doping of QDs using solution route methods. They identified the presence of four individual processes, namely surface adsorption, lattice incorporation, lattice diffusion and lattice ejection, with a critical temperature characterizing each of the processes as shown in the schematic in figure 1.2. They further characterize effective doping into suitable programming of reaction temperatures to accommodate all the individual processes. However, with intuitively contrasting processes being involved, generic extension into the synthesis of any QD was largely limited.

Very recently it was shown by Saha et al.^{43,57} that the problem of doping is highly intricate, involving several thermodynamic factors such as diffusion constant of the dopant within the host lattice, bond dissociation energy of the dopant metal precursor. However, they also showed the bonding energy of the dopant with the host anion does not play a major role in the systems studied by them. In this case, they made constructive use of the self-purification process and hence the initial adsorption of the dopant ion on to the lattice was not relevant. Although there has been tremendous progress in recent years, uniform doping with desirable compositions remains a challenge in colloidal QDs due to clustering and phase separation, motivating the development of new techniques. Researchers have been exploring this long-standing problem of introducing impurity ions into QDs and strategies are beginning to emerge that apply to diverse doping compositions. Here we enumerate various techniques for doping from the literature along with their achievements and their limitations with an emphasis on recent progress in the development of cluster free transition metal-doped QDs through synthetic engineering of composition, size, and interfaces.

1.3 Doping methods

Impurity doping into QDs can be largely classified into extrinsic and intrinsic doping.

1.3.1 Extrinsic doping

The various options involved in extrinsic doping can be majorly divided into the charge injection method and the use of appropriate surface ligands to induce functionality into QDs.

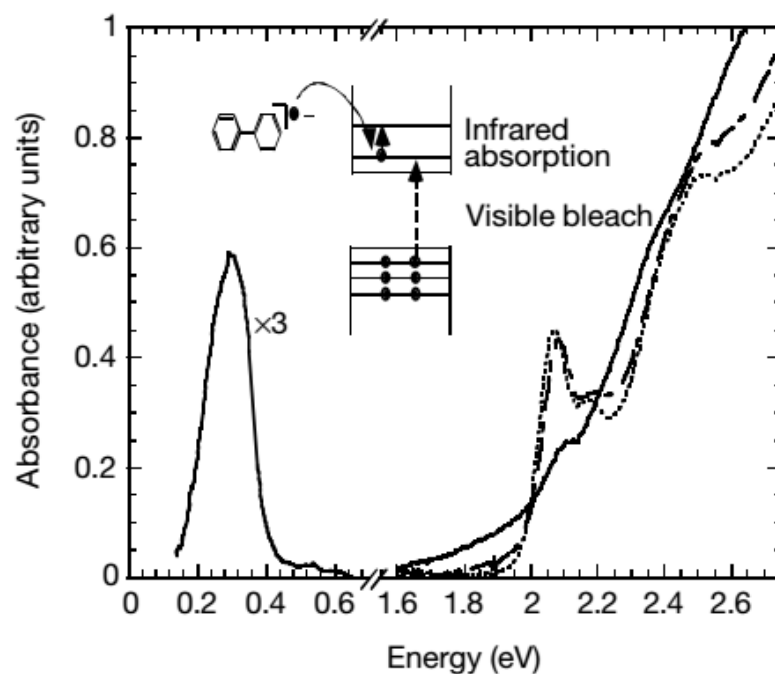


Figure 1.3. Absorption spectra of CdSe nanocrystals before (dotted line), immediately after (solid line), and 27 hours after (dashed line) the addition of sodium biphenyl reagent. The concurrent optical bleach of the first two exciton transitions and the appearance of the infrared absorption is seen. The blue-shift of the optical spectra after the disappearance of the infrared absorption suggests that the n-type nanocrystals decompose by the loss of the outermost layer of the semiconductor. Adapted with permission from ref 47.

Charge injection method: The conventional doping method of introducing impurity atoms was unsuccessful in many of the early cases as the impurities tend to be expelled from the small crystalline cores as well as thermal ionization of the impurities (which provides free carriers) was hindered by strong confinement. One direction towards overcoming these shortcomings included the extrinsic injection of dopant ions. Guyot-Sionnest et al.⁵⁸⁻⁵⁹ have investigated colloidal QDs of various materials like CdSe, CdS and ZnO and have shown that they can be reduced to n-type by Na, K, biphenyl radical anions, or electrochemical doping with electrons occupying the quantum confined states of the conduction band. Figure 1.3 shows the infrared and visible absorption spectra of

CdSe nanocrystals after the addition of sodium biphenyl demonstrating bleaching and broadening of the first and second excitonic peaks.

The appearance of the $1S_e-1P_e$ infrared absorption arising at 0.3 eV confirms n-type character of the nanocrystals. They showed stability of hours to days at room temperature and the authors predicted further improvements. They also showed that the electron occupation of the $1S_e$ state dramatically affects the optical properties, creating the possibility for strong electrochromic response in the visible and mid-infrared regions. The other opportunities include the study of the conductivity of films of n-type QDs due to their enhanced inter-QD electron transfer leading to photovoltaic or electronic applications.^{58,60} However, all these measurements were carried out in an inert atmosphere and exposure to air accelerated the decay within minutes making the charge injection method highly specific and impractical for wide-scale use in applications.

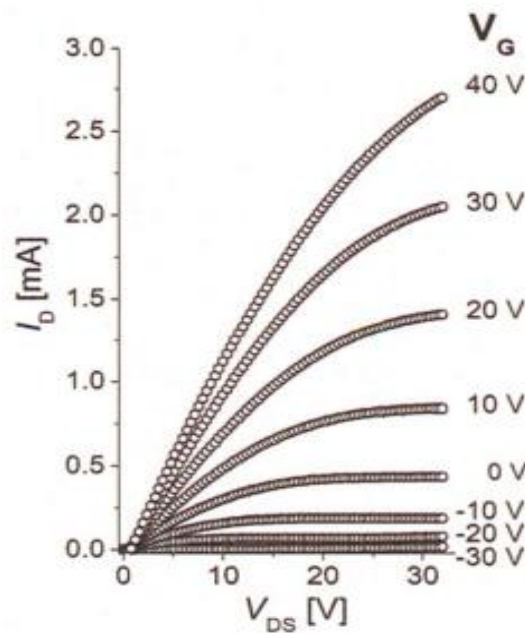


Figure 1.4. The plot of drain current I_D versus drain-source voltage V_{DS} , as a function of gate voltage V_G for a nanocrystal FET with a channel composed of 8 nm PbSe nanocrystals treated with hydrazine solution for 12 hours. Adapted with permission from ref 50.

Ligand modulated QD reduction: One of the other extrinsic doping techniques includes the treatment of the QD surface with a Bronsted base like hydrazine that replaces bulky

oleic acid groups reducing the intermolecular spacing as well as passivating the dangling bonds on the surface by the lone pair of electrons on the base similar to the primary amines. This also assists in improving the conductivity of the QD solids increasing the functionality of the QDs in places like field-effect transistors as shown in figure 1.4 where the conductance of PbSe nanocrystal solids was observed to increase by 10 orders of magnitude after hydrazine treatment. However, the widespread applicability of this technique, though demonstrated on a wide range of materials, is rather limited due to the unstable nature of these ligands.⁶¹

More recently, the hydrazine molecules are replaced by more environmentally benign and stable molecules demonstrating the further applicability of this method.⁶²

1.3.2 Intrinsic doping:

Despite these limited successes, extrinsic doping is not a very feasible option to impart other functionalities like magnetic, optical and optoelectronic functions. Hence it is important to come up with methodologies for efficient intrinsic doping of the dopant ions.

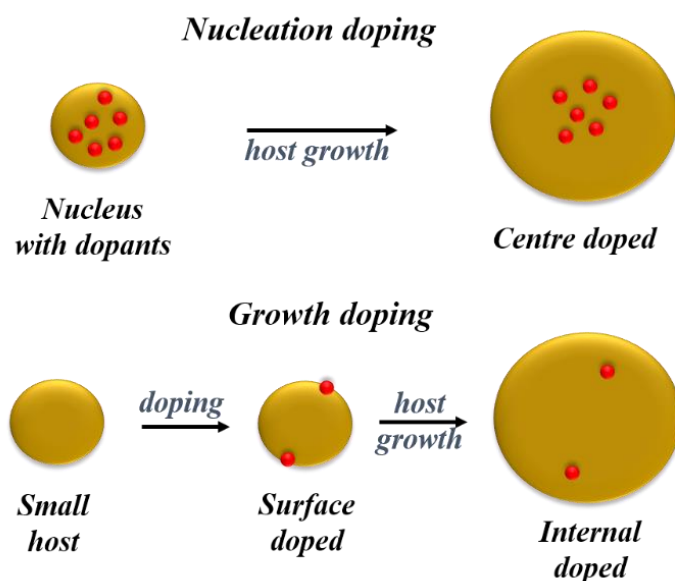


Figure 1.5. Schematic of the proposed radial position of dopant in nucleation- and growth-doping.

Nucleation and growth doping: Though doping had been extensively carried out and high-quality QDs have been obtained in some cases, mechanistically important methods were first proposed by Pradhan et al.⁶³ for doping of Mn and Cu in ZnSe based systems.

To accommodate the differential reactivities of the dopant and host precursors, they proposed methods to decouple the two using either nucleation or growth doping to effectively dope these QDs as shown in figure 1.5. In the case of nucleation doping, the small dopant compound was first formed. These core nuclei are then overcoated with a host shell resulting in a graded alloy or sharp interface depending on the conditions.

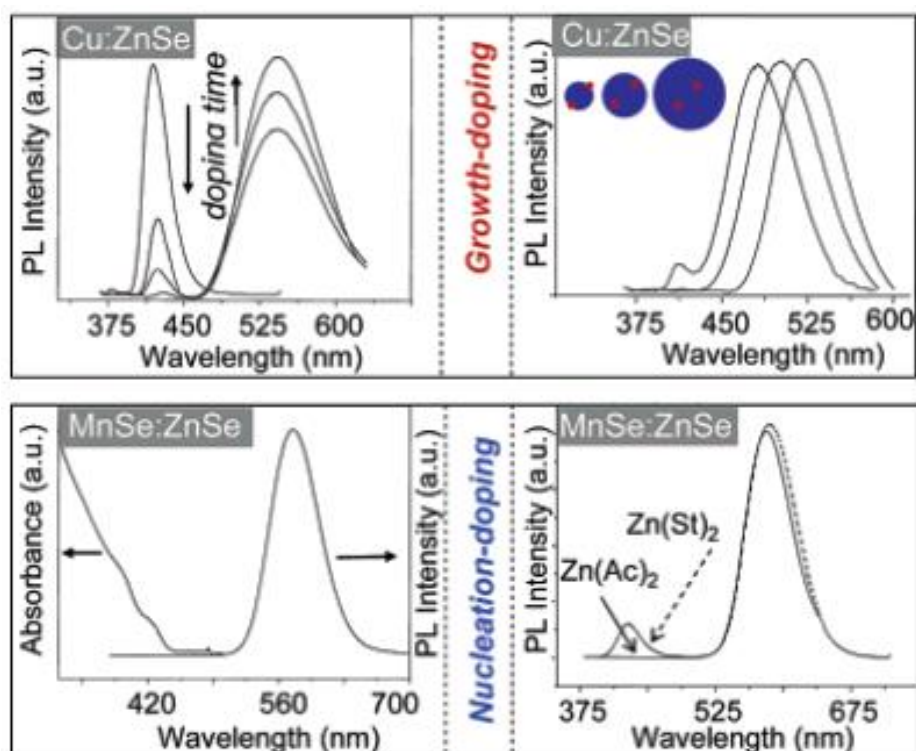


Figure 1.6: Spectroscopic presentation of nucleation- and growth-doping. Adapted with permission from ref 52.

However, in the case of growth doping, they demonstrated the formation of small host QDs, followed by surface adsorption of the dopant ion at reduced temperature and dopant metal precursor addition. Isocrystalline or hetero-crystalline shells are then grown to encapsulate the dopant ions demonstrating widespread applicability.^{15, 64} Prototype example for this proposed mechanism was carried out for Cu or Mn doped ZnSe QDs and is shown in figure 1.6 wherein effective doping and decoupling from nucleation and growth is indicated by the increase of the photoluminescence (PL) intensity of the dopant emission and decrease in the PL intensity of the host (top, left). Regrowth of ZnSe on the surface of doped QDs results in the redshift of PL (top, right). The above process would have gone ungovernable without the decoupling technique as it took 100 minutes to

complete. However, nucleation doping was realized for Mn doped ZnSe using different dopant precursors. The Mn^{2+} precursor should be less reactive than Zn^{2+} precursor with the same ligand, as Mn^{2+} is a harder Lewis acid compared to Zn^{2+} . Zinc acetate was preferable for the formation of MnSe: ZnSe nanocrystals as compared to zinc stearate when manganese stearate was used as the precursor for the nucleation step. Zinc stearate needed higher reaction temperature causing homogeneous nucleation of ZnSe, resulting in bandgap PL as shown in figure 1.6.

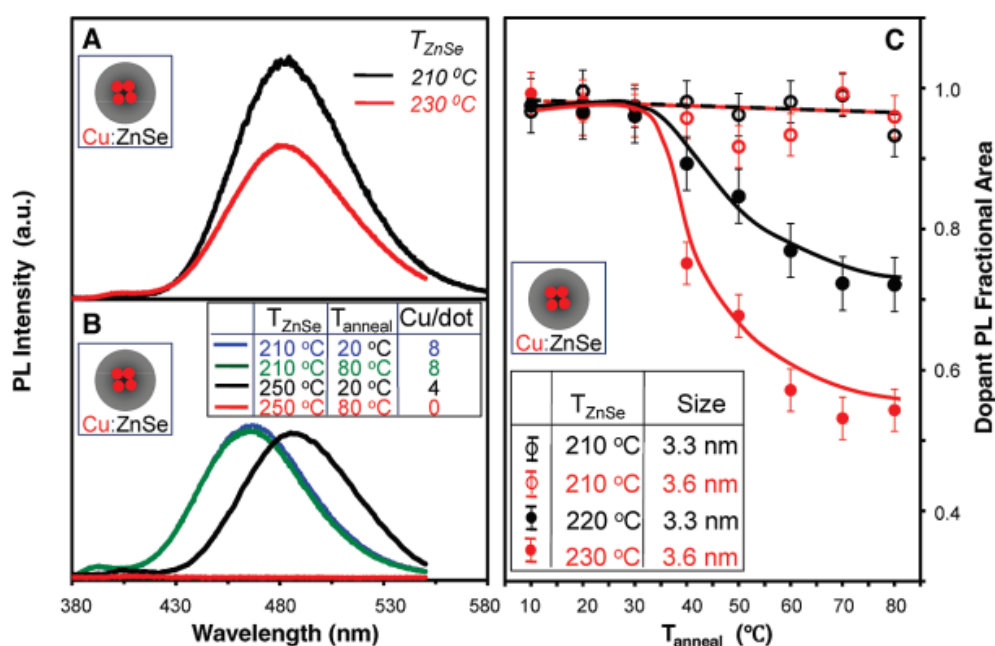


Figure 1.7 (a) PL spectra of similar-size Cu doped ZnSe QDs prepared at different ZnSe overcoating temperatures (T_{ZnSe}), 230 °C and 210 °C. (b) PL spectra of Cu doped ZnSe QDs with T_{ZnSe} of 250 °C and 210 °C, and their corresponding spectra after thermal annealing at 80 °C (T_{anneal}). The inset table shows the number of Cu ions per nanocrystal (Cu/dot) for the four samples. (c) Fractional area of the Cu dopant PL of the Cu doped ZnSe QDs as a function of thermal annealing temperatures (T_{anneal}) for different overcoating temperatures and different sizes of the nanocrystals. Cu dopant PL at its maximum brightness for each case was set as 1. Adapted with permission from ref 45.

However, the major drawback of this technique is the high-temperature annealing during growth of the shell resulting in the expulsion of dopants and they ultimately leach out of the surface undergoing self-purification. This was explicitly verified in the case of Cu doped ZnSe QDs as shown in figure 1.7. It is evident from the figure that the overcoating

at 210 °C contained the dopants within the host lattice without the diffusion of dopants from the nucleus to the surface. However, upon annealing at 220 °C or higher, ejection of the dopants from the lattice was observed for all sizes as shown in figure 1.7 (a), (b), (c). Additionally, with an increase in overcoating temperature, significant quenching of the dopant PL was observed upon annealing between 20 and 80 °C (figure 1.7 (c)). Thus, overcoating ZnSe at higher temperatures results in dramatic diffusion of Cu dopants towards the surface. Hence despite extended efforts from various groups on different systems to obtain internally doped QDs, it has not been possible to obtain internally doped QDs.

More recently, Manna et al.⁶⁵ have used the concept of magic-sized metal clusters held together by stable metal to metal bonds to seed the growth of QDs to obtain more uniformly doped QDs. They have used clusters composed of four copper atoms (Cu₄) capped with d-penicillamine to seed the growth of CdS QDs in water at room temperature which acts as a quantized source of dopant impurities. While the authors claim an insensitivity of the optical properties to external factors and surface changes, the major drawback of this technique is the clustering of the dopant ions leading to the absence of dopant- host interactions, at least within the first shell of atoms. This could also lead to the insensitivity of the doped QDs to the external factors. Hence while uniform dots are obtained from this method, this method also ensures clustering of dopant atoms, albeit limited to the first shell of atoms.

Ion diffusion methods: In all these cases, the major bottleneck preventing the application of the above-mentioned doping methods to a variety of materials is the constant battle against the inherent nature of the system to expel the impurity atoms to minimize the energy of the system. Hence until recently, doping in QDs has remained a challenge. However, amongst the multitude of techniques, two techniques differ in this aspect wherein ion diffusion has also been used as a potential strategy for doping. The cation exchange method and the diffusion doping method have made productive use of the self-purification nature instead of combating it. In the cation exchange method, dopants ions through diffusion are incorporated into the preformed hosts⁶⁶ whereas, in the diffusion doping method, the dopants are formed as a clustered solid and allowed to diffuse out along with the growth of the host solids. In these cases, host dopant precursor reactivity can be controlled by tuning the metal-ligand bond strength.⁶⁷

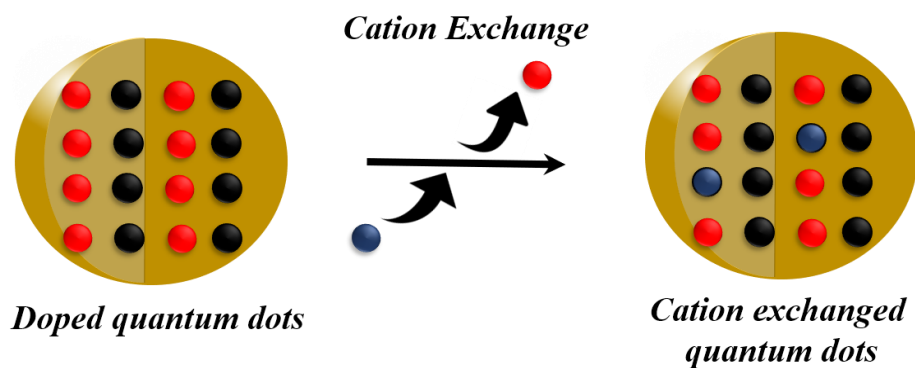


Figure 1.8. Schematic for cation exchange.

Cation exchange: Cation exchange reactions are widely applied for doping QDs where the cation of the QDs can be exchanged with dopant cations.^{44, 68-69} A typical scheme for the cation exchange is shown in figure 1.8. TEM images of a specific example of doped nanocrystals in the case of Mn doped CdSe are shown in figure 1.9. Varying the solution concentration of the incoming dopant cations and the nature of ligands attached to them can tune the extent of cation exchange. However, these processes are not very trivial in semiconductor QDs as ascertained by the high energetics involved in doping. Additionally, clustering or directional doping based on the reactivities is the inherent nature of this doping technique. While the directional nature has been used constructively to obtain different hetero-structure morphologies, clustering of dopant ions does not allow for uniform doping of impurities.⁷⁰⁻⁷²

Diffusion doping: Diffusion doping, first designed by Saha et.al, on the other hand, has also used the self-purification technique as an aid instead of trying to combat this problem even though it was once considered a hindrance.⁴³ Here a small magnetic core was overcoated with a thick shell of the host semiconductor using SILAR (successive ionic layer adsorption and reaction) technique. Annealing this core-shell at high temperature allows diffusion at the interface and into the semiconductor shell and eventually, it diffuses out of the system. The model system studied by Saha et al. was Fe_3O_4 core overcoated with CdS shell as shown in figure 1.10. The strained interface with a lattice mismatch of approximately 4 % and high-temperature annealing drives the diffusion of the core into the shell with a reduction in the size of the core, ultimately leading to uniformly doped QDs.

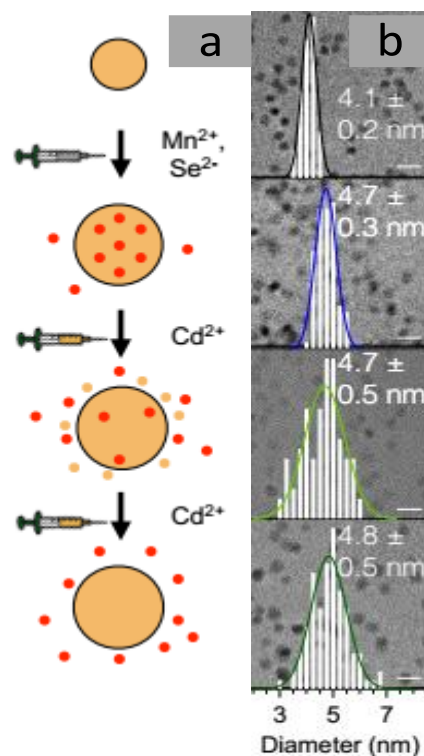


Figure 1.9: TEM images of the Mn doped CdSe. Adapted with permission from ref 33.

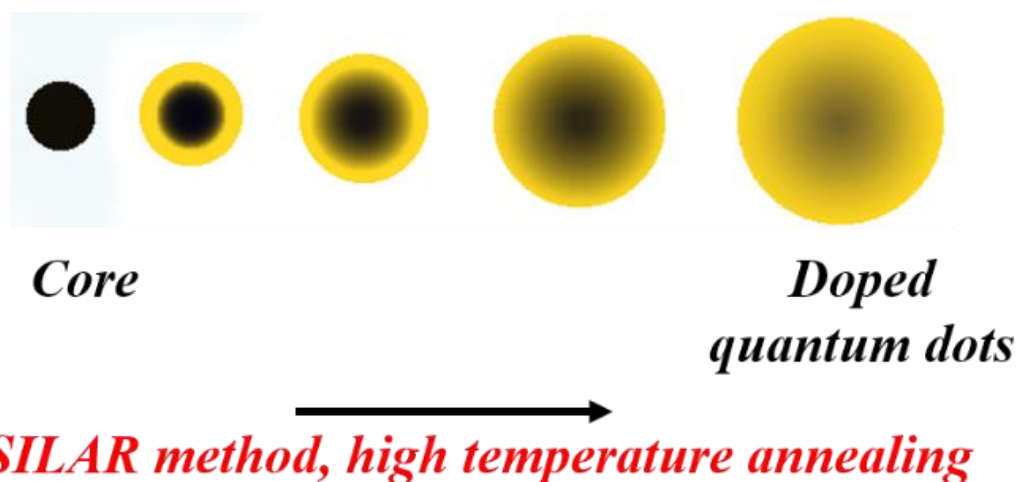


Figure 1.10. Diffusion of dopants into the CdS matrix to get Fe doped CdS QDs.

The controlled diffusion was achieved by controlling the rate of outward diffusion of the core to be slower than the rate of growth of the semiconductor shell. By controlling the parameters like annealing time and temperature as well as bond dissociation energy of the core, effective doping was achieved with control over percentage and uniformity of doping as well as the size of the QDs. Uniform doping has been achieved using different sizes of

oxides and sulfide cores. Local structure investigation through XAFS⁷³ and element-specific mapping through STEM-EDX confirm the uniform distribution of Fe in the CdS matrix precluding any cluster formation as shown in figure 1.11. Thus, this technique has been demonstrated to result in uniformly doped QDs where QDs of different sizes and dopant concentrations have been obtained using inside out-diffusion.

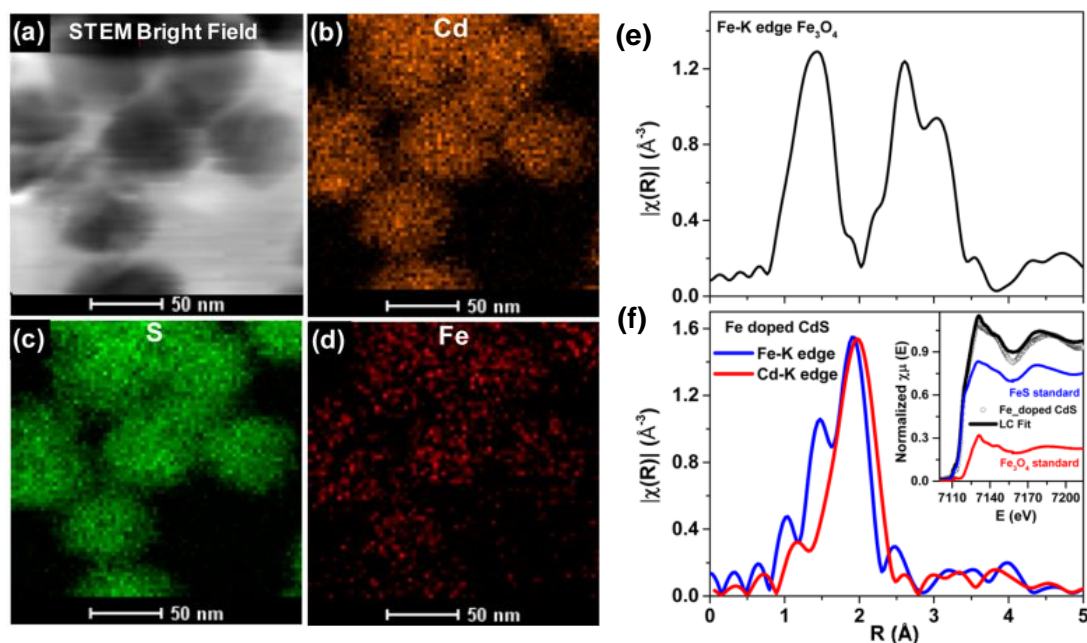


Figure 1.11. TEM elemental map of Fe doped CdS showing STEM (a) bright-field image, (b) Cd map, (c) S map, and (d) Fe map. The magnitude of Fourier-transformed Fe-K edge EXAFS spectra for Fe_3O_4 (e) and a comparison of Fe and Cd K-edge Fe doped CdS (f). The linear combination fit (black solid line) of Fe K-edge XANES spectra with FeS (blue solid line) and FeO standard (red solid line) is shown in the inset. Adapted with permission from ref 32.

EDX elemental mapping in figure 1.11(d) shows clear evidence for the uniform distribution of Fe in CdS matrix. Fe, Cd and S span the complete area of nanocrystal precluding clustering by the Fe_3O_4 core. Also, visual inspection of Fe and Cd K-edge EXAFS data in real space for Fe_3O_4 and Fe-doped CdS QDs show that the local structure around Fe in Fe-CdS is very different than that of Fe in Fe_3O_4 as shown in figure 1.11(e) & (f). However, the local structure around Fe in Fe-CdS matches well with that of Cd in CdS implying that the environment around the Cd atom in Fe-CdS is very similar to that

of Fe. Also, the absence of second nearest neighbor Fe-Fe path further verifies the absence of iron oxide clusters. The inset to figure 1.11(f) shows the XANES spectrum showing a linear combination of Fe₃O₄ and FeS paths for Fe-CdS sample with FeS dominating the contribution. This confirms that Fe has been incorporated into the CdS lattice after undergoing a reduction in oxidation state from +2.66 to +2.

Further, the generality and universality of this technique were established for other dopant ions like M²⁺ (Fe²⁺, Ni²⁺, Co²⁺, Mn²⁺).⁵⁷ The effectiveness of the inside-out-diffusion doping depends on the ability of the core to penetrate the CdS lattice followed by potential of the metal ion to diffuse within the lattice and the ease of cation exchange as shown in the schematic in figure 1.12.

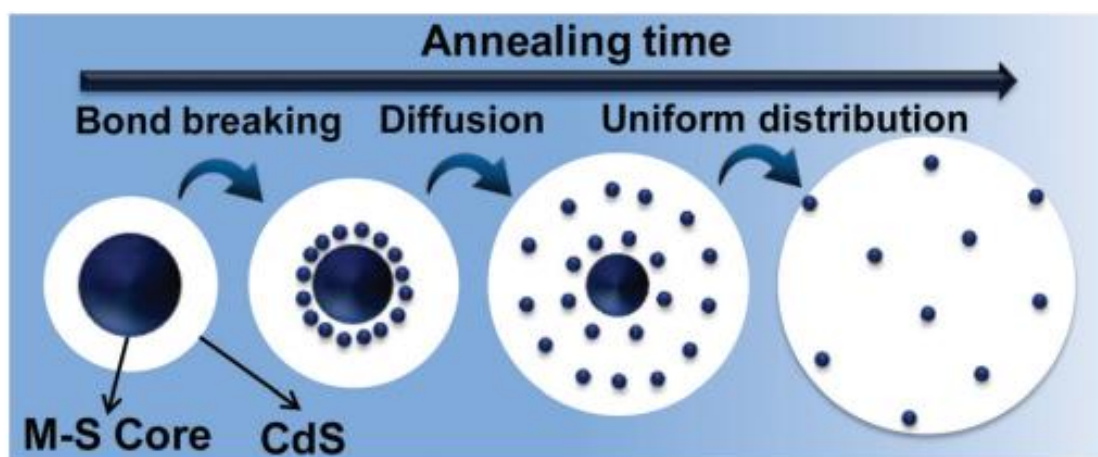


Figure 1.12. The scheme shows the formation of uniformly doped QDs through bond breaking and diffusion of ions inside CdS matrix during thermal annealing. Adapted from ref 46.

Effective doping was confirmed through steady-state optical emission spectra and time-resolved photoluminescence spectra at the dopant peaks, figure 1.13(a) and (b) where these dots showed superior properties as compared to the previous reports. A broad dopant emission peak at a lower energy in the PL steady-state spectra is present only in doped CdS samples suggesting that the emission arises due to dopant states and is not due to surface states. Long-lived time-resolved photoluminescence spectra of the dopant peaks further confirm that broad emission is due to doped states. This work describes efficient doping of various dopants by controlling thermodynamic parameters and the process is

described in three steps, namely diffusion at the interface followed by diffusion of dopant ions within the host matrix and finally the ease of cation exchange.⁵⁷

Factors like differing bond strengths of the cores (sulfides or oxides), diffusing abilities of the dopant ions and ease of cation exchange based on the HSAB effect⁷⁴ are being explored in this work. Here sulfides of (Fe, Mn, Ni, Co) were used as cores as their diffusion into the host CdS lattice is more facile. This highlights the suitability to tailor-make QDs with the required size and dopant percentage. This inside-out diffusion doping is thus a promising technique that endows these cluster free dots with interesting optical and magnetic properties.

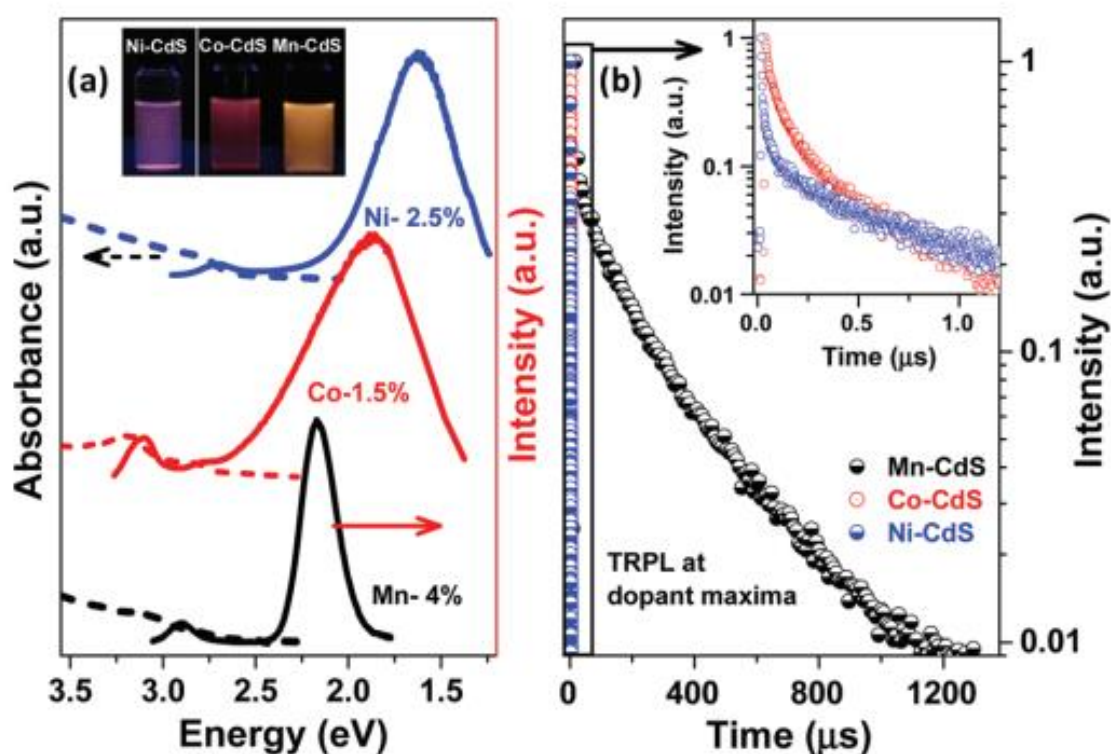


Figure 1.13. (a) Steady-state PL (solid line) and absorption (dashed line) of Ni^{2+} (blue), Co^{2+} (red) and Mn^{2+} (black) doped QDs. (b) Lifetime decay plots for Ni^{2+} , Co^{2+} and Mn^{2+} doped CdS collected at the maxima of the broad dopant peaks. Inset of (b) shows the enlarged portion of the lifetime decay of Ni^{2+} and Co^{2+} doped CdS. Adapted from ref 46.

Table 1.1: A comparison of various doping techniques for QDs.

Doping Method	Advantage	Disadvantage	Ref.
Stoichiometric addition of dopant and host precursor	Inclusion of high percentage of dopants	Small portion gets incorporated, large portion on the surface	46-47
Surface kinetic model	Doping controlled by kinetics	High defect formation energy, self-purification	52
Thermodynamic model	In solution phase at low temperatures kinetics control dopant incorporation	High defect formation energy	53
Charge injection method	No expulsion of dopants	Air accelerated decay, specific, impractical for wide-scale use	58-59
Ligand modulated QD reduction	Passivate dangling bonds, reduces intermolecular spacing	Unstable nature of Bronsted base	61
Decoupling nucleation and growth Doping	Efficient intrinsic doping	High-temperature expulsion of dopants	63
Use of magic-sized dopant clusters	Uniform dots	Clustering of dopant ions within first shell	65
Cation exchange	Productive use of self-purification	High energetics involved	69
Diffusion Doping	Self-purification as an aid, uniformly doped QDs, control over percentage and size of QDs, universal technique, co-doping	Limited by penetration capability of core ions into host lattice, diffusivity of metal ions in host lattice, cation exchange	5, 43, 57

A comparison of various doping techniques discussed above for QDs is summarized in table 1.1. An aspect that has not been addressed much in the QD literature is the efficiency of doping as a function of the size of these dots. This is primarily due to the inability to control the percentage of doping simultaneously with the QD size. Though the doping

efficiency is not expected to vary much from 3-20 nm size regime, this has only been studied recently by Saha et al.^{5, 43} using doped QDs obtained using the diffusion doping method. It should also be noted that in this specific case, a long-range size variation of up to 60 nm with 5% Fe doping has been achieved by appropriately tuning the synthesis conditions, allowing a study of doping efficiency in large QDs, which is specifically critical for the study of magneto-optical and magnetic properties.

1.4 Open challenges

Despite a lot of progress in the synthesis of doped QDs, with the evolution of newer and more facile designs to obtain cluster free QDs, one of the major challenges that remain is the study of the absence of clusters. The other major bottleneck in this field is indeed the absence of appropriate characterization techniques to study the internal structure of QDs. The internal structure of QDs is challenged with several issues including surface and internal defects, clusters, quality of the interface between the dopant cluster and the host that are key players in the determination of the properties of the QDs. For example, it has been extensively demonstrated that the presence of a sharp interface is suitable for a photo-absorbing material in type-II semiconductor.⁷⁵ Similarly, the presence of a smooth interface between the core and the shell is responsible for substantially increasing the quantum yield (QY) of the materials⁷⁶ as well as introducing an exchange bias at the interface of magnetic and non-magnetic materials.⁶ Similarly, surface defects are known to play important role in the determination of the material properties.⁷⁷ The radial position of the dopant atom is key to the determination of the several optical properties.⁷⁸ However, lacking in all these and several other techniques is a good characterization technique to study these parameters, such as defects, clusters, interface and radial position of dopant ions.

To date, only a few characterization techniques were able to distinguish between surface doping and lattice incorporation. The location and distribution of dopants have been studied through EXAFS and STEM-EDX by Saha et al and Chen et. al.^{43, 56} Also by the use of high-frequency electron paramagnetic resonance (HF-EPR) spectroscopy, the site-dependent perturbation experienced by Mn²⁺ ions in CdSe lattice allows distinguishing local environments of the Mn²⁺ ions in the core and the surface of the QD⁵¹ as shown in figure 1.14. The global fitting of the frequency-dependent EPR spectra for the two discrete sextet patterns for a Mn doped CdSe sample measured at 406.4 GHz allows accurate assignment of sites.

Variable energy photoemission has been used to study the nature of the interface⁷⁹ as well as the nature of the surface.⁸⁰⁻⁸¹ Optical techniques such as the use of Cu dopant emission mechanism to study the surface of QDs have also been proposed.¹⁵ However, most of these techniques are indirect and highly specialized. All of these techniques are quite indirect and subject to the validity of various models and do not provide a straightforward easy method to study the radial position of the dopants or the presence of clusters. Further, they also require a specialized study making them not very suitable as a characterization methodology.

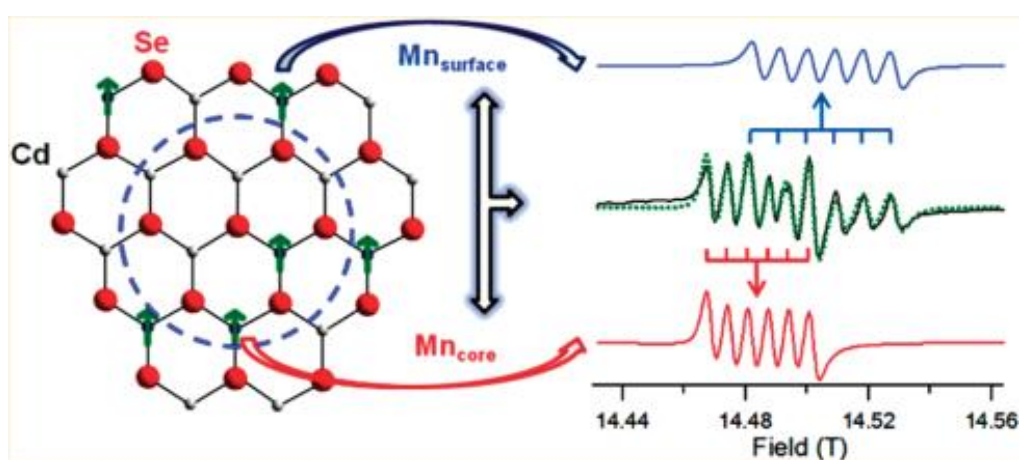


Figure 1.14. Theoretical fit and deconvolution of the 406.4 GHz HF-EPR spectra allowing assignment of discrete sites for the Mn^{2+} occupying a substitutional Cd^{2+} site within the core (red) and surface (blue). Adapted with permission from ref 40.

XRD and TEM are usually insensitive to the presence of such small clusters or the dopant positions. Hence the development of a straightforward method to study clustering with atomic resolution could be a giant step in taking the doping of QDs using colloidal synthesis further. Secondly, the uniformity of the various QDs obtained during colloidal synthesis can be quite varied making them not very suitable for high-quality applications. To date, the synthesis of monodisperse ensembles of QDs individually doped with an identical number of impurity atoms is still an open challenge, and its achievement would enable the realization of advanced QD devices, such as optically/electrically controlled magnetic memories and intragap state transistors and solar cells, relying on precise tuning of the impurity states within the QDs. Additionally, it is also very important to design

appropriate characterization techniques to obtain high-quality QDs doped with a required number of dopant ions.

Thus, lying at the heart of many technologies, the impurity dopant ions control the behavior of the QDs. These doped materials cultivate inimitable properties arising out of exchange interactions between the dopant ions and the delocalized charge carriers. The physical effects are further enhanced in these QDs due to carrier confinement with the observation of these effects even at room temperature. A lot of efforts are being put experimentally and theoretically⁸² to get QDs with high dopant concentrations and also down to a single dopant regime. Careful control of parameters like dopant core size, core lattice strength, temperature, etc can lead to effective doping. The type of dopant precursors and their lattice strength play a key role in the aforementioned doping technique. Colloidal synthesis is known to be cost-effective and results in most uniform QDs where surfactants control the growth and passivate the dangling bonds. Even though the controlled incorporation of dopants in QDs has made great strides in recent years, it is still one of the frontier challenges in doping chemistry. Further, to determine the triumph of these techniques, whether the impurity is effectively incorporated into the lattice or just adsorbed on the surface, careful characterization of the resulting QDs is required.

Thus, with the evolution of various synthesis techniques, DMS QDs of different sizes and dopant concentrations have been prepared over the past several years and have been studied for various interesting properties of these materials. We further discuss the magnetic properties arising within these systems.

1.5 Dilute magnetic semiconductor QDs

DMS materials, wherein non-magnetic semiconductors and insulators were found to be magnetic upon doping with a small percentage of magnetic metal cations like Cr, Mn, Fe, have galvanized the field of magnetism since their discovery several decades ago due to their potential as spin-polarized carrier sources and ease with which they can be integrated into a semiconducting device. Simultaneous manipulation of charge and spin⁸³⁻⁸⁴ of electrons can enhance the performance and functionality of semiconductor devices as compared to only charge-based electronics. DMS materials are potential candidates for these spin-based electronic devices.⁸⁵ This counterintuitive, surprising yet significant phenomena, has given rise to several interesting properties suitable for various applications such as non-volatile memory, quantum computing and communication in the

solid-state, magneto-optical communication devices, high-density magnetic data recording,⁸⁶⁻⁸⁷ and energy storage catalysis⁸⁸⁻⁹¹ and have remained in the forefront of research for years. Specifically, early studies proving cooperative effects via spin-exchange interactions in Mn doped GaAs⁹²⁻⁹⁵ both theoretically and experimentally have demonstrated the extensive potential of this field. Transition metal-doped bulk oxides⁹⁶⁻⁹⁷ with probable ferromagnetic transition temperature above room temperature⁹⁸ have further enhanced the interest in this field. However, though the prospect of high-temperature ferromagnetism in these materials for use in spintronics has been envisaged in a variety of research papers,⁹⁹⁻¹⁰² lack of stability and reproducibility as discussed above have prevented the establishment of definitive conclusions in this field. Nevertheless, interest in DMS materials is sustained by a variety of other interesting properties arising out of a strong interaction of the metal ion with the electronic structure of the host material via *sp-d* exchange interaction between band electrons and localized magnetic moments leading to properties like giant Zeeman splitting,¹⁰³⁻¹⁰⁴ Faraday rotation, magnetic polarons,¹⁰⁵ carrier-induced magnetic ordering,¹⁰⁶ electrical spin polarization, magnetically tunable lasing and so on.

With the advent of nanomaterials, the study of magnetism in the scale of quantum confinement has become interesting due to several fundamentally exciting¹⁰⁷⁻¹⁰⁸ and technologically¹⁰⁹⁻¹¹⁰ important properties. For example, though all open-shell atoms are magnetic in their ground state as described by Hund's rule, electronic state delocalization in the solid-state quenches their magnetization and only Fe, Co, Ni exhibit ferromagnetism in their solid form.¹¹¹ However, upon decreasing their sizes to a quantum-confined regime, magnetic properties in this confined state are discernible and can be modulated by engineering their size and morphology. Furthermore, Frenkel and Dorfman in 1930 predicted that any ferromagnetic material below a critical size limit would result in large magnetization due to the formation of a single domain wherein the magnetic moments of free electrons would be aligned with respect to the magnetic field.¹¹² This prediction resulted in an enormous interest to study magnetism at quantum-confined level. It is well known that, with a decrease in size of ferromagnetic material, the number of domains decreases, eventually leading to the formation of single-domain magnetic nanocrystals with enhancement in coercivity¹¹³⁻¹¹⁴ when the diameter is below critical diameter (D_c). This diameter is given by

$$D_c \approx \frac{36\sqrt{AK}}{\mu_0 M_s^2}$$

where A is the exchange constant, K the measure of energy per unit volume required to flip magnetization direction (effective anisotropy constant), μ_0 is the vacuum permeability and M_s is the saturation magnetization. However, when the size of a ferromagnetic nanoparticle is below critical diameter, the spins of unpaired electrons are aligned in one direction due to ferromagnetic coupling. Single domain nanocrystals further observe an increase in coercivity due to the absence of domain wall contribution.¹⁰⁷ Finally, upon further decrease in size, the thermal energy ($k_B T$) outweighs anisotropic energy and coercivity goes down to zero. The other parameters governed by size include size enhanced spin canting effect,¹¹⁵ Neel relaxation time and magneto-crystalline anisotropy. Neel relaxation time describes the thermal fluctuation time scale of magnetization direction for nanoparticles and is given by

$$\tau_N = \tau_0 \exp \frac{KV}{k_B T}$$

where τ_0 is a constant. Materials with shorter relaxation time τ_N than the measurement time τ_m , typically about 100 s, exhibit superparamagnetic behaviour. On the other hand, when relaxation time is longer than measurement time, the magnetization direction cannot be reversed within the duration of measurement and hence it does not come to zero. The temperature at which relaxation time is equal to measurement time is called the blocking temperature T_B and is given by

$$T_B = \frac{KV}{k_B \ln \frac{\tau_m}{\tau_0}}$$

while the superparamagnetic particles are known to be in a blocked state. Magnetocrystalline anisotropy also expressed as spin-orbit interaction of a material is dependent on its crystal structure that in turn affects the coercivity of a material. The higher the anisotropy constant, higher is the coercivity. Shape-anisotropy also affects magnetic properties mainly in terms of its coercivity. Confinement in one direction leads to shape anisotropy and hence enhances coercivity. Magnetization as well as coercivity of nanoparticles can also be tuned by varying the composition of constituent materials. Properties related to magnetism arising in nanoscale systems can be sub-divided into three

categories: DMS QDs, magnetism from non-magnetic clusters with subnanometer diameter and QD magnetic materials including metals, alloys and oxides of Fe, Co and Ni. Size-dependent and chemically induced nano-magnetism has been observed and reported in otherwise non-magnetic systems.¹¹⁶ For example, the strong binding of dodecanethiol with 1.4 nm Au clusters is shown to display ferromagnetism while weak binding of tetraoctylammonium ion shows diamagnetic behaviour.¹¹⁷ In addition, magnetic materials like metals, alloys and oxides of Fe, Co and Ni QDs also display size-specific magnetic behaviour. This has been extensively summarized in many comprehensive reviews.^{108, 118} In this chapter, we give an overview of the recent advances in the field of nanoscale magnetism with emphasis on DMS QDs.

With the advent of DMS QDs, wherein wave functions of the electrons and holes are confined within a limited volume leading to an extended overlap of the dopant *d* electrons and host *sp* electrons, the possibility of manipulating their exchange coupling strength via quantum confinement has captured the interest of several researchers.¹¹⁹⁻¹²⁰ Additionally, QDs leads to a decrease in the coordination number due to increased surface-to-volume ratio, and an increase in the moment per atom is observed, as the extent of localization increases and valence bandwidth decreases.¹¹¹ Further, it has been well-known in literature that quantum confinement can give rise to completely new and interesting properties that have not been observed in bulk materials. However, major bottleneck till date in the study of DMS QDs is the synthesis of uniformly doped QDs with controlled size, morphology and dopant concentration without the formation of magnetic islands as discussed above. So far, incorporation of a few atoms in a lattice of a few hundred atoms has proven to be energetically hostile and successful doping without the formation of clusters of dopant ions, either at the surface or in bulk of QDs, is challenging. In most of the early techniques used, while a few atoms were doped into the host lattice, a majority of the dopant atoms remained on the surface or formed magnetic clusters.¹²¹ In such cases, it is non-trivial to assign properties observed in these materials, e.g. magnetism, to *sp-d* exchange interaction with the host rather than from magnetic islands. Apart from this, properties arising out of surface doping or magnetic clusters are plagued with problems of reproducibility and are, in general, not useful for applications. Several reports in bulk, as well as nanomaterials, highlight the significance of dopant uniformity in the host matrix on their properties.¹²²⁻¹²³ Hence, to study the properties associated with DMS QDs, effective synthetic methods are required to synthesize uniformly doped semiconductor nanocrystals.

Varied nanoscale synthetic strategies have made it possible to chemically synthesize these DMS QDs with high monodispersity as discussed above which in turn can be used for various fundamental studies as well as technological applications. The most common magnetic dopants include Fe, Co, Ni, Mn and semiconductor hosts include alloys and heterostructures of II-VI semiconductors. They can be synthesized by various chemical routes of which colloidal synthesis is the most explored technique due to the ease of controlling size, shape and protecting them against uncontrolled oxidation.

1.6 Properties of DMS QDs

Properties specific to DMS QDs can be broadly divided into magnetic and magneto-optical as well as magnetoelectrical properties. Here we provide an overview of the recent advances in DMS QDs in both these sections and compare them with their bulk counterparts wherever appropriate.

Magnetism in DMS materials¹²⁴⁻¹²⁹ is expected to arise from the *sp-d* exchange interaction of dopant ions with the host semiconductor. However, the exact origin and the factors governing magnetism are unknown in these DMS materials. Despite this, the research into understanding the magnetism in DMS QDs is powered by the potential of using spins of small size magnetic materials that can be manipulated by an external magnetic field to serve as extremely small-sized memory storage bits for future technology. One of the first impediments arose from the absence of a method to quantify magnetism arising from DMS QDs. Most of the early reports expressed magnetic moments in emu per gram of the material rather than the well-known moment per magnetic ion. This is due to the presence of quantitatively unknown weight of ligands on the surface of QDs that makes the conversion to moment per magnetic ion impossible. Early reports on magnetism in DMS QDs showed the presence of small moments arising due to magnetic ion doping in the order of a few memu/g.¹³⁰ However, it was observed around the same time that even non-magnetic QDs like CeO₂ show ferromagnetic behaviour with similar moments attributed to oxide vacancies at the surface of QD¹³¹ making it difficult to separate the contribution arising out of the magnetic dopant. More recent papers have not shown substantial improvement in magnetic moment¹³²⁻¹³⁴ despite improved synthesis methods, possibly due to clustering of magnetic dopants and/or due to the inherent nature of *sp-d* exchange interaction. Further, the absence of quantitative magnetic moment per ion has also hindered the comparison of absolute magnetic moment with bulk materials. One of the notable breakthroughs was obtained by co-doping of ZnO with Fe and Cu.¹³⁵ Interestingly,

individually doped Fe-ZnO and Cu-ZnO are antiferromagnetic with no evidence of ferromagnetic order. This work demonstrates the presence of antiferromagnetically ordered Cu doped ZnO from M versus H plot and the antiferromagnetic interactions in Fe doped QDs using inverse susceptibility plots as a function of temperature that exhibits a negative intercept. However, it is worth noting that the Fe, Cu co-doped system shows clear signatures of ferromagnetism in these dots with magnetic moments as high as 600 memu/g. This anomalous ferromagnetism in these QDs was explained by a direct correlation between electronic structure changes and ferromagnetic coupling demonstrating one of the sparse examples of dual doping in QDs.

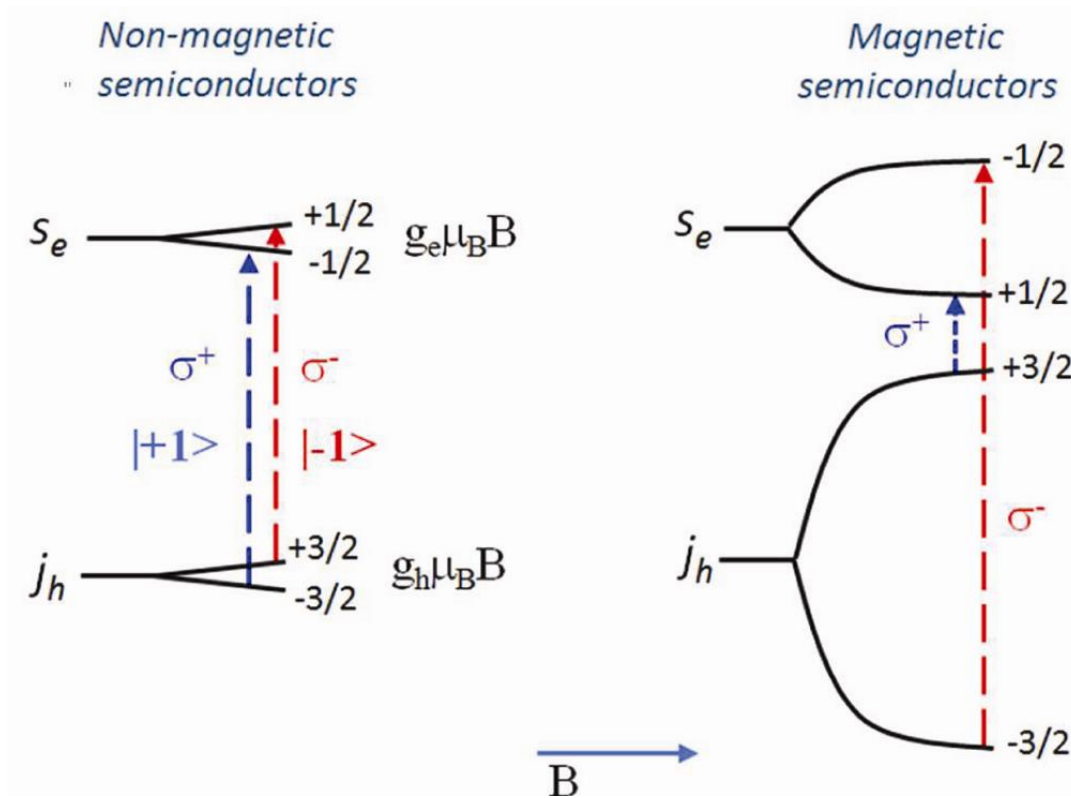


Figure 1.15. Exciton Zeeman spin splitting for non-magnetic and magnetic semiconductors in presence of an external magnetic field.

It was demonstrated using x-ray absorption spectroscopy (XAS) that both Fe^{2+} and Fe^{3+} species were present and the relative percentage of the species was dependent on the presence of Cu as a dopant. More recently, it was observed that upon synthesis of DMS QDs using the inside-out method, it was possible to obtain a much higher magnetic moment compared to earlier counterparts. In this work, it was shown that smaller QDs

showed a moment of 80 memu/g at room temperature and the surface-only magnetism on undoped CdS also shown in the same scale was negligible. Recent reports^{43, 136} have used thermogravimetric analysis in these high quality uniformly doped QDs to realize the quantitative percentage of ligand weight and hence obtain the moment per magnetic ion. From these measurements, it can be observed that the magnetic moment per magnetic ion was found to be about $0.45 \mu_B/\text{ion}$ for smaller particles which increased to $1.6 \mu_B/\text{ion}$ for larger particles suggesting comparable values with that of the bulk Fe.

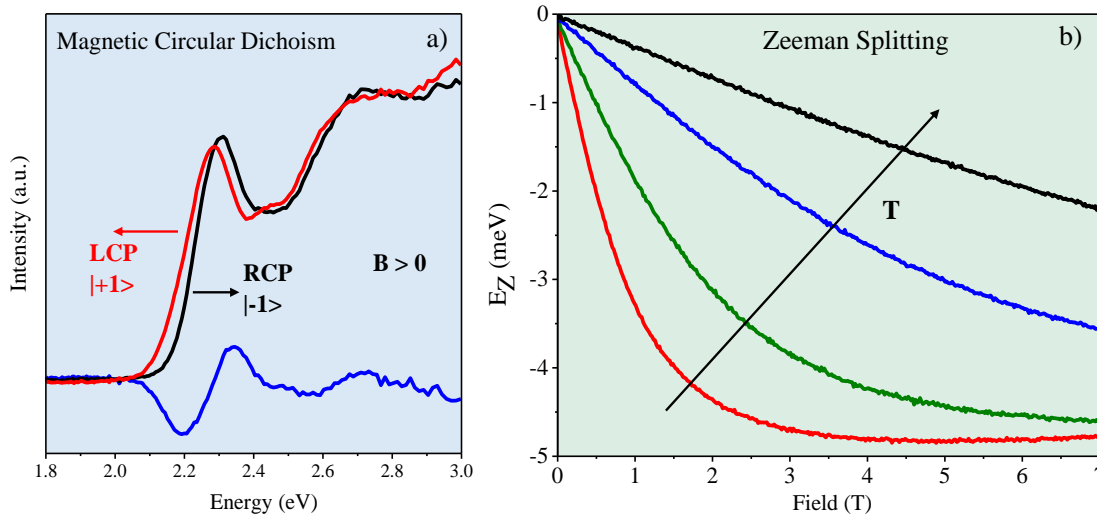


Figure 1.16. MCD spectra showing (a) host absorption in presence of external magnetic field using left and right circularly polarized light, (b) intensity of the difference spectrum versus applied field as a function of temperature.

Traditionally, magnetic fields were used to address individual storage elements in magnetic storage materials. However, the flexibility and storage density of these devices can be improved if magnetic properties are addressed via electrical or optical means other than the use of a magnetic field alone. DMS materials have proven themselves as ideal materials with classic signature response to optical and electrical excitations. When an external magnetic field is passed through a non-magnetic substance, a small internal magnetic field is generated due to splitting of the exciton given by $g_{e,h}\mu_B B$, where $g_{e,h}$ is the excitonic Zeeman splitting and B is the external magnetic field. This is typically around $100 \mu\text{eV}/\text{T}$. However, in the presence of a few magnetic ions, a strong internal magnetic field is generated in a small external magnetic field due to the alignment of magnetic ions in the direction of the magnetic field. This splitting is given by $J_{sp-d} \cdot S \cdot \sigma_{e,h}$, where J_{sp-d} is

the exchange interaction between the magnetic ion and the host and S , the effective spin given by paramagnetic Brillouin function. The effective spin is sensitively dependent on temperature. Further from these expressions, it is evident that while the non-magnetic splitting is linearly proportional to the applied magnetic field, the splitting for magnetically doped QDs with strong exchange interaction is highly non-linear with applied magnetic field as shown in figure 1.15.

Hence, the most direct measurement of DMS materials is the measurement of magnetic circular dichroism wherein, the host absorption is probed in presence of an external magnetic field using left circularly polarized (LCP) and right circularly polarized (RCP) light as shown in figure 1.16. The intensity of the difference spectrum is plotted as a function of the applied field for varying temperatures as shown in a typical curve in figure 1.16(b) to obtain DMS signature of the magnetically doped QDs. The solid lines are the Brillouin function fit to the experimental data. These data have been studied in a variety of host semiconductors, largely for Mn doping but also for Cu¹³⁷ and Co¹³⁸ doping and effective g -factors as high as 1000 have been demonstrated in DMS QDs. Further use of hetero-structures of semiconductor QDs is shown to assist in tuning the magnitude as well as the sign of exchange correlations.¹¹⁹ Theoretical modeling of electronic and magneto-optical properties of core-shell nanoparticles doped with a magnetic impurity, i.e. Mn doped CdS–ZnS, predicts that, by controlling the position of magnetic impurities, the g factor in these nanocrystals can be attuned over a wide range and forge them as potential candidates for spintronic applications.¹³⁹ Spectral fingerprints of spin-spin interaction between the dopant and excitons of the host are also revealed by single-particle spectroscopy with discrete spin projections of individual Mn²⁺ ions as obtained from spectrally well-resolved emission peaks. These QDs show enhancement in exchange splitting by an order of magnitude compared to their epitaxial counterparts paving the path for solotronics applications at elevated temperatures. The other interesting and classic signature of DMS materials is the study of circularly polarized photoluminescence in the presence of a magnetic field, also known as MCPL. MCPL has largely been studied for Mn doped materials due to the presence of band edge emission and a strong Mn emission at 580 nm or 2.15 eV in many materials. Typically, bulk DMS materials have shown a strong polarization of band edge emission due to splitting of the band as discussed in figure 1.15. However, the Mn emission which is spin and orbital forbidden emission does not demonstrate any polarization¹⁴⁰ as expected and is shown in figure 1.17(a) and (b). Surprisingly, it was observed that in three-dimensionally confined QDs, Mn emission was

observed to be polarized in the presence of magnetic field¹⁴¹ as shown in figure 1.17(c) and (d). Though a complete understanding of the polarization of Mn emission is not yet achieved, it can be expected that due to confinement, we observe a stronger overlap of wave functions leading to unexpected results.

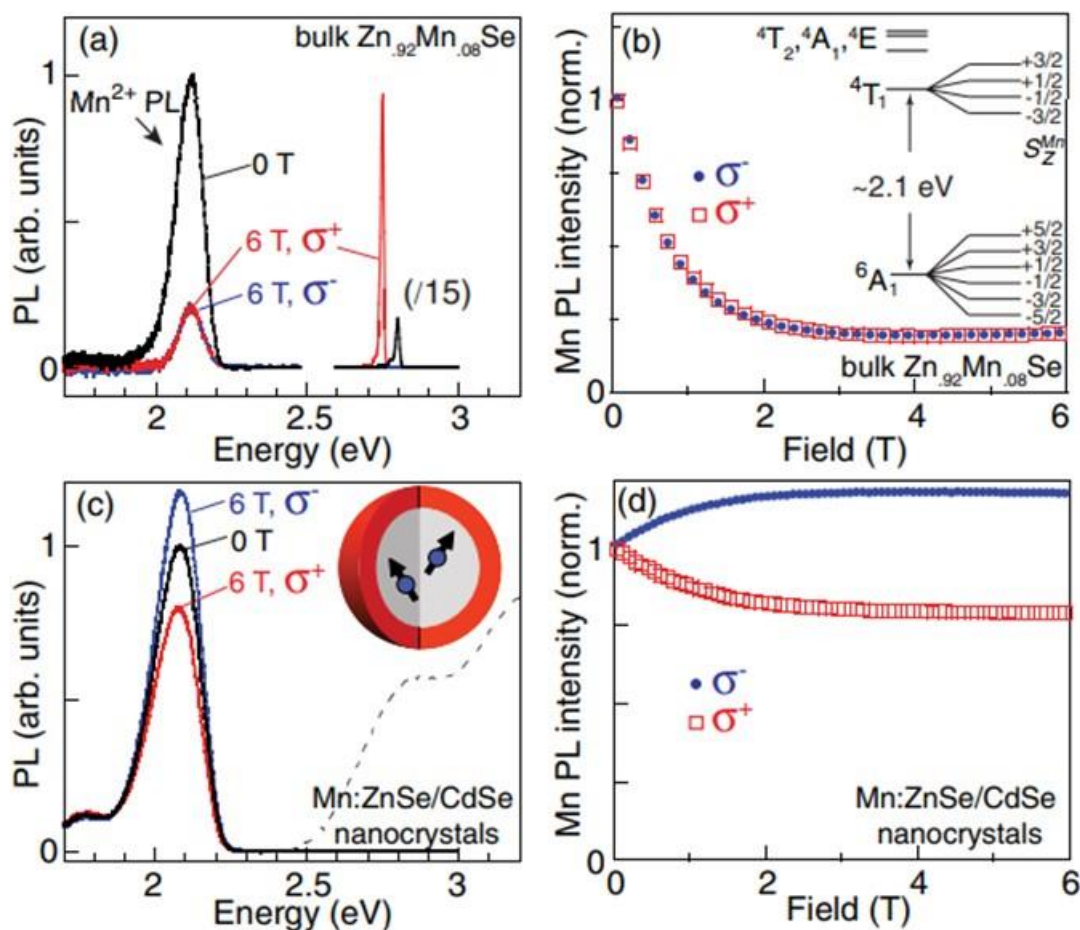


Figure 1.17. (a), (b), Magneto-PL from bulk ZnMnSe at 4 K, showing conventional DMS behaviour. 4T_1 to 6A_1 Mn^{2+} PL at 2.1 eV is suppressed by magnetic fields and remains unpolarized, while 2.8 eV exciton PL (scaled-down 15*) increases. (c), (d), The contrasting magneto-PL from Mn : ZnSe/CdSe nanocrystals. The dashed line shows the QD absorption (reproduced from ref. 126).

A fascinating example of magneto-optical response displayed in DMS QDs is the magnetism induced due to photoexcitation in Cu doped chalcogenide QDs due to strong spin-exchange interaction between paramagnetic Cu dopants and conduction and valence bands of the host semiconductor.¹³⁷ In these Cu doped ZnSe/CdSe QDs, it has been shown

that the paramagnetic response is enhanced up to 100% upon illumination with UV light as revealed by magnetic circular dichroism (MCD) studies. In dark, these materials are shown to retain a photomagnetization memory for timescales of hours. Another example of light-induced spontaneous magnetization is Mn doped CdSe QDs where spin effects are controlled in semiconductor nanostructures to generate, manipulate and read out spins.¹²⁰ Here in the absence of an applied magnetic field large dopant-carrier exchange fields are generated in strong spatial confinement giving rise to giant Zeeman splitting as a result of photoexcitation. These magnetic effects present due to photoexcitation are observed up to room temperature. These materials have prospective applications for magneto-optical storage and optically controlled magnetism.

DMS QDs are not only known to respond to optical cues but also to charged carriers. For example, Zheng and Strouse¹⁴² have shown carrier-mediated ferromagnetic interaction in Mn-doped CdSe QDs arising from photoexcited carriers from surface defect states of ultra-small (<3 nm) QDs. Similarly, conduction band electron generated during photoexcitation is also shown to exhibit ferromagnetic exchange interactions in Mn doped ZnO QDs under anaerobic conditions¹⁴³ as well as in air-stable Fe-Sn co-doped In₂O₃¹⁰⁶ and Mn-Sn co-doped In₂O₃.¹³⁶ In fact, despite the intrinsic antiferromagnetic super-exchange coupling between next-nearest neighbour, magnetic cations such as Mn²⁺-O²⁻-Mn²⁺,¹⁴³ Mn-Sn co-doped In₂O₃ was found to exhibit nearly ideal ($\sim 4.8 \mu_B/\text{Mn}^{2+}$ ion) magnetic moment at 2 K and 70 kOe, thus overcoming the antiferromagnetic super-exchange interaction completely.¹³⁶ These results confirm the conduction band electron-dopant ferromagnetic exchange interaction, which can lead to magneto-electric and magneto-plasmonic properties.

As a search for a viable DMS material for incorporation into spintronic device progresses, the fundamental understanding of dopant incorporation and its behaviour into the semiconductor matrix needs to be explored. Presently, the synthesis of DMS QDs has been the major bottleneck in the study of this class of compounds. Various techniques used to obtain these materials have been discussed here and the current state-of-the-art techniques to synthesize these QD systems are highlighted. Fundamental insights can be gained from Faraday rotation, Kerr rotation, magnetic circular dichroism, magnetic circularly polarized photoluminescence spectroscopies, magnetism induced through optical excitation, magneto-electric and magneto-plasmonic excitations. This can be used to reinforce cognizance related to spin dynamics and magnetic exchange interactions in DMS QDs

with a potential upshot for spin-based information technologies as discussed in this chapter.

1.7 Present study: Impurity doping in semiconductor QDs has numerous prospects in implementing and altering their properties and technologies. However, further progress of applications is dependent on the development of reliable methods for the effective incorporation of impurities into the semiconductor matrix. In this thesis, we have modeled various structural and synthetic aspects to synthesize singly and dual doped QDs and have studied their magnetic and magneto-optical properties.

Chapter 1 as discussed above, provides an overview of the existing literature in doping QDs.

Chapter 2 describes the principles of various advanced techniques used to study the doped quantum dots like extended x-ray absorption fine structure (EXAFS), magnetic circular dichroism (MCD), transient absorption spectroscopy (TA). This chapter further discusses various characterization techniques used to study the doped QDs and their experimental details.

The research findings of the work are divided into two sections in the thesis. **Section I** discusses the study of surface properties of the undoped nanocrystal host and the spintronic-like properties of singly doped nanocrystal (where “singly doped” refers to single type of dopant and not single atom doping) which is divided into chapter 3 and 4 respectively.

Chapter 3 involves the study of transient absorption dynamics in CdS nanocrystals using the ultrafast pump-probe technique. Here the long-lived excited state in CdS QDs arising from the absence of surface states presents an appropriate platform for the study of vibrational dynamics. Transient absorption studies at non-resonant and near-resonance excitation corroborated the vibrational cooling mechanism in these defect-free dots which can further serve as a good host to study dopant-host interactions and is discussed in the next chapter.

Chapter 4. focuses on the study of Fe-host interactions in the doped system. Fe doping in semiconductor nanocrystals has largely been treated as uninteresting from the spintronics perspective, due to the absence of an energetically accessible second spin state. In this chapter, we demonstrate the presence of two magnetically inequivalent states in the Fe doped CdS nanocrystals arising out of optical perturbation and uneven interaction of the two spins with the host. Ultrafast pump-probe spectroscopy and density functional theory-

based calculations were used to demonstrate the presence of the Magneto-Optical Stark Effect in these systems.

Further, **Section II** talks about dual doping (where “dual doping” refers to two different type of dopants in the lattice) in semiconductor QDs where dual doping can introduce new synergistic properties that are otherwise not present in the individually doped systems. Here, we have discussed the challenges associated with dual doping in quantum dots as it has not been viable to dual dope quantum dots deftly with reproducibility. In chapter 5 we have addressed various synthetic and structural aspects for dual doping followed by studying their magnetic and magneto-optical properties in chapter 6 & 7.

Chapter 5, Part A discusses dual doping as a powerful strategy to tailor the properties of semiconductor nanocrystals arising out of host-dopant and dopant-dopant interactions. Here we talk about various challenges involved in administering dual dopants within the constraints of one host under similar conditions using CoPt-doped CdS nanocrystals as a model system. In addition, the various chemical and physical forces in play are studied to understand the feasibility of the core to doped transformation. **Part B** describes that the precise control of crystal orientation and the exposed surface is critical for the engineering of heterostructures. Here, using CoPt as a model system, different heterostructures are grown ranging from core/shell structure, diffused interface, dumbbell structured dimers, and embedded island structures wherein these hybrids are fabricated via micro/macrolevel facet-selective growth.

Chapter 6. discusses the magnetic and magneto-optical properties of doped nanocrystals wherein the clustering of magnetic impurities has been well established as a deterrent to observe magnetic behavior in doped semiconductors. Clustering in most cases has been random and irreproducible and the microscopic origin of these effects has so far not been established. In this work, we have systematically obtained clustered and uniformly diffused CoPt/CdS to study the effect of clustering on the magnetic and magneto-optical properties of nanocrystals. The generality has been established by performing a similar study on FePt/CdS nanocrystals. Here the role of diamagnetic Pt spacer between the ferromagnetic Co dopants has been studied. Similar-sized diffused nanocrystals of Co doped CdS were considered for the comparative magnetic and magneto-optical study with the Co, Pt co-doped nanocrystals in **Part B**. After studying the effect of clustering, we have studied the magnetic properties of the Fe, Co dual-doped systems in the next chapter. **Chapter 7** discusses the magnetic properties of CdS nanocrystals simultaneously doped

with Fe and Co with varying Fe/Co compositions. The co-doped nanocrystals show magnetic properties that are different from the singly doped counterparts.

Bibliography

- (1) Pradhan, N. Mn-Doped Semiconductor Nanocrystals: 25 Years And Beyond. *J. Phys. Chem. Lett.*: 2019; Vol. 10, pp 2574–2577.
- (2) Zhang, J.; Di, Q.; Liu, J.; Bai, B.; Liu, J.; Xu, M.; Liu, J. Heterovalent Doping In Colloidal Semiconductor Nanocrystals: Cation-Exchange-Enabled New Accesses To Tuning Dopant Luminescence And Electronic Impurities. *J. Phys. Chem. Lett.* **2017**, *8*, 4943-4953.
- (3) Makkar, M.; Saha, A.; Khalid, S.; Viswanatha, R. Thermodynamics of Dual Doping in Quantum Dots. *J. Phys. Chem. Lett.* **2019**, *10*, 1992-1998.
- (4) Makkar, M.; Dheer, L.; Singh, A.; Moretti, L.; Maiuri, M.; Ghosh, S.; Cerullo, G.; Waghmare, U. V.; Viswanatha, R. Magneto-Optical Stark Effect in Fe-Doped CdS Nanocrystals. *Nano Lett.* **2021**, *21*, 3798–3804.
- (5) Saha, A.; Viswanatha, R. Volume and Concentration Scaling of Magnetism in Dilute Magnetic Semiconductor Quantum Dots. *J. Phys. Chem. C* **2017**, *121*, 21790-21796.
- (6) Saha, A.; Viswanatha, R. Magnetism at the Interface of Magnetic Oxide and Nonmagnetic Semiconductor Quantum Dots. *ACS Nano* **2017**, *11*, 3347-3354.
- (7) Baruah, J. M.; Narayan, J. Dilute Magnetic Semiconducting Quantum Dots: Smart Materials For Spintronics. *Nonmagn. Magn. Quantum Dots* **2018**, 87-199.
- (8) Sun, Y.-Q.; Gao, T. The Influence of Electron-Electron Interaction on RKKY Magnetic Coupling between Local Spins of Diluted Magnetic Semiconductor Quantum Dots. *Int. J. Theor. Phys.* **2021**, *60*, 143-154.
- (9) Pradhan, N.; Peng, X. Efficient and Color-Tunable Mn-Doped ZnSe Nanocrystal Emitters: Control of Optical Performance Via Greener Synthetic Chemistry. *J. Am. Chem. Soc.* **2007**, *129*, 3339-3347.
- (10) Beaulac, R.; Archer, P. I.; Ochsenein, S. T.; Gamelin, D. R. Mn²⁺-Doped CdSe Quantum Dots: New Inorganic Materials for Spin-Electronics and Spin-Photonics. *Adv. Funct. Mater.* **2008**, *18*, 3873-3891.
- (11) Norris, D. J.; Yao, N.; Charnock, F. T.; Kennedy, T. A. High-Quality Manganese-Doped ZnSe Nanocrystals. *Nano Lett.* **2001**, *1*, 3-7.
- (12) Saha, A.; Makkar, M.; Shetty, A.; Gahlot, K.; Pavan, A.; Viswanatha, R. Diffusion Doping in Quantum Dots: Bond Strength and Diffusivity. *Nanoscale* **2017**, *9*, 2806-2813.

- (13) Suo, Z.; Dai, J.; Gao, S.; Gao, H. Effect of Transition Metals (Sc, Ti, V, Cr and Mn) Doping on Electronic Structure and Optical Properties of CdS. *Results Phys.* **2020**, *17*, 103058.
- (14) Cao, S.; Li, C.; Wang, L.; Shang, M.; Wei, G.; Zheng, J.; Yang, W. Long-Lived and Well-Resolved Mn²⁺ Ion Emissions in CuInS-ZnS Quantum Dots. *Sci. Rep.* **2014**, *4*, 7510.
- (15) Grandhi, G. K.; Tomar, R.; Viswanatha, R. Study of Surface and Bulk Electronic Structure of II-VI Semiconductor Nanocrystals Using Cu as a Nanosensor. *ACS Nano* **2012**, *6*, 9751-9763.
- (16) Bhargava, R. N.; Gallagher, D.; Hong, X.; Nurmikko, A. Optical Properties of Manganese-Doped Nanocrystals of ZnS. *Phys. Rev. Lett.* **1994**, *72*, 416-419.
- (17) Hanif, K. M.; Meulenberg, R. W.; Strouse, G. F. Magnetic Ordering in Doped Cd_{1-x}Co_xSe Diluted Magnetic Quantum Dots. *J. Am. Chem. Soc.* **2002**, *124*, 11495-11502.
- (18) Bonanni, A.; Dietl, T. A Story of High-Temperature Ferromagnetism In Semiconductors. *Chem. Soc. Rev.* **2010**, *39*, 528-539.
- (19) Lorenz, S.; Erickson, C. S.; Riesner, M.; Gamelin, D. R.; Fainblat, R.; Bacher, G. Directed Exciton Magnetic Polaron Formation in a Single Colloidal Mn²⁺: CdSe/CdS Quantum Dot. *Nano Lett.* **2020**, *20*, 1896-1906.
- (20) Fainblat, R.; Muckel, F.; Bacher, G. Tailoring Exchange Interactions In Magnetically Doped II-VI Nanocrystals. *Chalcogenide* **2020**, 271-304.
- (21) Shanker, G. S.; Tandon, B.; Shibata, T.; Chattopadhyay, S.; Nag, A. Doping Controls Plasmonics, Electrical Conductivity, and Carrier-Mediated Magnetic Coupling in Fe and Sn Codoped In₂O₃ Nanocrystals: Local Structure is the Key. *Chem. Mater.* **2015**, *27*, 892-900.
- (22) Sahu, A.; Kang, M. S.; Kompch, A.; Notthoff, C.; Wills, A. W.; Deng, D.; Winterer, M.; Frisbie, C. D.; Norris, D. J. Electronic Impurity Doping in CdSe Nanocrystals. *Nano Lett.* **2012**, *12*, 2587-2594.
- (23) Grandhi, G. K.; Swathi, K.; Narayan, K. S.; Viswanatha, R. Cu Doping in Ligand Free CdS Nanocrystals: Conductivity and Electronic Structure Study. *J. Phys. Chem. Lett.* **2014**, *5*, 2382-2389.
- (24) Chuang, C.-H. M.; Brown, P. R.; Bulović, V.; Bawendi, M. G. Improved Performance and Stability In Quantum Dot Solar Cells Through Band Alignment Engineering. *Nat. Mater.* **2014**, *13*, 796-801.

- (25) Carey, G. H.; Kramer, I. J.; Kanjanaboos, P.; Moreno-Bautista, G.; Voznyy, O.; Rollny, L.; Tang, J. A.; Hoogland, S.; Sargent, E. H. Electronically Active Impurities in Colloidal Quantum Dot Solids. *ACS Nano* **2014**, *8*, 11763-11769.
- (26) Kufer, D.; Nikitskiy, I.; Lasanta, T.; Navickaite, G.; Koppens, F. H. L.; Konstantatos, G. Hybrid 2D–0D MoS₂–PbS Quantum Dot Photodetectors. *Adv. Mater.* **2015**, *27*, 176-180.
- (27) Konstantatos, G.; Badioli, M.; Gaudreau, L.; Osmond, J.; Bernechea, M.; de Arquer, F. P. G.; Gatti, F.; Koppens, F. H. L. Hybrid Graphene–Quantum Dot Phototransistors With Ultrahigh Gain. *Nat. Nanotechnol.* **2012**, *7*, 363-368.
- (28) Deng, Z.; Jeong, K. S.; Guyot Sionnest, P. Colloidal Quantum Dots Intraband Photodetectors. *ACS Nano* **2014**, *8*, 11707-11714.
- (29) Sun, L.; Choi, J. J.; Stachnik, D.; Bartnik, A. C.; Hyun, B. R.; Malliaras, G. G.; Hanrath, T.; Wise, F. W. Bright Infrared Quantum Dot Light-Emitting Diodes Through Inter-Dot Spacing Control. *Nat. Nanotechnol.* **2012**, *7*, 369-373.
- (30) Yang, Y.; Zheng, Y.; Cao, W.; Titov, A.; Hyvonen, J.; Manders, J. R.; Xue, J.; Holloway, P. H.; Qian, L. High-Efficiency Light-Emitting Devices Based on Quantum Dots With Tailored Nanostructures. *Nat. Photonics* **2015**, *9*, 259-266.
- (31) Stavrinadis, A.; Pelli Cresi, J. S.; d’Acapito, F.; Magén, C.; Boscherini, F.; Konstantatos, G. Aliovalent Doping in Colloidal Quantum Dots and Its Manifestation on Their Optical Properties: Surface Attachment versus Structural Incorporation. *Chem. Mater.* **2016**, *28*, 5384-5393.
- (32) Rao, C. N. R. Notable Effects of Aliovalent Anion Substitution on the Electronic Structure and Properties of Metal Oxides and Sulfides. *J. Phys. Chem. Lett.* **2015**, *6*, 3303-3308.
- (33) Lingampalli, S. R.; Manjunath, K.; Shenoy, S.; Waghmare, U. V.; Rao, C. N. R. Zn₂NF and Related Analogues of ZnO. *J. Am. Chem. Soc.* **2016**, *138*, 8228-8234.
- (34) Delikanli, S.; Akgul, M. Z.; Murphy, J. R.; Barman, B.; Tsai, Y.; Scrace, T.; Zhang, P.; Bozok, B.; Hernández-Martínez, P. L.; Christodoulides, J.; Cartwright, A. N.; Petrou, A.; Demir, H. V. Mn²⁺-Doped CdSe/CdS Core/Multishell Colloidal Quantum Wells Enabling Tunable Carrier–Dopant Exchange Interactions. *ACS Nano* **2015**, *9*, 12473-12479.
- (35) Yu, J. H.; Liu, X.; Kweon, K. E.; Joo, J.; Park, J.; Ko, K. T.; Lee, D. W.; Shen, S.; Tivakornsasithorn, K.; Son, J. S.; Park, J. H.; Kim, Y. W.; Hwang, G. S.; Dobrowolska,

M.; Furdyna, J. K.; Hyeon, T. Giant Zeeman Splitting in Nucleation-Controlled Doped CdSe: Mn²⁺ Quantum Nanoribbons. *Nat. Mater.* **2010**, *9*, 47-53.

(36) Beaulac, R.; Schneider, L.; Archer, P. I.; Bacher, G.; Gamelin, D. R. Light-Induced Spontaneous Magnetization In Doped Colloidal Quantum Dots. *Science* **2009**, *325*, 973-976.

(37) Makkar, M.; Viswanatha, R. Recent Advances in Magnetic Ion-Doped Semiconductor Quantum Dots. *Curr. Sci.* **2017**, *112*, 1421-1429.

(38) Barrows, C. J.; Vlaskin, V. A.; Gamelin, D. R. Absorption and Magnetic Circular Dichroism Analyses of Giant Zeeman Splittings in Diffusion-Doped Colloidal Cd_{1-x}Mn_xSe Quantum Dots. *J. Phys. Chem. Lett.* **2015**, *6*, 3076-3081.

(39) Furdyna, J. K. Diluted Magnetic Semiconductors. *J. Appl. Phys.* **1988**, *64*, R29-R64.

(40) Bera, D.; Qian, L.; Tseng, T.-K.; Holloway, P. H. Quantum Dots and Their Multimodal Applications: A Review. *Materials* **2010**, *3*, 2260-2345.

(41) Wu, P.; Yan, X. P. Doped Quantum Dots for Chemo/Biosensing and Bioimaging. *Chem. Soc. Rev.* **2013**, *42*, 5489-5521.

(42) Xiu, F. X.; Yang, Z.; Mandalapu, L. J.; Zhao, D. T.; Liu, J. L.; Beyermann, W. P. High-Mobility Sb-Doped p-Type ZnO by Molecular-Beam Epitaxy. *Appl. Phys. Lett.* **2005**, *87*, 152101-3.

(43) Saha, A.; Shetty, A.; Pavan, A. R.; Chattopadhyay, S.; Shibata, T.; Viswanatha, R. Uniform Doping In Quantum-Dots-Based Dilute Magnetic Semiconductor. *J. Phys. Chem. Lett.* **2016**, *7*, 2420-2428.

(44) Barrows, C. J.; Chakraborty, P.; Kornowske, L. M.; Gamelin, D. R. Tuning Equilibrium Compositions in Colloidal Cd_{1-x}Mn_xSe Nanocrystals Using Diffusion Doping and Cation Exchange. *ACS Nano* **2016**, *10*, 910-918.

(45) Murray, C. B.; Norris, D. J.; Bawendi, M. G. Synthesis and Characterization of Nearly Monodisperse CdE (E= Sulfur, Selenium, Tellurium) Semiconductor Nanocrystallites. *J. Am. Chem. Soc.* **1993**, *115*, 8706-8715.

(46) Viswanatha, R.; Sapra, S.; Sen Gupta, S.; Satpati, B.; Satyam, P. V.; Dev, B. N.; Sarma, D. D. Synthesis and Characterization of Mn-Doped ZnO Nanocrystals. *J. Phys. Chem. B* **2004**, *108*, 6303-6310.

(47) Murase, N.; Jagannathan, R.; Kanematsu, Y.; Watanabe, M.; Kurita, A.; Hirata, K.; Yazawa, T.; Kushida, T. Fluorescence and EPR Characteristics of Mn²⁺-Doped ZnS

Nanocrystals Prepared by Aqueous Colloidal Method. *J. Phys. Chem. B* **1999**, *103*, 754-760.

(48) Bhattacharyya, B.; Gahlot, K.; Viswanatha, R.; Pandey, A. Optical Signatures of Impurity-Impurity Interactions in Copper Containing II-VI Alloy Nanocrystals. *J. Phys. Chem. Lett.* **2018**, *9*, 635-640.

(49) van Schilfgaarde, M.; Mryasov, O. N. Anomalous Exchange Interactions In III-V Dilute Magnetic Semiconductors. *Phys. Rev. B* **2001**, *63*, 233205.

(50) Sato, K.; Katayama -Yoshida, H.; Dederichs, P. H. High Curie Temperature and Nano-Scale Spinodal Decomposition Phase in Dilute Magnetic Semiconductors. *Jpn. J. Appl. Phys.* **2005**, *44*, L948-L951.

(51) Zheng, W.; Wang, Z.; Wright, J.; Goundie, B.; Dalal, N. S.; Meulenberg, R. W.; Strouse, G. F. Probing the Local Site Environments In Mn: CdSe Quantum Dots. *J. Phys. Chem. C* **2011**, *115*, 23305-23314.

(52) Buonsanti, R.; Milliron, D. J. Chemistry of Doped Colloidal Nanocrystals. *Chem. Mater.* **2013**, *25*, 1305-1317.

(53) Erwin, S. C.; Zu, L.; Haftel, M. I.; Efros, A. L.; Kennedy, T. A.; Norris, D. J. Doping Semiconductor Nanocrystals. *Nature* **2005**, *436*, 91-94.

(54) Karan, N. S.; Sarkar, S.; Sarma, D. D.; Kundu, P.; Ravishankar, N.; Pradhan, N. Thermally Controlled Cyclic Insertion/Ejection of Dopant Ions and Reversible Zinc Blende/Wurtzite Phase Changes in ZnS Nanostructures. *J. Am. Chem. Soc.* **2011**, *133*, 1666-1669.

(55) Dalpian, G. M.; Chelikowsky, J. R. Self-Purification in Semiconductor Nanocrystals. *Phys. Rev. Lett.* **2006**, *96*, 226802.

(56) Chen, D.; Viswanatha, R.; Ong, G. L.; Xie, R.; Balasubramanian, M.; Peng, X. Temperature Dependence of “Elementary Processes” In Doping Semiconductor Nanocrystals. *J. Am. Chem. Soc.* **2009**, *131*, 9333-9339.

(57) Saha, A.; Makkar, M.; Shetty, A.; Gahlot, K.; Pavan, A. R.; Viswanatha, R. Diffusion Doping in Quantum Dots: Bond Strength and Diffusivity. *Nanoscale* **2017**, *9*, 2806-2813.

(58) Shim, M.; Guyot -Sionnest, P. N-Type Colloidal Semiconductor Nanocrystals. *Nature* **2000**, *407*, 981-983.

(59) Shim, M.; Wang, C.; Guyot Sionnest, P. Charge-Tunable Optical Properties In Colloidal Semiconductor Nanocrystals. *J. Phys. Chem. B* **2001**, *105*, 2369-2373.

- (60) Yu, D.; Wang, C.; Guyot Sionnest, P. n-Type Conducting CdSe Nanocrystal Solids. *Science* **2003**, *300*, 1277-1280.
- (61) Talapin, D. V.; Murray, C. B. PbSe Nanocrystal Solids For n-and p-Channel Thin Film Field-Effect Transistors. *Science* **2005**, *310*, 86-89.
- (62) Kovalenko, M. V.; Bodnarchuk, M. I.; Zaumseil, J.; Lee, J. S.; Talapin, D. V. Expanding the Chemical Versatility of Colloidal Nanocrystals Capped With Molecular Metal Chalcogenide Ligands. *J. Am. Chem. Soc.* **2010**, *132*, 10085-10092.
- (63) Pradhan, N.; Goorskey, D.; Thessing, J.; Peng, X. An Alternative of CdSe Nanocrystal Emitters: Pure and Tunable Impurity Emissions in ZnSe Nanocrystals. *J. Am. Chem. Soc.* **2005**, *127*, 17586-17587.
- (64) Grandhi, G. K.; Viswanatha, R. Demystifying Complex Quantum Dot Heterostructures Using Photogenerated Charge Carriers. *J. Phys. Chem. Lett.* **2017**, *8*, 2043-2048.
- (65) Santiago -González, B.; Monguzzi, A.; Pinchetti, V.; Casu, A.; Prato, M.; Lorenzi, R.; Campione, M.; Chiodini, N.; Santambrogio, C.; Meinardi, F.; Manna, L.; Brovelli, S. “Quantized” Doping of Individual Colloidal Nanocrystals Using Size-Focused Metal Quantum Clusters. *ACS Nano* **2017**, *11*, 6233-6242.
- (66) Rivest, J. B.; Jain, P. K. Cation Exchange on the Nanoscale: An Emerging Technique for New Material Synthesis, Device Fabrication, and Chemical Sensing. *Chem. Soc. Rev.* **2013**, *42*, 89-96.
- (67) Deng, Z.; Tong, L.; Flores, M.; Lin, S.; Cheng, J.-X.; Yan, H.; Liu, Y. High-Quality Manganese-Doped Zinc Sulfide Quantum Rods With Tunable Dual-Color and Multiphoton Emissions. *J. Am. Chem. Soc.* **2011**, *133*, 5389-5396.
- (68) Son, D. H.; Hughes, S. M.; Yin, Y.; Alivisatos, A. P. Cation Exchange Reactions In Ionic Nanocrystals. *Science* **2004**, *306*, 1009-1012.
- (69) Beberwyck, B. J.; Surendranath, Y.; Alivisatos, A. P. Cation Exchange: A Versatile Tool for Nanomaterials Synthesis. *J. Phys. Chem. C* **2013**, *117*, 19759-19770.
- (70) Robinson, R. D.; Sadtler, B.; Demchenko, D. O.; Erdonmez, C. K.; Wang, L. W.; Alivisatos, A. P. Spontaneous Superlattice Formation In Nanorods Through Partial Cation Exchange. *Science* **2007**, *317*, 355-358.
- (71) Sadtler, B.; Demchenko, D. O.; Zheng, H.; Hughes, S. M.; Merkle, M. G.; Dahmen, U.; Wang, L. W.; Alivisatos, A. P. Selective Facet Reactivity During Cation Exchange In Cadmium Sulfide Nanorods. *J. Am. Chem. Soc.* **2009**, *131*, 5285-5293.

- (72) Demchenko, D. O.; Robinson, R. D.; Sadtler, B.; Erdonmez, C. K.; Alivisatos, A. P.; Wang, L.-W. Formation Mechanism and Properties of CdS-Ag₂S Nanorod Superlattices. *ACS Nano* **2008**, *2*, 627-636.
- (73) Saha, A.; Chattopadhyay, S.; Shibata, T.; Viswanatha, R. Core-Shell to Doped Quantum Dots: Evolution of the Local Environment Using XAFS. *J. Phys. Chem. C* **2016**, *120*, 18945-18951.
- (74) Pearson, R. G. Hard and Soft Acids and Bases, HSAB, Part 1: Fundamental Principles. *J. Chem. Educ.* **1968**, *45*, 581.
- (75) Saha, A.; Chattopadhyay, S.; Shibata, T.; Viswanatha, R. The Curious Case of CdTe/CdS: Photoabsorption versus Photoemission. *J. Mater. Chem. C* **2014**, *2*, 3868-3872.
- (76) Saha, A.; Chellappan, K. V.; Narayan, K. S.; Ghatak, J.; Datta, R.; Viswanatha, R. Near-Unity Quantum Yield in Semiconducting Nanostructures: Structural Understanding Leading to Energy Efficient Applications. *J. Phys. Chem. Lett.* **2013**, *4*, 3544-3549.
- (77) Tang, J.; Kemp, K. W.; Hoogland, S.; Jeong, K. S.; Liu, H.; Levina, L.; Furukawa, M.; Wang, X.; Debnath, R.; Cha, D.; Chou, K. W.; Fischer, A.; Amassian, A.; Asbury, J. B.; Sargent, E. H. Colloidal-Quantum-Dot Photovoltaics Using Atomic-Ligand Passivation. *Nat. Mater.* **2011**, *10*, 765-771.
- (78) Pandey, A.; Sarma, D. D. Recent Advances in Manganese Doped II-VI Semiconductor Quantum Dots. *Z. Anorg. Allg. Chem.* **2016**, *642*, 1331-1339.
- (79) Santra, P. K.; Viswanatha, R.; Daniels, S. M.; Pickett, N. L.; Smith, J. M.; O'Brien, P.; Sarma, D. D. Investigation of the Internal Heterostructure of Highly Luminescent Quantum Dot-Quantum Well Nanocrystals. *J. Am. Chem. Soc.* **2008**, *131*, 470-477.
- (80) Sapra, S.; Nanda, J.; Pietryga, J. M.; Hollingsworth, J. A.; Sarma, D. D. Unraveling Internal Structures of Highly Luminescent PbSe Nanocrystallites Using Variable-Energy Synchrotron Radiation Photoelectron Spectroscopy. *J. Phys. Chem. B* **2006**, *110*, 15244-15250.
- (81) Nanda, J.; Kuruvilla, B. A.; Sarma, D. D. Photoelectron Spectroscopic Study of CdS Nanocrystallites. *Phys. Rev. B* **1999**, *59*, 7473.
- (82) Du, M.-H.; Erwin, S. C.; Efros, A. L. Trapped-Dopant Model of Doping in Semiconductor Nanocrystals. *Nano Lett.* **2008**, *8*, 2878-2882.
- (83) Wolf, S. A.; Awschalom, D. D.; Buhrman, R. A.; Daughton, J. M.; Von Molnar, S.; Roukes, M. L.; Chtchelkanova, A. Y.; Treger, D. M. Spintronics: A Spin-Based Electronics Vision for the Future. *Science* **2001**, *294*, 1488-1495.

- (84) Žutić, I.; Fabian, J.; Sarma, S. D. Spintronics: Fundamentals and Applications. *Rev. Mod. Phys.* **2004**, *76*, 323.
- (85) Ohno, H. Making Nonmagnetic Semiconductors Ferromagnetic. *Science* **1998**, *281*, 951-956.
- (86) Weller, D.; Moser, A. Thermal Effect Limits In Ultrahigh-Density Magnetic Recording. *IEEE Trans. Magn.* **1999**, *35*, 4423-4439.
- (87) Weller, D.; Mosendz, O.; Parker, G.; Pisana, S.; Santos, T. S. L10 FePtX–Y Media for Heat-Assisted Magnetic Recording. *Phys. Status Solidi A* **2013**, *210*, 1245-1260.
- (88) Guo, S.; Zhang, S.; Sun, S. Tuning Nanoparticle Catalysis for the Oxygen Reduction Reaction. *Angew. Chem. Int. Ed.* **2013**, *52*, 8526-8544.
- (89) Govan, J.; Gun'ko, Y. K. Recent Advances In the Application of Magnetic Nanoparticles as a Support for Homogeneous Catalysts. *Nanomaterials* **2014**, *4*, 222-241.
- (90) Polshettiwar, V.; Luque, R.; Fihri, A.; Zhu, H.; Bouhrara, M.; Basset, J. M. Magnetically Recoverable Nanocatalysts. *Chem. Rev.* **2011**, *111*, 3036-3075.
- (91) Shylesh, S.; Schünemann, V.; Thiel, W. R. Magnetically Separable Nanocatalysts: Bridges Between Homogeneous and Heterogeneous Catalysis. *Angew. Chem. Int. Ed.* **2010**, *49*, 3428-3459.
- (92) Van Esch, A.; Van Bockstal, L.; De Boeck, J.; Verbanck, G.; Van Steenberghe, A. S.; Wellmann, P. J.; Grietens, B.; Bogaerts, R.; Herlach, F.; Borghs, G. Interplay Between the Magnetic and Transport Properties in the III-V Diluted Magnetic Semiconductor Ga_{1-x}Mn_xAs. *Phys. Rev. B* **1997**, *56*, 13103.
- (93) Ohno, H.; Shen, A.; Matsukura, F.; Oiwa, A.; Endo, A.; Katsumoto, S.; Iye, Y. (Ga, Mn)As: A New Diluted Magnetic Semiconductor Based on GaAs. *Appl. Phys. Lett.* **1996**, *69*, 363-365.
- (94) Blinowski, J.; Kacman, P. Spin Interactions of Interstitial Mn Ions in Ferromagnetic GaMnAs. *Phys. Rev. B* **2003**, *67*, 121204.
- (95) Edmonds, K. W.; Bogusławski, P.; Wang, K.; Champion, R. P.; Novikov, S. N.; Farley, N. R. S.; Gallagher, B. L.; Foxon, C. T.; Sawicki, M.; Dietl, T. Mn Interstitial Diffusion in (Ga, Mn)As. *Phys. Rev. Lett.* **2004**, *92*, 037201.
- (96) Hong, N. H.; Sakai, J.; Huong, N. T.; Poirot, N.; Ruyter, A. Role of Defects In Tuning Ferromagnetism In Diluted Magnetic Oxide Thin Films. *Phys. Rev. B* **2005**, *72*, 045336.
- (97) Ogale, S. B.; Choudhary, R. J.; Buban, J. P.; Lofland, S. E.; Shinde, S. R.; Kale, S. N.; Kulkarni, V. N.; Higgins, J.; Lanci, C.; Simpson, J. R. High Temperature

Ferromagnetism With a Giant Magnetic Moment in Transparent Co-Doped SnO_{2-δ}. *Phys. Rev. Lett.* **2003**, *91*, 077205.

(98) Dietl, T. A Ten-Year Perspective on Dilute Magnetic Semiconductors and Oxides. *Nat. Mater.* **2010**, *9*, 965-974.

(99) Pearton, S. J.; Abernathy, C. R.; Overberg, M. E.; Thaler, G. T.; Norton, D. P.; Theodoropoulou, N.; Hebard, A. F.; Park, Y. D.; Ren, F.; Kim, J. Wide Band Gap Ferromagnetic Semiconductors and Oxides. *J. Appl. Phys.* **2003**, *93*, 1-13.

(100) Liu, C.; Yun, F.; Morkoc, H. Ferromagnetism of ZnO and GaN: A Review. *J. Mater. Sci. Mater. Electron.* **2005**, *16*, 555-597.

(101) MacDonald, A. H.; Schiffer, P.; Samarth, N. Ferromagnetic Semiconductors: Moving Beyond (Ga, Mn)As. *Nat. Mater.* **2005**, *4*, 195-202.

(102) Chambers, S. A.; Droubay, T. C.; Wang, C. M.; Rosso, K. M.; Heald, S. M.; Schwartz, D. A.; Kittilstved, K. R.; Gamelin, D. R. Ferromagnetism In Oxide Semiconductors. *Mater. Today* **2006**, *9*, 28-35.

(103) Sarkar, I.; Sanyal, M. K.; Kar, S.; Biswas, S.; Banerjee, S.; Chaudhuri, S.; Takeyama, S.; Mino, H.; Komori, F. Ferromagnetism in Zinc Sulfide Nanocrystals: Dependence on Manganese Concentration. *Phys. Rev. B* **2007**, *75*, 224409.

(104) Norberg, N. S.; Parks, G. L.; Salley, G. M.; Gamelin, D. R. Giant Excitonic Zeeman Splittings in Colloidal Co²⁺-Doped ZnSe Quantum Dots. *J. Am. Chem. Soc.* **2006**, *128*, 13195-13203.

(105) Cheng, S.-J. Theory of Magnetism in Diluted Magnetic Semiconductor Nanocrystals. *Phys. Rev. B* **2008**, *77*, 115310.

(106) Shanker, G. S.; Tandon, B.; Shibata, T.; Chattopadhyay, S.; Nag, A. Doping controls plasmonics, electrical conductivity, and carrier-mediated magnetic coupling in Fe and Sn codoped In₂O₃ nanocrystals: local structure is the key. *Chem. Mater.* **2015**, *27*, 892-900.

(107) Leslie-Pelecky, D. L.; Rieke, R. D. Magnetic Properties of Nanostructured Materials. *Chem. Mater.* **1996**, *8*, 1770-1783.

(108) Wu, L.; Mendoza Garcia, A.; Li, Q.; Sun, S. Organic Phase Syntheses of Magnetic Nanoparticles and Their Applications. *Chem. Rev.* **2016**, *116*, 10473-10512.

(109) Daniel, M.-C.; Astruc, D. Gold Nanoparticles: Assembly, Supramolecular Chemistry, Quantum-Size-Related Properties, and Applications Toward Biology, Catalysis, and Nanotechnology. *Chem. Rev.* **2004**, *104*, 293-346.

- (110) Talapin, D. V.; Lee, J. S.; Kovalenko, M. V.; Shevchenko, E. V. Prospects of Colloidal Nanocrystals for Electronic and Optoelectronic Applications. *Chem. Rev.* **2009**, *110*, 389-458.
- (111) Ganteför, G.; Eberhardt, W. Localization of 3d and 4d Electrons in Small Clusters: The “Roots” of Magnetism. *Phys. Rev. Lett.* **1996**, *76*, 4975.
- (112) Frenkel, J.; Dorfman, J. Spontaneous and Induced Magnetisation in Ferromagnetic Bodies. *Nature* **1930**, *126*, 274-275.
- (113) Kittel, C. Theory of the Structure of Ferromagnetic Domains in Films and Small Particles. *Phys. Rev.* **1946**, *70*, 965.
- (114) Kneller, E. F.; Luborsky, F. E. Particle Size Dependence of Coercivity and Remanence of Single-Domain Particles. *J. Appl. Phys.* **1963**, *34*, 656-658.
- (115) Morales, M. P.; Veintemillas-Verdaguer, S.; Montero, M. I.; Serna, C. J.; Roig, A.; Casas, L. I.; Martinez, B.; Sandiumenge, F. Surface and Internal Spin Canting in γ -Fe₂O₃ Nanoparticles. *Chem. Mater.* **1999**, *11*, 3058-3064.
- (116) Nealon, G. L.; Donnio, B.; Greget, R.; Kappler, J. P.; Terazzi, E.; Gallani, J. L. Magnetism in Gold Nanoparticles. *Nanoscale* **2012**, *4*, 5244-5258.
- (117) Crespo, P.; Litrán, R.; Rojas, T.; Multigner, M.; De la Fuente, J. M.; Sánchez-López, J. C.; García, M.; Hernando, A.; Penadés, S.; Fernández, A. Permanent Magnetism, Magnetic Anisotropy, and Hysteresis of Thiol-Capped Gold Nanoparticles. *Phys. Rev. Lett.* **2004**, *93*, 087204.
- (118) Lu, A. H.; Salabas, E. L.; Schüth, F. Magnetic Nanoparticles: Synthesis, Protection, Functionalization, and Application. *Angew. Chem. Int. Ed.* **2007**, *46*, 1222-1244.
- (119) Bussian, D. A.; Crooker, S. A.; Yin, M.; Brynda, M.; Efros, A. L.; Klimov, V. I. Tunable Magnetic Exchange Interactions in Manganese-Doped Inverted Core–Shell ZnSe–CdSe Nanocrystals. *Nat. Mater.* **2009**, *8*, 35-40.
- (120) Beaulac, R.; Schneider, L.; Archer, P. I.; Bacher, G.; Gamelin, D. R. Light-induced spontaneous magnetization in doped colloidal quantum dots. *Science* **2009**, *325*, 973-976.
- (121) Chattopadhyay, S.; Kelly, S. D.; Shibata, T.; Viswanatha, R.; Balasubramanian, M.; Stoupin, S.; Segre, C. U.; Sarma, D. D. EXAFS Studies of Nanocrystals of Zn_{1-x}Mn_xO: A Dilute Magnetic Semiconductor Oxide System. *X-Ray Absorption Fine Structure-XAFS* **2007**, *882*, 809-811.

- (122) Yuhas, B. D.; Fakra, S.; Marcus, M. A.; Yang, P. Probing the Local Coordination Environment for Transition Metal Dopants In Zinc Oxide Nanowires. *Nano Lett.* **2007**, *7*, 905-909.
- (123) Segura Ruiz, J.; Martinez Criado, G.; Chu, M. H.; Geburt, S.; Ronning, C. Nano-X-Ray Absorption Spectroscopy of Single Co-Implanted ZnO Nanowires. *Nano Lett.* **2011**, *11*, 5322-5326.
- (124) Ibraheem, F.; Mahdy, M. A.; Mahmoud, E. A.; Ortega, J. E.; Rogero, C.; Mahdy, I. A.; El-Sayed, A. Tuning Paramagnetic Effect of Co-Doped CdS Diluted Magnetic Semiconductor Quantum Dots. *J. Alloys Compd.* **2020**, *834*, 155196.
- (125) Zhao, X.; Liang, H.; Chen, Y.; Chen, X.; Zhang, W.; Wang, J.; Zhang, G.; Belotelov, V. I.; Song, Y. Magnetic Field Coupling Microfluidic Synthesis of Diluted Magnetic Semiconductor Quantum Dots: The Case of Co Doping ZnSe Quantum Dots. *J. Mater. Chem. C* **2021**, *9*, 4619-4627.
- (126) Abo-Naf, S. M.; Ibrahim, S.; Marzouk, M. A. Structure, Optical and Ferromagnetic Properties of $Zn_{1-x-y}Mn_xCr_yO$ Nanoparticles Diluted Magnetic Semiconductors Synthesized By Citrate Sol-Gel Method. *Appl. Phys. A* **2021**, *127*, 1-11.
- (127) Bandyopadhyay, A.; Gupta, N.; Nath, M.; Chakraborty, S.; Sutradhar, S. Magnetic Properties of Mn Doped ZnO: A Monte Carlo Simulation Analysis. *Vacuum* **2021**, *183*, 109786.
- (128) Pandey, A.; Brovelli, S.; Viswanatha, R.; Li, L.; Pietryga, J. M.; Klimov, V. I.; Crooker, S. A. Long-Lived Photoinduced Magnetization In Copper-Doped ZnSe-CdSe Core-Shell Nanocrystals. *Nat. Nanotechnol.* **2012**, *7*, 792-797.
- (129) Radovanovic, P. V.; Gamelin, D. R. High-Temperature Ferromagnetism in Ni^{2+} -Doped ZnO Aggregates Prepared from Colloidal Diluted Magnetic Semiconductor Quantum Dots. *Phys. Rev. Lett.* **2003**, *91*, 157202.
- (130) Sharma, P.; Gupta, A.; Rao, K. V.; Owens, F. J.; Sharma, R.; Ahuja, R.; Guillen, J. M. O.; Johansson, B.; Gehring, G. A. Ferromagnetism Above Room Temperature In Bulk and Transparent Thin Films of Mn-Doped ZnO. *Nat. Mater.* **2003**, *2*, 673-677.
- (131) Sundaresan, A.; Bhargavi, R.; Rangarajan, N.; Siddesh, U.; Rao, C. N. R. Ferromagnetism As a Universal Feature of Nanoparticles of the Otherwise Nonmagnetic Oxides. *Phys. Rev. B* **2006**, *74*, 161306.
- (132) Jana, S.; Srivastava, B. B.; Jana, S.; Bose, R.; Pradhan, N. Multifunctional Doped Semiconductor Nanocrystals. *J. Phys. Chem. Lett.* **2012**, *3*, 2535-2540.

- (133) Bogle, K. A.; Ghosh, S.; Dhole, S. D.; Bhoraskar, V. N.; Fu, L.-f.; Chi, M.-f.; Browning, N. D.; Kundaliya, D.; Das, G. P.; Ogale, S. B. Co: CdS Diluted Magnetic Semiconductor Nanoparticles: Radiation Synthesis, Dopant–Defect Complex Formation, and Unexpected Magnetism. *Chem. Mater.* **2007**, *20*, 440-446.
- (134) Giribabu, G.; Murali, G.; Reddy, D. A.; Liu, C.; Vijayalakshmi, R. P. Structural, Optical and Magnetic Properties of Co Doped CdS Nanoparticles. *J. Alloys Comp.* **2013**, *581*, 363-368.
- (135) Viswanatha, R.; Naveh, D.; Chelikowsky, J. R.; Kronik, L.; Sarma, D. D. Magnetic Properties of Fe/Cu codoped ZnO Nanocrystals. *J. Phys. Chem. Lett.* **2012**, *3*, 2009-2014.
- (136) Tandon, B.; Yadav, A.; Nag, A. Delocalized Electrons Mediated Magnetic Coupling in Mn-Sn codoped In₂O₃ Nanocrystals: Plasmonics Shows the Way. *Chem. Mater.* **2016**, *28*, 3620–3624.
- (137) Pandey, A.; Brovelli, S.; Viswanatha, R.; Li, L.; Pietryga, J. M.; Klimov, V. I.; Crooker, S. A. Long-Lived Photoinduced Magnetization in Copper-Doped ZnSe-CdSe Core-Shell Nanocrystals. *Nat. Nanotechnol.* **2012**, *7*, 792-797.
- (138) Radovanovic, P. V.; Gamelin, D. R. Electronic Absorption Spectroscopy of Cobalt Ions In Diluted Magnetic Semiconductor Quantum Dots: Demonstration of an Isocrystalline Core/Shell Synthetic Method. *J. Am. Chem. Soc.* **2001**, *123*, 12207-12214.
- (139) Sanders, G. D.; Musfeldt, J. L.; Stanton, C. J. Tuning g Factors of Core-Shell Nanoparticles by Controlled Positioning of Magnetic Impurities. *Phys. Rev. B* **2016**, *93*, 075431.
- (140) MacKay, J.; Becker, W.; Spaek, J.; Debska, U. Temperature and Magnetic-Field Dependence of the Mn²⁺ ⁴T₁(4 G) → ⁶A₁(6 S) Photoluminescence Band in Zn_{0.5}Mn_{0.5}Se. *Phys. Rev. B* **1990**, *42*, 1743.
- (141) Viswanatha, R.; Pietryga, J. M.; Klimov, V. I.; Crooker, S. A. Spin-Polarized Mn²⁺ Emission from Mn-Doped Colloidal Nanocrystals. *Phys. Rev. Lett.* **2011**, *107*, 067402.
- (142) Zheng, W.; Strouse, G. F. Involvement of Carriers in the Size-Dependent Magnetic Exchange for Mn: CdSe Quantum Dots. *J. Am. Chem. Soc.* **2011**, *133*, 7482-7489.
- (143) Ochsenein, S. T.; Feng, Y.; Whitaker, K. M.; Badaeva, E.; Liu, W. K.; Li, X.; Gamelin, D. R. Charge-Controlled Magnetism in Colloidal Doped Semiconductor Nanocrystals. *Nat. Nanotechnol.* **2009**, *4*, 681-687.

CHAPTER 2

Methodology

2.1 Summary

In this chapter, we describe briefly the experimental techniques that have been employed to characterize and study different doped and undoped nanocrystal systems reported in this thesis. The various experimental techniques are outlined here: X-ray absorption fine structure spectroscopy, transient absorption spectroscopy, magnetic circular dichroism, SQUID magnetometer, x-ray diffraction, transmission electron microscopy, UV-visible absorption, inductively coupled plasma optical emission spectrometry.

2.2 Experimental techniques

2.2.1 X-ray absorption fine structure spectroscopy

X-ray absorption fine structure (XAFS)¹⁻³ spectroscopy is used to investigate the local structure around elements in doped and undoped nanocrystals. It is used to determine the distribution of the dopants, detecting the presence of secondary phases or metal clusters, occupation sites and also identifying the coordination number of elements for doped/undoped nanocrystals in the thesis.

The properties of doped semiconductors are widely known to be primarily determined by their atomic and electronic structures which are crucially dependent on the amount of dopant ions and their distributions over different positions (such as interstitial site, substitutional site, metallic clusters or secondary phases) in the host lattice. Developed in early 1970,¹ XAFS has become a powerful probe for identifying the occupation sites of the dopants in semiconductors due to its sensitivity to the local atomic structure.

X-rays are absorbed by an element through the photoelectric effect, where a core level electron is ejected from the atom resulting in an empty electronic level with a hole (in the core) and the excess energy is given to the ejected photoelectron.

Further, when the excited electron relaxes back to the ground state, a higher level core electron occupies the core hole position, resulting in fluorescent x-ray or Auger electron is emitted. X-ray fluorescence describes the process when an electron from a higher energy level comes down and fills the empty core level releasing energy. The fluorescence energies are characteristic of the particular atom and can be used to identify an atom. In the Auger effect as the electron from the higher level comes down to the empty core level, the relaxation energy is transferred to any other second electron in the same higher energy

level. Absorbing the energy, the second electron gets excited to the continuum or leaves the system.

The intensity of an x-ray beam passing through a material of thickness t is given by the absorption coefficient μ :

$$I=I_0 e^{-\mu t}$$

where I_0 and I are incident and transmitted x-ray intensity respectively.

Further, the absorption coefficient (μ) is can be expressed as,

$$\mu \approx \frac{\rho z^4}{AE^3}$$

where ρ is sample density, z is the atomic number, A is atomic mass, E is the energy of x-rays. XAFS measures the absorption coefficient as a function of x-ray energy. At certain energy where the x-ray energy matches with the binding energy of the core-electron, the absorption is increased drastically giving rise to the absorption edge. At this energy, the core electron is excited to the continuum state and produces a photoelectron.

Further, the information about the neighbouring atoms can be obtained from the energy-dependent oscillations in $\mu(E)$, where EXAFS represents an oscillatory behavior of absorption coefficient (μ) as a function of x-ray energy.

All the atoms surrounding the absorbing atom take part in EXAFS signal formation. The nearest atoms form the first shell and the number of atoms in the first shell is called the coordination number. The second nearest atoms form the second shell and so on.

The EXAFS spectra are defined as fine structure-function given by-

$$\chi(E) = \frac{\mu(E) - \mu_0(E)}{\Delta\mu_0(E)}$$

where $\mu(E)$ is the experimental absorption coefficient, $\mu_0(E)$ is slowly varying absorption from an isolated atom and $\Delta\mu_0(E)$ is a jump in the absorption coefficient $\mu(E)$ at the threshold.

Expressing XAFS in terms of photo-electron wavenumber as it is an interference effect and depends on the wave nature of photoelectron. Therefore, expressing x-ray energy in terms of wavenumber k , of the photoelectron that can be defined as

$$k = \left(\frac{2m(E - E_0)}{\hbar^2}\right)^{\frac{1}{2}}$$

where E_0 is absorption edge energy and m is mass of the electron.

Scattering from different neighbouring atoms give rise to different frequencies and the EXAFS oscillation $\chi(k)$ can be expressed as

$$\chi(k) = \sum \frac{N_j f_j(k) e^{-2k^2 \sigma_j^2}}{k R_j^2} \sin[2k(R_j + \delta_j(k))]$$

where $f(k)$ and $\delta(k)$ are scattering properties of the neighbouring atoms, R is the distance of the interacting neighbour, N is the coordination number and σ^2 is the Debye-Waller factor. By appropriate modeling of EXAFS spectra, one can determine N , R , σ^2 from this equation knowing the scattering amplitude $f(k)$ and phase shift $\delta(k)$.

Thus, the matter interacts with electromagnetic radiation through the dominant photoelectric absorption in the x-ray spectral region. There are characteristic energies for a specific element called absorption edges at which excitation of particular core-level electrons is energetically allowed. A jump across the absorption edge is exhibited by the x-ray absorption coefficient $\mu(E)$, followed by an oscillatory structure at higher energies. The attributes of x-ray absorption at energies near and above the absorption edge are described by the XAFS spectrum. XANES spectral region is described by the energy range from the absorption edge to typically 30-50 eV above it. EXAFS describes oscillation over a wide energy range extending 1000 eV or more above the absorption edge. There is no fundamental difference in physics giving rise to the fine structures of XANES and EXAFS and the distinction between these two spectral regions is somewhat arbitrary.

So, XAFS has various advantages such as sensitivity to the short-range order (typically several Å), element specificity, and chemical state of the element. It provides quantitative structural information about the local environment around the absorbing atom at an atomic scale, i.e., near-neighbour species and distance, fluctuation in bond distance and coordination number. XANES can distinguish the electronic state and the three-dimensional coordination geometry. EXAFS is specifically sensitive to the distance, species of the atoms immediately surrounding the absorbing atoms and coordination number. The sensitivity to the short-range order makes XAFS capable of probing the local structure for a diversity of systems irrespective of the phase. Using synchrotron radiation light sources, many kinds of measurement methods have been developed to obtain high-quality XAFS data, such as transmission XAFS for bulk material, grazing-incidence XAFS for surface research, fluorescence XAFS for dilute impurities and thin films, magnetic XAFS for spin study, in situ (high-temperature, high-pressure) XAFS for state

or stress transformation investigation, space-resolved XAFS and even time-resolved XAFS for kinetics studies.

2.2.2 Transient absorption spectroscopy

The dopant host interactions in transition metal doped II-VI semiconductors typically happen on a time scale of fewer than 10 ps and ultrafast pump-probe spectroscopy has opened up a way to understand this extremely fascinating area of research. In transient absorption (TA) spectroscopy, using an excitation pump pulse, the system is promoted to an electronically excited state. A weak probe pulse with a delay with respect to the pump pulse is then sent through the sample. A difference in the absorption spectrum (ΔA) is recorded. ΔA profile as a function of delay time and probe energy is generated by changing the time delay between the pump and the probe and recording a ΔA spectrum at each time delay. This can provide information about the excitation and de-excitation processes happening within the doped/undoped semiconductor nanocrystals.

Various processes contribute to a ΔA spectrum

- *Ground state bleach* - the action of a pump pulse results in excitation of a fraction of the species involved and a reduction in the number of species in the ground state. Thus, the ground state absorption for the excited system is lower than the non-excited state. Thus, a negative signal in the differential absorption (positive signal in the differential transmission) is observed in the wavelength regime of ground state absorption.
- *Stimulated emission* - the Einstein coefficients are identical for a two-level system involving absorption from the ground to the excited state and stimulated emission from the excited state to the ground state. After excitation, stimulated emission (for optically allowed transitions) to the ground state takes place when the probe pulse interacts with the excited species. Stimulated emission will have a Stoke shifted spectral profile (like fluorescence spectrum) with respect to the ground state bleach. Interaction of probe pulse induces emission of another photon from the excited molecule which returns to the ground state during the process of stimulated emission. Photon produced during stimulated emission is emitted in the same direction as the probe photon, resulting in the detection of both. The feeble probe pulse doesn't affect the excited-state population. Further, stimulated

emission results in enhancement of the intensity (negative ΔA signal) reaching the detector.

- *Excited-state absorption* - Optically allowed transitions from the excited (populated) states of a species to higher excited states may occur resulting in a positive signal in the ΔA spectrum for excited-state absorption.
- *Product absorption*. After excitation of the system, further processes may occur that result in a long-lived or a transient state, such as triplet states, isomerized states, charge-separated states. A positive signal in the ΔA spectrum is observed as a result of the absorption of a (transient) product. A ground-state bleach is observed at the wavelengths where the species on which the product state resides has a ground-state absorption.

2.2.3 Magnetic circular dichroism

Faraday effect forms the basis of magnetic circular dichroism (MCD), which states that optical activity can be induced within the system by an applied magnetic field that induces changes in the electronic states of the system. In magnetic circular dichroism (MCD) spectroscopy, differential absorption of right circularly polarised (RCP) light and left circularly polarised (LCP) light is observed in a sample in presence of a strong external magnetic field applied parallel to the light of propagation. MCD can detect overlapping transitions and also those transitions that are too weak to be detected by optical absorption.

The incorporation of open-shell transition metal impurities into the semiconductor system introduces localized unpaired spins that are magnetically coupled to delocalized (free or photogenerated) charge carriers, with coupling strengths that depend on the dopant-carrier spatial overlap. These *sp-d* exchange interactions are the defining feature of a DMS, giving rise to a suite of remarkable magneto-optical properties. An external magnetic field can be used to induce excitonic Zeeman splittings in doped semiconductors.

The sign and magnitude of the excitonic Zeeman splitting (ΔE_Z) is given by-

$$\Delta E_Z = \Delta E_{\text{int}} + \Delta E_{sp-d} = g_{\text{int}} \mu_B B + x \gamma N_0 (\alpha - \beta) \langle S_Z \rangle$$

The first term describes the relatively small intrinsic excitonic Zeeman splitting (ΔE_{int}), where g_{int} is the exciton's intrinsic g value, μ_B is the Bohr magneton, and B is the external magnetic field. The second term describes contributions from the *sp-d* exchange, where x is

is the fractional dopant concentration and γ describes the exciton-dopant spatial overlap. $\langle S_Z \rangle$ represents the dopant's spin expectation value, quantized along the magnetic field axis.

$\langle S_Z \rangle$ is described by the Brillouin-type function, with g_{TM} representing the isotropic g-factor of the transition metal ion.

$$\langle S_Z \rangle = -1/2 [(2S+1)\coth\{(2S+1) g_{TM}\mu_B B/2kT\} - \coth\{g_{TM}\mu_B B/2kT\}]$$

The terms $N_0\alpha$ and $N_0\beta$ describe the mean-field dopant-carrier exchange coupling constants, where N_0 is the lattice cation density and α and β are the pairwise exchange energies. The Zeeman splitting arising from the *sp-d* exchange, therefore, opposes the relatively weak intrinsic Zeeman splitting. ΔE_{int} is small, positive, and temperature-independent for the first exciton of II-VI semiconductors.

Also, excitonic Zeeman splittings (ΔE_Z) can be calculated from the absorption and MCD data using the expression

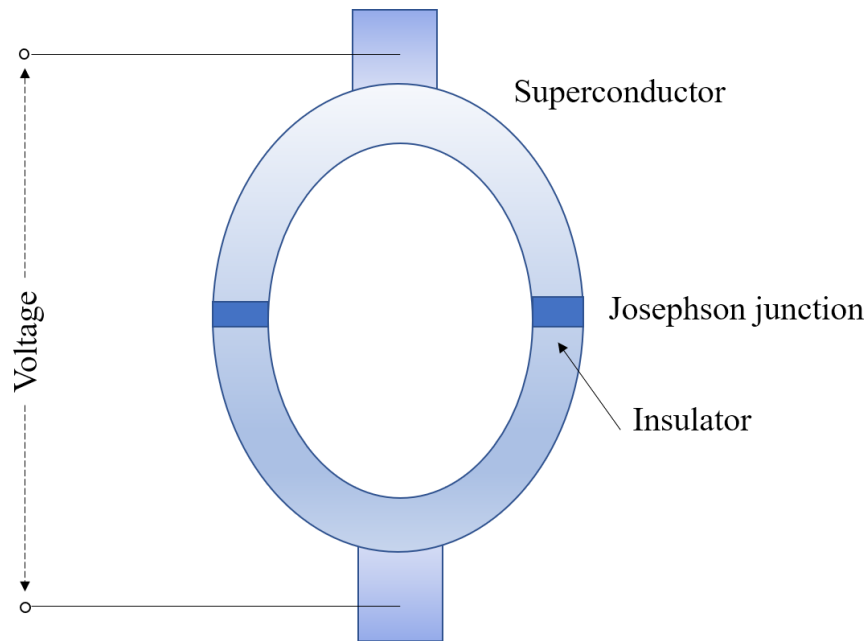
$$\Delta E_Z = \frac{\sqrt{2}e}{2} \sigma \frac{\Delta A}{A_0}$$

where ΔA corresponds to the maximum amplitude of the lowest-energy leading-edge MCD feature and A_0 and σ are the height and Gaussian width of the absorption peak respectively.

Here in the thesis, MCD studies were used to elucidate the structural information of excitonic transition in clustered and diffused systems. Further, MCD experiments were used to investigate the *sp-d* exchange interaction between the magnetic dopants and the charge carriers of the host lattice to probe the magneto-optical activity. The temperature and field-dependent studies were performed to study the behavior of different transitions.

2.2.4 SQUID magnetometer

Magnetic measurements (magnetization vs. magnetic field and D. C. susceptibility) were conducted using a superconducting quantum interference device (SQUID) magnetometer. It consists of two superconductors separated by a thin insulating layer to form two parallel Josephson junctions (shown in the schematic below) where Josephson junctions laid the foundation of a SQUID.



Scheme: Schematic of a SQUID device.

Faraday's law of electromagnetic induction describes the working principle of the SQUID magnetometer⁴ where an electromotive force (voltage) is induced in the coil as a result of a change in magnetic flux, which is equal to the rate of change of flux. Thus, a small change in magnetic flux can induce a voltage that reduces the current on one side and increases on the other side of the Josephson junction where superconducting current tunnel through both the junctions. The variation in each flux across boundary of the rings gives rise to a voltage step. The SQUID is placed inside the helium bath and linked to a superconducting pick-up coil to detect the variation in magnetic flux as a result of sample vibration inside it. A superconducting magnet is placed around the pickup coil that generates the magnetic field. The magnetic flux from the sample to the SQUID is transferred using the coil along with the SQUID antenna that acts as a magnetic flux to voltage converter. This voltage is further amplified and read out by the electronics circuit attached to the device.

2.2.5 X-ray diffraction

All diffraction techniques are based on the generation of x-rays. Diffraction effects are perceived when electromagnetic radiation interacts with periodic structures with geometrical variations on the length scale of the wavelength of the radiation. The interatomic distances in crystals are in the range which corresponds to that of x-rays.

X-ray diffraction is an important structural technique for the characterization of nanocrystals. It is based on constructive interference of monochromatic x-rays (generated by a cathode ray tube) and the sample when Bragg's condition $n\lambda = 2d \sin \theta$ is satisfied, where, $n=1,2,3$, and λ = wavelength of the x-ray radiation.

According to Bragg's law, when an x-ray beam incident on a set of parallel planes with an interplanar spacing d and the two parallel incident rays make an angle θ with these planes, constructive interference will occur if the path difference between the x-rays scattered from parallel planes is an integer number of the wavelength of radiation. This condition correlates the diffraction angle and the lattice spacing in a crystalline sample to the wavelength of electromagnetic radiation. The diffracted x-rays are then detected and processed. All possible diffraction directions of the lattice are attained by scanning the sample through a range of 2θ angles and the random orientation of the powdered material gives access to all possible diffraction directions of the lattice.

Further, the finite size of the nanocrystals results in broadening of the XRD peaks. The correlation between the size of the nanocrystals and peak broadening is given by Scherrer's equation, $D_{hkl} = (0.89 \lambda / \beta_{hkl} \cos \theta)$, where D_{hkl} = thickness of the crystal, λ = x-ray wavelength, β = line broadening at FWHM (full width at half maximum), θ = Bragg angle.

Thus apart from identifying the crystal structure and phase purity of the nanocrystals, this technique also provides an estimate of the size of the nanocrystals using the above Scherrer formula.

2.2.6 Transmission electron microscopy

Here, transmission electron microscopy (TEM) is used as proof for the formation of nanocrystals. TEM when combined with other chemical techniques allows for the study of surfaces, interfaces, or the distribution of elements in a sample.

TEM operates on the same principle as a light microscope but uses electrons instead of light. Because of the wavelength range involved in TEM, the images are better resolved than the light microscope down to about 0.1 nm resolution. TEM uses a beam of electrons produced by heating a tungsten filament, that passes through an ultra-thin sample interacting with the sample as it passes through. The beam is directed using electromagnetic lenses and strikes the sample, where a part of the beam is transmitted

depending on electron transparency and thickness of the sample. The objective lens focuses this transmitted beam into an image on a phosphor screen or charge-coupled device (CCD) camera. Transmission of fewer electrons results in darker areas of the image while lighter areas represent transmission of more electrons determining the non-uniformity in density if any. Thus, a TEM sample must be thin enough to transmit sufficient electrons avoiding energy loss. Also, the electrons are either inelastically or elastically scattered as they pass through the sample where the scattered or transmitted electrons can be imaged, known as light-field and dark-field imaging, respectively. High-resolution imaging (HRTEM) provides lattice-resolved images of the sample where it is used to study the defects or phase transitions in the system. Selected area electron diffraction (SAED) patterns provide information about the crystalline phase of the nanocrystals.

Scanning transmission electron microscope – energy dispersive x-ray spectroscopy

Scanning transmission electron microscopy (STEM) combines the principles of scanning electron microscopy and transmission electron microscopy and analyzes the beam transmitted by the sample. It is used to study the distribution of elements within the sample. Here, transmitted beam electrons that are scattered through a relatively large angle are detected using a high angle annular dark-field (HAADF) detector. We used STEM-EDX mapping to visualize the distribution of dopants within the nanocrystals.

2.2.7 UV-visible absorption

The UV-visible absorption is dominated by features related to the exciton formation and transition across the bandgap in nanocrystals. Here, the absorption characteristics are sensitive to the size and shape of nanocrystals. Thus this method is most often used to study systematic changes in the electronic structure of nanocrystals as a function of its size and morphology where a blue shift of the absorption edge corresponds to the quantum confinement in a nanometer-sized regime.

Beer-Lambert law describes how light is absorbed by a system. According to the law, for absorbing material the intensity of light coming out of the sample is determined by i) the concentration of the absorbing material (c), ii) optical path length (l) i.e. distance travelled by light through the sample, (iii) extinction coefficient of the substance (ϵ) that gives the probability that a photon of particular energy will be absorbed by the sample.

When a beam of light hits an absorbing material, the spectrometer measures the intensity before it strikes the substance (I_0), and then after it passes through the substance (I_t). The incident light may undergo absorption, reflection, interference, and scattering before it is transmitted to the detector. Thus, the intensity of light through the substance (I_t) will be reduced by a certain amount. For a homogeneous sample, the fractional decrease in light intensity will be the same across a small interval dx , regardless of the value of x and will depend linearly on the concentration of the absorbing material. The fractional change in intensity of light can therefore be equated as:

$$\frac{-dI}{I} = \alpha c dx$$

where α is a constant of proportionality. The integration between limits I_0 at $x = 0$ and I_t at $x = l$ provides

$$\ln \frac{I_0}{I_t} = \alpha c l \quad \text{or} \quad I_t = I_0 e^{-\alpha c l}$$

The optical density or absorbance (A) is defined as base 10 rather than a natural logarithm.

$$A = \log \frac{I_0}{I_t} = \epsilon c d$$

where $\epsilon = \alpha/2.303$ is the molar extinction coefficient (with units $M^{-1}cm^{-1}$), c is the concentration (M), and d is the path length (cm). The Lambert-Beer Law shows that the absorbance is proportional to the path length and concentration of the solute where ϵ is the proportionality constant. The relationship between absorbance and transmission is given by

$$A = -\log (I_t/I_0), \text{ where } I_t/I_0 = \text{Transmittance (T)}$$

Thus, for recording the absorption spectra, the samples were loaded in quartz cuvettes by dissolving in hexane. A blank cuvette containing only hexane was used as a reference. The absorption spectra were recorded for the nanocrystals.

2.2.8 Inductively coupled plasma - optical emission spectrometry

Inductively coupled plasma optical emission spectrometry (ICP-OES), is an analytical technique used for the determination of the relative percentage of elements present in the samples. It is a type of emission spectroscopy that works on the principle that atoms/ions can absorb energy to move electrons from the ground state to the excited state by argon

plasma that works as a source of heat energy. The plasma is extremely hot and can reach up to 10000 K in the induction zone. Due to the energy taken up by the electrons, they reach the excited state. The intensity of emitted light when the electrons in atoms/ions return to the lower energy state/ground state is then measured. As an electron returns from a higher energy level, it emits light of a very specific wavelength characteristic of a particular element. Further, the amount of light emitted at each wavelength is used to calculate the concentration of elements in the sample as the amount of light that is released at a particular wavelength is proportional to the number of species (atoms/ions) making the transition.

The accuracy in quantitative analysis through ICP-OES depends on the linearity of the calibration plot obtained from the standards. For calibrating ICP-OES, solutions with known concentrations are measured and a calibration curve is generated. The curve determines the correspondence between the concentration of an element in the sample and the intensity of light emitted at a specific wavelength. The concentrations of the unknown are determined from these calibration curves.

Here, we have used ICP-OES to determine the elemental concentration of dopants in the nanocrystals.

Bibliography

- (1) Sayers, D. E.; Stern, E. A.; Lytle, F. W. New Technique for Investigating Noncrystalline Structures: Fourier Analysis of the Extended X-Ray-Absorption Fine Structure. *Phys. Rev. Lett.* **1971**, *27*, 1204.
- (2) Rehr, J. J.; Albers, R. C. Theoretical Approaches to X-ray Absorption Fine Structure. *Rev. Mod. Phys.* **2000**, *72*, 621-654.
- (3) Newville, M. IFEFFIT: Interactive XAFS Analysis and FEFF Fitting. *J. Synchrotron Rad.* **2001**, *8*, 322-324.
- (4) B. D. Cullity, C. D. G. *Introduction to Magnetic Materials*. Wiley-IEEE Press: 2008.

CHAPTER 3

Ultrafast electron-hole relaxation dynamics in CdS nanocrystals.

3.1 Summary

Surface traps significantly influence the charge carrier dynamics within semiconductor nanocrystals, introducing non-radiative exciton recombination channels which are detrimental for their applications. Understanding the nature of these trap states and modulating them synthetically bears immense potential in designing defect-free colloidal semiconductor nanocrystals for efficient optoelectronic devices. Thus, systems devoid of surface traps can be used to study the relaxation pathways of excitons generated within these nanocrystals. In this work, we study the ultrafast charge carrier relaxation dynamics upon near-edge resonance excitation and above-resonance excitation in CdS nanocrystals using ultrafast transient absorption spectroscopy, in order to understand intraband cooling and mid-gap trap states. The time-resolved studies reveal that the above bandgap excitation results in a three-step process, including instantaneous growth followed by a fast sub-picosecond decay and a long-lived (> 1 ns) excited state or a trap state recombination. The large percentage of long-lived excitons in CdS nanocrystals elucidates the defect-free nature of the system arising from the absence of surface states.

3.2 Introduction

Semiconductor nanocrystals (NCs) serve as promising functional materials in solar energy conversion,¹ optoelectronics,² biological imaging³ etc due to their tunable size and shape-dependent quantum effects. The electronic structure⁴⁻⁵ and origin of these size and shape-dependent properties⁶ have also been a subject of great interest in fundamental research. Due to the strong three-dimensional quantum confinement when the radius is smaller than the exciton Bohr radius, they present sharp, atom-like transitions between the discrete hole and electron levels, whose energies depend on the NC size. Also, the quantum efficiency of radiative recombination displayed by semiconductor NCs exceeds that of their bulk counterparts, due to the strong overlap between the spatially confined hole and electron wave functions, while excitons within the bulk semiconductors can easily dissociate leading to trapping of charge carriers.

Although the optical properties of NCs are mainly determined by the internal structure of the semiconductor, as the particle size decreases, the contribution of incompletely bonded surface atoms increases.⁷ The energy of these surface trap states generally lies within the bandgap, leading to trapping of charge carriers that prevents other useful photoinduced processes, like radiative recombination in photoemissive materials or charge separation in

photovoltaic materials. Thus, it is important to suppress the surface trap states in order to increase the device efficiency. Understanding the nature of these trap states and controlling their occurrence, especially with surfaces playing a large role due to the large surface to volume ratio in NCs, has recently gained a lot of attention.⁸⁻¹⁰

Further, the device photophysics/chemistry of these NCs is largely determined by the relaxation dynamics of the photoexcited electrons/holes. Thermalization of hot carriers is normally a fast process occurring on sub-picosecond time scales¹¹⁻¹² and is a major factor determining the power conversion efficiencies of optoelectronic devices based on NCs. This intraband relaxation is much faster than the radiative interband recombination (occurring on the nanosecond timescale) and has been the focus of various research directions like intraband lasing,¹³ mid-infrared light sources and detectors¹⁴ depending on different stages of carrier cooling. For instance, hot carrier relaxation should happen before photon emission in the case of quantum dot lasers.¹⁵ On the other hand, optimization of solar energy conversion efficiency is highly dependent on the utilization of hot carriers before they cool down.¹⁶⁻¹⁷ Thus it is important to characterize and control intraband carrier relaxation rates that can also be utilized to understand the host-dopant interactions in doped semiconductor NCs.

Understanding trap states essentially boils down to an understanding of the interaction of the host with very specific surface functionalization. The surface capped ligands can modulate the charge carrier relaxation affecting the carrier cooling dynamics.¹⁸⁻¹⁹ The ligand shell enfolds the semiconductor in a potential well so that the charges are concentrated within the core isolated from the surface, which has minimal impact on photoexcited charge carriers. Additionally, it has been shown that Auger-type recombination is mainly responsible for hot electron cooling.²⁰ However, surface ligands contribute to the hot hole relaxation via non-adiabatic pathway.²¹⁻²² Thus it is important to study the carrier cooling dynamics, as it has a direct impact on the performance of these NCs within optoelectronic devices. The femtosecond pump-probe technique is an ideal tool to shed light on carrier population dynamics in these NCs on a timescale of hundreds of femtoseconds to nanoseconds.

In this work we study the intraband relaxation of CdS NCs at near resonance and above-resonance excitations, where these NCs are known to have well-defined intraband transitions. The colloiddally synthesized CdS NCs were further overgrown with CdS shells (S-surface coverage being the last shell) to reduce the surface defects. Further, S²⁻ on the

surface increases the photooxidative degradation potential reducing the surface defects.²³ The defect states have been suggested to play an important role in excitation dynamics and carrier transport.²⁴⁻²⁶ However, our observation of long-lived excitonic states in CdS can be linked to the absence of defect/surface states in these NCs. When exciting above bandgap, we time-resolve a quick, sub-picosecond intraband relaxation to the bandgap exciton, followed by a long-lived photobleaching signal. These results indicate a negligible weight of competing relaxation channels and demonstrate the high quality of the CdS NCs, with a low density of surface defects.

3.3 Experimental section

Materials and synthesis.

Cadmium oxide (CdO), oleic acid (OA, 90%), 1-octadecene (ODE, 90%), oleylamine (OlAm, 70%), and sulfur powder (S, 99.5%) were purchased from Sigma Aldrich. All these chemicals were used without further purification.

Precursors for synthesis.

Cadmium oleate, a precursor for the synthesis of CdS NCs, was synthesized using cadmium oxide (CdO). Oleic acid and octadecene were used as coordinating solvents. For the synthesis of 0.2 M cadmium oleate, 0.3204 g cadmium oxide (CdO), 9 mL of octadecene (ODE) and 7 mL of oleic acid (OA) were taken in a three-necked round bottom flask. The system was degassed at 80 °C for two hours under constant stirring. The temperature was raised to 250 °C after degassing and kept under argon flow. The system was kept for some time until the precursors were completely dissolved and a clear solution was obtained. It was then cooled down to room temperature.

S-ODE, S-precursor for the synthesis of CdS nanostructures, was synthesized using sulfur powder. For the synthesis of S-ODE, 65 mg of sulfur powder and 10 mL of octadecene (ODE) were taken in a vial. The system was degassed at room temperature for 15-20 minutes. Argon was purged. Sonication and heating were performed to get a clear solution.

Synthesis of undoped CdS NCs. CdS core was synthesized and was further overcoated with CdS multilayers. 0.2 M cadmium oleate (0.5 mL) and ODE (4 mL) were taken in a three-necked flask and degassed at 80 °C. After 2 hours of degassing, the temperature was raised to 280 °C under constant Ar atmosphere and 0.2 M S-ODE (0.8 mL) was

quickly injected into the reaction mixture, with sulfur precursor being in excess to avoid S^{2-} vacancies, thus reducing the surface defects. The temperature was quickly brought down to 250 °C and 3 mL of OIAm was added to the reaction mixture. Further, CdS shells were grown using the successive ionic layer adsorption and reaction (SILAR) technique.²⁷ As S^{2-} vacancies are major contributors to surface defects,⁷ we have made sure that the system is rich in sulfur at every synthesis step. The core CdS nanoparticles were synthesized with excess sulfur. Further, the overcoating was initiated with sulfur precursor addition and the last step of the overcoating was also the addition of the sulfur precursor, where S^{2-} on the surface makes the system less susceptible to photooxidative degradation.

Characterization.

Transmission electron microscopy (TEM) was performed on a Tecnai F30 UHR version electron microscope, using a field emission gun (FEG) operating at an accelerating voltage of 200 kV in bright field mode using Cu coated holey carbon TEM grids. Powder x-ray diffraction (XRD) pattern for the NCs was recorded on a Bruker D8 advance diffractometer using $Cu-K_{\alpha}$ radiation (1.5418 Å). For recording the absorption spectra, the samples were dissolved in hexane and loaded in quartz cuvettes. A blank cuvette containing only hexane was used as a reference. The optical absorption spectra were obtained using an Agilent 8453 UV visible spectrometer. Pump-probe measurements were carried out using an amplified Ti: sapphire laser (Coherent Libra) as source, with maximum output energy of about 4 mJ, 1 kHz repetition rate, a central wavelength of 800 nm and pulse duration of about 100 fs. A fraction of the laser output was split to generate the required pulses. One part was used for generating the excitation (pump) pulses: the pump at 400 nm (3.1 eV) was generated by frequency doubling in a β -barium borate crystal, while the pump at 480 nm (2.58 eV) was generated using optical parametric amplification in a β -barium borate crystal. Pump pulses were modulated by a mechanical chopper at a 500 Hz repetition rate and were delayed in time using a mechanical stage. Finally, the pump was focused with a lens to obtain a fluence of around 24 $\mu J/cm^2$. The other part of the beam was used to generate the probe pulses by the white light continuum generation process, by focusing the 800 nm beam into a thin calcium fluoride plate, obtaining a spectrum ranging from 340 nm (3.65 eV) to 700 nm (1.77 eV). The probe pulse was focused on the sample non-collinearly with the pump beam and the spectrum of the transmitted probe beam was measured by an optical multichannel analyzer (OMA) working at the full 1 kHz laser repetition rate. Thanks to the modulation of the pump pulse, two consecutive probe pulses measure the sample in the excited and the ground state. By

measuring their corresponding intensities (I_{on} and I_{off}) one can calculate the normalized transmission change: $\Delta T/T = (I_{\text{on}}/I_{\text{off}}) - 1$, both as a function of wavelength (OMA detection) and time delay (mechanical delay). Chirp-free transient absorption spectra were obtained by using a dechirping algorithm.

3.4 Results and discussion

CdS NCs were obtained via colloidal synthesis and further overcoated with shells of CdS using the SILAR²⁷ technique to minimize the density of surface trap states. The careful control over the synthesis allowed precise engineering of defects. Further, thicker shells achieved through SILAR overcoating can quarantine a core exciton state and reduce the interaction between a core exciton state and the surface traps, leading to long-lived excitonic bleaching.²⁸⁻²⁹ The XRD pattern, as shown in figure 3.1, confirms the presence of hexagonal (space group) CdS NCs without any impurities. The reference XRD pattern for CdS (obtained from the inorganic crystal structure database) is also shown in figure 3.2. The particles exhibit uniform spherical morphology with a diameter of 12 ± 0.7 nm, as shown by the TEM image in figure 3.2. Figure 3.3 shows the absorption spectrum, with an onset at around 2.45 eV, along with a typical differential transmission ($\Delta T/T$) spectrum at 0.5 ps, following photoexcitation at 3.1 eV. The decay dynamics of CdS NCs were studied using a femtosecond transient absorption technique with a pump fluence of $24 \mu\text{J}/\text{cm}^2$ and acquired at 3.1 eV and 2.58 eV photoexcitation energies. The 3.1 eV (400 nm) pump photon energy corresponds to an off-resonance excitation above the bandgap for CdS NCs (~ 2.54 eV), while the 2.58 eV (480 nm) excitation is in near resonance with the first excitonic transition of CdS NCs, as shown by dotted lines in figure 3.3.

Figure 3.4(a) shows the time trace of the $\Delta T/T$ signal at probe energy of 2.54 eV upon excitation with pump energy of 3.1 eV. We observe a positive signal due to photobleaching (PB) of the excitonic transition. The trace displays a relatively fast rise, followed by fast decay for the first 20 ps with almost no further decay within the time frame of the study. The initial fast decay within the first few ps cannot be a result of electron-hole recombination. Hence it could either be the intraband cooling or the non-radiative recombination into the trap states. The schematic shown in Figure 3.4(b) shows the probable paths with the quantum mechanical states of the CdS NCs³⁰ as well as the trap states and/or Auger recombination states as observed from the data in Figure 3.4(a).

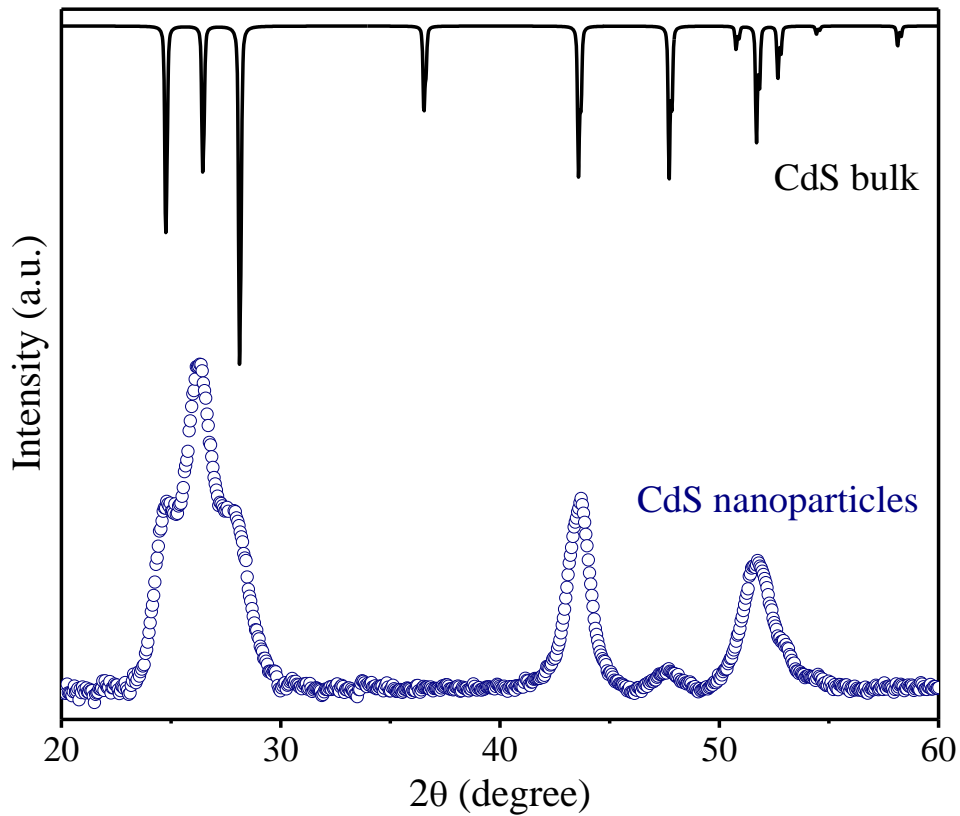


Figure 3.1. XRD pattern of CdS NCs along with bulk CdS obtained from inorganic crystal structure database (ICSD).

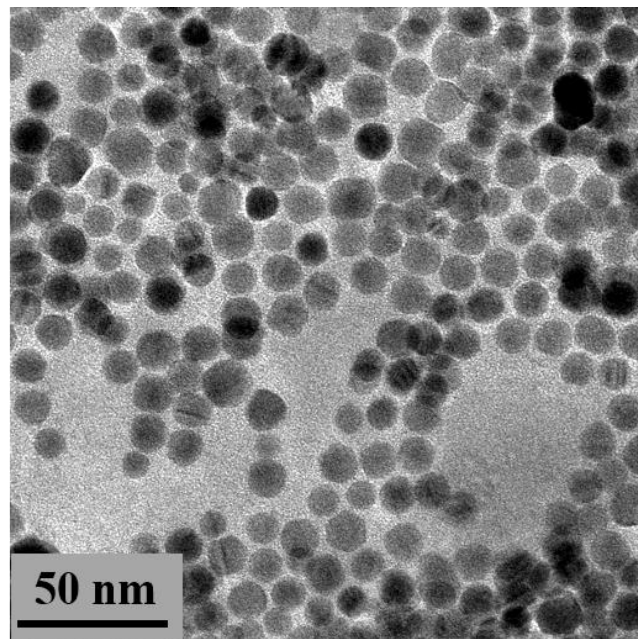


Figure 3.2. TEM image of CdS NCs with uniform size distribution.

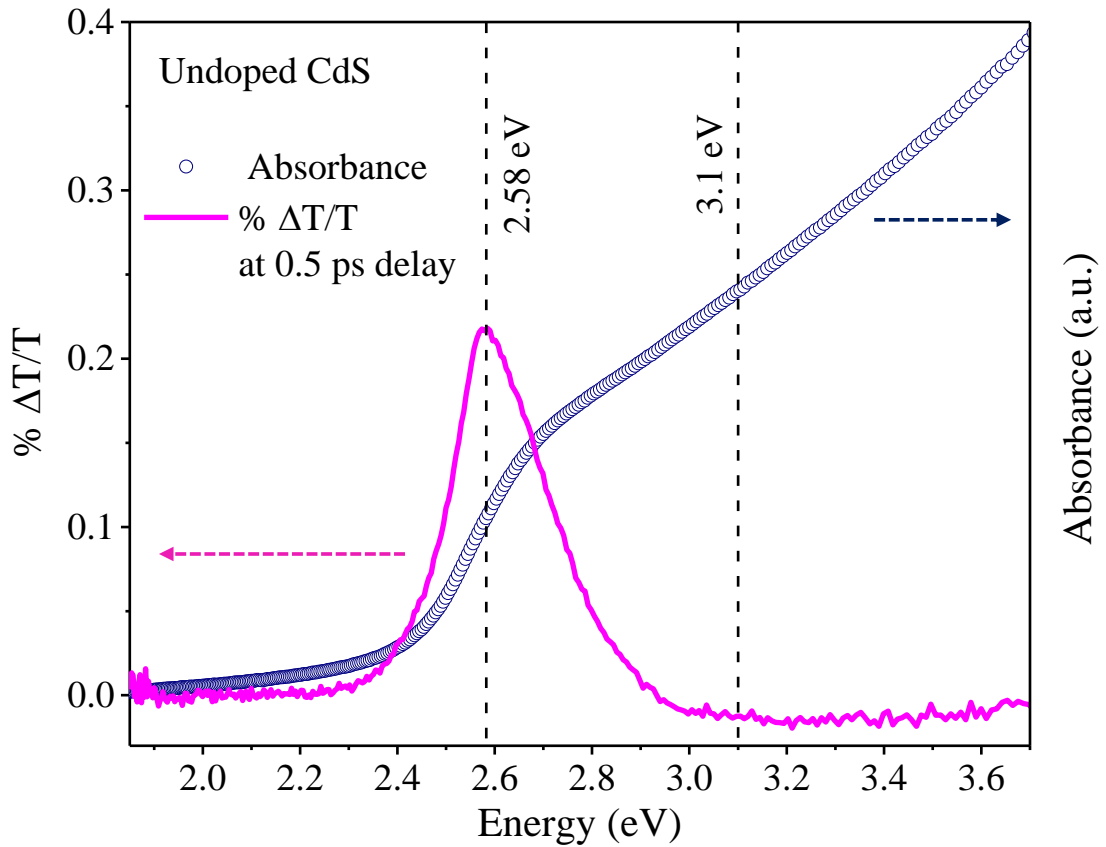


Figure 3.3. Absorption and differential transmission spectrum (at 0.5 ps delay) for CdS NCs. The dotted lines show the near-resonance and off-resonance pump photon energy.

However, upon zooming into the rise, we observe that the rise is not instantaneous within the instrumental response function (IRF) of the pump-probe apparatus, but rather takes a finite time, as shown in the inset to figure 3.4(a). To study the path of excited carriers, we have fitted the curve with a single exponential build-up followed by a biexponential decay as shown by the solid line in figure 3.4(a). From this fit, we obtain the time constant of growth to be 460 ± 10 fs and the decay time constants to be 4.85 ± 0.2 ps and >1000 ps. The data indicate that about 90 % of the signal does not decay within the timeframe of our observation, suggesting the high quality of the sample with very small non-radiative recombination sites like the surface trap states. The decay constant of 4.85 ± 0.2 ps can be assigned either to the Auger processes or to the recombination via surface trap states. However, its intensity is observed to be 10 % or smaller at the band gap energy. Most interestingly, the finite build-up time of the $\Delta T/T$ signal at the band edge energy suggests the gradual population of the charge carriers at the band edge. Following the instantaneous excitation of higher excited states (ES) of CdS, we assign the growth time to the relaxation of the charge carriers respectively to the conduction band minimum (CBM) and valence

band maximum (VBM) in a finite time frame, thus slowly populating the $1S-1S_{1/2}$ transition at 2.49 ± 0.01 eV. If this is indeed true, the growth and decay should change as a function of probe energy. The observation that the decay of the PB signal of the higher energy states is complete within the growth time of the PB of the band edge state would imply that the relaxation of both hot electrons and hot holes occurs within this time interval, with no intervention from either electron or hole traps. On the other hand, the observation that the PB (ground state depletion) recovery is incomplete at higher energies would imply that there exist two excited states that share the same ground state and hence demonstrate the presence of electron/hole trap states that can compete with the intraband cooling.

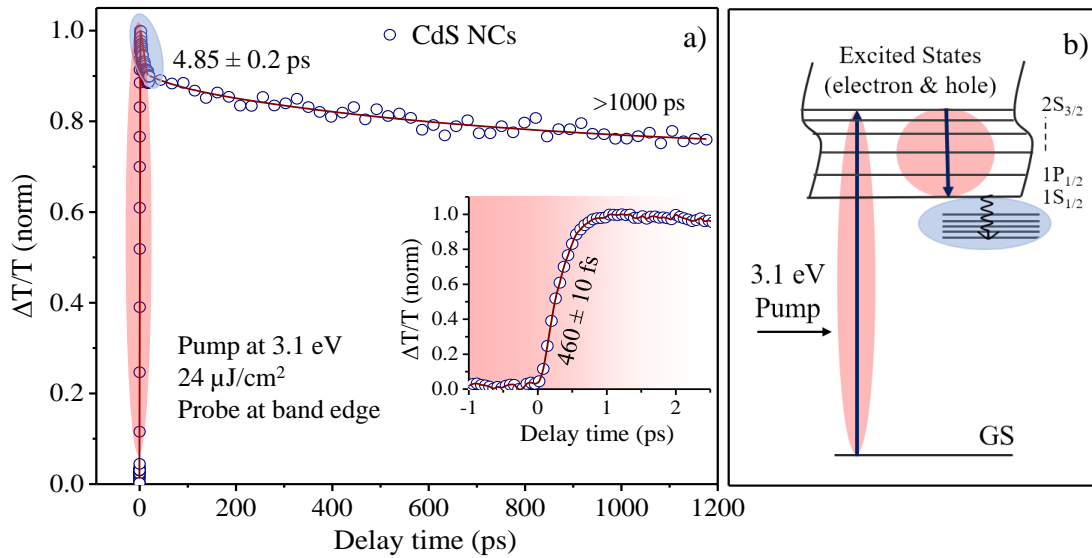


Figure 3.4. (a) Differential transmission dynamics for CdS NCs under 3.1 eV (400 nm) laser excitation with a fluence of $24 \mu\text{J}/\text{cm}^2$. Inset: zoom-in of the dynamics up to 2.5 ps. (b) Schematic representing the process of non-resonant excitation, intraband relaxation and decay into trap states for CdS NCs.

To clarify the cooling dynamics in CdS NCs, we measured differential transmission spectra as a function of the probe energy at 3.1 eV excitation. Figure 3.5(a) shows the time plots at various probe photon energies. Interestingly, high probe energies highlight not only an instantaneous rise of the PB signal but also a rapid and complete decay, suggesting a simultaneous decay of both the hot charge carriers. On the other hand, at lower probe energies there is a clear build-up time, on the picosecond timescale, followed by saturation suggesting that the CBM is being populated due to the relaxation from higher ESs, as shown in the schematic in figure 3.5(b).

Figure 3.5(c) reports a sequence of $\Delta T/T$ spectra at different delays. We performed a global analysis using the least square error minimization method on these spectra by fitting them to the sum of two Gaussians, with the energy of one of the Gaussians being fixed to 2.49 ± 0.01 eV, which corresponds to the lowest $1S-1S_{1/2}$ excitonic state. The energy of the higher ES corresponds to 2.63 ± 0.01 eV, with a gap of 140 meV between the two states. Based on the theoretical calculations of energy levels of CdS NC reported in the literature,³⁰ we assign this ES to the $1S-2S_{3/2}$ transition. A sample fit at early times is shown in figure 3.5(d). The 2.63 ± 0.01 eV peak decays to zero within a few picoseconds, implying a complete relaxation of both the hot charge carriers while the 2.49 ± 0.01 eV peak grows in and does not appreciably decay on the picosecond timescale.

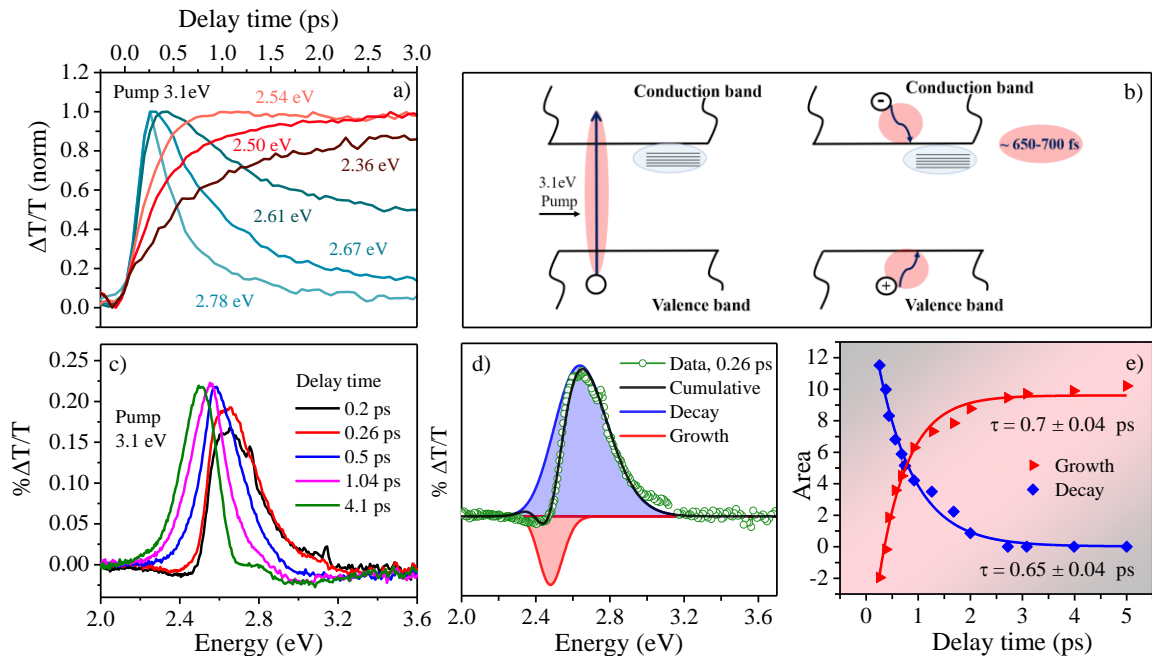


Figure 3.5. (a) Differential transmission dynamics for CdS NCs up to 3 ps at different probe energies under non-resonant excitation (3.1 eV). (b) Schematic describing the excitation and intraband cooling process under non-resonant excitation (c) Differential transmission spectra of CdS NCs measured at different pump-probe delays at 400 nm (3.1eV) excitation (d) Typical fitting of the $\Delta T/T$ spectrum obtained at a delay of 0.26 ps with two Gaussian peaks corresponding to excitonic states at 2.49 ± 0.01 eV and 2.63 ± 0.01 eV. (e) The area under these peaks at various delay times are plotted as red and blue diamonds while the solid line is a fit to a single exponential decay/growth with the given time constants.

The area under the curve for the two Gaussians (red and blue symbols) is plotted as a function of probe delay time and the corresponding fits to these two dynamics at 2.49 eV \pm 0.01 and 2.63 \pm 0.01 eV are shown as solid lines in figure 3.5(e). The time constants obtained after fitting with a single exponential decay/growth are observed to be similar for both the signals, that is, 700 \pm 40 fs for the growth of the band edge peak and 650 \pm 40 fs for the decay of higher ES, suggesting that one state is growing at the expense of the other. Thus, the observed time-dependent red-shift of the $\Delta T/T$ spectrum in the first few picoseconds is understood in terms of intraband relaxation.

To confirm that this fast decay is indeed from intraband relaxation and not any other non-radiative pathways, we excited the system near resonance (excitation at 2.58 eV) and investigated the decay dynamics and energy dependence of the differential transmission spectra, as shown in figure 3.6. At near-resonant excitation, we observe a transient PB with an IRF-limited fast rise (<100 fs) followed by an additional sub-picosecond evolution and a long-lived excited state, as shown in the $\Delta T/T$ dynamics for different energies in figure 3.6(a) and at the band-edge up to 1200 ps in figure 3.7.

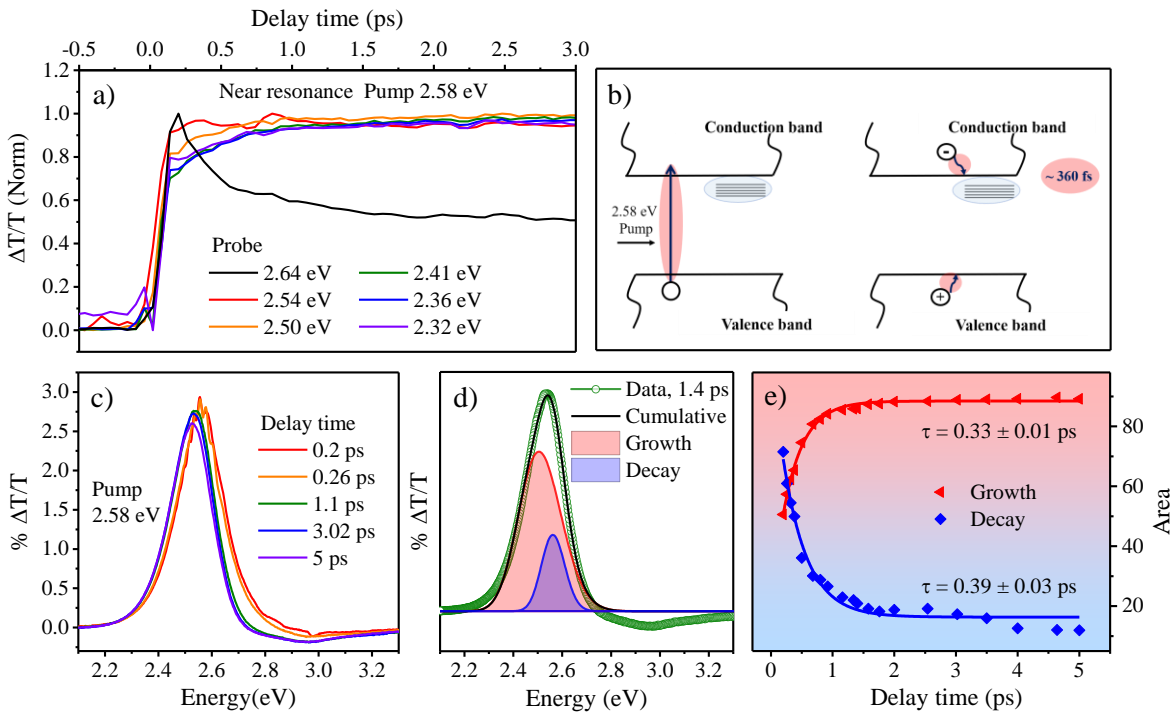


Figure 3.6. (a) Differential transmission dynamics for CdS NCs up to 3 ps at different probe energies under near-resonance excitation (2.58 eV). (b) Schematic describing near-resonance excitation and intraband cooling (c) differential transmission spectra of CdS NCs measured at different pump-probe delays at 2.58 eV (480 nm) excitation (d) Typical

fitting of the $\Delta T/T$ spectrum obtained at a delay of 1.4 ps with two Gaussian peaks at $2.56 \pm 6.8 \cdot 10^{-4}$ eV and $2.50 \pm 4.5 \cdot 10^{-4}$ eV (e) The area under these deconvoluted peaks at various delay times plotted as red ($2.50 \pm 4.5 \cdot 10^{-4}$ eV) and blue diamonds ($2.56 \pm 6.8 \cdot 10^{-4}$ eV) while the solid line is a single exponential decay/growth fit with the given time constants.

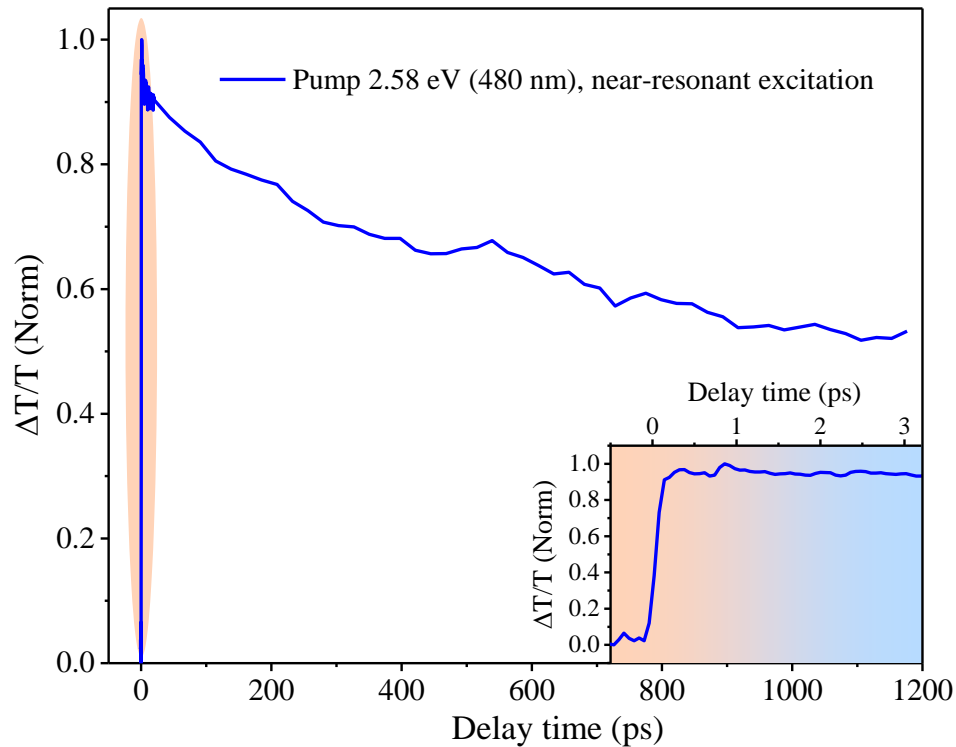


Figure 3.7. Differential transmission dynamics for CdS NCs under 480 nm (2.58 eV) laser excitation and zoom-in of the dynamics up to 3 ps region in inset to the figure.

The differential transmission spectra are nearly independent of the probe energy as the excitation is carried out at near resonance and hence with little excess energy. This excitation condition is further reflected in the schematic in figure 3.6(b). Additionally, the $\Delta T/T$ spectrum for the 2.58 eV laser excitation can be largely characterized by a PB peak centered around $2.50 \pm 4.5 \cdot 10^{-4}$ eV, characteristic of the bandgap exciton spectrum as shown in figure 3.6(c). Deconvolution of these spectra using global analysis demonstrates the presence of two states, one at an energy of $2.56 \pm 6.8 \cdot 10^{-4}$ eV, while the second at the band edge or $1S-1S_{1/2}$ state at $2.50 \pm 4.5 \cdot 10^{-4}$ eV and a sample fit at early times is shown in figure 3.6(d). The $2.50 \pm 4.5 \cdot 10^{-4}$ eV state arises from the same states in the two experiments at near-resonance ($2.50 \pm 4.5 \cdot 10^{-4}$) and above-resonance excitation (2.49 ± 0.01 eV) cases and are the same within the experimental error. We believe that the $2.56 \pm$

6.8×10^{-4} eV peak arises from the vibrationally excited state and not an electronically excited state. This is concluded based on the quick time scale of its decay as well as the narrow FWHM of the peak. It is quite possible that this component exists even in the off-resonance case along with several other components. However, it is impossible to deconvolute all the components with a high degree of confidence, and hence we have only deconvoluted the major components arising from the electronic states of the NCs. Kinetic traces demonstrate that the decay of the higher ES has a time constant (390 ± 30 fs) that is very similar to the time constant (330 ± 10 fs) obtained for the growth of CBM as shown in figure 3.6(e). This confirms the nature of intraband relaxation that the carriers undergo after excitation. As compared to the non-resonant case wherein higher electronic states could be accessed, intraband cooling in the near-resonant excitation is much faster as expected.³¹ Taken together, our experimental data show that the fast dynamics observed on the sub-picosecond timescale are due to intraband relaxation. Further, it is important to note that these samples are largely free of surface trap states as evidenced by the long-lived PB component that is essentially constant over the ≈ 1 -ns observation time window, suggesting them to be good candidates for any photovoltaic or photoemissive device application.

3.5 Conclusion

Our pump-probe studies on high-quality CdS NCs prepared via colloidal SILAR technique show that the band edge states are populated by the simultaneous decay of hot electrons and holes over a period of several hundreds of femtoseconds. The low density of surface states in the NC allows for a long-lived excited state as accessed by pump-probe measurements and is suitable for radiative recombination. We also develop an understanding of the processes involved in charge carrier dynamics starting from the excitation to the carrier stabilization where the multi-component behavior is associated with the growth, intraband cooling and a long-lived excited state component that doesn't decay up to 1000 ps. Decoupling of growth and intraband relaxation could be achieved only with the above band-gap excitation unlike the resonant case and it can further be employed for applications. Our attempt to study these hot carriers and what happens to them before cooling to thermal equilibrium was possible in our case because of the long-lived excitonic bleaching of the excited state. The relatively long carrier lifetimes with small recombination coefficient, slow thermalization dynamics of hot carriers are believed to originate from the protection offered to these carriers in the absence of surface trap

states. Thus, this robust system can be utilized to study the intraband transitions and associated processes that occur on similar time scales like dopant-host interactions within the doped semiconductors.

Bibliography

- (1) Klimov, V. I. Mechanisms for Photogeneration and Recombination of Multiexcitons in Semiconductor Nanocrystals: Implications for Lasing and Solar Energy Conversion. ACS Publications: 2006.
- (2) Isshiki, M.; Wang, J. II-IV Semiconductors for Optoelectronics: CdS, CdSe, CdTe. In *Springer Handbook of Electronic and Photonic Materials*, Springer: 2017; pp 1-1.
- (3) Kairdolf, B. A.; Smith, A. M.; Stokes, T. H.; Wang, M. D.; Young, A. N.; Nie, S. Semiconductor Quantum Dots for Bioimaging and Biodiagnostic Applications. *Annu. Rev. Anal. Chem.* **2013**, *6*, 143-162.
- (4) Grandhi, G. K.; Tomar, R.; Viswanatha, R. Study of Surface and Bulk Electronic Structure of II–VI Semiconductor Nanocrystals Using Cu as a Nanosensor. *ACS Nano* **2012**, *6*, 9751-9763.
- (5) Grandhi, G. K.; Swathi, K.; Narayan, K. S.; Viswanatha, R. Cu Doping in Ligand Free CdS Nanocrystals: Conductivity and Electronic Structure Study. *J. Phys. Chem. Lett.* **2014**, *5*, 2382-2389.
- (6) Ngo, C. Y.; Yoon, S. F.; Fan, W. J.; Chua, S. J. Effects of Size and Shape on Electronic States of Quantum Dots. *Phys. Rev. B* **2006**, *74*, 245331.
- (7) Veamatahau, A.; Jiang, B.; Seifert, T.; Makuta, S.; Latham, K.; Kanehara, M.; Teranishi, T.; Tachibana, Y. Origin of Surface Trap States in CdS Quantum Dots: Relationship Between Size Dependent Photoluminescence and Sulfur Vacancy Trap States. *Phys. Chem. Chem. Phys.* **2015**, *17*, 2850-2858.
- (8) Grandhi, G. K.; Viswanatha, R. Understanding the Role of Surface Capping Ligands in Passivating the Quantum Dots Using Copper Dopants as Internal Sensor. *J. Phys. Chem. C* **2016**, *120*, 19785-19795.
- (9) Flatae, A. M.; Tantussi, F.; Messina, G. C.; De Angelis, F.; Agio, M. Plasmon-Assisted Suppression of Surface Trap States and Enhanced Band-Edge Emission in a Bare CdTe Quantum Dot. *J. Phys. Chem. Lett.* **2019**, *10*, 2874-2878.
- (10) Giansante, C.; Infante, I. Surface Traps in Colloidal Quantum Dots: A Combined Experimental and Theoretical Perspective. *J. Phys. Chem. Lett.* **2017**, *8*, 5209-5215.
- (11) Klimov, V. I. Optical Nonlinearities and Ultrafast Carrier Dynamics in Semiconductor Nanocrystals. ACS Publications: 2000.
- (12) Wehrenberg, B. L.; Wang, C.; Guyot-Sionnest, P. Interband and Intraband Optical Studies of PbSe Colloidal Quantum Dots. *J. Phys. Chem. B* **2002**, *106*, 10634-10640.

- (13) Markus, A.; Chen, J. X.; Gauthier-Lafaye, O.; Provost, J. G.; Paranthoën, C.; Fiore, A. Impact of Intraband Relaxation on the Performance of a Quantum Dot Laser. *IEEE J. Sel. Top. Quantum Electron.* **2003**, *9*, 1308-1314.
- (14) Livache, C.; Martinez, B.; Goubet, N.; Gréboval, C.; Qu, J.; Chu, A.; Royer, S.; Ithurria, S.; Silly, M. G.; Dubertret, B. A Colloidal Quantum Dot Infrared Photodetector and Its Use for Intraband Detection. *Nat. Commun.* **2019**, *10*, 1-10.
- (15) Htoon, H.; Hollingworth, J. A.; Malko, A. V.; Dickerson, R.; Klimov, V. I. Light Amplification in Semiconductor Nanocrystals: Quantum Rods Versus Quantum Dots. *Appl. Phys. Lett.* **2003**, *82*, 4776-4778.
- (16) Nozik, A. J. Quantum Dot Solar Cells. *Physica E Low Dimens. Syst. Nanostruct.* **2002**, *14*, 115-120.
- (17) Nozik, A. J. Spectroscopy and Hot Electron Relaxation Dynamics in Semiconductor Quantum Wells and Quantum Dots. *Annu. Rev. Phys. Chem.* **2001**, *52*, 193-231.
- (18) Guyot-Sionnest, P.; Wehrenberg, B.; Yu, D. Intraband Relaxation in CdSe Nanocrystals and the Strong Influence of the Surface Ligands. *J. Chem. Phys.* **2005**, *123*, 074709.
- (19) Peterson, M. D.; Cass, L. C.; Harris, R. D.; Edme, K.; Sung, K.; Weiss, E. A. The Role of Ligands in Determining the Exciton Relaxation Dynamics in Semiconductor Quantum Dots. *Annu. Rev. Phys. Chem.* **2014**, *65*, 317-339.
- (20) Rabouw, F. T.; Vaxenburg, R.; Bakulin, A. A.; van Dijk-Moes, R. J. A.; Bakker, H. J.; Rodina, A.; Lifshitz, E.; Efros, A. L.; Koenderink, A. F.; Vanmaekelbergh, D. Dynamics of Intraband and Interband Auger Processes in Colloidal Core–Shell Quantum Dots. *ACS Nano* **2015**, *9*, 10366-10376.
- (21) Cooney, R. R.; Sewall, S. L.; Dias, E. A.; Sagar, D. M.; Anderson, K. E. H.; Kambhampati, P. Unified Picture of Electron and Hole Relaxation Pathways in Semiconductor Quantum Dots. *Phys. Rev. B* **2007**, *75*, 245311.
- (22) Kambhampati, P. Unraveling the Structure and Dynamics of Excitons in Semiconductor Quantum Dots. *Acc. Chem. Res.* **2011**, *44*, 1-13.
- (23) Smith, A. M.; Nie, S. Semiconductor Nanocrystals: Structure, Properties, and Band Gap Engineering. *Acc. Chem. Res.* **2010**, *43*, 190-200.
- (24) Li, W.; Long, R.; Tang, J.; Prezhdov, O. V. Influence of Defects on Excited-State Dynamics in Lead Halide Perovskites: Time-Domain Ab Initio Studies. *J. Phys. Chem. Lett.* **2019**, *10*, 3788-3804.

- (25) Hoch, L. B.; Szymanski, P.; Ghuman, K. K.; He, L.; Liao, K.; Qiao, Q.; Reyes, L. M.; Zhu, Y.; El-Sayed, M. A.; Singh, C. V. Carrier Dynamics and the Role of Surface Defects: Designing a Photocatalyst for Gas-Phase CO₂ Reduction. *Proc. Natl. Acad. Sci.* **2016**, *113*, E8011-E8020.
- (26) Ding, J.; Lian, Z.; Li, Y.; Wang, S.; Yan, Q. The Role of Surface Defects in Photoluminescence and Decay Dynamics of High-Quality Perovskite MAPbI₃ Single Crystals. *J. Phys. Chem. Lett.* **2018**, *9*, 4221-4226.
- (27) Li, J. J.; Wang, Y. A.; Guo, W.; Keay, J. C.; Mishima, T. D.; Johnson, M. B.; Peng, X. Large-Scale Synthesis of Nearly Monodisperse CdSe/CdS Core/Shell Nanocrystals Using Air-Stable Reagents Via Successive Ion Layer Adsorption And Reaction. *J. Am. Chem. Soc.* **2003**, *125*, 12567-12575.
- (28) Sun, J.; Zhao, J.; Masumoto, Y. Shell-Thickness-Dependent Photoinduced Electron Transfer from CuInS₂/ZnS Quantum Dots to TiO₂ Films. *Appl. Phys. Lett.* **2013**, *102*, 053119.
- (29) Neo, D. C.; Cheng, C.; Stranks, S. D.; Fairclough, S. M.; Kim, J. S.; Kirkland, A. I.; Smith, J. M.; Snaith, H. J.; Assender, H. E.; Watt, A. A. Influence of Shell Thickness and Surface Passivation on PbS/CdS Core/Shell Colloidal Quantum Dot Solar Cells. *Chem. Mater.* **2014**, *26*, 4004-4013.
- (30) Horodyská, P.; Němec, P.; Sprinzl, D.; Malý, P.; Gladilin, V. N.; Devreese, J. T. Exciton Spin Dynamics In Spherical CdS Quantum Dots. *Phys. Rev. B* **2010**, *81*, 045301.
- (31) Stoll, T.; Branchi, F.; Réhault, J.; Scotognella, F.; Tassone, F.; Kriegel, I.; Cerullo, G. Two-Dimensional Electronic Spectroscopy Unravels Sub-100 fs Electron And Hole Relaxation Dynamics in Cd-Chalcogenide Nanostructures. *J. Phys. Chem. Lett.* **2017**, *8*, 2285-2290.

CHAPTER 4

Magneto-Optical Stark Effect in Fe doped CdS
Nanocrystals.

4.1 Summary

Fe^{2+} doping in semiconductors, due to the absence of energetically accessible multiple spin state configurations, has not given rise to interesting spintronic applications. In this work, we demonstrate for the first time that the interaction of homogeneously doped Fe^{2+} ions with the host CdS nanocrystal with no clustering is different for the two spin states and produces two magnetically inequivalent excitonic states upon optical perturbation. We combine ultrafast transient absorption spectroscopy and density functional theoretical analysis within the ground and excited states to demonstrate the presence of the Magneto-Optical Stark Effect (MOSE). The energy gap between the spin states arising due to MOSE does not decay within the time frame of observation, unlike optical and electrical Stark shifts. This demonstration provides a stepping-stone for spin-dependent applications.

4.2 Introduction

The combination of nanotechnologies with quantum physics uses the power of laws of physics for practical purposes. The use of the spin degree of freedom of an electron, specifically in a system with strong spin-orbit coupling leading to ultrafast spin selectivity,¹ promises to lead to enhancement of data processing speed and integration densities, allowing a reduction in electrical power consumption in comparison to the conventional electronic devices.²⁻⁴ However, the most important parameter for potential applications in spintronics is the presence of multiple low energy spin configurations of the transition metal ions. Hence, even though iron is naturally magnetic, so far there has been no demonstration of spintronic-like states in Fe^{2+} doped simple II-VI semiconductors.⁵⁻⁶ However, the spin of the Fe dopant is very sensitive to the local environment and CdS nanocrystals (NCs) have the potential to strongly hybridize with magnetic ions, beyond the classical description of diluted magnetic semiconductors.^{5,7} Until now, however, the power of spatial confinement of the wavefunction as well as the role of dopant-host interactions, free of dopant-dopant interactions, has not been explored. Here we combine ultrafast transient absorption spectroscopy and density functional theory within the ground and excited states to demonstrate that the uneven interaction of the two spin states for uniformly doped Fe^{2+} ions in spatially confined CdS NCs produces two magnetically inequivalent excitonic states upon mild optical perturbation. Interestingly, this energy gap arises from a newly discovered phenomenon that we label as Magneto-Optical Stark Effect (MOSE) and does not decay within the time frame of observation.

Further, this gap corresponds to ~ 2 T external magnetic field that would be required to obtain this splitting from the Zeeman effect at room temperature, thus demonstrating a long-lived splitting.

Modulation of the absorption edge of semiconductors with external perturbations like an applied electric field⁸⁻⁹ or an optical pulse,^{1,10} leads to transient shifts in energy within the bandgap region, due to the non-linear interaction of electronic states with the electric field/photons, and is known as the Stark shift. In a system wherein the quantum states are strongly coupled to phonons through exciton-phonon interactions, the optical Stark effect (OSE) can be used to generate closely spaced spin selective states. However, most often the quantum states affected by OSE are buried deep in the continuum¹¹ and OSE is only present for the duration of the illuminating light pulse, typically on ultrafast (femtosecond) timescales¹²⁻¹³ and are hence not very practical for use in device applications. Additionally, the possibility of impact ionization¹⁴ due to the intense external stimulus limits the modulation of the absorption edge through the Stark effect. However, the observation of an enhanced Stark effect in quantum-confined materials compared to their bulk counterparts significantly enhances their chances in real applications.¹⁵⁻¹⁶

In this work, we demonstrate the power of small optical perturbations in presence of a Fe^{2+} dopant uniformly distributed in a semiconductor to generate long-lived spin-selective excited states using the example of Fe^{2+} doped CdS NCs. We observe that the interaction of Fe^{2+} acceptor states, uniformly doped within the CdS host semiconductor, is strong and interestingly spin selective. Upon excitation with a weak optical pulse, we demonstrate that the spin-down transition interacts strongly with the host while the spin-up states are largely unaffected, as clearly observed from the DFT calculations, leading to a spin splitting of the degenerate excitonic states in Fe^{2+} doped CdS systems. In contrast to OSE, this effect is long-lived and stronger than the best reported shifts so far at room temperature, using a weak excitation fluence of $24\mu\text{J}/\text{cm}^2$ (table 4.1). We term this phenomenon as MOSE and establish it with a combination of ultrafast transient absorption (TA) spectroscopy and theoretical analysis of ground and excited states.

4.3 Experimental/theoretical details

Materials and synthesis

Iron(II)acetate ($\text{Fe}(\text{ac})_2$ 95%), cadmium oxide (CdO), oleic acid (OA, 90%), 1-octadecene (ODE, 90%), oleylamine (OIAm, 70%), and sulfur powder (S, 99.5%) were purchased from Sigma Aldrich. All these chemicals were used without further purification.

Synthesis. Fe_3O_4 NCs. Core Fe_3O_4 was prepared by high-temperature decomposition of $\text{Fe}(\text{ac})_2$ in oleic acid and oleylamine. 0.35 g of $\text{Fe}(\text{ac})_2$, 2.5 mL oleic acid and 5 mL of oleylamine were taken in a three-necked flask and degassed at 120 °C under constant stirring. Then the temperature was raised to 220 °C under constant Ar flow. After 20 min, the temperature of the reaction mixture was raised to 300 °C very slowly (4 °C/min). This temperature was maintained for 5 minutes and then the reaction mixture was cooled down to room temperature. As synthesized nanoparticles were washed with the hexane-ethanol mixture.

Fe doped CdS NCs. 0.2 M cadmium oleate ($\text{Cd}(\text{Ol})_2$) and 0.2 M S/ODE solution were prepared using the method described in chapter 3. Successive ionic layer adsorption and reaction (SILAR) technique was used to synthesize these doped NCs. 20 mg of pre-synthesized iron oxide nanocrystals (powder form), 3 mL of OIAm and 5 mL of ODE were taken in a three-necked flask and degassed at 80 °C. After 2 hr of degassing the reaction flask was backfilled with Ar and the temperature was raised to 250 °C. The stoichiometric amount of $\text{Cd}(\text{Ol})_2$ was injected into the reaction mixture. After 40 min the same amount of S precursor was injected into the system and annealed for 20 min. These cycles of Cd and S precursor addition were continued until the formation of an ultra-thick CdS shell (up to 15 cycles). Annealing at high temperature (250 °C) for a long time (1 hour per cycle) along with the CdS shell formation allows the core to diffuse into the shell matrix.

Undoped CdS NCs. Undoped CdS was synthesized using similar experimental conditions as described for the doped system without any Fe precursor. CdS NCs were synthesized at 240 °C and overcoated at 140 °C.

Characterization.

Transmission electron microscopy (TEM) was performed on a Tecnai F30 UHR version electron microscope, using a field emission gun (FEG) operating at an accelerating voltage

of 200 kV in bright field mode using Cu coated holey carbon TEM grids. Powder x-ray diffraction pattern for the NCs was recorded on Bruker D8 Advance diffractometer using Cu-K α radiation (1.5418 Å). Absorption spectra of samples were recorded using an Agilent 8453 UV visible spectrometer. To determine the Cd and Fe ratio, the elemental analysis was carried out using inductively coupled plasma optical emission spectrometry (Perkin Elmer optima 7000 DV machine). Samples were dissolved in 2-5% HNO₃ solution, and the Fe and Cd concentrations were measured against high purity Fe and Cd standards.

Pump-probe spectroscopy setup. The laser source employed for the pump-probe Spectroscopy setup was an amplified Ti:sapphire laser (Libra from Coherent), with maximum output energy of about 1 mJ, 1 kHz repetition rate, the central wavelength of 800 nm and pulse duration of about 100 fs. The beam was split to generate the required pulses. One part was used for generating the excitation (pump) pulses: the pump at 400 nm (3.1 eV) was generated by means of frequency doubling in a β -barium borate crystal, while the pump at 480 nm (2.58 eV) was generated by means of optical parametric amplification in a β -barium borate crystal. Pump pulses were modulated by a mechanical chopper at 500 Hz repetition rate and were delayed in time by means of a mechanical stage. Finally, the pump was focused with a lens in order to obtain a fluence of around 24 $\mu\text{J}/\text{cm}^2$. The other part of the beam was used to generate the probe pulses by the white light continuum generation process, by focusing the 800 nm beam into a thin calcium fluoride plate, obtaining a spectrum ranging from 340 nm (3.65 eV) to 700 nm (1.77 eV). The probe pulse was focused on the sample non-collinearly with the pump beam and the spectrum of the transmitted probe beam was measured by an optical multichannel analyzer (OMA) working at the full 1 kHz laser repetition rate. Thanks to the modulation of the pump pulse, two consecutive probe pulses are measuring the sample in the excited and the ground state. By measuring their corresponding intensities (I_{on} and I_{off}) one can calculate the normalized transmission change: $\Delta T/T = (I_{\text{on}}/I_{\text{off}}) - 1$, both as a function of wavelength (OMA detection) and time delay (mechanical delay). Chirp-free transient absorption spectra were collected by using a dechirping algorithm. Measurements were performed with the same linear polarization for pump and probe beams. In addition, a set of measurements on the 5% Fe doped CdS NCs was performed with circularly polarized beams. The probe beam was set to right circular polarization by means of a broadband quarter-wave plate. The 400 nm pump beam was alternatively set to right or left circular

polarization (by means of a second independent quarter-wave plate) in order to excite the sample with the same or opposite circular polarization wrt the probe.

Theoretical details. Our first-principles calculations are based on density functional theory (DFT) as implemented in the Quantum ESPRESSO code¹⁷ employing plane-wave basis sets and ultra-soft pseudopotentials¹⁸ to represent the interaction between ionic cores and valence electrons. We adopt the exchange-correlation energy functional of Perdew-Burke-Ernzerhof (PBE)¹⁹ obtained within a generalized gradient approximation (GGA). We smear the discontinuity in occupation numbers of electronic states with Fermi-Dirac distribution having a smearing width ($k_B T$) of 0.04 eV. An energy cutoff of 80 Ry is used to truncate the plane-wave basis used in representation of Kohn-Sham wave functions, and of 640 Ry to represent the charge density. Valence electron configurations used in the Ultrasoft potentials of Cd, S and Fe are $5s^2 4d^{9.5} 5p^{0.5}$, $3s^2 3p^4$ and $3s^2 3p^6 4s^2 3d^6$ respectively. Optimized structures were determined through minimization of energy until the Hellmann-Feynman force on each atom was smaller than 0.03 eV/Å in magnitude. We used a 2x2x2 supercell of Wurtzite CdS made of 36 atoms (16 Cd and 16 S atoms) and replaced one and two Cd atoms with Fe atoms. We sampled Brillouin-zone integrations on a uniform grid of 6x6x4 k-points in the Brillouin zones of the supercells. The projected density of states of each structure was obtained from calculations on a denser, 12x12x8, k-point mesh. The calculated lattice constant of bulk CdS ($a = 4.19 \text{ \AA}$, $c = 6.83 \text{ \AA}$), is within the typical GGA errors of the experimental value ($a = 4.14 \text{ \AA}$, $c = 6.75 \text{ \AA}$).

Estimation of MOSE. We calculated the change in the absorbance spectrum due to the shift of energy levels near CBM (conduction band minimum) and VBM (valence band maximum), where the change in the absorbance spectrum is illustrated below.

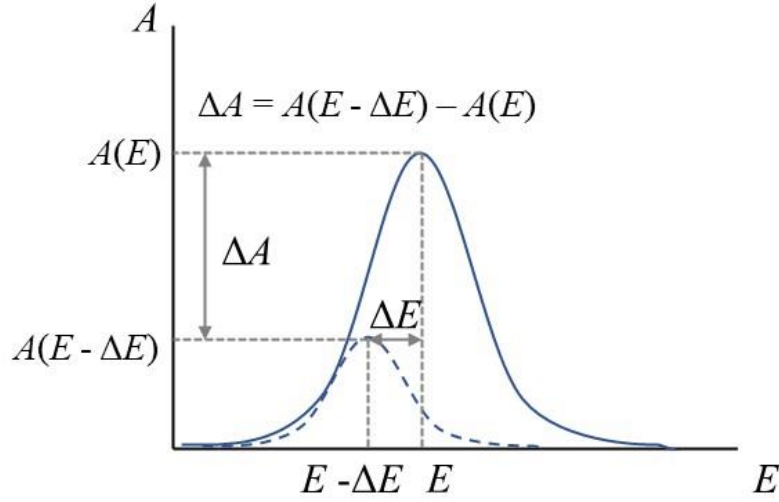
Thus, the change in absorbance due to change in E is given by

$$\Delta A(E) = A(E - \Delta E) - A(E) \approx -\frac{dA(E)}{dE} \Delta E$$

For estimating the shift in E, i.e. ΔE , we take an approach of spectral weight transfer

where

$$\text{SWT} = \int_0^{E_0} \Delta A(E) dE$$



E_0 is the peak absorption energy. Thus, combining the above 2 equations, we get

$$SWT = -\Delta E \int_0^{E_0} \frac{dA(E)}{dE} dE = \Delta E (A(E_0) - A(0))$$

where $A(E)$ is the absorbance of the material as a function of photon energy E . Since we have $A(0) = 0$, the energy shift ΔE due to the Stark effect can be estimated as-

$$\Delta E = \frac{SWT}{A(E_0)} = -\frac{1}{A(E_0)} \int_0^{E_0} \Delta A(E) dE$$

As the Stark effect signal vanishes below a certain value (y), the integration limits are set within range (y) $eV \leq E \leq E_0$ eV.

4.4 Results and discussion

It is important to note here that uniformity of the Fe^{2+} doping in the NCs is crucial to observe interesting magnetic phenomena.²⁰⁻²² Doping in NCs with uniform distribution of the dopants in the bulk rather than the surface is plagued with non-trivial problems of phase segregation, leading to the non-uniform distribution of magnetic dopants. However, recent literature has shown that the use of diffusion of the dopants inside out is successful in generating uniform doping of Fe^{2+} in the NCs.²³⁻²⁴ Here we use a similar technique to obtain Fe^{2+} doped CdS NCs wherein Fe_3O_4 was overcoated with a thick shell of CdS using the successive ionic layer adsorption and reaction technique²⁵ followed by high temperature annealing.

Table 4.1. Stark shift values obtained from literature for different systems.

System	Temp	Pump energy	Fluence	Applied electric field	Stark shift	References
hBN (Single photon emitters) <i>Nanoflakes</i>	Room Temp	Excitation intensity 100 $\mu\text{W}/\mu\text{m}^2$	-	± 100 V	43 meV	8
$(\text{C}_6\text{H}_4\text{C}_2\text{H}_4\text{NH}_3)_2\text{PbI}_4$ <i>Solution-processed 2D perovskite thin films</i>	Room Temp	Pump 2.16 eV Probe 2.37 eV	1.66 mJ/cm^2	-	6 meV	1
WS_2/WSe_2 <i>vdW heterostructure</i>	Theoretically calculated			40 $\text{V}/\mu\text{m}$	~ 38 meV	26
Ge <i>Quantum wells</i> grown on Si	7 K	0.95 eV	4×10^{15} photons/ cm^2	-	150 meV	27
	Room Temp	0.87 eV	1×10^{17} photons/ cm^2	-	6 meV	
InAs <i>QDs</i> coupled to a newly-designed H1 PhC nanocavity		< 0.45 μW			~ 70 μeV	28
PbBr <i>layers</i> containing Methylammonium cations				20 kV/cm	~ 1 meV	29
Few <i>layered</i> black phosphorus	Theoretically calculated			50 kV/cm	~ 17 meV	30
<i>Step quantum well</i> made of $\text{Ga}_{1-x}\text{Al}_x\text{As}/\text{GaAs}$				20 kV/cm	~ 10 meV	31
Ge/SiGe Multiple Quantum Wells	Room Temp			102 kV/cm	~ 30 meV	32
<i>Quantum wells</i> of $\text{Ga}_{0.27}\text{Al}_{0.73}\text{As}/\text{GaAs}$	Theoretically calculated			90 kV/cm	~ 13 meV	33
Fe doped CdS NCs	Room Temp	3.1 eV	24 $\mu\text{J}/\text{cm}^2$		~ 0.46 meV	Current work (MOSE)

X-ray diffraction confirmed the hexagonal structure for the doped as well as undoped CdS, (figure 4.1) with no signature of any impurity phase. Transmission electron microscopy confirmed the uniform spherical morphology of both undoped and doped systems (figure 4.2). The comparison of Fe and Cd K-edge in Fe doped CdS obtained by extended x-ray absorption fine structure (figure 4.3) suggests that Fe is replacing Cd in the CdS lattice, corroborating the fact that Fe is acquiring a +2 oxidation state in the CdS lattice similar to earlier literature.³⁴⁻³⁵ Further, the doped system is devoid of any impurity phase of the Fe₃O₄ core, as the Fe K-edge for the doped system is very different from the Fe K-edge for the core (figure 4.3). Similar to earlier literature,³⁴⁻³⁵ no other oxidation state of Fe ions has been observed in our work in the final sample due to the extended annealing. The absorption spectra exhibit a bandgap of ~2.5 eV for both pristine and Fe²⁺ doped systems, as shown in figure 4.4. TA spectroscopy³⁶ both with linearly and circularly polarized light, was used to study the de-excitation pathways of the doped and pristine CdS. Non-resonant excitation was performed at 3.1 eV photon energy, while resonant excitation was carried out at 2.58 eV.

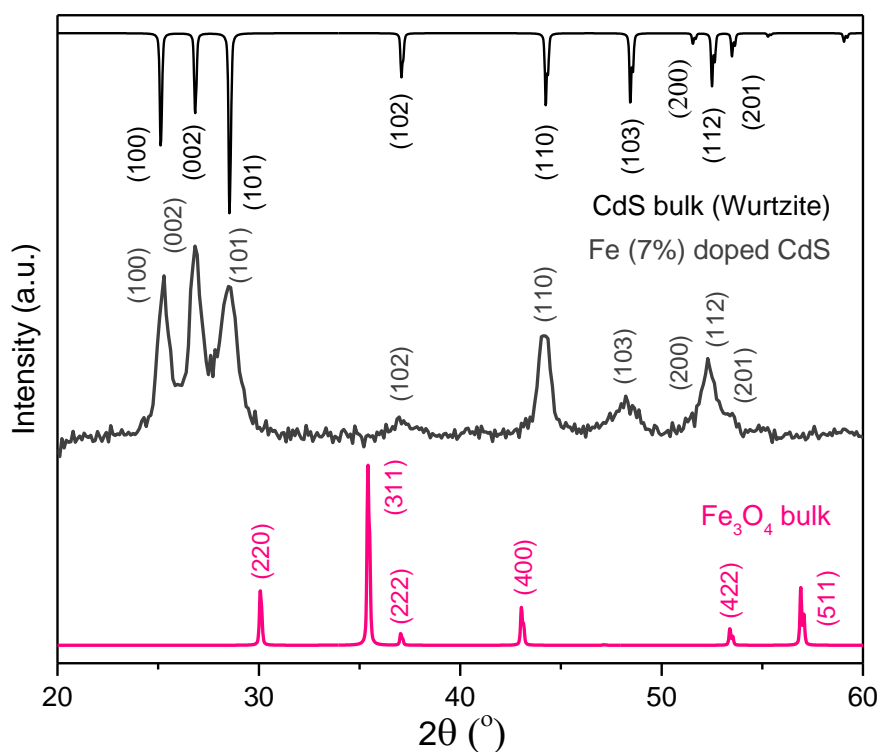


Figure 4.1. XRD pattern of the Fe doped CdS NCs along with bulk Fe₃O₄ and bulk CdS obtained from inorganic crystal structure database (ICSD). The Fe doped NCs show only CdS character indicating that the sample crystallizes in the Wurtzite phase.

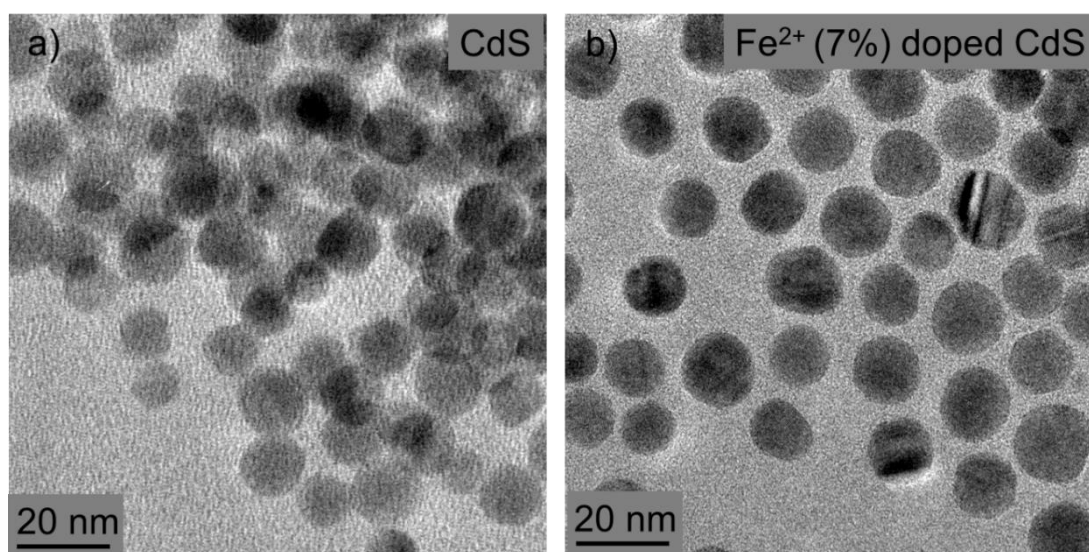


Figure 4.2. TEM image of similar-sized NCs of (a) pristine CdS, (b) Fe²⁺ doped CdS with uniform size distribution.

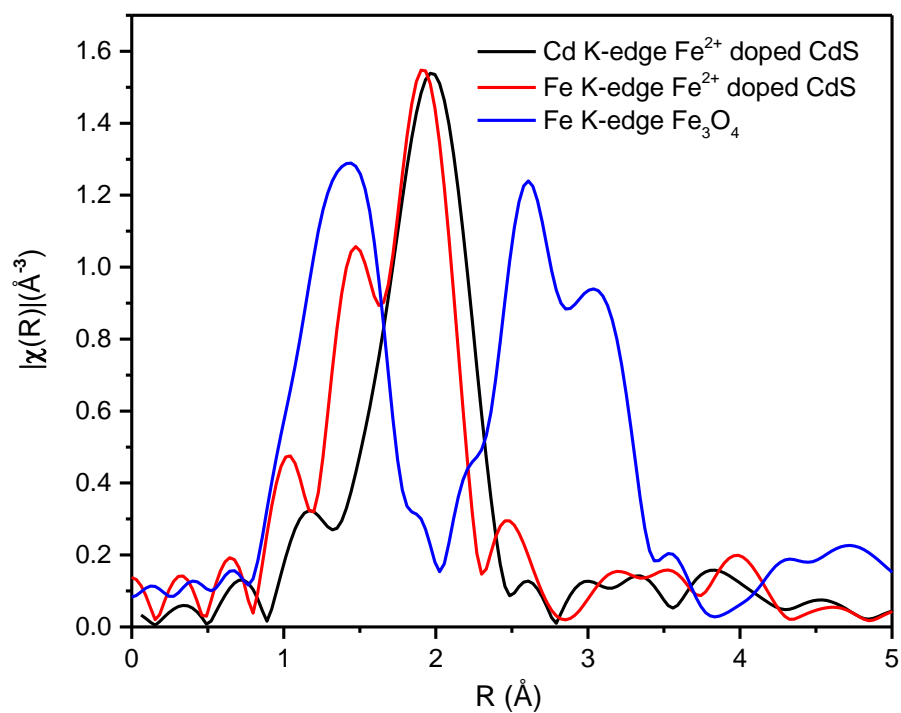


Figure 4.3. Magnitude of Fourier-transformed Fe-K edge EXAFS spectra for Fe₃O₄ and a comparison of Fe and Cd K-edge for Fe²⁺ doped CdS.

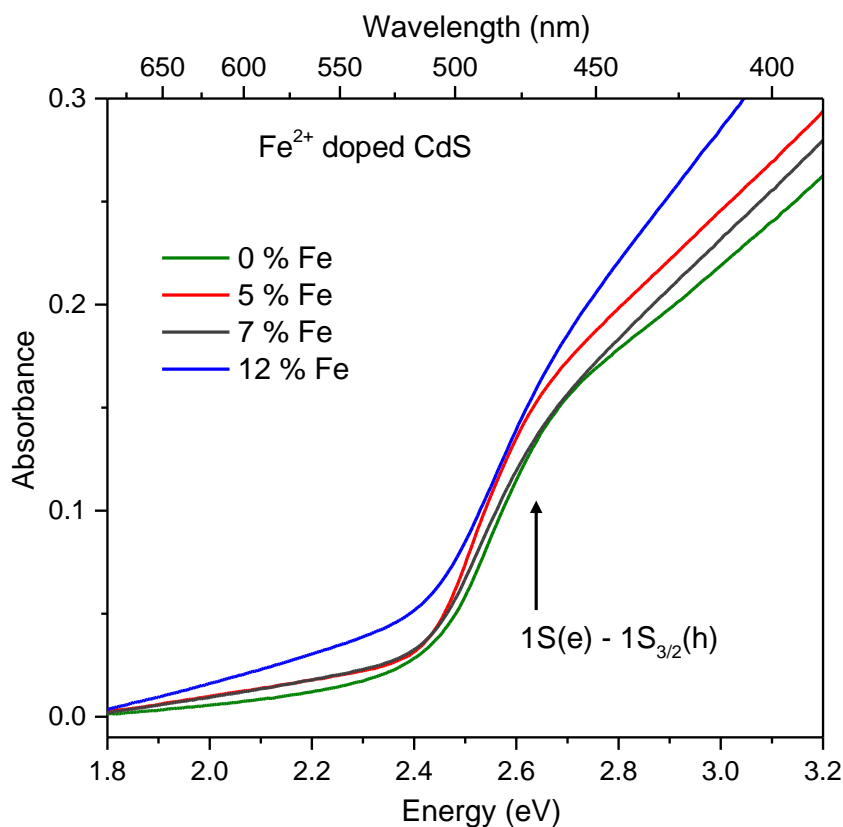


Figure 4.4. Linear absorption spectra of Fe²⁺ doped CdS with different % of Fe and pristine CdS NCs. Arrow shows position of the well-resolved transition involving 1S electron states.

For non-resonant excitation, the TA time trace for pristine CdS NCs at 2.5 eV probe energy (shown in figure 4.5(a)) reveals a very long excited-state lifetime (> 1 ns measurement window, as shown in figure 4.6(a)), demonstrating the high quality of NCs and the absence of surface trap states for the electron/hole. The positive differential transmission ($\Delta T/T$) signal is assigned to transient photobleaching (PB) of the band-edge excitonic transition. The signal also shows a build-up time constant of 460 ± 10 fs (figure 4.5(b)), due to electron/hole relaxation from the higher energy excitonic states, followed by a biexponential decay, with a small amplitude component with a time constant of 4.85 ± 0.2 ps and a long-lived signal > 1000 ps. In contrast, Fe²⁺ doped CdS NCs reveal a dramatic difference in the dynamics, namely the PB signal decays within a few picoseconds as shown in figure 4.5(a) and the $\Delta T/T$ colour maps (figure 4.6(b)). This difference is attributed to acceptor states created by Fe²⁺ doping. Early time data of Fe²⁺ doped CdS decay demonstrates that all concentrations of Fe²⁺ doping show an instantaneous rise and a very fast decay, as shown in figure 4.5(b). The decay time constant of the PB signal of Fe²⁺ doped CdS decreases from 1.37 ± 0.04 ps to 312 ± 10 fs

with an increasing percentage of Fe (table 4.2). This decay is similar to the rise time in undoped CdS, explaining the absence of band-edge PL in Fe²⁺ doped CdS. Importantly, the gradual and systematic decrease in the exciton lifetime of Fe²⁺ doped CdS with an increasing percentage of Fe (table 4.2) indicates the involvement of a density of states arising from the interaction of Fe²⁺ with the host rather than just one single acceptor state of Fe.

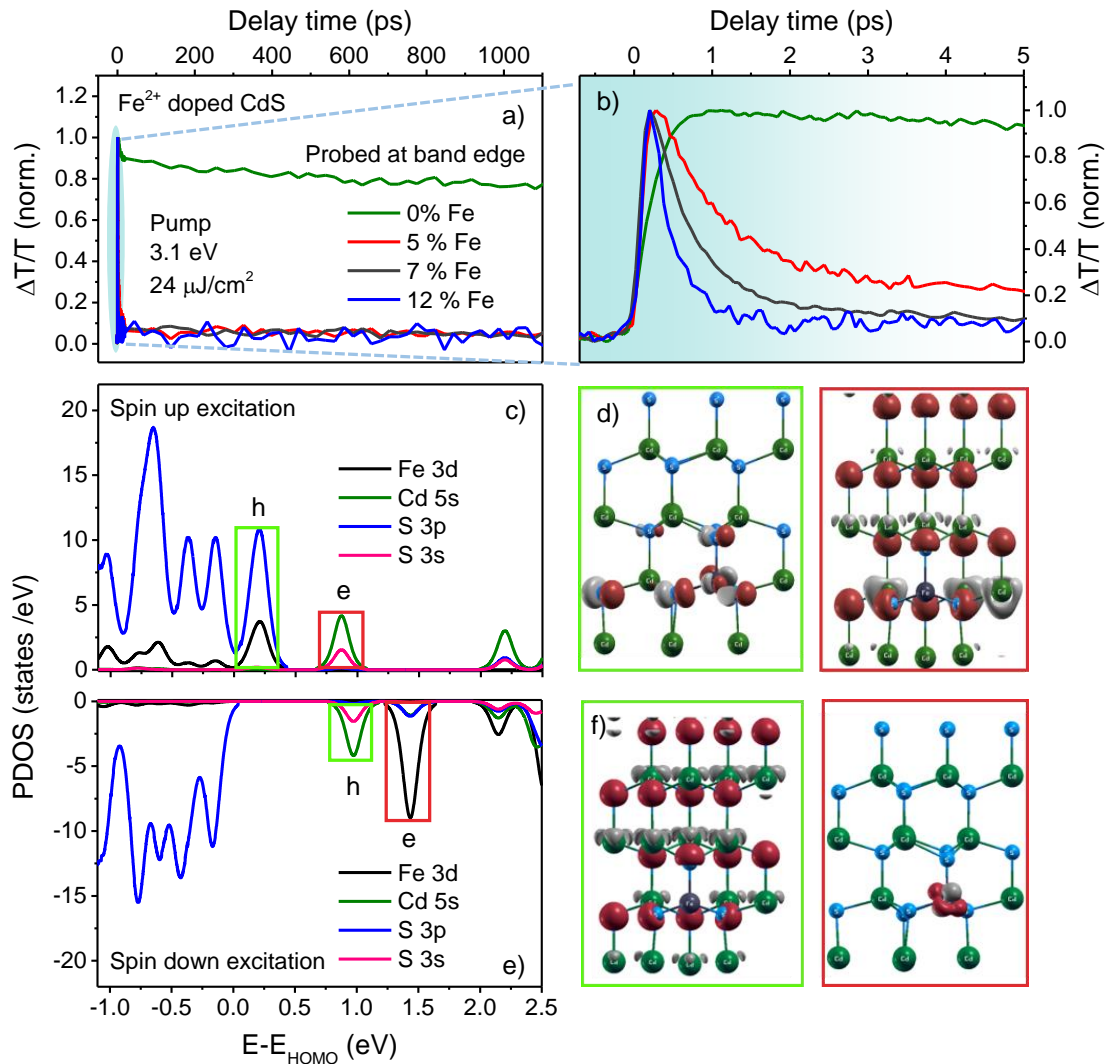


Figure 4.5. (a) Differential transmission dynamics of Fe²⁺ doped and undoped CdS NCs and zoom-in of the dynamics up to 5 ps region in (b). Spin-resolved projected density of states (PDOS) of (c) Spin-up excitation, (d) Charge density iso-surfaces depicting the spin-up excited state hole and electron position; (e) PDOS of spin-down excitation of Fe²⁺ doped CdS. (f) Charge density iso-surfaces depicting the spin-down excited state hole and electron position. Red and silver colours represent positive and negative charge density respectively. Green, grey and blue spheres correspond to Cd, Fe and S atoms, respectively. Green and red open rectangles denote the hole and electron states, respectively.

Additionally, when the decay time-constant is longer than the rise time of pristine CdS exciton (for example, 1.37 ± 0.04 ps in 5% Fe^{2+} doped CdS), we do not observe a complete decay of the PB signal, suggesting that few of the excitons do not decay through the fast Fe channel.

To shed light on the electronic properties of pristine/ Fe^{2+} doped CdS, we used the first-principles density functional theory (DFT) to determine the spin-resolved projected density of states (PDOS). Undoped CdS, being a non-magnetic system, exhibits degeneracy between the two spin states (figure 4.7). Conduction band minimum (CBM) of undoped CdS is primarily comprised of Cd-5s orbitals while the valence band maximum (VBM) has major contributions from S-3p orbitals. DFT calculations with substitution of single and pairs of Fe ions in a $2 \times 2 \times 2$ supercell of CdS reveal Fe acceptor states. The negative formation energy of Fe substituted CdS confirms the stability of substitution. Using Lowdin charge analysis it has been shown that the s-orbitals of Fe lose ~ 2 electrons, forming Fe^{2+} ions. There is not a significant change in the Lowdin charges of Fe going from ground state to excited state and hence the oxidation state remains +2. In its ground state, Fe states are mainly observed as spin-up states along with the S-3p states in the VBM while the CBM largely comprises the spin-down states at ~ 1 eV resulting in mid-gap states as evident in figure 4.8 due to the magnetic nature of Fe ion.

Table 4.2. Excited-state decay lifetimes for Fe doped CdS NCs.

System	Decay lifetime (ps)
$\text{Fe}_{0.05}\text{Cd}_{0.95}\text{S}$	1.37 ± 0.04
$\text{Fe}_{0.07}\text{Cd}_{0.93}\text{S}$	0.578 ± 0.008
$\text{Fe}_{0.12}\text{Cd}_{0.88}\text{S}$	0.312 ± 0.01

We modelled an exciton using the constrained occupation of electronic states to estimate the exciton formation energy. Since Fe^{2+} doped CdS is a magnetic system, excitation of a spin-up/down electron is not equivalent. We find that the excitation of a spin-up electron involves exciton formation energy of 0.70 eV, while that of a spin-down electron being 0.14 eV (table 4.3) with strictly enforced spin selection rules. To understand the interaction of Fe^{2+} with the host, we examine the PDOS and their respective charge density of frontier states in figure 4.5(c-f). For spin-down excitation, the acceptor state is delocalized within the host while the electron state is localized at the Fe ion, suggesting

the decay through the Fe states to the host. In contrast, when the electron is excited from the spin-up states, both electron and hole are delocalized within the host with no involvement of the Fe states, suggesting a decay through the band-edge. This not only demonstrates the non-equivalence of the two spin states but also corroborates the fact that the exciton decay involves the host and hence depends on the density of states and not just on the atomic-like Fe levels. Further, calculation reveals a reduction in the magnetic moment of the Fe ion from its value of $3.25 \mu_B/\text{Fe}$ in the ground state to $2.56 \mu_B/\text{Fe}$ in the spin-up and $3.00 \mu_B/\text{Fe}$ in the spin-down excited states, reflecting the different interaction of the spin states with the host material.

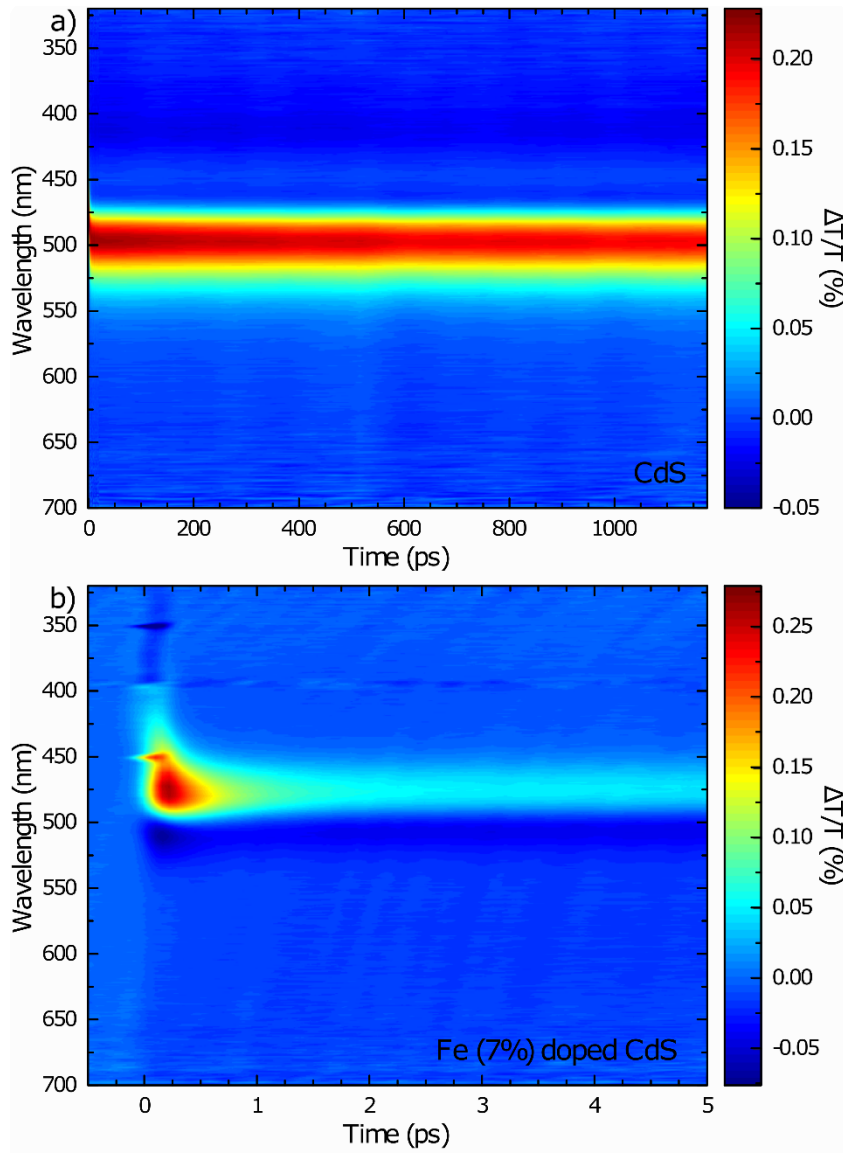


Figure 4.6. $\Delta T/T$ maps as a function of probe wavelength and time delay for (a) pristine CdS and (b) Fe doped CdS NCs.

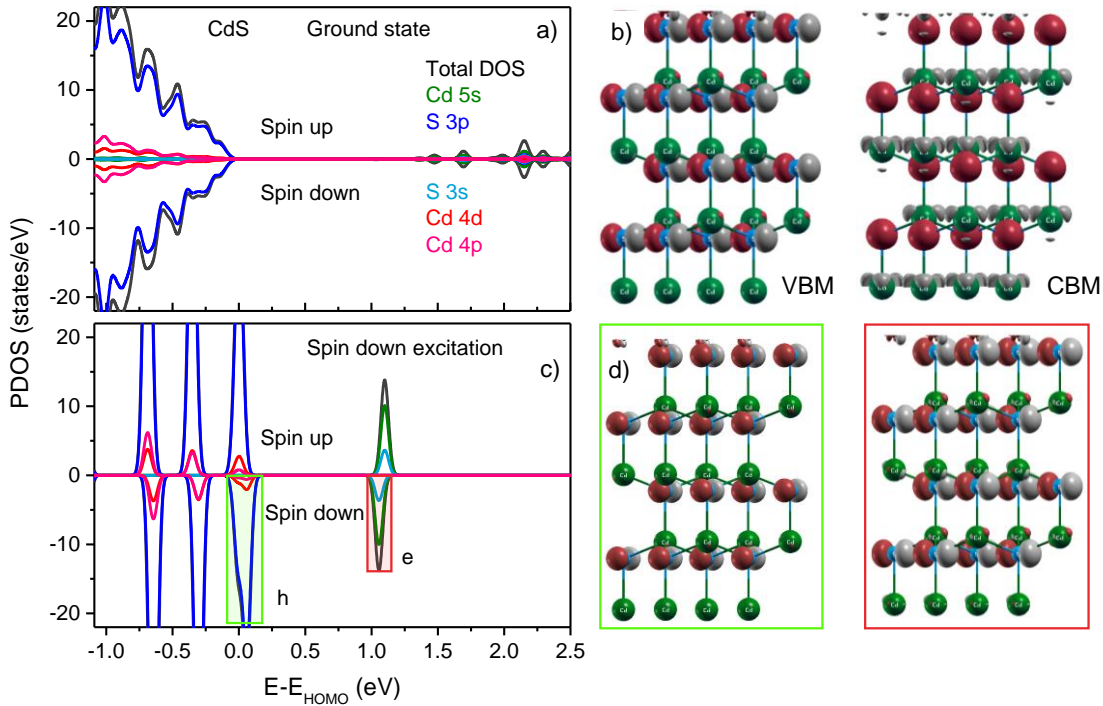


Figure 4.7. (a) Spin-resolved projected density of states (PDOS) of ground state for pristine CdS, (b) charge density maps depicting the orbital contribution at valence band maximum (VBM) and conduction band minimum (CBM). (c) PDOS of spin down excitation of pristine CdS. (d) Charge density maps depicting the spin down excited state hole and electron position. Red and silver colors represent positive and negative charge density respectively. Green, grey and blue spheres correspond to Cd, Fe and S atoms, respectively. Green and red open rectangles denote the hole and electron states, respectively.

However, it is important to note that this strong hybridization of Fe with the valence band of the host is only true for low concentration of Fe ions, that is, within the regime, wherein a Fe atom would not see the presence of other Fe atoms. We study the role of Fe-Fe interactions by substituting two Fe atoms/cell in our calculations. The relative positions of the two Fe-atoms (figure 4.9) were finalized using energy minimization calculations (DFT). The lowest energy structure (figure 4.9 (a)) shows an exciton formation energy of the spin-down electrons of 0.17 eV that is much lower than the spin-up electrons (1.59 eV). Furthermore, Fe-3d states behave as both donor and acceptor for the spin-down states, while the spin-up states are dominated by contributions from the Cd 5s and S 3p, with the same magnetic moment of $3.42 \mu_B/\text{Fe}$ in both ground and excited states (figure 4.10).

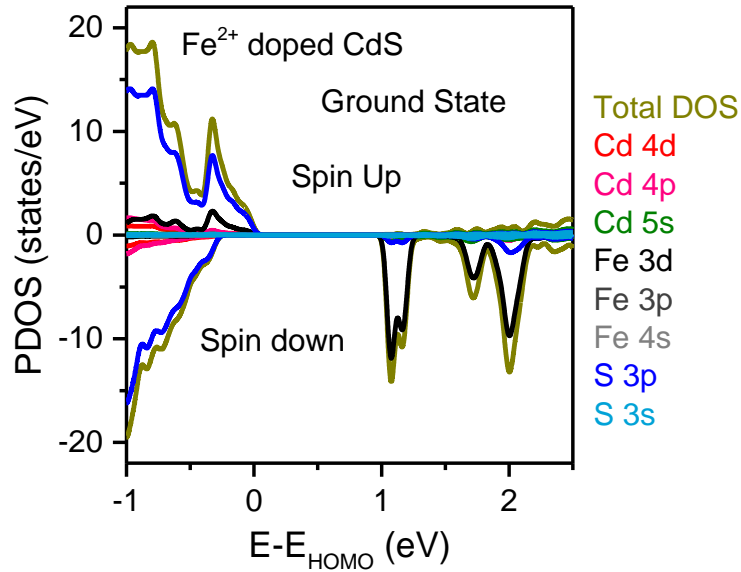


Figure 4.8. Spin-resolved projected density of states (PDOS) of the ground state of Fe^{2+} doped CdS NCs.

Table 4.3. DFT computed values of formation energy, exciton formation energy and magnetic moment for pristine and Fe doped CdS.

		Pristine CdS	1 Fe ion per cell	2 Fe ion per cell
E_{form} (eV/Fe atom)		0	-2.933	-2.934
$E_{form}^{exciton}$ (eV)	Spin up ES	1.51	0.70	1.59
	Spin down ES		0.14	0.17
Fe Magnetic moment (μ_B)	Ground State	-	3.25	3.42
	Spin up ES	-	2.56	3.43
	Spin down ES	-	3.00	3.42

Hence magneto-optical interaction of the magnetic ion with the host is destroyed and localized Fe acceptor states lead to instantaneous quenching of the excitonic states as observed in earlier literature due to intraionic transitions of magnetic dopants in semiconductors.³⁷⁻³⁹ Thus, clearly, the presence of Fe-Fe interactions is detrimental to the observed magneto-optical splitting of the spin states.

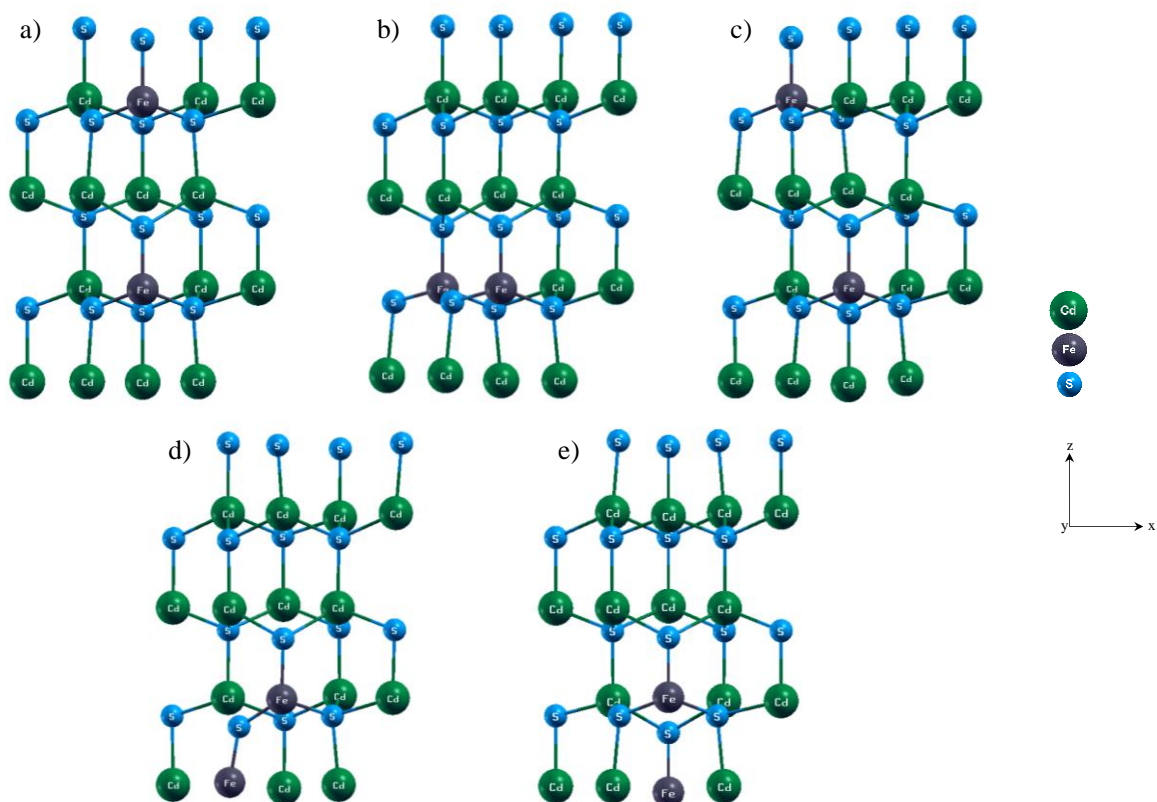


Figure 4.9. Optimized structures of crystallographic inequivalent configurations of 2 Fe per CdS. (a) Lowest energy structure, the coordinates of Fe atoms are (0.334, 0.167, 0.250) and (0.334, 0.167, 0.750) respectively. Note that the structure shown in (a) is considered for all the calculations performed for 2 Fe per CdS. Green, grey and blue spheres correspond to Cd, Fe and S atoms, respectively.

We propose a simplified energy line diagram with the contributions from the various atomic orbitals to the spin-up/down excited states in figure 4.11(a/b) respectively based on observations from the PDOS and the charge density iso-surfaces. The spin-up excitation is relatively unhindered as shown in figure 4.11(a) with regular photobleaching in TA spectra. However, the absorption is particularly relevant in the spin-down excitation as shown in figure 4.11(b) wherein it exhibits a reduction below the resonance energy and an increase above the resonance energy leading to a nearly symmetrical derivative-like feature. The photoexcitation is just a small perturbation that initiates the magneto-optical splitting leading to MOSE that would however persist even beyond the duration of the excitation light pulse if the spin selection rules remain valid. Therefore, the excitation fluence required to achieve the currently reported splitting is also much lower ($24 \mu\text{J}/\text{cm}^2$) than the optical Stark shifts in non-magnetic systems reported in the literature. Typical experimental signatures of a simple OSE include a transient shift of the optical absorption

edge upon excitation with a non-resonant laser and a near symmetrical derivative-like feature in differential transmission spectra arising from the shift in energy levels.

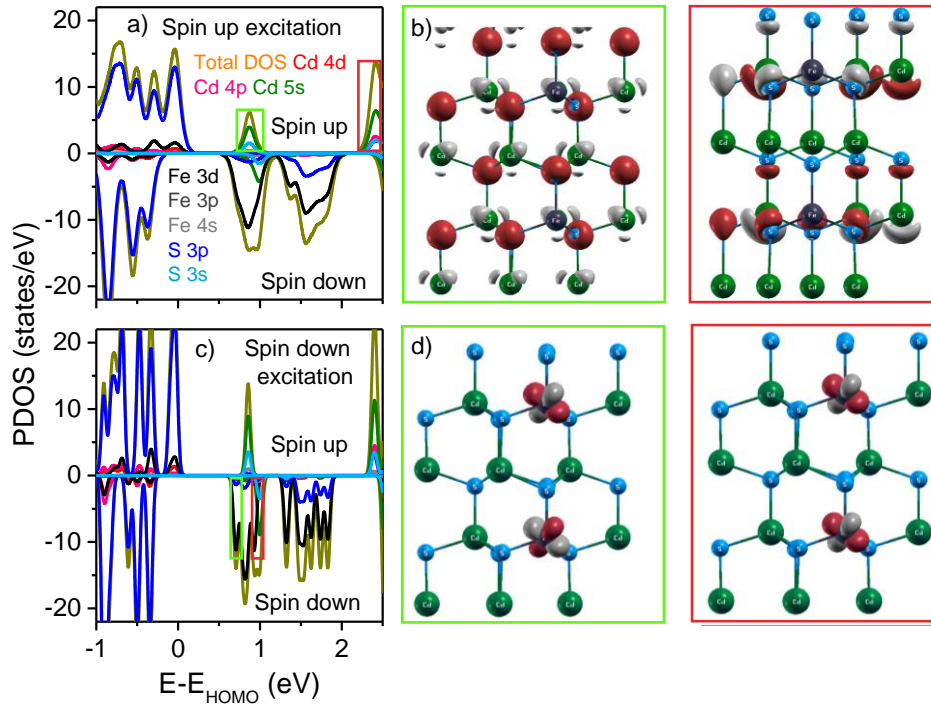


Figure 4.10. Illustration of (a) spin-up excitation and (b) spin-down excitation along with the corresponding line diagram showing the spin-up and spin-down excited states. Schematic representing (c) sum of spin-up and spin-down excitation, (d) Stark shift calculation.

However, in this case, wherein the excitation is not spin-selective, we observe a sum of these effects along with normal PB as shown in figure 4.11(c). The exact Stark shift for different Fe concentrations at different time intervals is calculated similar to literature¹ and is discussed briefly in experimental section and depicted in figure 4.11(d).

Figures 4.12(a) and (b) show the TA spectra at two different time delays of the NCs, under non-resonant excitation (3.1 eV) using linearly polarised light. Undoped CdS NCs are characterized by a single PB peak centered around 2.49 ± 0.01 eV. Fe²⁺ doped systems manifest instead typical Stark shift spectral signature, namely a derivative-like feature, characterized by a shifting (ΔE) of the excitonic absorption peak (E_0). This shift signifies the shift of energy levels, specifically near the VBM-CBM energies. It is important to note here that the energy splitting is quite small, and both the states would be accessible during the excitation at room temperature due to the intrinsic width of the laser excitation.

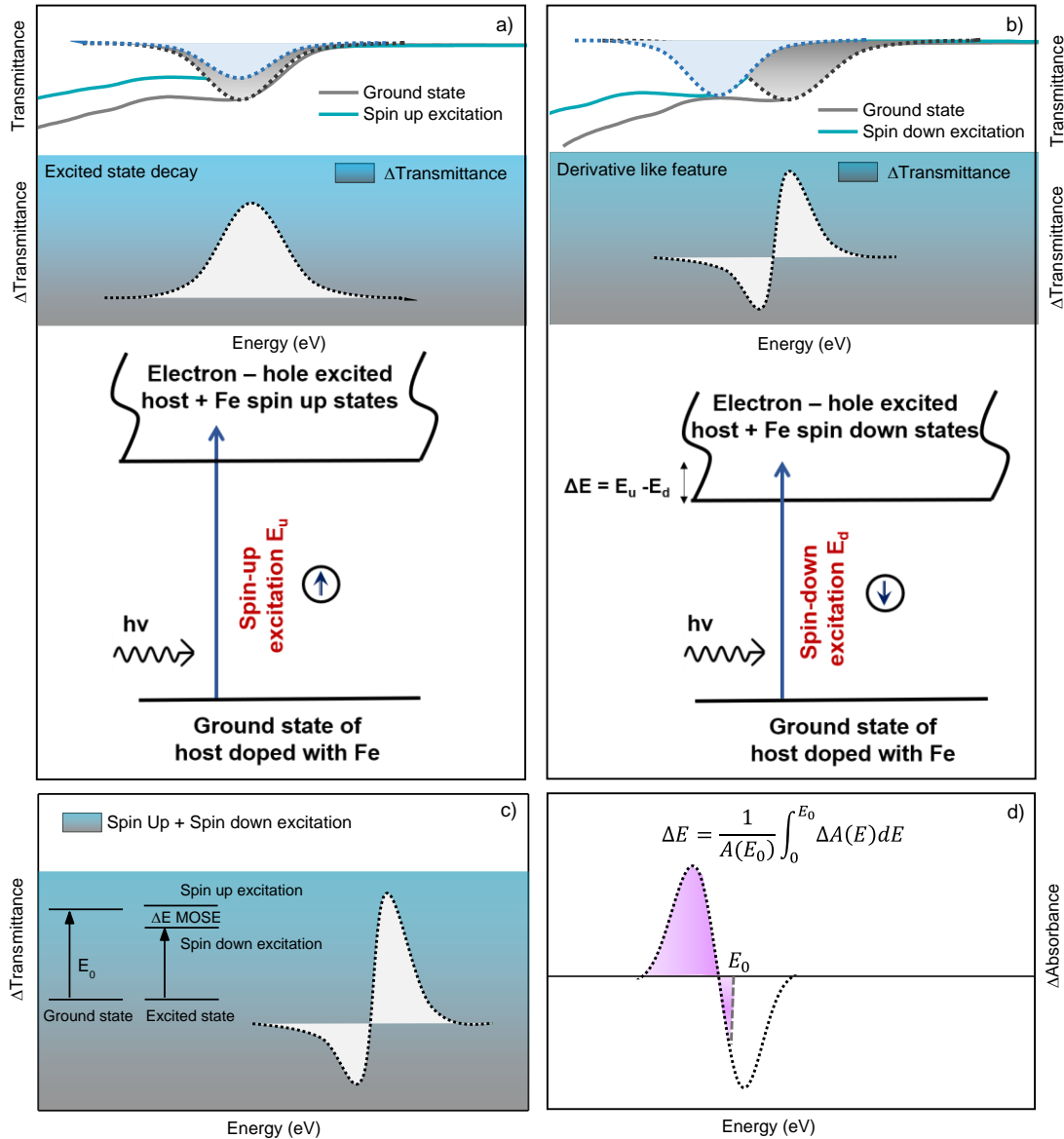


Figure 4.11. Illustration of (a) spin-up excitation and (b) spin-down excitation along with the corresponding line diagram showing the spin-up and spin-down excited states. Schematic representing (c) sum of spin-up and spin-down excitation, (d) Stark shift calculation.

However, the derivative-like difference spectrum suggests the presence of more than one pathway. One such pathway would be the conventional biexciton effect⁴⁰⁻⁴² wherein a derivative-like signature stems from the overall sum of the PB signal and photoinduced absorption. However, we are working with very low fluence ($24 \mu\text{J}/\text{cm}^2$) corresponding to an average exciton $\langle N \rangle$ of about 0.335. Additionally, our studies at other lower fluences showed identical data (figure 4.13) suggesting that the biexciton effect is not responsible for these observations. We also note that in literature this derivative-like

feature due to a biexciton effect is present only “immediately after excitation” ($< 2\text{ps}$) at higher than band gap excitation.

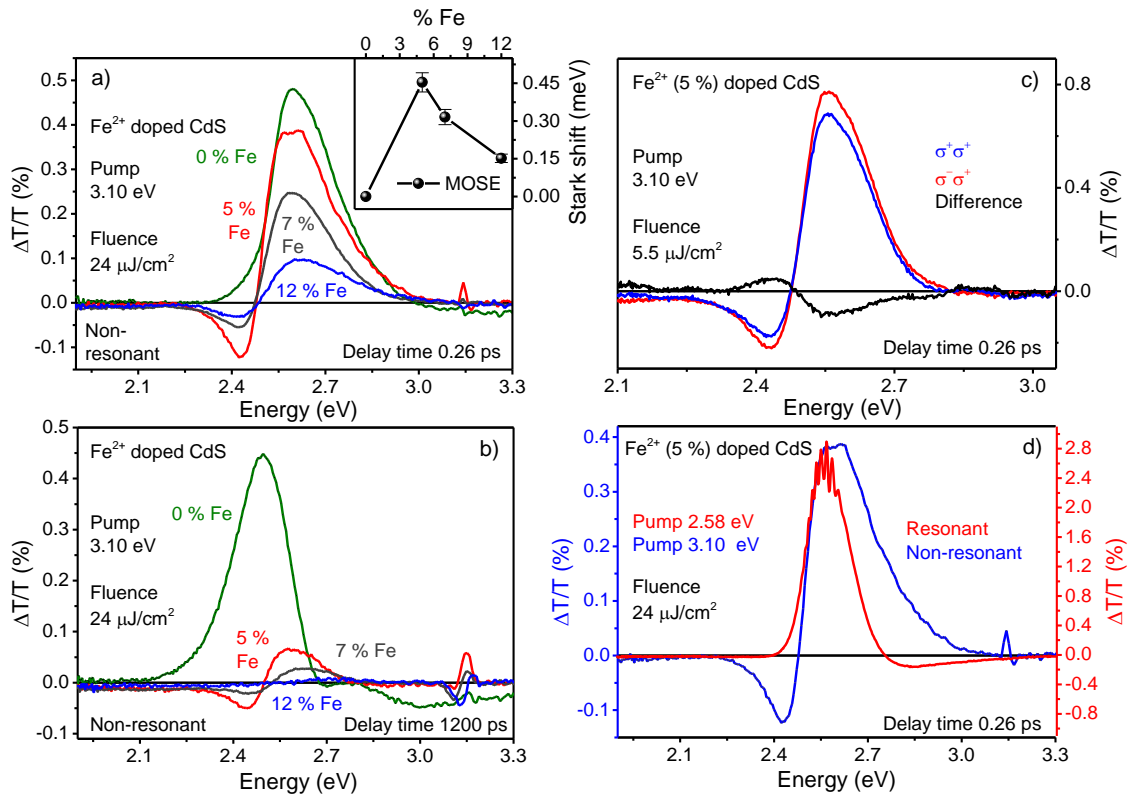


Figure 4.12. TA spectra of Fe²⁺ doped and undoped CdS shown at different pump-probe delay of 0.26 ps (a) and 1200 ps (b), for a pump photon energy of 3.1 eV which is above the exciton resonance energy. Magnitude of Stark shifts (with error bars) in the inset to (a). (c) TA spectra of Fe²⁺ (5%) doped CdS using same and opposite pump-probe circular polarizations shown at a pump-probe delay of 0.26 ps, along with the difference spectrum (d) TA spectra of Fe²⁺ (5%) doped CdS under resonant and non-resonant excitations at a pump-probe delay of 0.26 ps.

Further, this characteristic feature persists at all measured times after the excitation in the case of Fe²⁺ doped CdS NCs (figure 4.12(b), with a similar magnitude beyond the duration of the pulse but dependent on the Fe concentration in the host as shown in the inset to Fig. 3a. This splitting of the host spin states in presence of a magnetic ion like Fe is comparable to a Zeeman effect with a ~ 2 T magnetic field at room temperature. On the other hand, the use of light as a perturbation without the magnetic ion would require an increase in the fluence by at least one order of magnitude, as observed from references in table 4.1. However, a combination of OSE with the internal perturbative field through the magneto-optical effects generates a spin-dependent quantum-confined Stark effect.

To obtain definitive proof of our proposed mechanism of spin-dependent magneto-optical effect within the excited state, we have performed helicity-resolved pump-probe measurements. These measurements were carried out using right circularly polarized probe pulses while the pump pulses were alternatively polarized with left or right circular polarization. Polarization-resolved spectra (figure 4.12(c) and figure 4.14(a)) and dynamics of $\Delta T/T$ (figure 4.14(b)) are measured for 5 % Fe^{2+} doped CdS at $5.5 \mu\text{J}/\text{cm}^2$ pump fluence and 3.1 eV pump energy with same and opposite helicities. The difference signal for the same and opposite circular polarisations of the pump and probe pulses is also shown in the figures, demonstrating a clear $\Delta T/T$ dependence on the circular polarization. This suggests the presence of two different states that show a change in the orientation of a component of the angular momentum of the system. This effect instead does not occur in a purely spin-independent wavepacket.^{1,43} Additionally, we also show that the difference TA spectrum is non-zero even up to the largest time scale of measurement (1200 ps) supporting our observation of long-lived spin-dependent optical phenomena (figure 4.14 (a,b)).

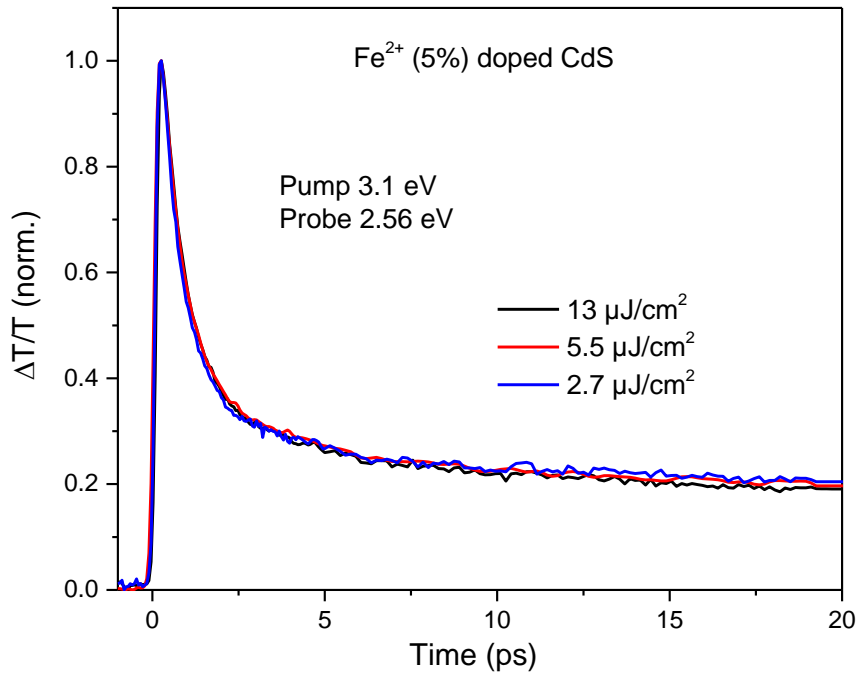


Figure 4.13. Differential transmission dynamics of Fe^{2+} (5%) doped CdS NCs under a pump photon energy of 3.1 eV at different fluences for opposite circularly polarized pump-probe beams.

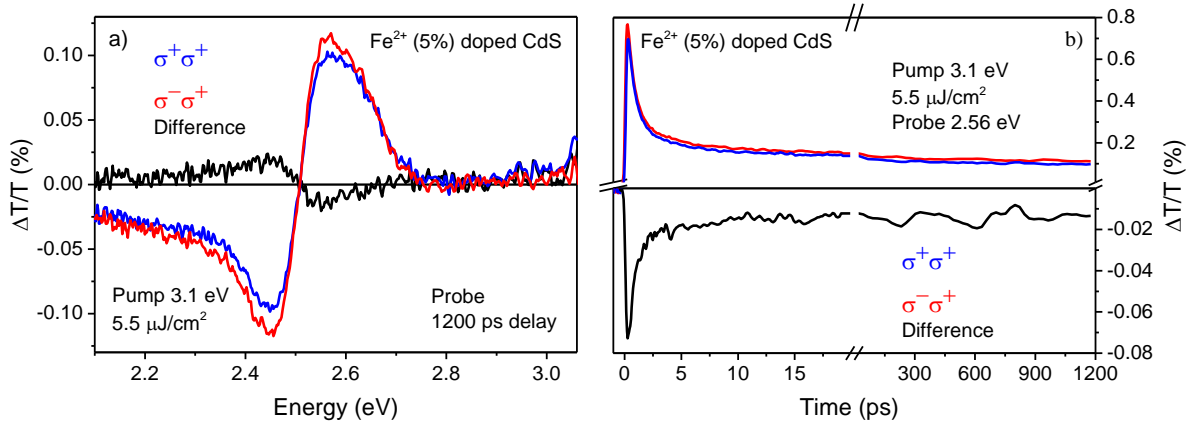


Figure 4.14. (a) Circularly polarized TA spectra of Fe^{2+} (5%) doped CdS using same and opposite pump-probe circular polarizations along with the difference spectrum at a pump-probe delay of 1200 ps, for a pump photon energy of 3.1 eV. (b) Differential transmission dynamics at 2.56 eV using same and opposite circular pump polarizations for Fe^{2+} (5%) doped CdS NCs. During measurements, the probe was kept with a right circular polarization while the pump was alternatively set at a right or left circular polarization.

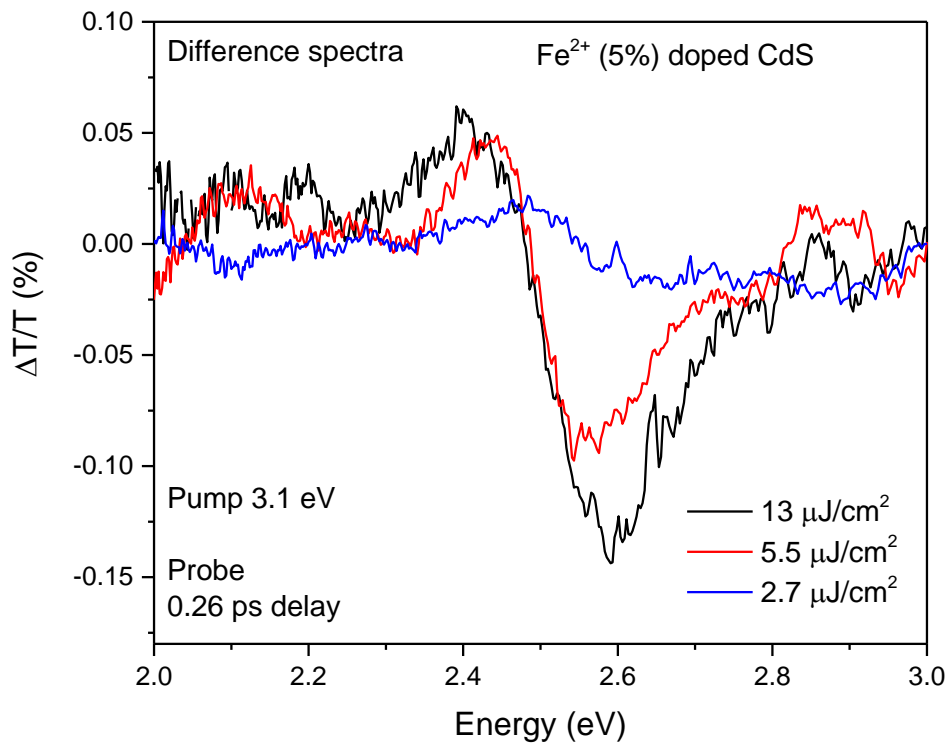


Figure 4.15. a) Difference spectra between same and opposite pump-probe polarizations for Fe^{2+} (5%) doped CdS, pumped at 3.1 eV. Spectra are shown at a pump-probe delay of 0.26 ps under different fluences.

Further, we have studied the fluence dependence of magneto-optical splitting. Even with the lowest fluence used ($2.7 \mu\text{J}/\text{cm}^2$), the derivative signal persists for extended time scales supporting the occurrence of MOSE (figure 4.15). Further, to ensure that these observed signatures correspond to the Stark shift, we performed linearly polarized pump-probe measurements under resonant conditions wherein an energy splitting rather than a Stark shift should be present. We expect a decrease in transmission at energies both above and below the resonance and an increase in transmission at resonance. This typical response is indeed shown in figure 4.12(d) (red line) in contrast to the Stark shift in the non-resonant excitation (blue line).

4.5 Conclusion

In summary, we demonstrated the MOSE by studying the magneto-optical interactions of the dopant states with the host electronic states in Fe^{2+} doped CdS NCs, in the absence of Fe-Fe interactions. Linearly and circularly polarized TA spectroscopy and DFT calculations were combined to understand the electron transfer within the host into Fe-3d states, elucidating the quenching behaviour as well as the Stark shift. We showed the emergence of MOSE due to the magneto-optical interaction for an extended amount of time at room temperature. DFT calculations of transient and ground-state electronic structure and properties also mirrored these changes in the transition.

Bibliography

- (1) Giovanni, D.; Chong, W. K.; Dewi, H. A.; Thirumal, K.; Neogi, I.; Ramesh, R.; Mhaisalkar, S.; Mathews, N.; Sum, T. C. Tunable Room-Temperature Spin-Selective Optical Stark Effect In Solution-Processed Layered Halide Perovskites. *Sci. Adv.* **2016**, *2*, e1600477.
- (2) Amo, A.; Liew, T. C. H.; Adrados, C.; Houdré, R.; Giacobino, E.; Kavokin, A. V.; Bramati, A. Exciton–Polariton Spin Switches. *Nat. Photonics* **2010**, *4*, 361-366.
- (3) Reiter, D. E.; Axt, V. M.; Kuhn, T. Optical Signals of Spin Switching Using the Optical Stark Effect in a Mn-Doped Quantum Dot. *Phys. Rev. B* **2013**, *87*, 115430.
- (4) Wolf, S. A.; Awschalom, D. D.; Buhrman, R. A.; Daughton, J. M.; von Molnár, v. S.; Roukes, M. L.; Chtchelkanova, A. Y.; Treger, D. M. Spintronics: A Spin-Based Electronics Vision for the Future. *Science* **2001**, *294*, 1488-1495.
- (5) Udo, M. K.; Villeret, M.; Miotkowski, I.; Mayur, A. J.; Ramdas, A. K.; Rodriguez, S. Electronic Excitations of Substitutional Transition-Metal Ions in II-VI Semiconductors: CdTe: Fe²⁺ and CdSe: Fe²⁺. *Phys. Rev. B* **1992**, *46*, 7459-7468.
- (6) Vallin, J. T.; Slack, G. A.; Bradley, C. C. Far-Infrared Absorption of ZnS: Fe²⁺ in Strong Magnetic Fields. *Phys. Rev. B* **1970**, *2*, 4406-4413.
- (7) Smoleński, T.; Kazimierczuk, T.; Kobak, J.; Goryca, M.; Golnik, A.; Kossacki, P.; Pacuski, W. Magnetic Ground State of an Individual Fe²⁺ Ion in Strained Semiconductor Nanostructure. *Nat. Commun.* **2016**, *7*, 10484.
- (8) Xia, Y.; Li, Q.; Kim, J.; Bao, W.; Gong, C.; Yang, S.; Wang, Y.; Zhang, X. Room-Temperature Giant Stark Effect of Single Photon Emitter in Van der Waals Material. *Nano Lett.* **2019**, *19*, 7100-7105.
- (9) Perebeinos, V.; Avouris, P. Exciton Ionization, Franz–Keldysh, and Stark Effects in Carbon Nanotubes. *Nano Lett.* **2007**, *7*, 609-613.
- (10) Yang, Y.; Yang, M.; Zhu, K.; Johnson, J. C.; Berry, J. J.; Van De Lagemaat, J.; Beard, M. C. Large Polarization-Dependent Exciton Optical Stark Effect in Lead Iodide Perovskites. *Nat. Commun.* **2016**, *7*, 12613.
- (11) Joffre, M.; Hulin, D.; Migus, A.; Combescot, M. Laser-Induced Exciton Splitting. *Phys. Rev. Lett.* **1989**, *62*, 74-77.
- (12) Stern, L.; Desiatov, B.; Mazurski, N.; Levy, U. Strong Coupling and High-Contrast All-Optical Modulation in Atomic Cladding Waveguides. *Nat. Commun.* **2017**, *8*, 14461.

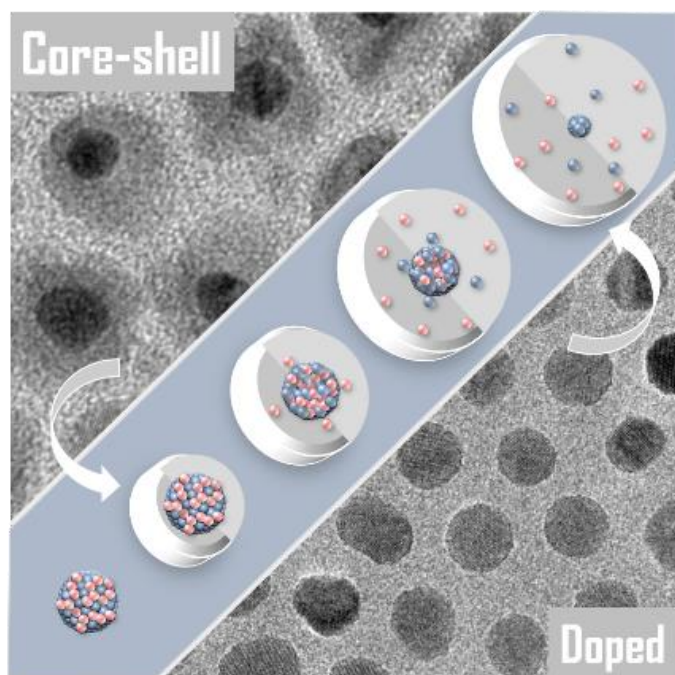
- (13) Liu, M.; Yin, X.; Ulin-Avila, E.; Geng, B.; Zentgraf, T.; Ju, L.; Wang, F.; Zhang, X. A Graphene-Based Broadband Optical Modulator. *Nature* **2011**, *474*, 64-67.
- (14) Bludau, W.; Wagner, E. Impact Ionization of Excitons in GaAs. *Phys. Rev. B* **1976**, *13*, 5410-5414.
- (15) Empedocles, S. A.; Bawendi, M. G. Quantum-Confined Stark Effect in Single CdSe Nanocrystallite Quantum Dots. *Science* **1997**, *278*, 2114-2117.
- (16) Walters, G.; Wei, M.; Voznyy, O.; Quintero-Bermudez, R.; Kiani, A.; Smilgies, D. M.; Munir, R.; Amassian, A.; Hoogland, S.; Sargent, E. The Quantum-Confined Stark Effect in Layered Hybrid Perovskites Mediated by Orientational Polarizability of Confined Dipoles. *Nat. Commun.* **2018**, *9*, 4214.
- (17) Giannozzi, P.; Baroni, S.; Bonini, N.; Calandra, M.; Car, R.; Cavazzoni, C.; Ceresoli, D.; Chiarotti, G. L.; Cococcioni, M.; Dabo, I. QUANTUM ESPRESSO: A Modular and Open-Source Software Project for Quantum Simulations of Materials. *J. Phys. Condens. Matter* **2009**, *21*, 395502.
- (18) Vanderbilt, D. Soft Self-Consistent Pseudopotentials in a Generalized Eigenvalue Formalism. *Phys. Rev. B.* **1990**, *41*, 7892.
- (19) Perdew, J. P.; Burke, K.; Ernzerhof, M. Generalized Gradient Approximation Made Simple. *Phys. Rev. Lett.* **1996**, *77*, 3865.
- (20) Yuhas, B. D.; Fakra, S.; Marcus, M. A.; Yang, P. Probing the Local Coordination Environment for Transition Metal Dopants in Zinc Oxide Nanowires. *Nano Lett.* **2007**, *7*, 905-909.
- (21) Segura-Ruiz, J.; Martinez-Criado, G.; Chu, M.; Geburt, S.; Ronning, C. Nano-X-Ray Absorption Spectroscopy of Single Co-Implanted ZnO Nanowires. *Nano Lett.* **2011**, *11*, 5322-5326.
- (22) Keavney, D. J.; Cheung, S. H.; King, S. T.; Weinert, M.; Li, L. Role of Defect Sites and Ga Polarization in the Magnetism of Mn-Doped GaN. *Phys. Rev. Lett.* **2005**, *95*, 257201.
- (23) Saha, A.; Makkar, M.; Shetty, A.; Gahlot, K.; Pavan, A. R.; Viswanatha, R. Diffusion Doping in Quantum Dots: Bond Strength and Diffusivity. *Nanoscale* **2017**, *9*, 2806-2813.
- (24) Makkar, M.; Viswanatha, R. Frontier Challenges in Doping Quantum Dots: Synthesis and Characterization. *RSC Adv.* **2018**, *8*, 22103-22112.

- (25) Valkonen, M. P.; Kanninen, T.; Lindroos, S.; Leskelä, M.; Rauhala, E. Growth of ZnS, CdS and Multilayer ZnS/CdS Thin Films by SILAR Technique. *Appl. Surf. Sci.* **1997**, *115*, 386-392.
- (26) Kamban, H. C.; Pedersen, T. G. Interlayer Excitons in Van der Waals Heterostructures: Binding Energy, Stark Shift, and Field-Induced Dissociation. *Sci. Rep.* **2020**, *10*, 1-10.
- (27) Kolata, K.; Köster, N.; Woscholski, R.; Lange, C.; Chatterjee, S.; Isella, G.; Chrastina, D.; von Känel, H. In *Giant AC Stark Shift in Germanium*, CLEO: 2011-Laser Science to Photonic Applications, IEEE: 2011; pp 1-2.
- (28) Takagi, H.; Ota, Y.; Kumagai, N.; Ishida, S.; Iwamoto, S.; Arakawa, Y. In *Nanocavity-Enhanced Optical Stark Shift in a Single Quantum Dot Under Extremely Low Excitation Power*, 2012 Conference on Lasers and Electro-Optics (CLEO), IEEE: 2012; pp 1-2.
- (29) Walters, G.; Wei, M.; Voznyy, O.; Quintero-Bermudez, R.; Kiani, A.; Smilgies, D. M.; Munir, R.; Amassian, A.; Hoogland, S.; Sargent, E. The Quantum-Confined Stark Effect in Layered Hybrid Perovskites Mediated by Orientational Polarizability of Confined Dipoles. *Nat. Commun.* **2018**, *9*, 1-11.
- (30) Chaves, A.; Low, T.; Avouris, P.; Çakır, D.; Peeters, F. M. Anisotropic Exciton Stark Shift in Black Phosphorus. *Phys. Rev. B.* **2015**, *91*, 155311.
- (31) Karunasiri, R. P. G.; Mii, Y. J.; Wang, K. L. Tunable Infrared Modulator and Switch Using Stark Shift in Step Quantum Wells. *IEEE Electron Device Lett.* **1990**, *11*, 227-229.
- (32) Kuo, Y.-H.; Lee, Y. K.; Ge, Y.; Ren, S.; Roth, J. E.; Kamins, T. I.; Miller, D. A. B.; Harris, J. S. Strong Quantum-Confined Stark Effect in Germanium Quantum-Well Structures on Silicon. *Nature* **2005**, *437*, 1334-1336.
- (33) Gug, R. K.; Hagston, W. E. Large Blue Shifts Induced by the Quantum Confined Stark Effect in Asymmetric Quantum Wells. *Appl. Phys. Lett.* **1998**, *73*, 1547-1549.
- (34) Saha, A.; Shetty, A.; Pavan, A.; Chattopadhyay, S.; Shibata, T.; Viswanatha, R. Uniform Doping in Quantum-Dots-Based Dilute Magnetic Semiconductor. *J. Phys. Chem. Lett.* **2016**, *7*, 2420-2428.
- (35) Saha, A.; Chattopadhyay, S.; Shibata, T.; Viswanatha, R. Core-Shell to Doped Quantum Dots: Evolution of the Local Environment Using XAFS. *J. Phys. Chem. C* **2016**, *120*, 18945-18951.

- (36) Maiuri, M.; Garavelli, M.; Cerullo, G. Ultrafast Spectroscopy: State of the Art and Open Challenges. *J. Am. Chem. Soc.* **2020**, *142*, 3-15.
- (37) Zanella, M.; Falqui, A.; Kudera, S.; Manna, L.; Casula, M. F.; Parak, W. J. Growth of Colloidal Nanoparticles of Group II–VI and IV–VI Semiconductors on Top of Magnetic Iron–Platinum Nanocrystals. *J. Mater. Chem.* **2008**, *18*, 4311-4317.
- (38) Mirov, S.; Fedorov, V.; Moskalev, I.; Mirov, M.; Martyshkin, D. Frontiers of Mid-Infrared Lasers Based on Transition Metal Doped II–VI Semiconductors. *J. Lumin.* **2013**, *133*, 268-275.
- (39) Piotrowski, P.; Pacuski, W. Photoluminescence of CdTe Quantum Wells Doped With Cobalt and Iron. *J. Lumin.* **2020**, *221*, 117047.
- (40) Makarov, N. S.; Guo, S.; Isaienko, O.; Liu, W.; Robel, I.; Klimov, V. I. Spectral and Dynamical Properties of Single Excitons, Biexcitons, and Trions in Cesium–Lead-Halide Perovskite Quantum Dots. *Nano Lett.* **2016**, *16*, 2349-2362.
- (41) Kambhampati, P. Hot Exciton Relaxation Dynamics in Semiconductor Quantum Dots: Radiationless Transitions on the Nanoscale. *J. Phys. Chem. C* **2011**, *115*, 22089-22109.
- (42) Yumoto, G.; Tahara, H.; Kawawaki, T.; Saruyama, M.; Sato, R.; Teranishi, T.; Kanemitsu, Y. Hot Biexciton Effect on Optical Gain in CsPbI₃ Perovskite Nanocrystals. *J. Phys. Chem. Lett.* **2018**, *9*, 2222-2228.
- (43) Sokell, E.; Zamith, S.; Bouchene, M. A.; Girard, B. Polarization-Dependent Pump-Probe Studies in Atomic Fine-Structure Levels: Towards the Production of Spin-Polarized Electrons. *J. Phys. B: At. Mol. Opt. Phys.* **2000**, *33*, 2005.

CHAPTER 5

Part A. Dual Doping in Nanocrystals via Kirkendall Diffusion.



The following paper has been published based on the work presented here.

Thermodynamics of dual doping in quantum dots.

J. Phys. Chem. Lett. 2019, 10, 8, 1992–1998.

5.1.1 Summary

Dual doping is a powerful way to tailor the properties of semiconductor nanocrystals arising out of host-dopant and dopant-dopant interactions. Nevertheless, it has seldom been explored due to a variety of thermodynamic challenges, such as the differential bonding strength and diffusion constant within the host matrix that integrates with the host in dissimilar ways. This work discusses the challenges involved in administering them within the constraints of one host under similar conditions of temperature, time, and chemical parameters such as solubility and reactivity using CoPt-doped CdS nanocrystals as a model system. In addition, the various forces in play, such as Kirkendall diffusion, solid- and liquid-state diffusion, hard acid soft base interaction with the host, and the effect of lattice strain due to lattice mismatch, are studied to understand the feasibility of the core to doped transformation. These findings suggest a potential approach for manipulating the properties of semiconductors by dual doping engineering.

5.1.2 Introduction

Doping in semiconductor nanocrystals (NCs) has emerged as a technologically important tool for inducing properties that are otherwise not present in the host. It produces intriguing properties that arise from new electronic states created by optically active dopants¹⁻³ resulting in different emissions,⁴⁻⁹ magnetic properties induced in nonmagnetic hosts through magnetic dopants,¹⁰⁻¹³ and surface plasmon resonance as a result of altering the charge carrier density in semiconductor NCs.¹⁴⁻¹⁶ These properties have been instrumental for various applications in the fields of optoelectronics,¹⁷ photovoltaics,¹⁸⁻¹⁹ photodetectors,²⁰⁻²² light emitting diodes,²³⁻²⁵ and spin photonics. In particular, along with the dopant-induced properties, dual doped NCs are expected to yield synergistic properties that are not observed in either of the individually doped systems. These properties include the change in the electrical properties arising from aliovalent doping.²⁶ The optical properties of a long-lived dopant emission can be influenced by another short-lived dopant emission and can provide extensive information about the spin dynamics of the long-lived emission from a fundamental perspective.²⁷ This, in turn, can be used to control the optical properties of a material by modulating the spin of the materials. Similarly, magnetic properties are also modulated by the presence of more than one dopant ion,¹² for example, the presence of a nonmagnetic spacer like Pt in the presence of either Fe or Co enhances its magnetism. Hence, it is important to be able to obtain uniformly doped NCs with more than one dopant ion. The most challenging bottleneck in the development of these

materials remains in the chemistry behind designing such materials with control over size, dopant distribution, and doping percentage where reproducibility remains difficult. This enormous challenge can be traced back to the stabilization of the metastable states overcoming the basic thermodynamically driven properties such as clustering of dopants, phase segregation, surface doping, and self-purification.²⁸⁻³⁰ It is important to note that while dopant-induced changes in the properties of materials have been well studied, the concept of doping and the thermodynamic challenges in the design of different doped nanostructures have rarely been investigated. One of the recently developed methods demonstrates the constructive use of self-purification to obtain a uniform distribution of dopants within the host in a controlled manner.³¹ The corresponding study of thermodynamics for the efficient use of this method yielded a few parameters that are responsible for effective doping, namely, the bond strength of the core and the diffusion constant of dopants in the host matrix.⁷ However, dual doping of NCs has not yet been studied from a thermodynamic perspective. Additional challenges of dual doping include the differential bonding strength, the diffusion kinetics of the two different dopants that are not necessarily similar, and their differential substitution into the lattice, and hence, they pose additional problems for attaining uniform doping.

The various methods used to achieve doping include remote doping or modulation doping^{26, 32-33} cation exchange,³⁴ surface doping, ligand modulation and other post-deposition techniques³⁵ as well as NC superlattice doping³⁶ as discussed in chapter 1. However, most of these techniques try to overcome the energetic barrier to achieve a metastable equilibrium and hence are nontrivial for achieving a high level of success across various systems. Recently, diffusion doping from within the core to the outside has been discussed because of its relative ease and success across various dopants.⁷

In this work, we study the various thermodynamic challenges specific to more than one impurity doping of NCs using CoPt/CdS as the model system, including the Kirkendall effect, transient lattice strain due to the lattice mismatch between the core and shell, and hard soft acid-base (HSAB) theory. Herein, we demonstrate the use of the Kirkendall effect to trigger the diffusion for the effective distribution of dual dopants in NCs. While the Kirkendall effect, which is the motion of the interface between two metals that occurs as a consequence of the difference in the diffusion rates of the metal atoms, has been used to obtain dopant-induced hollow nanostructures,^{37-38,39} its use to obtain uniformly doped NCs in this work is the first of its kind. Though the short bond length and high bond

dissociation energy of the CoPt alloy makes it a very sturdy material for various catalytic reactions,⁴⁰ this very same property hinders the diffusion of CoPt ions into the CdS matrix. For effective doping of Co and Pt into the host matrix, the first step is to overcome the lattice energy of the core. In this work, we increase the lattice strain due to the lattice mismatch at the interface with successive overcoating. This increase in transient stress during the shell growth is responsible for weakening the CoPt alloy core leading to diffusion of ions. We then use the differential diffusion coefficients of the components in an interdiffusion zone, also known as the Kirkendall effect, to trigger doping of CoPt in the CdS matrix. The lattice strain generated during overcoating of CoPt followed by the differential diffusion of the dopants due to the Kirkendall effect results in preferential diffusion of one element over the other. This preferential diffusion is studied using high-angle annular dark-field energy-dispersive x-ray spectroscopy (HAADF-EDS) mapping, extended x-ray absorption fine structure (EXAFS), and inductively coupled plasma optical emission spectroscopy (ICP-OES). It should be noted that even though energy-dispersive x-ray spectroscopy in a scanning transmission electron microscope (STEM-EDS) would give the most direct mapping, within the resolution of interest for the optical and magnetic properties, that is the cluster of two or three atoms, it would not be resolved within the constraints of this technique. However, this technique is useful for understanding the overall diffusion of Pt within NC. EXAFS, on the other hand, is a slightly indirect way, but because of its sensitivity to the local structure at the atomic level, EXAFS can provide the exact information about the coordination environment.⁴¹ Once the lattice is broken, similar to the single-dopant case, self-purification⁴²⁻⁴⁴ also assists in the process of diffusion, which is not discussed herein.

In this work, we have focused on equilibrium thermodynamics, via the systematic study of the transfer of matter and energy in systems as they pass from one state of a thermodynamic equilibrium to another. We have addressed the transformation of a stable core to a completely doped system, and the influence of thermodynamic parameters such as temperature and heat (annealing), energy (in the form of lattice strain), and work (diffusion of a stable core into the host matrix) has been studied. Also, the effect of HSAB theory on the efficiency of the bonding of the dopants in substitutional sites has been studied. We use x-ray diffraction (XRD), STEM-EDS, and EXAFS at various stages of material synthesis to understand the process of doping.

5.1.3 Experimental section

Chemicals used. Cobalt acetylacetonate ($\text{Co}(\text{acac})_2$), platinum acetylacetonate ($\text{Pt}(\text{acac})_2$), cadmium oxide (CdO), oleic acid (OA, 90 %), 1-octadecene (ODE, 90 %), oleylamine (OlAm, technical grade 70 %), and sulfur powder (S, 99.5 %) were purchased from Sigma Aldrich. Ethanol, acetone, and hexane were purchased from Merck (Emparta). All purchased chemicals and solvents were used without further purification.

CoPt NCs. CoPt NCs were first synthesized via co-reduction of metal salts cobalt acetylacetonate (0.05 mmol) and platinum acetylacetonate (0.05 mmol). These metal salts were dissolved in 4 mL oleylamine and 1 mL oleic acid in a three-necked flask. The system was degassed at 80 °C for two hours under constant stirring. The temperature was raised to 200 °C after degassing and kept under constant argon flow. After 10 minutes, the temperature of the reaction mixture was raised to 300 °C gradually (10 °C/3 min). After attaining the temperature, the reaction mixture was kept at 300 °C for 20 minutes and then cooled down to room temperature. The black precipitate was isolated by centrifuging and was then washed twice with hexane, ethanol and a few drops of acetone.

Precursors used for overcoating.

Cadmium oleate. Cadmium oleate, a precursor for the synthesis of CoPt-CdS systems, was synthesized using cadmium oxide (CdO). Oleic acid and octadecene were used as coordinating solvents. For the synthesis of 0.2 M cadmium oleate, 0.3204 g cadmium oxide (CdO), 9 mL of octadecene (ODE) and 7 mL of oleic acid (OA) were taken in a three-necked round bottom flask. The system was degassed at 80 °C for two hours under constant stirring. The temperature was raised to 250 °C after degassing and kept under argon flow. The system was kept for some time until the precursors were completely dissolved and a clear solution was obtained. It was then cooled down to room temperature.

S-ODE. S-ODE, S-precursor for the synthesis of CoPt-CdS nanostructures, was synthesized using sulfur powder. For the synthesis of S-ODE, 65 mg of sulfur powder and 10 mL of octadecene (ODE) were taken in a vial. The system was degassed at room temperature for 15-20 minutes. Argon was purged. Sonication and heating were performed to get a clear solution.

Core-shell CoPt/CdS NCs. For the synthesis of core-shell CoPt/CdS NCs, successive ionic layer adsorption and reaction (SILAR) technique was followed where 0.2 M

cadmium oleate ($\text{Cd}(\text{Ol})_2$) and 0.2 M solution of S/ODE were used. Approximately 20 mg of presynthesized CoPt NCs dissolved in 3 mL oleylamine, were taken in a three-necked round bottom flask and 6 mL of ODE was added to it. The system was degassed at 80 °C for 2 hours under constant stirring. After degassing, the reaction temperature was raised to 250 °C under argon flow. Overcoating was started with the addition of a stoichiometric amount of S-precursor i.e. S-ODE and was kept for 20 minutes. After 20 minutes the same amount of Cd precursor was injected into the system and annealed for 30 minutes. The cyclic addition of S precursor followed by Cd precursor was continued until an ultra-thick shell of CdS was formed over the core CoPt NCs. The reaction was stopped at the required thickness of the CdS shell. The samples were washed by centrifugation using a hexane-ethanol mixture and a few drops of acetone.

Diffused CoPt/CdS NCs. For the synthesis of the diffused NCs, the same procedure was followed as in the case of core-shell NCs. Here, for the growth of each shell, the system was annealed at 250 °C for three hours. Thick shell formation develops a strain and annealing at high temperature allows the core to diffuse inside the CdS matrix. Again, few layers of CdS were grown and the annealing procedure was continued to get completely diffused NCs.

Structural characterization. The as-synthesized NCs were characterized and studied through different techniques. NC size and shape identification were carried out using transmission electron microscopy (TEM). TEM and high-angle annular dark-field imaging (HAADF) and Energy-dispersive x-ray spectroscopy (EDS) mapping was performed on a Tecnai F30 UHR version electron microscope; using a field emission gun (FEG) operating at an accelerating voltage of 200 kV in bright field mode using Cu coated holey carbon TEM grids. HRTEM was performed on FEI TITAN3TM 80-300 kV aberration-corrected transmission electron microscope. Crystal structure identification of the particles was carried out using x-ray diffraction, recorded on Bruker D8 Advance diffractometer using Cu $K\alpha$ radiation. Perkin Elmer inductively coupled plasma-optical emission spectroscopy (ICP-OES) was used to obtain the elemental percentages present in the NCs. X-ray absorption fine structure (XAFS) spectroscopy was employed to probe the local structure around Co and Pt for core, core-shell and diffused NCs. The measurement was carried out at the Stanford Synchrotron Radiation Light source, SLAC National Accelerator Laboratory. Data collected was processed using Athena and Artemis software. The absorption spectrum of the sample was recorded using an Agilent 8453 UV

visible spectrometer. Steady-state PL spectrum was obtained using a 450 W xenon lamp as the source. Combining TEM, XRD, XAFS we characterized the core, core-shell and diffused NCs.

5.1.4 Results and discussion

CoPt core NCs were synthesized using colloidal methods as discussed above with a uniform size distribution as observed in the transmission electron microscopy (TEM) image (6.6 ± 0.56 nm) shown in figure 5.1.1(a). The high-quality crystalline nature of these NCs is evident from the high-resolution TEM (HRTEM) image shown in the inset of figure 5.1.1(a).

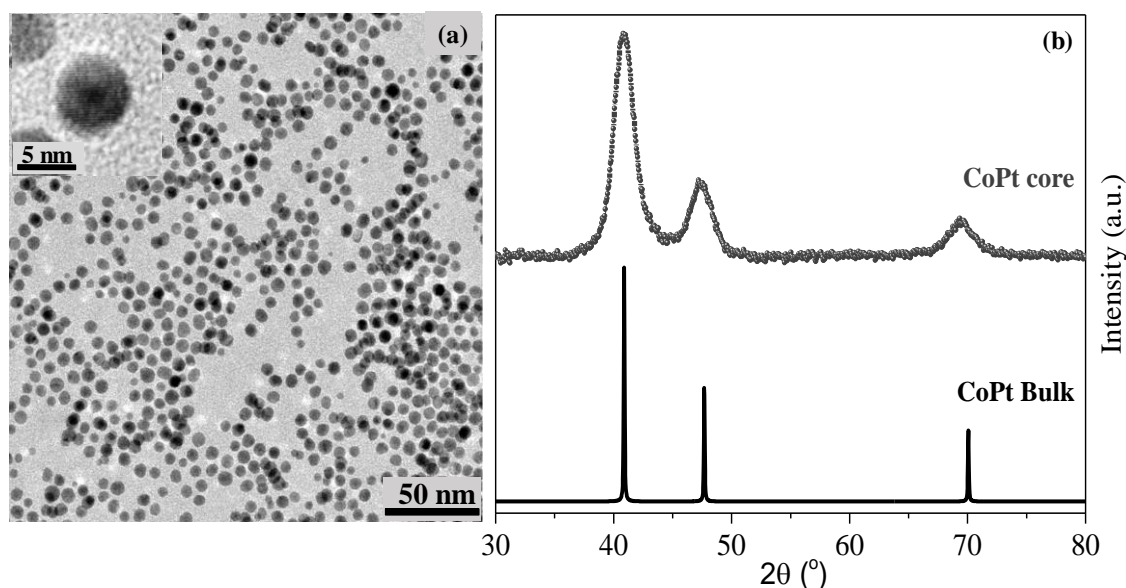
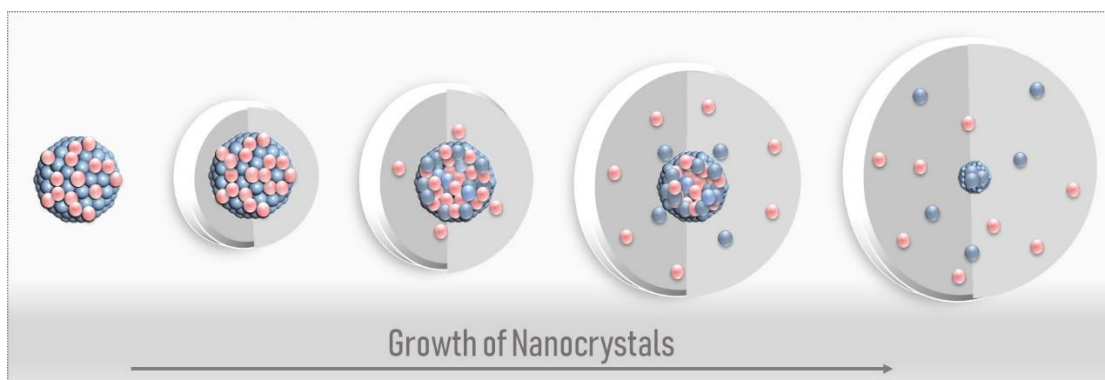


Figure 5.1.1 (a) TEM image showing CoPt core [6.6 ± 0.56 nm] NCs and the representative high-resolution TEM in the inset, (b) XRD pattern of CoPt core NCs.

The XRD pattern for the bimetallic CoPt NCs along with the bulk data obtained from the inorganic crystal structure database (ICSD) is shown in figure 5.1.1(b) with clear evidence of the formation of cubic CoPt NCs. The core CoPt NCs were then overcoated with a thick layer of CdS using the modified SILAR method⁴⁵ to obtain a core-shell system.

Various properties of this clustered CoPt/CdS with a core of CoPt and a shell of CdS have been extensively studied.⁴⁶⁻⁴⁷ The high bond strength of the CoPt alloy is responsible for a rather sharp interface between the clustered CoPt core and the CdS shell. In an effort to overcome this energy, we resort to Kirkendall diffusion along with the simultaneous increase in lattice strain as shown in Scheme 5.1.1.



Scheme 5.1.1: Schematic describing the diffusion of binary alloys into a solid matrix due to the Kirkendall effect and increased lattice strain.

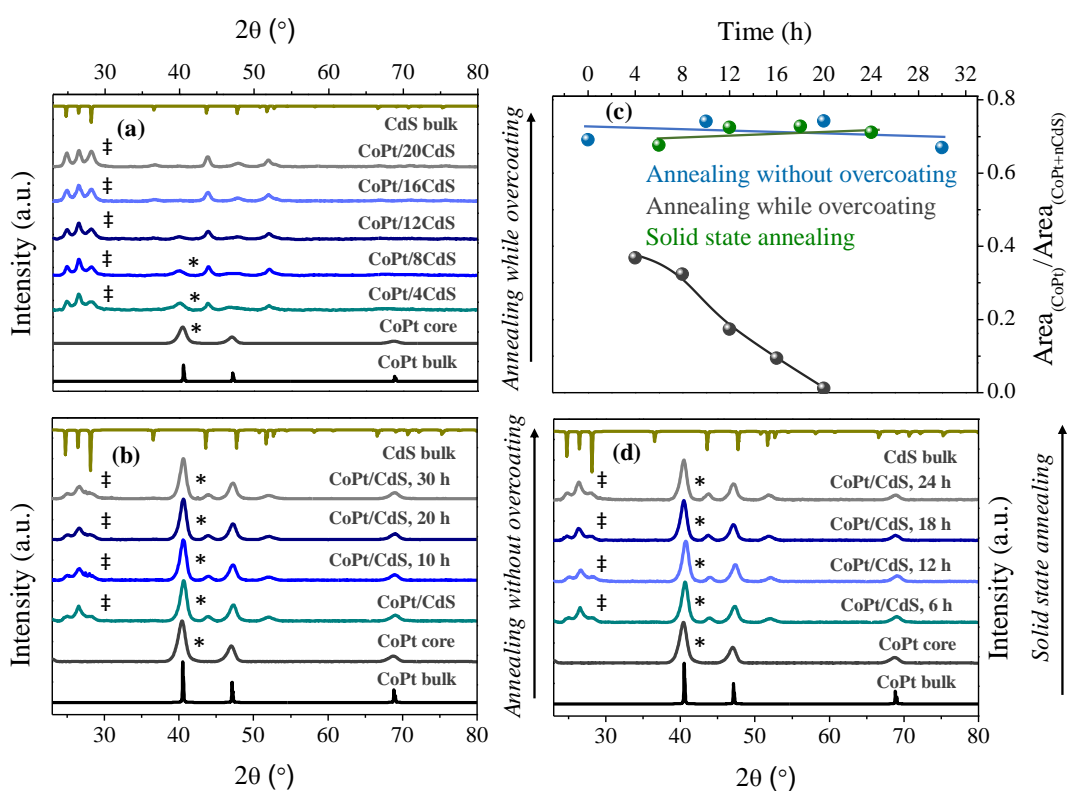


Figure 5.1.2. XRD patterns of CoPt/CdS NCs (a) annealing while overcoating where the number corresponds to the number of shells (b) annealing without overcoating of core-shell system with a particular shell thickness (c) ratio of the area of major XRD peaks of CoPt and CdS (d) solid-state annealing of core-shell system with a particular shell thickness.

In this specific case, high-temperature annealing initiates the diffusion of Co preferentially over Pt. Additionally, this process is further assisted by incrementally increasing the lattice strain by simultaneously overcoating further shells of CdS. In the following sections, we study the effect of solution route annealing with and without overcoating as well as solid-

state annealing as a function of time to understand the effect of differential diffusion and lattice strain. The first two parameters discussed herein include the presence of lattice strain as well as the state of the system. It is well-known that lattice mismatch leads to an increasing amount of lattice strain with an increasing thickness of the second material. In this work, we compare the XRD patterns in the presence and absence of overcoating during the annealing process to study the effect of an increase in lattice strain, and the results are plotted in panels (a) and (b) of figure 5.1.2, respectively. The diffusion of the dopants into the CdS lattice is quantified by considering the ratio of the area of major XRD peaks of CoPt (marked by an asterisk) and CdS (marked by a double dagger) as a function of time and is shown in figure 5.1.2(c).

From the figures, it is evident that when the annealing at high temperatures is carried out along with overcoating of thicker layers of CdS (figure 5.1.2(a)), the CoPt:CdS area ratio decreases, eventually exhibiting only the CdS feature with a complete absence of the CoPt feature. In contrast, annealing at high temperatures without simultaneous overcoating does not change the area ratio of these characteristic peaks, suggesting the absence of any diffusion of CoPt in these NCs as shown in figure 5.1.2(c). This suggests that the lattice strain created by continued overcoating of CdS is necessary to initiate the diffusion of CoPt into the CdS lattice. Second, even though solid-state diffusion is slower than that in the solution phase, it is unclear if diffusion can be triggered in the solid-state. Hence, we study the diffusion of CoPt by annealing of the drop-casted film of the CoPt/CdS core/shell system as shown in figure 5.1.2(d) in comparison to solution phase annealing. A similar study with the ratio of two peak areas as a function of annealing time in NC films is shown in figure 5.1.2(c), demonstrating the absence of diffusion in the solid state.

Thus, in the absence of strain due to lattice mismatch created by subsequent overcoating, simple high-temperature annealing is not enough to result in diffusion of the CoPt lattice. Hence, it is necessary to anneal the NCs while overcoating in the solution phase. It is important to note here that it is essential to carefully balance the annealing time and temperature of growth such that the rate of diffusion of the magnetic Kirkendall core is slower than the rate of growth of the shell by the SILAR technique. This controlled diffusion allows us to have command of the percentage and uniformity of dual doping and the size of the NCs.

It should be noted that within the core/shell architecture, it is apparent that the magnetic ions are localized within a particular nanoscopic volume of the semiconductor surrounded

by a nonmagnetic CdS matrix as shown in the TEM and HRTEM images in panels (a) and (c) of figure 5.1.3, respectively.

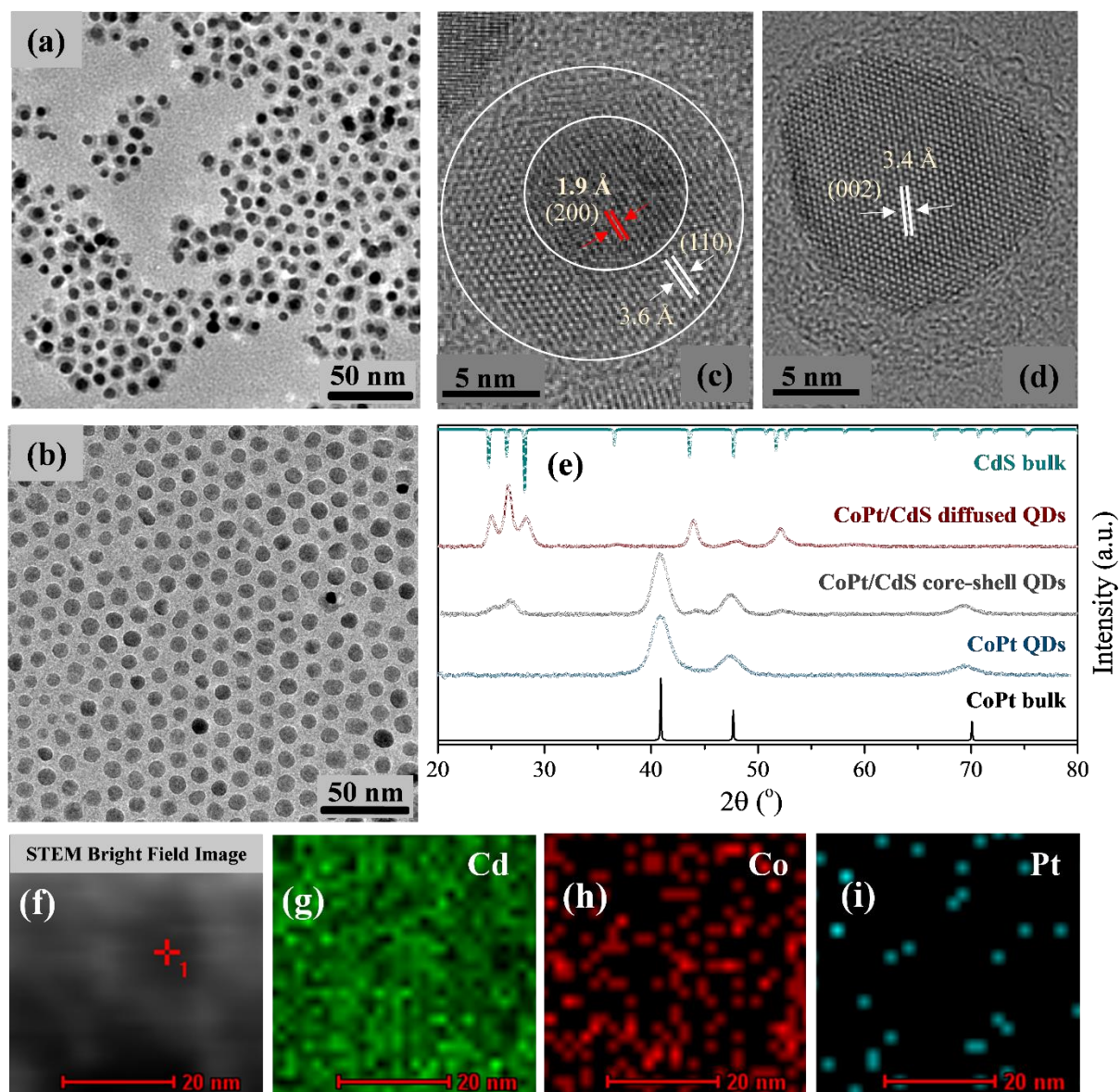


Figure 5.1.3. (a) TEM image showing CoPt/CdS core-shell NCs [$11.3 \text{ nm} \pm 1.71$] and the (b) TEM image showing Co, Pt diffused CdS NCs [$10.9 \text{ nm} \pm 1.04 \text{ nm}$] and the representative high-resolution TEM in (c) and (d) respectively. (e) XRD pattern of CoPt/CdS core-shell and Co, Pt diffused CdS NCs. STEM-EDS mapping of Co, Pt diffused CdS NCs showing STEM (f) bright field image, (g) Cd map, (h) Co map, and (i) Pt map.

From the HRTEM image (figure 5.1.3(c)), it is evident that the lattice planes in the core are different from that of the shell, suggesting a core/shell kind of structure as expected. Typical TEM and HRTEM images of these diffused CoPt/CdS are shown in panels (b) and (d) of figure 5.1.3, respectively. The absence of contrast in the electron density (figure

5.1.3(b)) unlike that of the core/shell demonstrates the absence of a metallic CoPt core. Moreover, the HRTEM image of the NCs, shown in figure 5.1.3(d), does not reveal any lattice mismatch or possible clustering of other materials, demonstrating the diffuse nature of Co and Pt in the host CdS lattice on the scale observable by TEM.

Similarly, the x-ray diffraction patterns shown in figure 5.1.3(e) demonstrate the absence of CoPt lattice peaks in the diffused structure that is otherwise observed in clustered (core-shell) CoPt/CdS. The average particle size for the diffused NCs is 10.9 ± 1.04 nm, and the magnetic ion percentage is found to be 5.8% as obtained by ICP-OES. To further confirm the distribution of dopants in the lattice, we carried out STEM-EDS mapping on the diffused CoPt/CdS, and the results are shown in figure 5.1.3(f-i). EDS mapping within the resolution range (~ 5 nm) shows a diffuse distribution of both dopants, Co (figure 5.1.3(h)) and Pt (figure 5.1.3(i)), within the selected area for the diffused CoPt/CdS structure. From a fundamental perspective, while it is evident from the XRD and TEM that the diffusion of CoPt into the CdS lattice has occurred, the mechanism of diffusion and the order of diffusion are unknown. For example, because Pt and Cd are considered softer than Co, by the HSAB principle,⁴⁸ one would expect Pt to replace Cd earlier than Co. However, it is well-known that the diffusion coefficient of Pt is lower than that of Co.⁴⁹ Hence, it is important to study the rate-determining step to understand the thermodynamically viable dual doping mechanism.

Additionally, even though XRD, TEM, and EDS mapping show the absence of clustering in the diffused NCs, on the typical length scales of XRD and TEM, it is nontrivial to locate clusters of 3-10 magnetic ions within the vicinity that can be detrimental to their properties. Hence, to study the local clustering and the doping mechanism, we measured the XAFS edges of both dopants for the core, clustered, and diffused NC systems in fluorescence mode. EXAFS spectra were modelled to a theoretical model to generate relevant paths using FEFF6 within the ARTEMIS program.⁵⁰ Figure 5.1.4 shows the experimental data and the fit for core, clustered and diffused NCs for the Co K-edge (figure 5.1.4(a-c), respectively) and the Pt L₃-edge (figure 5.1.4(d-f), respectively). Visual inspection of the data makes it evident that the local structure around Co and Pt has evolved within the NCs going from the core to the diffused NCs. In depth analysis of the data using the proposed model suggests that the overcoating of CoPt with CdS under the synthesis conditions presented here brings about a change in the local environment of Co and Pt atoms.

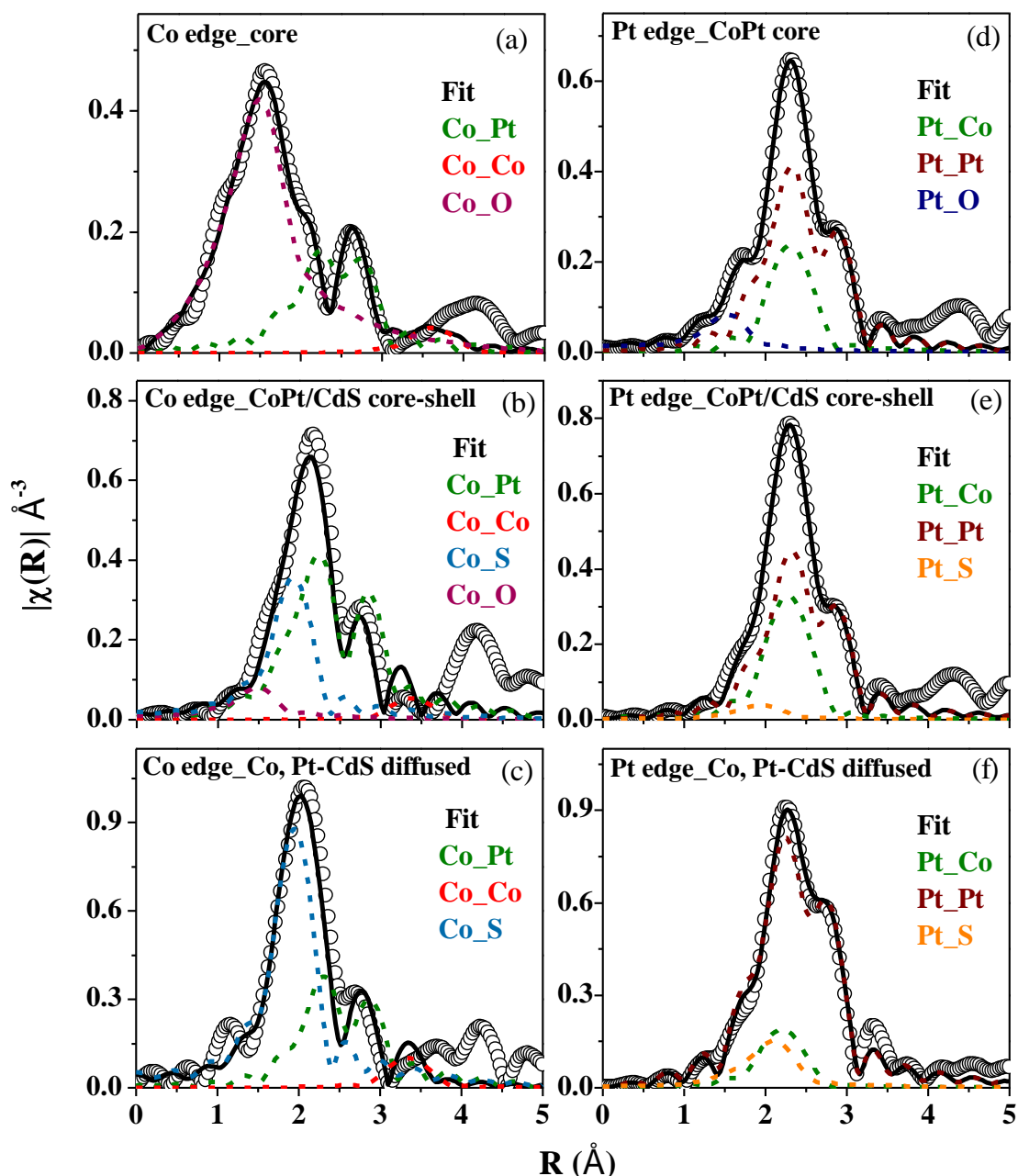


Figure 5.1.4. Magnitude of Fourier-transformed Co K-edge and Pt L₃-edge EXAFS spectra (open symbols) and their best fit (black line) for (a) Co edge core, (b) Co edge core-shell, (c) Co edge diffused, (d) Pt edge core, (e) Pt edge core-shell, and (f) Pt edge diffused. Dashed lines show their component fitting paths.

The presence of high intensity at low R in figure 5.1.4(a) suggests the presence of a Co-O layer on the surface of the core due to surface oxidation. In contrast, this oxidation is absent in the core/shell NCs as well as the diffused NCs. It is also interesting to note that this peak is either completely absent or minimal in the Pt environment, suggesting the presence of Co at the surface rather than Pt in the core confirming the Kirkendall diffusion leading to the formation of the CoO layer at the surface and voids with Pt clusters in the

diffusion zone. The presence of excess Co at the surface as compared to Pt in the core is further confirmed by the ICP-OES data as observed by the higher percentage of Co than of Pt, and these data are listed in table 5.1.1.

Table 5.1.1. ICP-OES data for CoPt core, CoPt/CdS core-shell and Co, Pt diffused CdS NCs.

System	Co %	Pt %	Cd %
CoPt core (6.6 nm)	68.8	31.2	-
CoPt core (10 nm)	70.0	30.0	-
CoPt/CdS core-shell system (11.3 nm)	16.3	21.5	62.2
CoPt/CdS diffused system (10.9 nm)	2.3	3.5	94.2
CoPt/CdS diffused system (17.3 nm)	0.75	1.46	97.79

With an increase in the CdS shell thickness and high temperature annealing, the contribution of the Co_S path is observed along with that of Co_{Pt} paths and minor contributions from other paths as shown in panels (b) and (c) of figure 5.1.4 due to outward diffusion of Co ions into the host matrix. It is interesting to note that even though the Co_S path is quite prominent (figure 5.1.4(b)) in the case of core/shell CoPt/CdS, the Pt_S path (figure 5.1.4(e)) is minor due to the faster diffusion of Co compared to that of Pt. This leads to an increase in Pt_{Pt} coordination in the case of a core/shell system. However, in the case of diffused CdS NCs, we note an increase in the Pt_S contribution (figure 5.1.4(f)), suggesting the successful diffusion of Pt into the CdS lattice, thus corroborating the XRD and TEM data. Various fitting parameters of the numerous paths used in fitting the data are listed in table 5.1.2.

The final proof of the formation of cluster-free diffused dual doped NCs is in its properties. These diffuse Co and Pt-doped CdS samples are optically active and exhibit strong absorption and emission.

Table 5.1.2. List of fit parameters (independent points (N_{idp}) and number of variables (N_{var}) for the fit, bond length (R), coordination number (N), Debye-Waller factor (σ^2), energy shift (ΔE) and R-factor) obtained from modeling the data for Co-K edge and Pt-L₃ edge.

Sample	Paths	R (Å)	N	(σ^2)	ΔE (eV)	R-factor
Co edge Core Nidp = 14 Nvar =7	Co_Pt Co_Co Co_O	2.69 ± 0.01 4.06 ± 0.23 1.99 ± 0.13	0.96 ± 0.01 0.52 ± 0.08 2.49 ± 0.02	0.005 0.01 0.016	-2.57± 3.12	0.01
Co edge CoPt/CdS core-shell Nidp = 14 Nvar =8	Co_Pt Co_Co Co_S Co_O	2.71 ± 0.001 3.74 ± 0.08 2.35 ± 0.17 1.92 ± 0.21	3.52 ± 0.07 0.37 ± 0.12 0.63 ± 0.06 0.17 ± 0.03	0.009 0.007 0.004 0.004	3	0.08
Co edge CoPt/CdS diffused Nidp = 14 Nvar =8	Co_Pt Co_Co Co_S	2.70 ± 0.003 3.67 ± 0.16 2.35 ± 0.17	1.96 ± 0.07 0.63 ± 0.13 1.48 ± 0.11	0.005 0.007 0.004±0.003	7.13± 3.31	0.05

Sample	Paths	R (Å)	N	(σ^2)	ΔE (eV)	R-factor
Pt edge Core Nidp = 14 Nvar =8	Pt_Co Pt_Pt Pt_O	2.66 ± 0.04 2.73 ± 0.02 1.96 ± 0.008	0.76 ± 0.04 3.77 ± 0.05 0.30 ± 0.01	0.006 0.007 ± 0.001 0.007	6.91± 0.80	0.008
Pt edge CoPt/CdS core-shell Nidp = 14 Nvar =7	Pt_Co Pt_Pt Pt_S	2.65 ± 0.06 2.72 ± 0.009 2.38 ± 0.14	1.45 ± 0.06 3.56 ± 0.04 0.18 ± 0.05	0.009 0.006 0.013	6.67 ± 1.40	0.008
Pt edge CoPt/CdS diffused Nidp = 14 Nvar =7	Pt_Co Pt_Pt Pt_S	2.62 ± 0.08 2.68 ± 0.02 2.59 ± 0.06	0.83 ± 0.12 6.83 ± 0.10 1.00 ± 0.24	0.009 0.006 0.013	-0.99 ± 2.91	0.02

The absorption spectra show a peak corresponding to the bandgap transition of CdS NCs in diffused CoPt/CdS, unlike the core-shell CoPt/CdS NCs that are optically inactive with no bandgap corresponding to the CdS NCs as shown in figure 5.1.5. Steady-state PL spectra show a broad dopant emission peak due to Co doping at a higher wavelength along with the band edge emission at a lower wavelength.

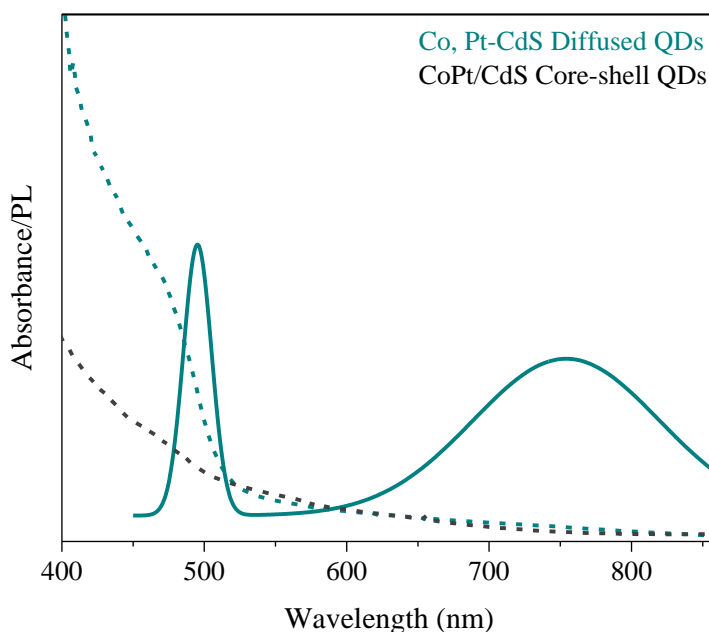


Figure 5.1.5. Steady-state PL (solid line) and absorption (dashed line) of Co, Pt diffused CdS and CoPt/CdS core-shell QDs.

5.1.5. Conclusion

In conclusion, we present experimental evidence that suggests that the Kirkendall effect and lattice strain can initiate the diffusion reactions of binary alloys into the II-VI semiconductor matrix. These parameters break ground for the systematic study of colloidal-state diffusion, and the results offer new insight into the microscopic mechanism of doping in colloidal NCs. We have demonstrated for the first time that the Kirkendall effect can be exploited for doping and can be extended to other Kirkendall pairs to result in a new class of dual-doped NCs.

Bibliography

- (1) Grandhi, G. K.; Viswanatha, R. Tunable Infrared Phosphors using Cu Doping in Semiconductor Nanocrystals: Surface Electronic Structure Evaluation. *J. Phys. Chem. Lett.* **2013**, *4*, 409-415.
- (2) Grandhi, G. K.; Swathi, K.; Narayan, K. S.; Viswanatha, R. Cu Doping in Ligand Free CdS Nanocrystals: Conductivity and Electronic Structure Study. *J. Phys. Chem. Lett.* **2014**, *5*, 2382-2389.
- (3) Zhang, J.; Di, Q.; Liu, J.; Bai, B.; Liu, J.; Xu, M.; Liu, J. Heterovalent Doping in Colloidal Semiconductor Nanocrystals: Cation-Exchange-Enabled New Accesses to Tuning Dopant Luminescence and Electronic Impurities. *J. Phys. Chem. Lett.* **2017**, *8*, 4943-4953.
- (4) Grandhi, G. K.; Tomar, R.; Viswanatha, R. Study of Surface and Bulk Electronic Structure of II–VI Semiconductor Nanocrystals Using Cu as a Nanosensor. *ACS Nano.* **2012**, *6*, 9751-9763.
- (5) Bhargava, R. N.; Gallagher, D.; Hong, X.; Nurmikko, A. Optical Properties of Manganese-Doped Nanocrystals of ZnS. *Phys. Rev. Lett.* **1994**, *72*, 416-419.
- (6) Norris, D. J.; Yao, N.; Charnock, F. T.; Kennedy, T. A. High-Quality Manganese-Doped ZnSe Nanocrystals. *Nano Lett.* **2001**, *1*, 3-7.
- (7) Saha, A.; Makkar, M.; Shetty, A.; Gahlot, K.; Pavan, A. R.; Viswanatha, R. Diffusion Doping in Quantum Dots: Bond Strength and Diffusivity. *Nanoscale.* **2017**, *9*, 2806-2813.
- (8) Grandhi, G. K.; Viswanatha, R. Understanding the Role of Surface Capping Ligands in Passivating the Quantum Dots Using Copper Dopants as Internal Sensor. *J. Phys. Chem. Lett.* **2016**, *120*, 19785-19795.
- (9) Pradhan, N.; Sarma, D. Advances in Light-Emitting Doped Semiconductor Nanocrystals. *J. Phys. Chem. Lett.* **2011**, *2*, 2818-2826.
- (10) Hanif, K. M.; Meulenberg, R. W.; Strouse, G. F. Magnetic Ordering in Doped Cd_{1-x}Co_xSe Diluted Magnetic Quantum Dots. *J. Am. Chem. Soc.* **2002**, *124*, 11495-11502.
- (11) Bonanni, A.; Dietl, T. A Story of High-Temperature Ferromagnetism in Semiconductors. *Chem. Soc. Rev.* **2010**, *39*, 528-539.
- (12) Viswanatha, R.; Naveh, D.; Chelikowsky, J. R.; Kronik, L.; Sarma, D. D. Magnetic Properties of Fe/Cu Codoped ZnO Nanocrystals. *J. Phys. Chem. Lett.* **2012**, *3*, 2009-2014.
- (13) Makkar, M.; Viswanatha, R. Recent Advances in Magnetic Ion-Doped Semiconductor Quantum Dots. *Curr. Sci.* **2017**, *112*, 1421-1429.

- (14) Garcia, G.; Buonsanti, R.; Runnerstrom, E. L.; Mendelsberg, R. J.; Llordes, A.; Anders, A.; Richardson, T. J.; Milliron, D. J. Dynamically Modulating the Surface Plasmon Resonance of Doped Semiconductor Nanocrystals. *Nano Lett.* **2011**, *11*, 4415-4420.
- (15) Luther, J. M.; Jain, P. K.; Ewers, T.; Alivisatos, A. P. Localized Surface Plasmon Resonances Arising from Free Carriers in Doped Quantum Dots. *Nat. Mater.* **2011**, *10*, 361.
- (16) Comin, A.; Manna, L. New Materials for Tunable Plasmonic Colloidal Nanocrystals. *Chem. Soc. Rev.* **2014**, *43*, 3957-3975.
- (17) Choi, J. H.; Fafarman, A. T.; Oh, S. J.; Ko, D. K.; Kim, D. K.; Diroll, B. T.; Muramoto, S.; Gillen, J. G.; Murray, C. B.; Kagan, C. R. Bandlike Transport in Strongly Coupled and Doped Quantum Dot Solids: A Route to High-Performance Thin-Film Electronics. *Nano Lett.* **2012**, *12*, 2631-2638.
- (18) Chuang, C.-H. M.; Brown, P. R.; Bulović, V.; Bawendi, M. G. Improved Performance and Stability in Quantum Dot Solar Cells Through Band Alignment Engineering. *Nat. Mater.* **2014**, *13*, 796-801.
- (19) Carey, G. H.; Kramer, I. J.; Kanjanaboos, P.; Moreno-Bautista, G.; Voznyy, O.; Rollny, L.; Tang, J. A.; Hoogland, S.; Sargent, E. H. Electronically Active Impurities in Colloidal Quantum Dot Solids. *ACS Nano.* **2014**, *8*, 11763-11769.
- (20) Kufer, D.; Nikitskiy, I.; Lasanta, T.; Navickaite, G.; Koppens, F. H. L.; Konstantatos, G. Hybrid 2D–0D MoS₂–PbS Quantum Dot Photodetectors. *Adv. Mater.* **2015**, *27*, 176-180.
- (21) Konstantatos, G.; Badioli, M.; Gaudreau, L.; Osmond, J.; Bernechea, M.; de Arquer, F. P. G.; Gatti, F.; Koppens, F. H. L. Hybrid Graphene–Quantum Dot Phototransistors With Ultrahigh Gain. *Nat. Nanotechnol.* **2012**, *7*, 363-368.
- (22) Deng, Z.; Jeong, K. S.; Guyot Sionnest, P. Colloidal Quantum Dots Intraband Photodetectors. *ACS Nano.* **2014**, *8*, 11707-11714.
- (23) Sun, L.; Choi, J. J.; Stachnik, D.; Bartnik, A. C.; Hyun, B.-R.; Malliaras, G. G.; Hanrath, T.; Wise, F. W. Bright Infrared Quantum Dot Light Emitting Diodes Through Inter-Dot Spacing Control. *Nat. Nanotechnol.* **2012**, *7*, 369-373.
- (24) Yang, Y.; Zheng, Y.; Cao, W.; Titov, A.; Hyvonen, J.; Manders, J. R.; Xue, J.; Holloway, P. H.; Qian, L. High-Efficiency Light-Emitting Devices Based on Quantum Dots with Tailored Nanostructures. *Nat. Photonics.* **2015**, *9*, 259-266.

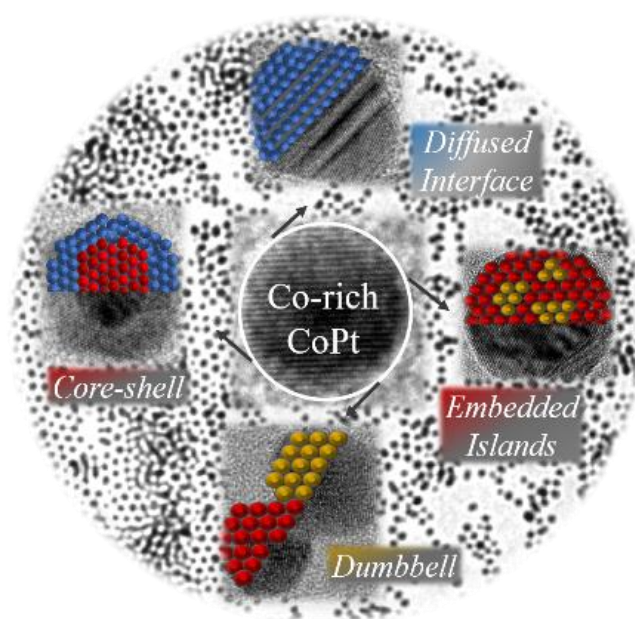
- (25) Saha, A.; Chellappan, K. V.; Narayan, K. S.; Ghatak, J.; Datta, R.; Viswanatha, R. Near-Unity Quantum Yield in Semiconducting Nanostructures: Structural Understanding Leading to Energy Efficient Applications. *J. Phys. Chem. Lett.* **2013**, *4*, 3544-3549.
- (26) Kagan, C. R.; Murray, C. B. Charge Transport in Strongly Coupled Quantum Dot Solids. *Nat. Nanotechnol.* **2015**, *10*, 1013.
- (27) Cao, S.; Li, C.; Wang, L.; Shang, M.; Wei, G.; Zheng, J.; Yang, W. Long-Lived and Well-Resolved Mn²⁺ Ion Emissions in CuInS-ZnS Quantum Dots. *Sci. Rep.* **2014**, *4*, 7510.
- (28) van Schilfgaarde, M.; Mryasov, O. N. Anomalous Exchange Interactions in III-V Dilute Magnetic Semiconductors. *Phys. Rev. B* **2001**, *63*, 233205.
- (29) Sato, K.; Katayama -Yoshida, H.; Dederichs, P. H. High Curie Temperature and Nano-Scale Spinodal Decomposition Phase in Dilute Magnetic Semiconductors. *Jpn. J. Appl. Phys.* **2005**, *44*, L948-L951.
- (30) Makkar, M.; Viswanatha, R. Frontier Challenges in Doping Quantum Dots: Synthesis and Characterization. *RSC Adv.* **2018**, *8*, 22103-22112.
- (31) Saha, A.; Shetty, A.; Pavan, A. R.; Chattopadhyay, S.; Shibata, T.; Viswanatha, R. Uniform Doping in Quantum Dots Based Dilute Magnetic Semiconductor. *J. Phys. Chem. Lett.* **2016**, *7*, 2420-2428.
- (32) Oh, S. J.; Kim, D. K.; Kagan, C. R. Remote Doping and Schottky Barrier Formation in Strongly Quantum Confined Single PbSe Nanowire Field-Effect Transistors. *ACS Nano.* **2012**, *6*, 4328-4334.
- (33) Luther, J. M.; Pietryga, J. M. Stoichiometry Control in Quantum Dots: A Viable Analog to Impurity Doping of Bulk Materials. *ACS Nano.* **2013**, *7*, 1845-1849.
- (34) Petralanda, U.; De Trizio, L.; Gariano, G.; Cingolani, R.; Manna, L.; Artyukhin, S. Triggering Cation Exchange Reactions by Doping. *J. Phys. Chem. Lett.* **2018**, *9*, 4895-4900.
- (35) Engel, J. H.; Alivisatos, A. P. Postsynthetic Doping Control of Nanocrystal Thin Films: Balancing Space Charge to Improve Photovoltaic Efficiency. *Chem. Mater.* **2013**, *26*, 153-162.
- (36) Cargnello, M.; Johnston Peck, A. C.; Diroll, B. T.; Wong, E.; Datta, B.; Damodhar, D.; Doan-Nguyen, V. V. T.; Herzing, A. A.; Kagan, C. R.; Murray, C. B. Substitutional Doping in Nanocrystal Superlattices. *Nature.* **2015**, *524*, 450.
- (37) Wang, W.; Dahl, M.; Yin, Y. Hollow Nanocrystals Through the Nanoscale Kirkendall Effect. *Chem. Mater.* **2012**, *25*, 1179-1189.

- (38) Yin, Y.; Rioux, R. M.; Erdonmez, C. K.; Hughes, S.; Somorjai, G. A.; Alivisatos, A. P. Formation of Hollow Nanocrystals Through the Nanoscale Kirkendall Effect. *Science*. **2004**, *304*, 711-714.
- (39) Guria, A. K.; Prusty, G.; Patra, B. K.; Pradhan, N. Dopant-Controlled Selenization in Pd Nanocrystals: The Triggered Kirkendall Effect. *J. Am. Chem. Soc.* **2015**, *137*, 5123-5129.
- (40) Guo, S.; Li, D.; Zhu, H.; Zhang, S.; Markovic, N. M.; Stamenkovic, V. R.; Sun, S. FePt and CoPt Nanowires as Efficient Catalysts for the Oxygen Reduction Reaction. *Angew. Chem.* **2013**, *125*, 3549-3552.
- (41) Saha, A.; Chattopadhyay, S.; Shibata, T.; Viswanatha, R. Core-Shell to Doped Quantum Dots: Evolution of the Local Environment Using XAFS. *J. Phys. Chem. C* **2016**, *120*, 18945-18951.
- (42) Erwin, S. C.; Zu, L.; Haftel, M. I.; Efros, A. L.; Kennedy, T. A.; Norris, D. J. Doping Semiconductor Nanocrystals. *Nature*. **2005**, *436*, 91-94.
- (43) Karan, N. S.; Sarkar, S.; Sarma, D. D.; Kundu, P.; Ravishankar, N.; Pradhan, N. Thermally Controlled Cyclic Insertion/Ejection of Dopant Ions and Reversible Zinc Blende/Wurtzite Phase Changes in ZnS Nanostructures. *J. Am. Chem. Soc.* **2011**, *133*, 1666-1669.
- (44) Dalpian, G. M.; Chelikowsky, J. R. Self-Purification in Semiconductor Nanocrystals. *Phys. Rev. Lett.* **2006**, *96*, 226802.
- (45) Li, J. J.; Wang, Y. A.; Guo, W.; Keay, J. C.; Mishima, T. D.; Johnson, M. B.; Peng, X. Large-Scale Synthesis of Nearly Monodisperse CdSe/CdS Core/Shell Nanocrystals Using Air-Stable Reagents Via Successive Ion Layer Adsorption and Reaction. *J. Am. Chem. Soc.* **2003**, *125*, 12567-12575.
- (46) Gu, H.; Zheng, R.; Zhang, X.; Xu, B. Facile One-Pot Synthesis of Bifunctional Heterodimers of Nanoparticles: A Conjugate of Quantum Dot and Magnetic Nanoparticles. *J. Am. Chem. Soc.* **2004**, *126*, 5664-5665.
- (47) Habas, S. E.; Yang, P.; Mokari, T. Selective Growth of Metal and Binary Metal Tips on CdS Nanorods. *J. Am. Chem. Soc.* **2008**, *130*, 3294-3295.
- (48) Pearson, R. G. Hard and Soft Acids and Bases, HSAB, Part II: Underlying Theories. *J. Chem. Educ.* **1968**, *45*, 643.
- (49) Xin, H. L.; Alayoglu, S.; Tao, R.; Genc, A.; Wang, C.-M.; Kovarik, L.; Stach, E. A.; Wang, L.-W.; Salmeron, M.; Somorjai, G. A. Revealing the Atomic Restructuring of Pt-Co Nanoparticles. *Nano Lett.* **2014**, *14*, 3203-3207.

(50) Ravel, B.; Newville, M. ATHENA and ARTEMIS: Interactive Graphical Data Analysis Using IFEFFIT. *Phys. Scr.* **2005**, 2005, 1007.

CHAPTER 5

Part B. Heterostructure Modeling Through Crystal Facet Engineering.



The following paper has been published based on the work presented here.

Crystal Facet Engineering of CoPt Quantum Dots for Diverse Colloidal Heterostructures.

J. Phys. Chem. Lett. 2020, 11, 6742-6748.

5.2.1 Summary

Precise control of crystal orientation, and specifically the exposed surface, is critical for the engineering of heterostructures. Here, using CoPt as a model system, we explore the energetics to expose suitable facets to promote the required heterostructure formation. Different heterostructures are grown ranging from core/shell structure, diffused interface, dumbbell structured dimers, and embedded island structures wherein these hybrids are fabricated via micro/macrolevel facet-selective growth. The reaction conditions used to achieve such diversity starting from the same seed offer insights into the growth mechanisms of these heterostructures. Such a microscopic understanding of surface chemistry paves the way for the design of new heterostructures with exciting properties.

5.2.2 Introduction

The integration of multiple nanoparticle components into a single framework is not only driven by the functions rendered by the composite nanostructures, but is also reinforced by the desire to solve the synthetic enigma leading to diverse heterostructures. For example, core/shell particles can facilitate charge separation for applications like photovoltaic cells by the formation of a Schottky barrier at the interface.¹ Similarly, controlled manipulation of multilevel twinning can be utilized for the formation of hyperbranching in heterostructures.² Since colloidal quantum dots (QDs) are grown via the solution route synthesis, the realm of combining individual nanocrystals (NCs) to tailor-make a quantum dot assembly, necessary to build electronic and optoelectronic devices is immense. This can be attained by tuning the size, shape, and connectivity of each QD. However, inherent to the simplicity of fabricating these heterostructured materials is the lack of precise morphological control required for the design of smart materials. A large surface area is one of the principal advantages of NCs that significantly increases the importance of surface facets. Thus, one of the prime strategies to attain this objective of controlled heterostructured growth is crystal facet engineering. Engineering the surface facets of the crystal provides a route to tune their reactivities and physicochemical properties that can lead to harmonious growth of heterogeneous QDs with minimal interfacial strains. Such interface effects with electronic communication along boundaries can lead to tunable or new chemical and/or physical responses that are not otherwise present in the single or physical mixture of these counterparts.³⁻⁷ These hybrids can manifest alterations in localization and plasmon-to-exciton coupling,⁸⁻⁹ which have

implications in optoelectronic,¹⁰⁻¹¹ magnetic,¹² photovoltaic,¹³ and photocatalytic¹⁴⁻¹⁵ applications.

Heterogeneous seeded growth¹⁶ is a novel strategy to fabricate hybrid architectures by the growth of a second inorganic domain directly from the surface of pre-existing NC seeds making their crystal facets an important parameter in this process of forming hybrids. This subject has been extensively explored in systems synthesized via molecular beam epitaxy (MBE) methods that exhibit a high level of control on the growth of NCs. These MBE methods have shown distinctly that the change of growth orientation can be used as a prime method to signify unconventional side facet combinations and cross-section shapes.¹⁷ This can be attained by opening up new families of available facets and their combinations resulting in atypical interactions between the heterostructured elements. However, crystal facet engineering in colloidal nanocrystals has not been extensively explored, though they render a powerful platform for device engineers with their ability to tailor size, shape, and composition. This could possibly be due to their surfaces being heavily functionalized with molecular ligands, allowing for a diverse surface chemistry with little cost in terms of energy. However, this same ease of surface control makes it difficult to pinpoint the exact energetics of the relevant surface facet and has hence not been extensively studied.

In this chapter, we aim to understand the role of exposed crystal facets in the synthesis of quantum dot heterostructures, namely, the facet-selective synthesis of CoPt NCs and their hybrids using the colloidal approach. The choice of CoPt NCs was made based on the wide domain of interesting properties displayed by this material,¹⁸⁻²⁰ also discussed in part A and its potential to form heterostructures with varying properties. Co, when alloyed with platinum, is among the best candidates for materials in high-density recording media due to their structural and magnetic properties.²¹ Hybridization between Pt and the Co results in high coercivity and a large magnetocrystalline anisotropy for these structures.²² In addition to these catalytic, electrical, transport, and magnetic properties in the nanocrystal regime, the importance of rather low reactivity and diffusivity of Pt²³⁻²⁴ in these materials cannot be undermined. The earlier part of the chapter has shown Pt to be stubborn while participating in diffusion compared to Co,²⁵ leading to a Kirkendall effect in CoPt structures. We employed the thermodynamics associated with the stubbornness of Pt to diffuse as per our advantage to form the heterostructures. Specifically, we show that the formation of heterostructures is critically dependent on the exposed surface facets while

almost independent of the crystal structure of the seed. A seed NC with the same crystal structure but different surface morphology results in a different outcome.

In this work, we demonstrate five different outcomes, namely, CoPt with no overcoating, core/shell structure, diffused interface, dumbbell structured dimers, and embedded island structures, by modifying the surface facets at a micro and a macrolevel as well as the required counter nanoparticles and surface oxidation via seed-mediated/simultaneous growth of CoPt NCs. The structure of the NCs was studied using x-ray diffraction (XRD), high-resolution transmission electron microscopy (HRTEM), high angle annular dark-field scanning transmission electron microscopy (HAADF-STEM), and electron diffraction (ED). Extended x-ray absorption fine structure (EXAFS) studies were used to probe the correlation of the local environment of the NCs. Temperature- and field-dependent magnetic studies have been performed to get more insight into the magnetic behavior. Optical absorption was performed to get insights into the optical and structural attributes of these NCs.

5.2.3 Experimental section

Chemicals: Cobalt acetylacetonate ($\text{Co}(\text{acac})_2$), platinum acetylacetonate ($\text{Pt}(\text{acac})_2$), cadmium oxide (CdO), oleic acid (OA, 90 %), 1-octadecene (ODE, 90 %), oleylamine (OlAm, technical grade 70 %), chloroauric acid (HAuCl_4 tetrahydrate) and sulfur powder (S, 99.5 %) were purchased from Sigma Aldrich. All chemicals were used without further purification. Ethanol, acetone, and hexane were purchased from Merck (Emparta). All solvents were used without further purification.

CoPt seeds. CoPt NCs were synthesized via co-reduction of cobalt acetylacetonate (0.05 mmol) and platinum acetylacetonate (0.05 mmol). These metal salts were dissolved in 4 mL oleylamine and 1 mL oleic acid in a three-necked flask. The system was degassed at 80 °C for two hours under constant stirring. The temperature was raised to 200 °C after degassing and kept under constant argon flow. After 10 minutes, the temperature of the reaction mixture was raised to 300 °C gradually (10 °C/3 minutes for Co-rich seeds and 10 °C/10 minutes for Pt-rich seeds). After attaining the temperature, the reaction mixture was kept at 300 °C for 20 minutes and then cooled down to room temperature. The black precipitate was isolated by centrifugation and was then washed twice with hexane, ethanol and a few drops of acetone.

Core-shell CoPt-CdS and CoPt-CoS. For the synthesis of core-shell nanostructures, successive ionic layer adsorption and reaction (SILAR) technique was followed. The CoPt reaction was continued in-situ to avoid oxidation of the NCs. To the reaction mixture, 3 mL oleylamine and 6 mL ODE was added. The reaction temperature was raised to 250 °C under argon flow. Overcoating was started with the addition of a stoichiometric amount of S-precursor i.e. S-ODE and was kept for 15 minutes. After 15 minutes the same amount of Cd/Co precursor was injected into the system and annealed for 30 minutes. The cyclic addition of S precursor followed by Cd/Co precursor was continued until an ultra-thick shell of CdS/CoS was formed over CoPt NCs. The reaction was stopped at the required thickness of the shell. The samples were washed by centrifugation using the hexane-ethanol mixture and a few drops of acetone.

Doped CoPt-CdS nanostructures. For the synthesis of the doped nanostructures, the same procedure was followed as in the case of core-shell nanostructures. Here, after the growth of a thick shell of CdS, the system was annealed at 250 °C for a long time (3 hours per shell) and the reaction was continued for 18 shells, with about 54 hours of high-temperature annealing. Thick shell formation develops a strain and annealing at high temperature allows the core to diffuse inside the CdS matrix. Again, few layers of CdS were grown and the annealing procedure was continued to get completely doped nanostructures.

Precursors used for overcoating. Cadmium oleate. Cadmium oleate, a precursor for the synthesis of CoPt-CdS systems, was synthesized using cadmium oxide (CdO) as discussed in part A. **S-ODE.** S-ODE, S-precursor for the synthesis of CoPt-CdS nanostructures, was synthesized using sulfur powder (detailed procedure is discussed in part A).

Au-CoPt dumbbell nanostructures. Presynthesized CoPt nanostructures were treated with Au precursor. Chloroauric acid tetrahydrate (0.025 mmol) was dissolved in 20 mL of toluene and a phase transferring agent, tetramethylammonium bromide (C₄H₁₂BrN, 0.2 mmol) was added to it. The mixture was slowly injected into the CoPt solution over 1 hour under Ar atmosphere at 60 °C (under reflux). The mixture was then kept under stirring for 20 hours at room temperature. The precipitate was isolated by centrifugation.

CoPtAu embedded nanostructures. CoPtAu NCs were synthesized via co-reduction of cobalt acetylacetonate (0.05 mmol), platinum acetylacetonate (0.05 mmol) and chloroauric acid (0.05 mmol). These metal salts were dissolved in 4 mL oleylamine and 1

mL oleic acid in a three-necked flask. Further, the same procedure as mentioned for Co-rich CoPt seeds was followed for the synthesis of CoPtAu nanostructures.

Sample characterization. The as-synthesized NCs were characterized and studied through different techniques. Nanostructure size and shape identification were carried out using transmission electron microscopy (TEM). TEM was performed on a Tecnai F30 UHR version electron microscope; using a field emission gun (FEG) operating at an accelerating voltage of 200 kV in bright field mode using Cu coated holey carbon TEM grids. HRTEM, high-angle annular dark-field imaging (HAADF) and Energy-dispersive x-ray spectroscopy (EDS) mapping were performed on FEI TITAN3TM 80-300 kV aberration-corrected transmission electron microscope. Crystal structure identification of the particles was carried out using x-ray diffraction, recorded on Bruker D8 Advance diffractometer using Cu K α radiation. Perkin Elmer inductively coupled plasma-optical emission spectroscopy (ICP-OES) was used to obtain the elemental percentages present in the NCs. DC magnetization measurements were carried out in a superconducting quantum interference device that employs the technique of vibrating sample magnetometer (SQUID-VSM) (Magnetic Property Measurement System MPMS-3, Quantum Design, U.S.). Few milligrams of the sample was packed in a piece of Teflon for the measurement. M vs H measurements were carried out at 2 K. Field cooled (FC) and zero field cooled (ZFC) measurements were performed for the temperature range of 2 K to 390 K using a 200 Oe constant magnetic field. The sample was first cooled from 400 K (above the ordering temperature of the sample) to 2 K in the absence of an external magnetic field. With heating, magnetization data was recorded in the field strength of 200 Oe (ZFC measurement). In the FC measurement, the sample was cooled in the presence of a magnetic field of 200 Oe. The magnetization was then recorded with a temperature up to 390 K in the presence of an applied field. X-ray absorption fine structure (XAFS) spectroscopy was employed to probe the local structure around Co and Pt. The measurement was carried out at the Stanford Synchrotron Radiation Light source, SLAC National Accelerator Laboratory. Data collected was processed using Athena and Artemis software.²⁶ The absorption spectra of samples were recorded using an Agilent 8453 UV visible spectrometer.

5.2.4 Results and discussion

CoPt seed structures were synthesized using colloidal synthesis that produced monodisperse NCs. Effectively all the metal salts with the ligands were mixed and heated to high temperatures. Since all the metals are already present, the reaction takes place as soon as these metal salts are activated, with the rate-controlling step being the activation of the metal salts. Since Pt bonds are generally stronger, it can take a long time and a higher temperature to activate the Pt salt. During the synthesis, we selectively activate both Co and Pt salts or only Co salts by a controlled rate of increase in temperature from 200 to 300 °C, namely, either at 10 °C per 10 min or in 3 min, respectively.

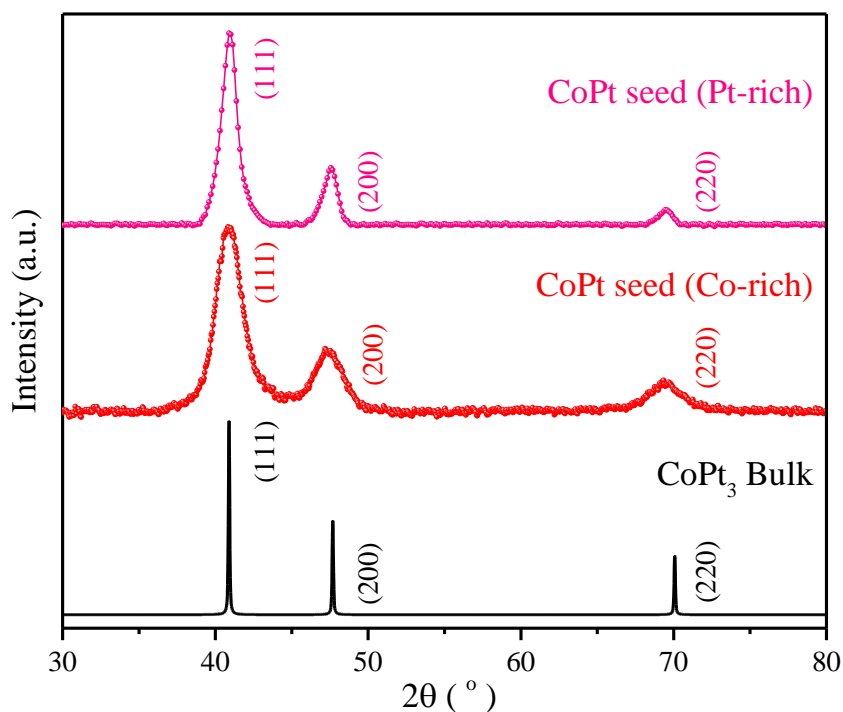


Figure 5.2.1. (a) XRD pattern of Co-rich CoPt and Pt-rich CoPt along with bulk CoPt_3 structure obtained from inorganic crystal structure database (ICSD).

Table 5.2.1. ICP-OES data for CoPt systems.

System	Co %	Pt %
Pt-rich CoPt seed	29.2	70.8
Co-rich CoPt seed	68.8	31.2
CoPt-doped CdS	2.5	3.9

The crystal structure of both systems as analyzed by XRD shows that both systems crystallize in the cubic CoPt_3 lattice as shown in figure 5.2.1. However, the results of this seemingly small change can be observed in ICP-OES analysis wherein we observe the presence of $\sim 70\%$ and $\sim 30\%$ Pt, respectively, from the slow and fast heating (table 5.2.1). Hence, we believe the excess of either Co or Pt is largely concentrated on the surface of the NCs. We distinguish the two systems, respectively, as Pt-rich and Co-rich CoPt NCs henceforth as we study the consequences of the relative composition. It is interesting to note that both the challenge as well as the tunability of the surface of colloidal NCs arises from the control of seemingly insignificant parameters.

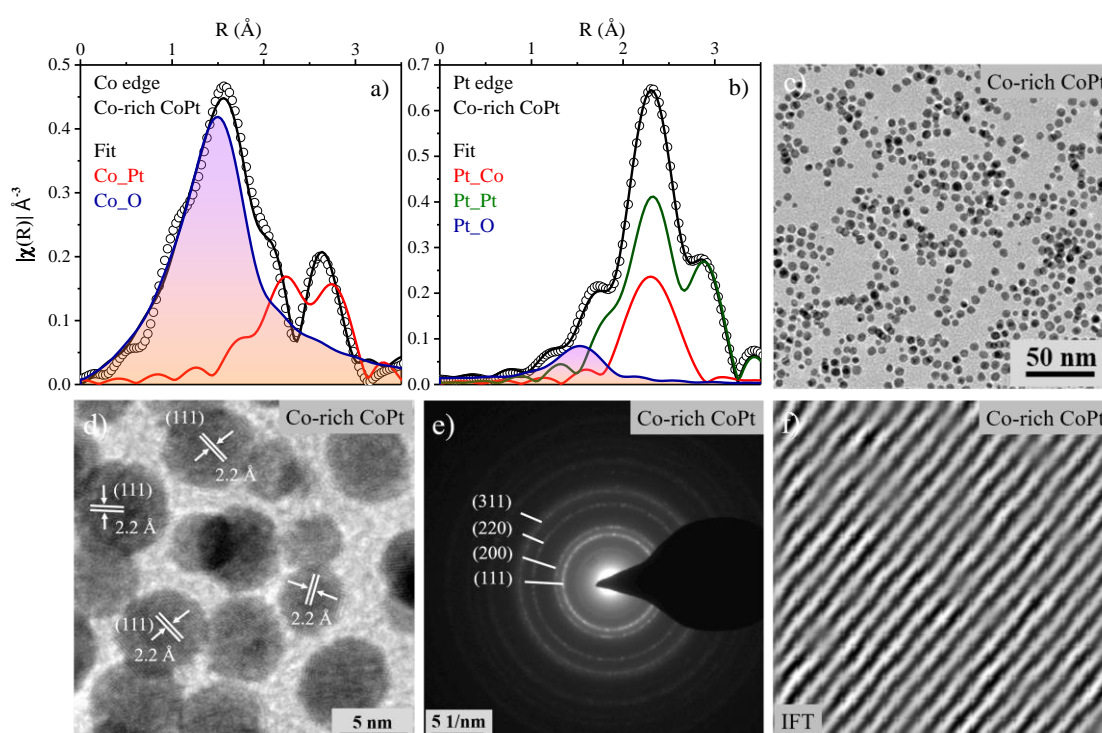


Figure 5.2.2. Magnitude of Fourier-transformed Co K-edge and Pt L_3 -edge EXAFS spectra (open symbols) and their best fit (black line) for (a) Co edge, (b) Pt edge along with their component fitting paths for Co-rich CoPt. TEM (c) and HRTEM (d) image of Co-rich CoPt NCs, (e) electron diffraction (ED) pattern and inverse Fourier transform (IFT) of HRTEM (f) for Co-rich CoPt.

For example, when we increase the synthesis temperature at a quicker pace of $10\text{ }^\circ\text{C}$ in 3 min, a study of the local environment around Co and Pt atoms through EXAFS at the Co and Pt edge shows the presence of high intensity at low R only for the Co edge as shown, respectively, in figure 5.2.2(a) and (b). This suggests surface oxidation resulting in the presence of a Co-O layer on the surface of the core, in contrast to the negligible oxidation

of the Pt as shown by the corresponding fits. This is further corroborated indeed by TEM and HRTEM results as shown in figure 5.2.2(c) and (d), respectively. Upon analysis of the HRTEM images, we observe only (111) planes corresponding to a d-spacing of 2.2 Å as shown by the representative image in figure 5.2.2(d).

This is further verified on a larger scale by the electron diffraction (ED) pattern as well as the inverse Fourier transform (IFT) of the HRTEM images in figure 5.2.2(e) and (f), respectively. Due to the quick heating procedure, it is observed that only Co diffuses out and we observe the formation of the Co-rich CoPt structure.

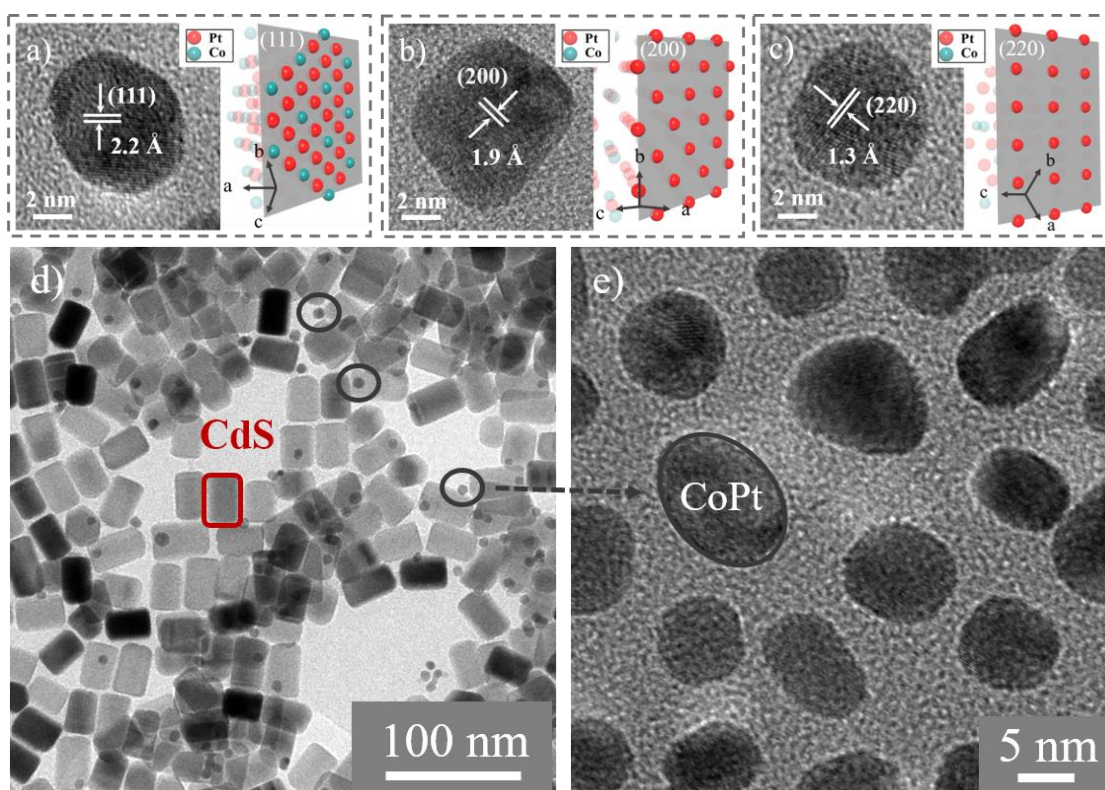


Figure 5.2.3. HRTEM showing lattice fringes for (a) (111), (b) (200), (c) (220) lattice planes exposed on surface of Pt-rich CoPt and respective atoms on these planes. TEM image of (d) overcoated system of CoPt-CdS using (e) Pt-rich CoPt seed NCs.

For example, in the current case, Pt-rich NC surfaces were synthesized and characterized by HRTEM to understand the other exposed facets. Figure 5.2.3 (a,b,c) shows the exposed planes with the d-spacing of the lattice fringes given by 2.2, 1.9, and 1.3 Å, respectively, corresponding to the (111), (200), and (220) planes. On studying the nature of these planes, we notice that all these exposed facets are largely or completely constituted by Pt atoms within the structure as shown with the respective HRTEMs. Pt on the surface can

protect the surface of NCs due to its low reactivity and diffusivity leading to the absence of overcoating.

Further, the presence of less preferred planes, rich in Pt, also hinders the heterostructure formation. This has been verified by trying to overcoat CdS on this lattice using SILAR technique, and we observe the formation of independent nuclei of CdS as well as CoPt rather than the expected core/shell structure from the TEM images shown in figure 5.2.3(d,e).

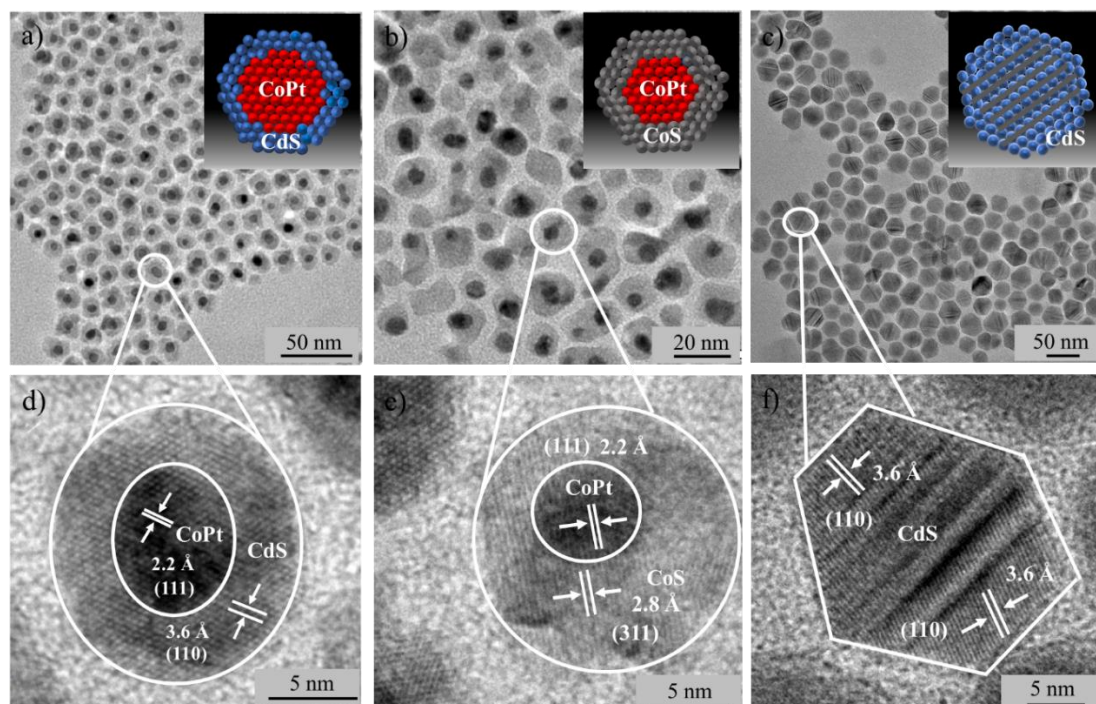


Figure 5.2.4. TEM images of (a) CoPt-CdS core-shell, (b) CoPt-CoS core-shell, (c) CoPt-CdS doped system, and their high-resolution TEM in (d), (e), (f) respectively.

Even though the core/shell heterostructures are among the most extensively studied heterostructures in the literature, there is little understanding of the factors, specifically the surface energetics leading to the formation of these heterostructures. In this case, Pt-rich facets do not result in heterostructure formation under the stated experimental conditions. The core-shell of CoPt-CdS was made from overcoating the Co-rich CoPt seed by adding elemental S in ODE directly to the reaction mixture. Sufficient care is taken to avoid independent nucleation of the secondary component by tuning the seed-to-precursor ratio and controlling the heating profile so that the concentration of the precursors was invariably well below the nucleation activation threshold. The high reactivity between the Co and S allowed S to be deposited on the surface of CoPt,²⁵ forming core/shell structured CoPt/S. The subsequent addition of the Cd or Co precursor resulted in a shell of CdS or

CoS over CoPt. TEM and HRTEM images along with the distinctive identification of the lattice spacings were used to prove the formation of core/shell hybrid structures.

Figure 5.2.4(a,b) shows the TEM images of CoPt/CdS and CoPt/CoS, while their HRTEM images are shown in figure 5.2.4(d,e), respectively. The lattice spacing for the core and the shell have been evaluated from the HRTEM micrographs and the presence of a distinctive set of fringes that could be unambiguously identified, such as the average d-spacing for the (111) plane of the CoPt core is found to be 2.2 Å, while that of CdS shell (110) plane was found to be 3.6 Å and that for the (311) plane of CoS shell to be 2.8 Å.

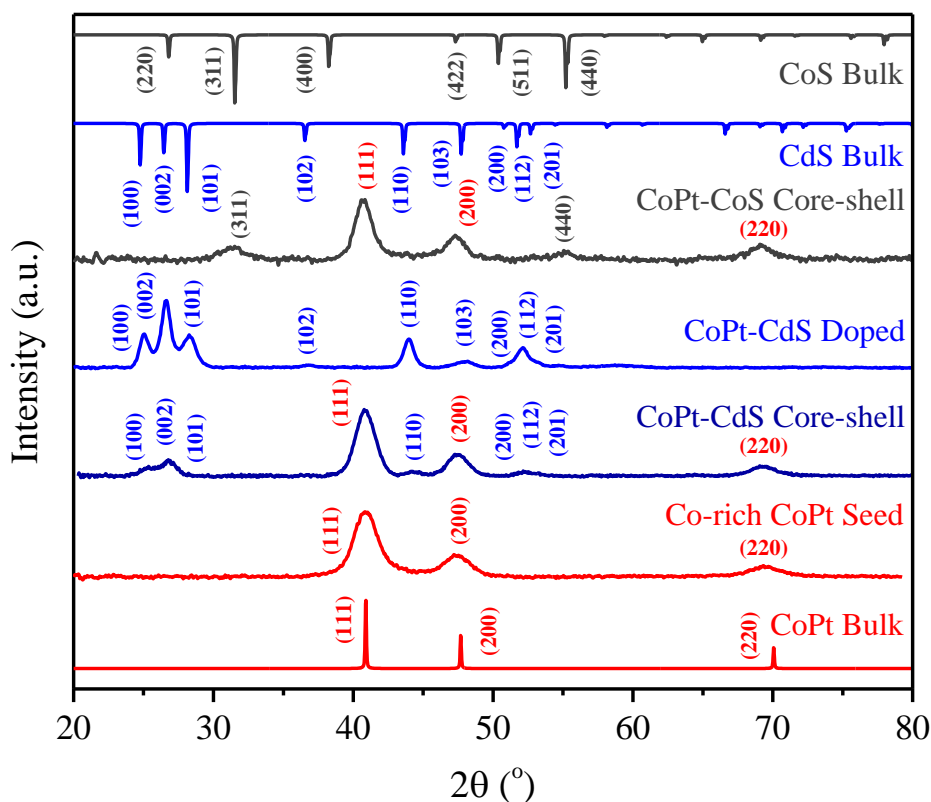


Figure 5.2.5. (a) XRD pattern of Co-rich CoPt seed, CoPt-CdS core-shell, CoPt-CdS doped system, CoPt-CoS core-shell along with bulk structures obtained from ICSD.

The lattice mismatch of CoPt/CdS is higher than that of CoPt/CoS, as manifested by the d-spacing values of planes constituting the interface, leading to faster growth of CoS in comparison to CdS under similar conditions as reflected from the HRTEM images. Additionally, the formation of core/shell particles was also evaluated from their XRD patterns as shown in figure 5.2.5 along with the bulk data obtained from the inorganic crystal structure database (ICSD).

The patterns provide evidence of both components within the NCs supporting the formation of core/shell hybrids. It should be noted here that the surface of the seed was controlled by changing the heating rate. Hence, in principle, it should be possible to have a continuous tuning of the surface. However, being a cubic lattice, the major peaks and crystal facets available for manipulating the surface are very limited. Thus, the use of any other heating rate produced a nonuniform distribution of surface facets, in between that of Pt-rich and Co-rich surfaces. Consequently, heterostructure formation on these systems was also nonuniform and is hence unsuitable for applications. Thus, we have not pursued the intermediate heating rates for manipulating the seed surface.

Further extended annealing during the synthesis led to the formation of doped NCs, where a thick shell of CdS was first grown on CoPt to increase the strain caused by the lattice mismatch at the metal-semiconductor interface. The overcoating was periodically characterized by XRD and TEM to assimilate the shell growth process. The system was then annealed for 3 h per shell allowing diffusion of the core into the shell. This process of growing a thick shell and diffusing the core out during annealing resulted in a uniform lattice with a small amount of dopant as shown in the TEM images in figure 5.2.4(c) and the HRTEM images in figure 5.2.4(f). The HRTEM images moreover reveal the existence of coherent growth defects in the doped system as shown in figure 5.2.4(f) suggesting the formation of twin boundaries. Though the identity of the CoPt core is lost due to the diffusion process, the effects of uniform distribution of magnetic ions like Co and Pt can be observed from optical, magnetic, and magneto-optical properties. ICP-OES data (table 5.2.1) also confirms the presence of Co and Pt in the doped structure. Additionally, while the XRD of the core-shell systems exhibits both CoPt and CdS/CoS characteristic peaks, the doped NCs largely show only CdS character, suggesting the absence of long-range ordering of CoPt in these NCs shown in figure 5.2.5.

The second class of heterostructures that have received minimal attention²⁷ so far is the formation of dimers, specifically with metallic nanoparticles. We purposely engineer the surface at the micro and macrolevel through synthetic control of the exposed (111) facet of CoPt so that the reactive Co atoms are exposed and can undergo further reaction. Dimer hybrids are a class of nanomaterials within which both physical and chemical properties can be tuned by controlling not only the size, shape, and composition of each NC but also the interparticle interactions. However, the reproducible formation of dimers has so far not been achieved largely due to the absence of studies understanding the factors

responsible for dimer formation. The success of dimer formation rests on the establishment of one and only one point contact with the host material. One of the ways to achieve this is to initiate a one-way flow of electrons into (out of) the host at the first point of contact leading to an electron-rich (-deficit) host that is not conducive for further overcoating as discussed in this paper.⁵

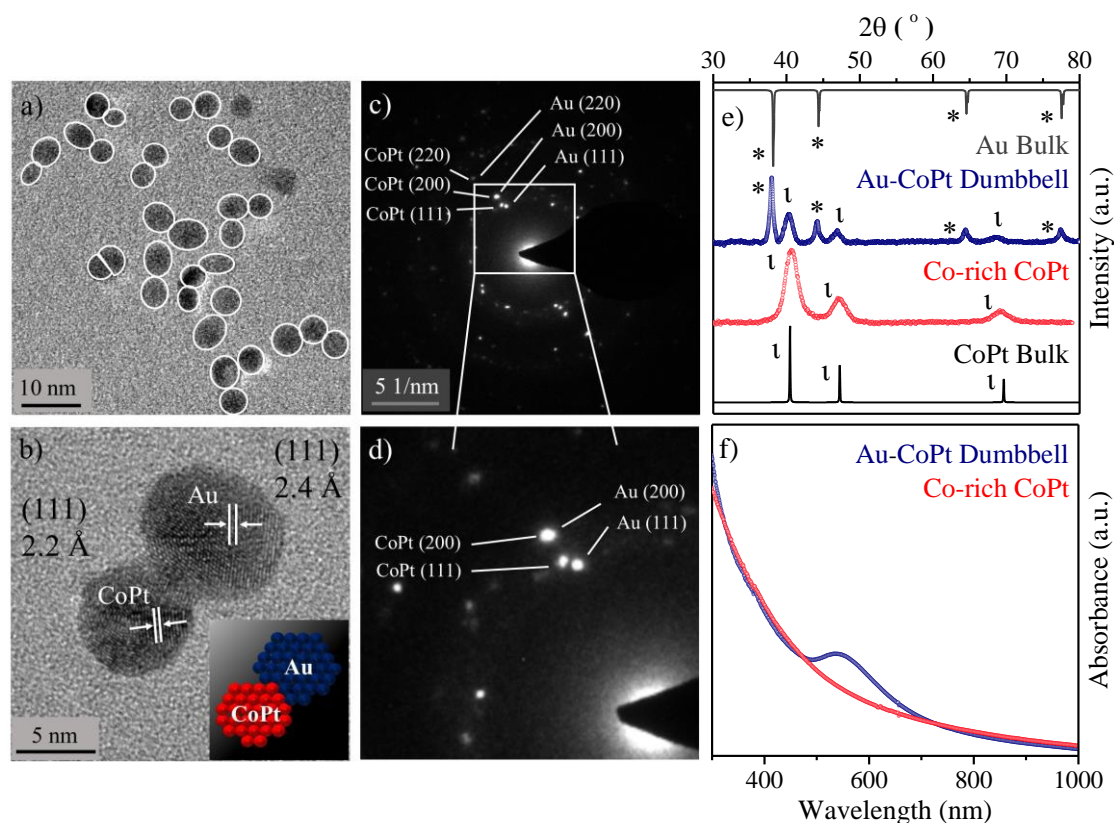


Figure 5.2.6. (a) TEM and (b) HRTEM image of dumbbell-like Au-CoPt nanoparticles, (c) ED pattern of Au-CoPt heterostructure (d) zoomed-in version of the same, (e) XRD pattern of Au-CoPt dumbbell structure, (f) UV-visible spectra of CoPt and Au-CoPt structures.

This allows for the formation of metastable nonsymmetric structures such as heterostructure dimers. Co-rich CoPt NCs are known to be electron-accepting, and hence, any metal that has ready free electrons to be donated will be a good match for the formation of dimers, like, for example, Au NCs. However, the heterostructure formation carried out in situ growth of CoPt without exposure to air does not lead to the formation of these dumbbell-like particles.

The oxidation layer of the Co, as supported by XAFS, is necessary to form these hybrids where the oxidized Co reduces the Au nanoparticles locally at the point of contact. The

next exposed plane is the (111) plane of CoPt that is favorable for the growth of Au NCs. Thus, upon receiving the free electrons from Au, CoPt facets become electron “rich”, and unsuitable for multinucleation, giving the dumbbell structure. To achieve this proposed dumbbell heterostructure, we decomposed HAuCl_4 into Au that nucleates on pre-existing CoPt NCs during the growth process. The so-formed heterostructures were characterized using the TEM images shown in figure 5.2.6(a).

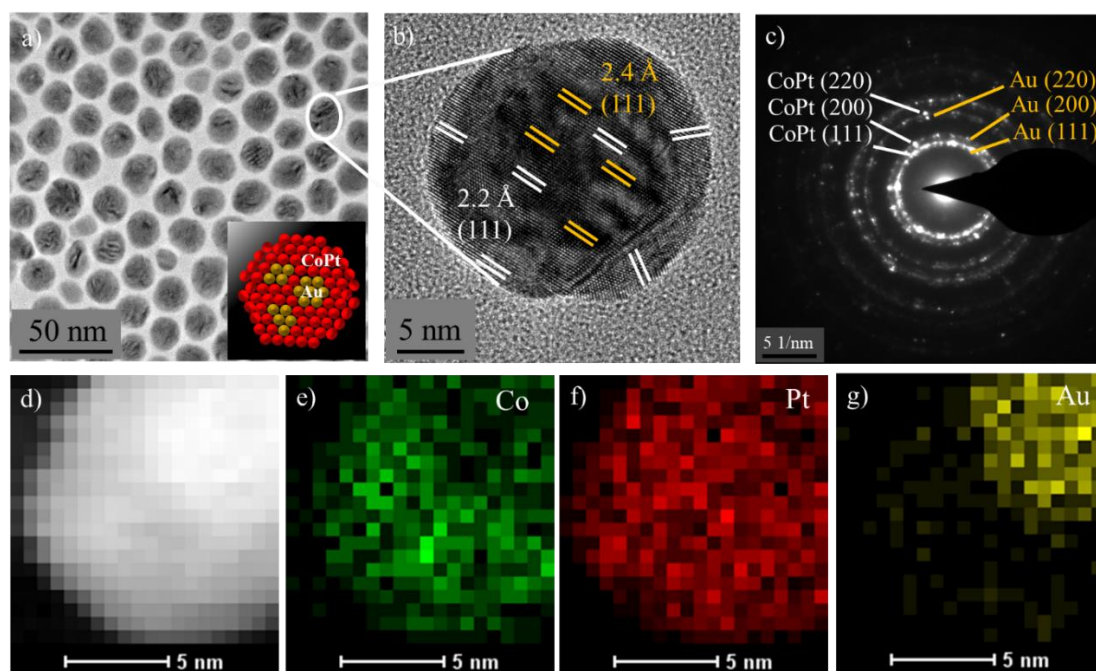


Figure 5.2.7 (a), (b) TEM and HRTEM image of embedded nanoparticles respectively, (c) ED pattern of CoPtAu embedded structure. The EDX mapping of (d) shows the spatial distribution of Co (e), Pt (f) and Au (g).

The HRTEM image of dimers with CoPt and Au show lattice fringes indicating that both particles are single crystals as shown in figure 5.2.6(b). The distance between two adjacent (111) planes of the fcc CoPt structure is measured to be 2.2 Å, while that of Au (111) planes is 2.4 Å. ED pattern shown in figure 5.2.6(c) demonstrates the presence of two different lattice planes as observed by the presence of two reflections at every spot as shown in the expanded version in figure 5.2.6(d) due to the similarity in their d-spacings. Also, the presence of spots confirms the single-crystalline nature of these particles. In XRD, the position and relative intensity of all diffraction peaks matching with standard CoPt_3 fcc and Au fcc powder diffraction data are shown in figure 5.2.6(e), indicating the phase purity of each part of the heterostructure. These heterostructure nanoparticles exhibit strong surface plasmon resonance (SPR) absorption at 545 nm as shown in figure 5.2.6(f). This red-shift of the SPR peak from the routine 520 nm ascertains the transfer of

electrons from Au to CoPt NCs at the nanocontact as documented extensively in the literature, albeit empirically, and resulting in electron deficiency in Au.^{5, 28}

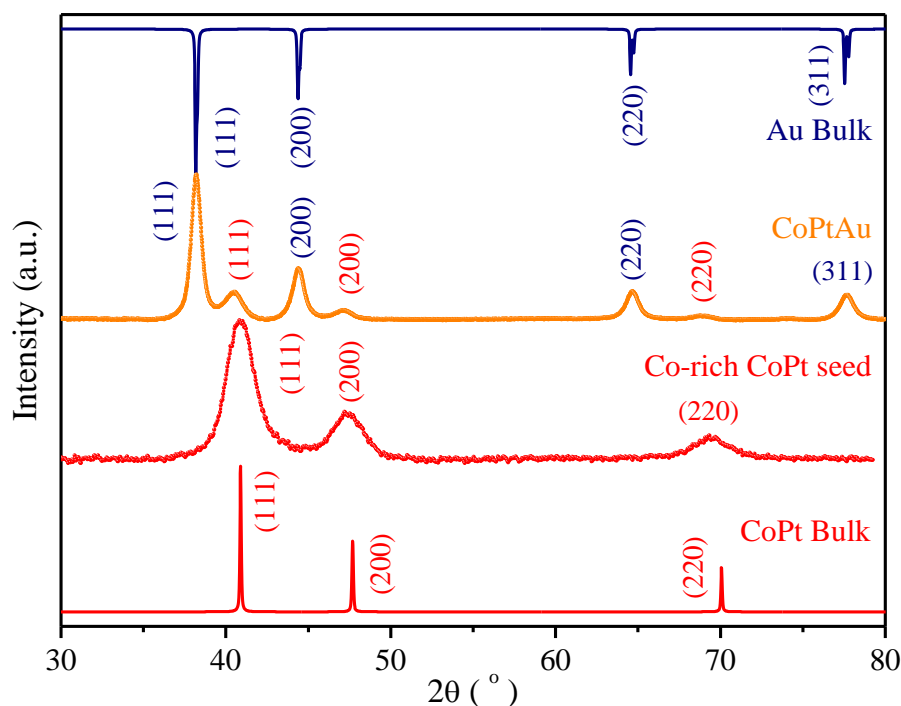


Figure 5.2.8. (a) XRD pattern of CoPtAu embedded structure along with bulk XRD structures obtained from ICSD.

Finally, using the combination of the chemistry described above as well as the understanding of surface facets obtained through this study, a more exotic heterostructure containing a solid solution of noble metal and magnetic nanoparticles with nanoislands has been synthesized wherein the surfaces can be engineered at a microlevel. To achieve a hybrid structure of CoPtAu, we aim for the simultaneous nucleation of CoPt and Au followed by the growth of a shared (111) plane. An interphase interface is created between CoPt-Au regions and propagates in the material by the stress-induced atomic organization. TEM analysis of CoPtAu heterostructure shows that Au (111) is growing along with CoPt (111), implying that it is not an intermetallic or an alloy but rather a hybrid structure.

Figure 5.2.7(a,b) shows the TEM and HRTEM images of the embedded nanoparticles, respectively, and XRD is shown in figure 5.2.8.

From HRTEM, we can see that Au epitaxially attaches to the (111) plane of CoPt through the (111) plane with a d spacing of 2.2 Å for CoPt and 2.4 Å for Au. Similar to the formation of dimers, the ED shown in figure 5.2.7(c) shows the presence of doublet in

each reflection spot demonstrating the presence of both (111) planes of CoPt and Au lattices.

To understand the distribution of the elements, we performed HAADF-STEM imaging of the embedded nanoparticles and a typical image is shown in figure 5.2.9. The inset in figure 5.2.9 shows one such image, and the elemental composition mapping (EDX) of the square marked by the “+” sign is shown in figure 5.2.7(d,e,f,g). The EDX mapping shows the spatial distribution of Co (figure 5.2.7(e)), Pt (figure 5.2.7(f)), and Au (figure 5.2.7(g)) in the embedded structure to be largely uniform within the resolution of this mapping. The important point to note here is whether they act as a large single domain structure or a multidomain particle from the optical and magnetic perspective.

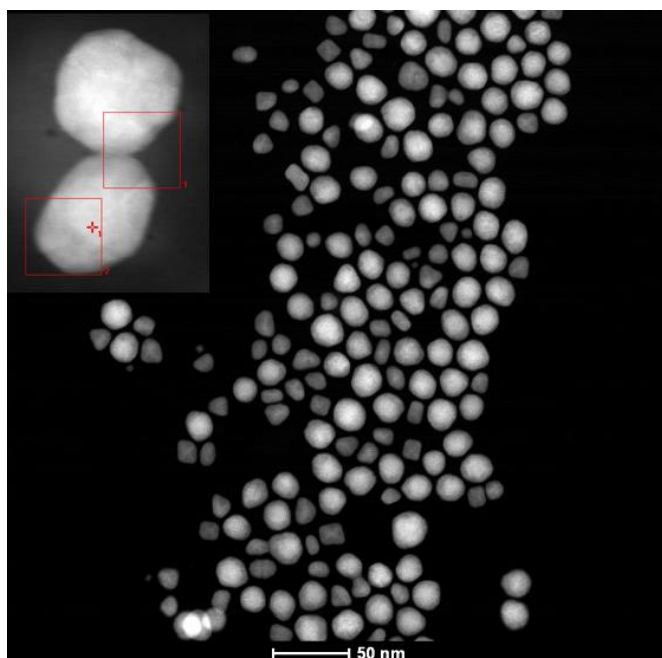


Figure 5.2.9 High angle annular dark-field scanning transmission electron microscopy (HAADF-STEM) image of the embedded nanoparticles, inset shows one such particle taken for elemental composition mapping.

These results are summarized in figure 5.2.10. Figure 5.2.10(a) shows the UV-vis spectra of CoPtAu particles, and we observe the absence of any plasmonic feature around 520 nm. This can be either due to the small size of these Au clusters that are incapable of generating collective oscillation frequency of the plasmon resonance or due to the electron deficiency on Au nanoclusters, or due to the mismatch of the refractive index when in contact with CoPt, suggesting that they indeed behave as small clusters as far as optical properties are

concerned. However, the magnetic properties of these heterostructures behave as a single domain of size of ~ 20 nm.

The magnetic hysteresis shown in figure 5.2.10(b) shows the saturation magnetization scales as a function of size suggesting that the small, discontinuous nanoclusters of CoPt and Au are indeed one unit and acts as a single domain within its magnetic structure. This is further confirmed by the temperature dependence of the magnetic cluster shown in figure 5.2.10(c). The increasing blocking temperature with increasing size has no effect by the interspersing of Au clusters within the NCs. Thus, Au clusters are acting as nano bridges between CoPt clusters.

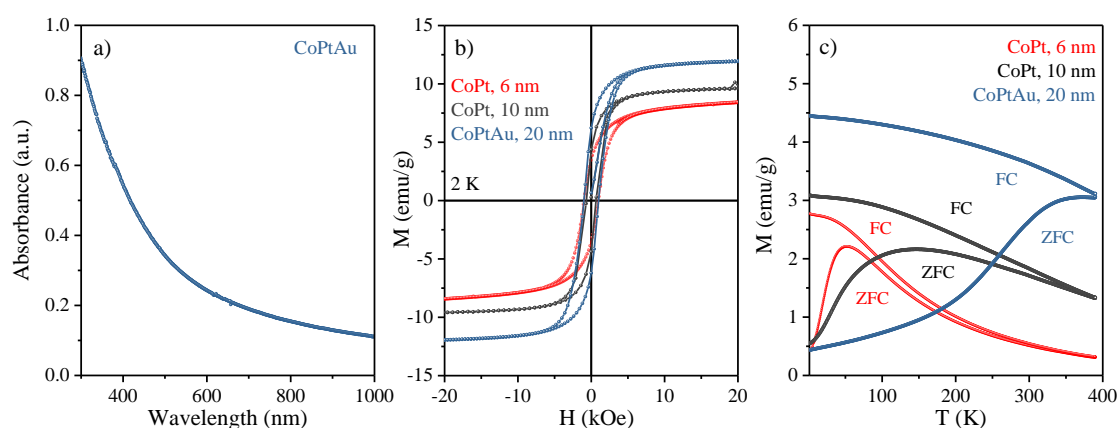


Figure 5.2.10. (a) UV-vis spectra of the CoPtAu particles, (b) magnetization (M) vs. magnetic field (H) for CoPt and CoPtAu heterostructure at 2 K. (c) Field-cooled (FC) and zero field-cooled (ZFC) for CoPt and CoPtAu heterostructure measured using 200 Oe field.

5.2.5 Conclusion

Thus, we have demonstrated the importance of surface morphology and surface energetics to stabilize the metastable structures of the heterostructures. Generally, during the crystal growth processes under equilibrium conditions, the high-energy facets diminish quickly and the crystal spontaneously evolves into a specific shape with exposed facets that minimize the total surface free energy. However, our current work reveals the importance of the role of exposed crystal facets for the nanoparticle attachment leading to suitably micro and macrolevel facet engineered nanostructures. It can be also envisioned that the creation of interface junctions between different heterostructures could be viable as a new tool to generate unprecedented properties that are distinct from those of single-component nanocrystals and their physical mixtures.

Bibliography

- (1) Liu, Y.; Stradins, P.; Wei, S. H. Van der Waals Metal-Semiconductor Junction: Weak Fermi Level Pinning Enables Effective Tuning of Schottky Barrier. *Sci. Adv.* **2016**, *2*, e1600069.
- (2) Jordan, V.; Javornik, U.; Plavec, J.; Podgornik, A.; Rečnik, A. Self-Assembly of Multilevel Branched Rutile-Type TiO₂ Structures via Oriented Lateral and Twin Attachment. *Sci. Rep.* **2016**, *6*, 24216.
- (3) Pellegrino, T.; Fiore, A.; Carlino, E.; Giannini, C.; Cozzoli, P. D.; Ciccarella, G.; Respaud, M.; Palmirotta, L.; Cingolani, R.; Manna, L. Heterodimers Based on CoPt₃- Au Nanocrystals With Tunable Domain Size. *J. Am. Chem. Soc.* **2006**, *128*, 6690-6698.
- (4) Mokari, T.; Rothenberg, E.; Popov, I.; Costi, R.; Banin, U. Selective Growth of Metal Tips onto Semiconductor Quantum Rods and Tetrapods. *Science* **2004**, *304*, 1787-1790.
- (5) Yu, H.; Chen, M.; Rice, P. M.; Wang, S. X.; White, R. L.; Sun, S. Dumbbell-Like Bifunctional Au-Fe₃O₄ Nanoparticles. *Nano Lett.* **2005**, *5*, 379-382.
- (6) Wang, C.; Xu, C.; Zeng, H.; Sun, S. Recent Progress in Syntheses and Applications of Dumbbell-Like Nanoparticles. *Adv. Mater.* **2009**, *21*, 3045-3052.
- (7) Saha, A.; Makkar, M.; Shetty, A.; Gahlot, K.; Pavan, A. R.; Viswanatha, R. Diffusion Doping in Quantum Dots: Bond Strength and Diffusivity. *Nanoscale.* **2017**, *9*, 2806-2813.
- (8) Sorokin, A. V.; Zabolotskii, A. A.; Pereverzev, N. V.; Yefimova, S. L.; Malyukin, Y. V.; Plekhanov, A. I. Plasmon Controlled Exciton Fluorescence of Molecular Aggregates. *J. Phys. Chem. C* **2014**, *118*, 7599-7605.
- (9) Cacciola, A.; Di Stefano, O.; Stassi, R.; Saija, R.; Savasta, S. Ultrastrong Coupling of Plasmons and Excitons in a Nanoshell. *ACS Nano* **2014**, *8*, 11483-11492.
- (10) de Arquer, F. P. G.; Konstantatos, G. Metal-Insulator-Semiconductor Heterostructures for Plasmonic Hot-Carrier Optoelectronics. *Opt. Express* **2015**, *23*, 14715-14723.
- (11) Saha, A.; Chellappan, K. V.; Narayan, K. S.; Ghatak, J.; Datta, R.; Viswanatha, R. Near-Unity Quantum Yield in Semiconducting Nanostructures: Structural Understanding Leading to Energy Efficient Applications. *J. Phys. Chem. Lett.* **2013**, *4*, 3544-3549.
- (12) Temnov, V. V.; Armelles, G.; Woggon, U.; Guzatov, D.; Cebollada, A.; Garcia Martin, A.; Garcia Martin, J. M.; Thomay, T.; Leitenstorfer, A.; Bratschitsch, R. Active

Magneto-Plasmonics in Hybrid Metal–Ferromagnet Structures. *Nat. Photonics* **2010**, *4*, 107.

(13) Jia, C.; Li, X.; Xin, N.; Gong, Y.; Guan, J.; Meng, L.; Meng, S.; Guo, X. Interface-Engineered Plasmonics in Metal/Semiconductor Heterostructures. *Adv. Energy Mater.* **2016**, *6*, 1600431.

(14) DuChene, J. S.; Sweeny, B. C.; Johnston Peck, A. C.; Su, D.; Stach, E. A.; Wei, W. D. Prolonged Hot Electron Dynamics in Plasmonic-Metal/Semiconductor Heterostructures with Implications for Solar Photocatalysis. *Angew. Chem. Int. Ed.* **2014**, *53*, 7887-7891.

(15) Jiang, R.; Li, B.; Fang, C.; Wang, J. Metal/Semiconductor Hybrid Nanostructures for Plasmon-Enhanced Applications. *Adv. Mater.* **2014**, *26*, 5274-5309.

(16) Yu, H.; Gibbons, P. C.; Kelton, K. F.; Buhro, W. E. Heterogeneous Seeded Growth: A Potentially General Synthesis of Monodisperse Metallic Nanoparticles. *J. Am. Chem. Soc.* **2001**, *123*, 9198-9199.

(17) Fortuna, S. A.; Li, X. Metal-Catalyzed Semiconductor Nanowires: A Review on the Control of Growth Directions. *Semicond. Sci. Technol.* **2010**, *25*, 024005.

(18) Galloway, J. M.; Talbot, J. E.; Critchley, K.; Miles, J. J.; Bramble, J. P. Developing Biotemplated Data Storage: Room Temperature Biomineralization of L10 CoPt Magnetic Nanoparticles. *Adv. Funct. Mater.* **2015**, *25*, 4590-4600.

(19) Guo, S.; Li, D.; Zhu, H.; Zhang, S.; Markovic, N. M.; Stamenkovic, V. R.; Sun, S. FePt and CoPt Nanowires as Efficient Catalysts for the Oxygen Reduction Reaction. *Angew. Chem. Int. Ed.* **2013**, *52*, 3465-3468.

(20) Wang, L. G.; Cao, Z. Y.; Qian, X.; Zhu, L.; Cui, D. P.; Li, A. D.; Wu, D. Atomic Layer Deposited Oxide-Based Nanocomposite Structures with Embedded CoPt_x Nanocrystals for Resistive Random Access Memory Applications. *ACS Appl. Mater. Interfaces* **2017**, *9*, 6634-6643.

(21) Hu, W. F.; Yuan, H. K.; Chen, H.; Wang, G. Z.; Zhang, G. L. Structural and Magnetic Properties of CoPt Clusters. *Phys. Lett. A* **2014**, *378*, 198-206.

(22) Barmak, K.; Kim, J.; Lewis, L. H.; Coffey, K. R.; Toney, M. F.; Kellock, A. J.; Thiele, J. U. On the Relationship of Magnetocrystalline Anisotropy and Stoichiometry in Epitaxial L10 CoPt (001) and FePt (001) Thin Films. *J. Appl. Phys.* **2005**, *98*, 033904.

(23) Grange, W.; Maret, M.; Kappler, J. P.; Vogel, J.; Fontaine, A.; Petroff, F.; Krill, G.; Rogalev, A.; Goulon, J.; Finazzi, M. Magnetocrystalline Anisotropy in (111) CoPt₃ Thin Films Probed by X-Ray Magnetic Circular Dichroism. *Phys. Rev. B* **1998**, *58*, 6298.

- (24) Shishidou, T.; Imada, S.; Muro, T.; Oda, F.; Kimura, A.; Suga, S.; Miyahara, T.; Kanomata, T.; Kaneko, T. Strong Fano Effect in the Magnetic Circular Dichroism of the Pt N 6, 7 Core Absorption of Ferromagnetic CoPt₃s. *Phys. Rev. B* **1997**, *55*, 3749.
- (25) Makkar, M.; Saha, A.; Khalid, S.; Viswanatha, R. Thermodynamics of Dual Doping in Quantum Dots. *J. Phys. Chem. Lett.* **2019**, *10*, 1992-1998.
- (26) Ravel, B.; Newville, M. ATHENA, ARTEMIS, HEPHAESTUS: Data Analysis for X-Ray Absorption Spectroscopy Using IFEFFIT. *J. Synchrotron Radiat.* **2005**, *12*, 537-541.
- (27) Debangshi, A.; Thupakula, U.; Khan, A. H.; Kumar, G. S.; Sarkar, P. K.; Acharya, S. Probing Local Electronic Structures of Au–PbS Metal–Semiconductor Nanodumbbells. *ACS Appl. Nano Mater.* **2018**, *1*, 2104-2111.
- (28) Daniel, M.-C.; Astruc, D. Gold Nanoparticles: Assembly, Supramolecular Chemistry, Quantum-Size-Related Properties, and Applications Toward Biology, Catalysis, and Nanotechnology. *Chem. Rev.* **2004**, *104*, 293-346.

CHAPTER 6

Probing the Effect of Clustering of Dopants on
Magnetic and Magneto-Optical Properties of
Nanocrystals.

Part A. Probing the Effect of Clustering of Dopants on Magnetic and Magneto-Optical Properties of Co, Pt co-doped CdS Nanocrystals.

6.1 Summary

Clustering of magnetic impurities has been well established as a deterrent to observe magnetic behavior in doped semiconductors. However, clustering in most cases has been random and irreproducible. Hence the microscopic origin of these effects has so far not been established. In this chapter, we have systematically obtained clustered and uniformly diffused CoPt/CdS nanocrystals to study the effect of clustering on the magnetic and magneto-optical properties of nanocrystals. The low magnetic and magneto-optical response has been attributed to the clustering of dopants within the host lattice. It is further confirmed that the properties within the diffused nanocrystals arise due to exchange interactions of the entire system including the non-magnetic host and not just due to the magnetic dopants. Thus, the effect of microscopic features arising due to clustering of magnetic impurities in doped semiconductors have been studied and the generality has been established by performing a similar study on FePt/CdS nanocrystals.

6.2 Introduction

Multicomponent hybrid nanocrystals (NCs) like the heterostructures and/or doped NCs have become increasingly explored and are actively pursued for multifunctional tunable properties including optical, electrical, magnetic and magneto-optical properties. The introduction of spin in addition to charge has been a promising way to introduce a new dimension to existing charge-based electronic devices. Along these lines, one class of compounds, namely, magnetic materials within semiconducting materials have shown immense potential in various applications. For example, NCs of magnetic CoPt and FePt alloys are among the candidates for applications in ultra-high density storage devices due to their large uniaxial anisotropy and high chemical stability.¹⁻³ Composites of these NCs with CdS have been integrated into different forms like heterodimers,⁴ fluorescent–magnetic core/shell,⁵ multifunctional NCs for multicolor labeling in biomedicine⁶ and other similar multifunctional properties. Talapin *et al.*⁷ reported the formation of a magnet in a semiconductor which is known to show a large magnetoresistance with the control of spin having important applications in magnetic storage. However, one aspect that is not addressed within this class of materials is the distribution of magnetic ions at the interface and within the non-magnetic lattice. However, recent literature⁸⁻¹⁰ has shown that the lines

between the heterostructure NCs with discrete domains of individual materials and hence different properties within the same structure and that of alloyed materials leading to new synergistic properties specific to the alloy materials have become vanishingly thin. Studies have shown that many of the critical properties are determined by the nature of the interface not only in bulk but also in NCs.^{9, 11-13} Nanocrystals of these materials along with their interface dependent properties have also been studied extensively in literature^{8, 10, 12} as the dopant-induced cooperative effects are also accompanied by the quantum confinement effects. This leads to enhanced effects due to the better overlap of the dopant and host orbitals¹⁴ as well as the size and shape-tuneable properties. Hence it is important to study the nature of the interface in these hybrid functional NCs.

One such stark example of an interface-driven application in CoPt/CdS system is the *sp-d* exchange interactions with potential applications in transmitting and processing quantum information. Chemically ordered bimetallic magnets like CoPt and FePt are known to possess high magnetic anisotropy energy. This property is known to give rise to promising ultrahigh density magnetic storage applications¹⁵⁻¹⁶ and is widely studied for CoPt/CdS and FePt/CdS systems. The other end of the spectrum, wherein we observe a complete lack of an interface between the magnetic and semiconducting material, includes the dilute magnetic semiconductors (DMS).¹⁷⁻¹⁹ Here a fraction of non-magnetic sites are replaced with their magnetic counterparts leading to large spin-dependent properties that can be amplified in the presence of a magnetic field and are thus considered to be potential candidates for storing, transmitting and processing quantum information and invoked a great deal of interest in the research community. Potential desired properties in these materials include properties like giant Zeeman splitting,²⁰⁻²¹ magnetic polaron,²² carrier induced magnetic ordering,²³ electrical spin polarization, magnetically tunable lasing, zero-field magnetizations.²⁴ Devices like spin valves and spin-based LEDs etc. are the corollary of the same. Unique magneto-optical²⁵ and magneto-transport²⁶ properties associated with exchange interactions between the dopant and the host have been studied in these materials. All these functionalities are derived from the exchange interaction between the host and the dopant orbitals well known to be *sp-d* exchange interactions.

Interest in these tremendously varying potential applications of the materials with fine-tuned interface warrants the enormous efforts⁹⁻¹⁰ that are already invested to synthesize and study hybrid semiconductor NCs. However, the major caveat for the success of these materials is the lack of characterization techniques to study their nature at the interface. It

is often difficult and indirect to observe the presence or absence of a hard interface at the junction of two materials. Nevertheless, to understand the origin and nature of magnetic properties clearly, the presence or the arrangement of these magnetic clusters forming the secondary phase and/or interaction of the magnetic dopant with the host semiconductor needs to be identified. Pioneering ab initio calculations by van Schilfgaarde and Mryasov²⁷ as well as others²⁸ have also revealed a particularly strong tendency of doped semiconductors to form non-random alloys and also doping is very hostile in quantum-confined semiconductors and transition metal dopants try to form energetically favorable clusters.¹⁷ Such a study is envisaged in this work and the magnetic and magneto-optical properties as a function of uniformity of doping are discussed.

In this work, we report the direct observation of the effect of clustered as well as diffused magnetic islands/dopant ions in the quantum confined regime. We have systematically controlled the degree of clustering, keeping size and other parameters similar, leading to an understanding of the effects of small magnetic islands of transition metal (TM) dopants on various properties. The magnetic properties of the clustered and diffused NCs were also compared with core only NCs of similar sizes. Temperature and field-dependent magnetic studies have been performed to get more insight into the magnetic behavior of these NCs. Signatures of *sp-d* exchange interactions are observed experimentally through the field and temperature-dependent magnetic circular dichroism (MCD) studies. It is interesting to note that the diffused NCs show better magnetic and magneto-optical properties as compared to the clustered counterparts suggesting the presence of magnetic exchange interactions between the host material and the dopant atoms. The hypothesis for the observation of these effects related to controlled aggregation and distribution of magnetic ions has been proposed.

6.3 Experimental section

The MPt (M = Co, Fe) NCs were synthesized using colloidal synthesis that produced monodisperse NCs. This was further overcoated with CdS matrix using successive ionic layer adsorption and reaction (SILAR) technique to get clustered and diffused NCs by diffusion doping method wherein the idea of self-purification of the magnetic core inside CdS host was utilized to synthesize these uniformly doped NCs.

Chemicals used. Cobalt acetylacetonate (Co(acac)₂), iron pentacarbonyl (Fe(CO)₅), platinum acetylacetonate (Pt(acac)₂), 1,2-hexadecanediol, cadmium oxide (CdO), oleic

acid (OA, 90%), 1-octadecene (ODE, 90%), oleylamine (OlAm, technical grade 70%), and sulfur powder (S, 99.5%) were purchased from Sigma Aldrich. All purchased chemicals were used without further purification. Ethanol, acetone and hexane were purchased from Merck (Emparta). All solvents were used without further purification.

Synthesis. FePt NCs. The FePt core was synthesized by thermal decomposition of iron pentacarbonyl ($\text{Fe}(\text{CO})_5$), and reduction of platinum acetylacetonate ($\text{Pt}(\text{acac})_2$) using 1,2-hexadecanediol at high temperature. Oleic acid and oleylamine were used as coordinating agents and solvents. For the synthesis, 0.1 mmol of $\text{Pt}(\text{acac})_2$, 0.3 mmol of 1,2-hexadecanediol were taken in a three-necked round bottom flask. 2 mL of oleic acid and 6 mL of oleylamine were added to it followed by the addition of 0.3 mmol of iron pentacarbonyl ($\text{Fe}(\text{CO})_5$) under vacuum. The system was degassed at 80 °C for two hours under constant stirring. The temperature was raised to 200 °C after degassing and kept under constant argon flow. After 10 min the temperature of the reaction mixture was raised to 300 °C gradually (10 °C/3 min). After attaining the temperature, the reaction mixture was kept at 300 °C for 10 min and then cooled down to room temperature. Then, the as-synthesized NCs were isolated by centrifugation, washed one time by the addition of ethanol-hexane mixture and a few drops of acetone, and used for the further synthesis of clustered and diffused NCs. **CoS NCs.** CoS NCs were synthesized using cobalt acetylacetonate (0.05 mmol) and S-powder (0.05 mmol). Precursors were dissolved in 4 mL oleylamine and 1 mL oleic acid in a three-necked round bottom flask. The system was degassed at 80 °C for two hours under constant stirring. The temperature was raised to 200 °C after degassing and kept under constant argon flow. After 10 min the temperature of the reaction mixture was raised to 250 °C gradually (10 °C/3 min). After attaining the temperature, the reaction mixture was kept at 250 °C for 20 min and then cooled down to room temperature. The black precipitate was isolated by centrifuging and was then washed twice by hexane, ethanol and a few drops of acetone. The as-synthesized NCs were then used for further synthesis of doped NCs. **CoPt NCs** were synthesized via co-reduction of metal salts cobalt acetylacetonate and platinum acetylacetonate. For the synthesis of **clustered MPt/CdS NCs**, SILAR technique was followed. Overcoating was performed by the cyclic addition of S precursor followed by Cd precursor and was continued until the required thickness of CdS shell was formed over the core MPt NCs. In order to synthesize **diffused MPt/CdS NCs**, we annealed the system at high temperature for a long time after the growth of a few nanometers of shell thickness. Again, few layers of CdS were grown and the annealing procedure was continued to get diffused NCs, (detailed

synthesis procedure for CoPt core, MPt/CdS clustered and diffused system is discussed in chapter 5). **Co doped CdS NCs.** Approximately 20 mg of presynthesized CoS NCs dissolved in 3 mL oleylamine, were taken in a three-necked round bottom flask and 6 mL of ODE was added to it. The system was degassed at 80 °C for 2 hours under constant stirring. After degassing, the reaction temperature was raised to 250 °C under argon flow. Overcoating was started with the addition of a stoichiometric amount of S-precursor i.e. S-ODE and was kept for 20 min. After 20 min the same amount of Cd precursor, cadmium oleate was injected into the system and annealed for 30 min. The cyclic addition of S precursor followed by Cd precursor was continued until an ultra-thick shell of CdS was formed over the core NCs. System was annealed at 250 °C to diffuse the core into the CdS lattice. The reaction was stopped at the required thickness of the CdS shell. Aliquots were collected in between. The samples were washed by centrifugation using hexane-ethanol mixture and a few drops of acetone.

Characterization. DC magnetic measurements were carried out in a superconducting quantum interference device that employs the technique of vibrating sample magnetometer (SQUID-VSM) (Magnetic Property Measurement System MPMS-3, Quantum Design, U.S.). Few milligrams of the sample was packed in a piece of Teflon for the measurement. M vs H measurements were carried out at 2 K. FC and ZFC measurements were performed for the temperature range of ~ 2 K to 390 K using a 200 Oe constant magnetic field. The sample was first cooled from 400 K (above the ordering temperature of the sample) to 2 K in the absence of an external magnetic field. With heating, magnetization data was recorded in the field strength of 200 Oe (ZFC measurement). In the FC measurement, the sample was cooled in the presence of a magnetic field of 200 Oe. The magnetization was then recorded with a temperature up to 390 K in the presence of an applied field.

For the MCD experiments, the wavelength-tunable light source is based on a 50 W xenon lamp and a monochromator (LOT Oriel Omni- λ 150, 1200 grooves/mm grating blazed at 500 nm). The modulation between right and left circularly polarized light at a frequency of 50 kHz is realized using a combination of a linear polarizer and a photoelastic modulator (PEM 90, Hinds Instruments). The cryostat (ST-300, Janis) is placed between two poles of an electromagnet (EM4-HVA, Lake Shore) in Faraday geometry and a photomultiplier (R928, Hamamatsu) detects the transmitted light. The dc (ac) component

of the optical signal is read out using an HP 34401A multimeter (lock-in amplifier Signal Recovery 7225 DSP).

6.4 Results and discussion

6.4.1 Magnetic properties

CoPt core, clustered and diffused NCs were studied for magnetic and magneto-optical properties. The extent of clustering was characterized through XRD, TEM, STEM-EDS, EXAFS as discussed in chapter 5. In this chapter, we study the effect of the same on the magnetic and magneto-optical properties of these materials.

Core. CoPt core NCs are known to be magnetic and is substantiated by the M vs H curves, with a coercivity of 976 Oe at 2 K, as shown in figure 6.1(a). The field cooled (FC) and zero-field cooled (ZFC) magnetization plots obtained using 200 Oe magnetic field as a function of temperature (figure 6.1(b)) show that the particles achieve a blocked state below 52 K.

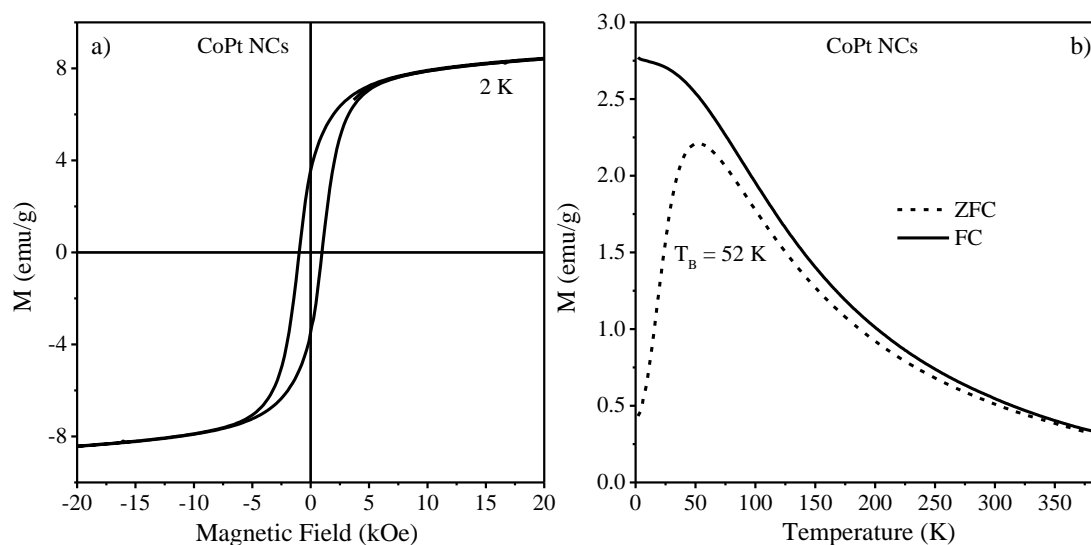


Figure 6.1. Magnetization vs. field plot for CoPt NCs at 2 K. Inset shows FC and ZFC for the same measured using 200 Oe field.

Clustered and diffused NCs. The plot of magnetization versus applied field (M vs H) for clustered and diffused NCs is shown in figure 6.2. Surprisingly, the saturation magnetization for the clustered NCs is much higher (3 emu/g) as compared to the diffused NCs (1.2 emu/g) as shown in figure 6.2, suggesting the absence of any effect on the magnetic properties due to clustering at first glance. However, it should be noted that this

is not a fair comparison due to the huge difference in the magnetic ion concentration ranging from 37.8% in the clustered NCs to 5.8% in the diffused NCs, even though the NCs have similar sizes. Therefore, to compare the magnetic behavior of these NCs, the magnetic ion percentage normalized magnetization for the similar size clustered and diffused NCs is plotted in figure 6.3(a). Figure 6.3 shows the magnetization vs applied field (M vs H) and magnetization as a function of temperature (M vs T) plots of clustered and diffused NCs of similar and different sizes. Here, consistent with the absence of clustering as obtained from EXAFS studies in chapter 5, the diffused NCs show a higher value of saturation magnetization (0.21 emu/g/CoPt) in comparison with the clustered NCs (0.08 emu/g/CoPt) at 2 K. The coercivity is observed to be ~ 1000 Oe in both cases.

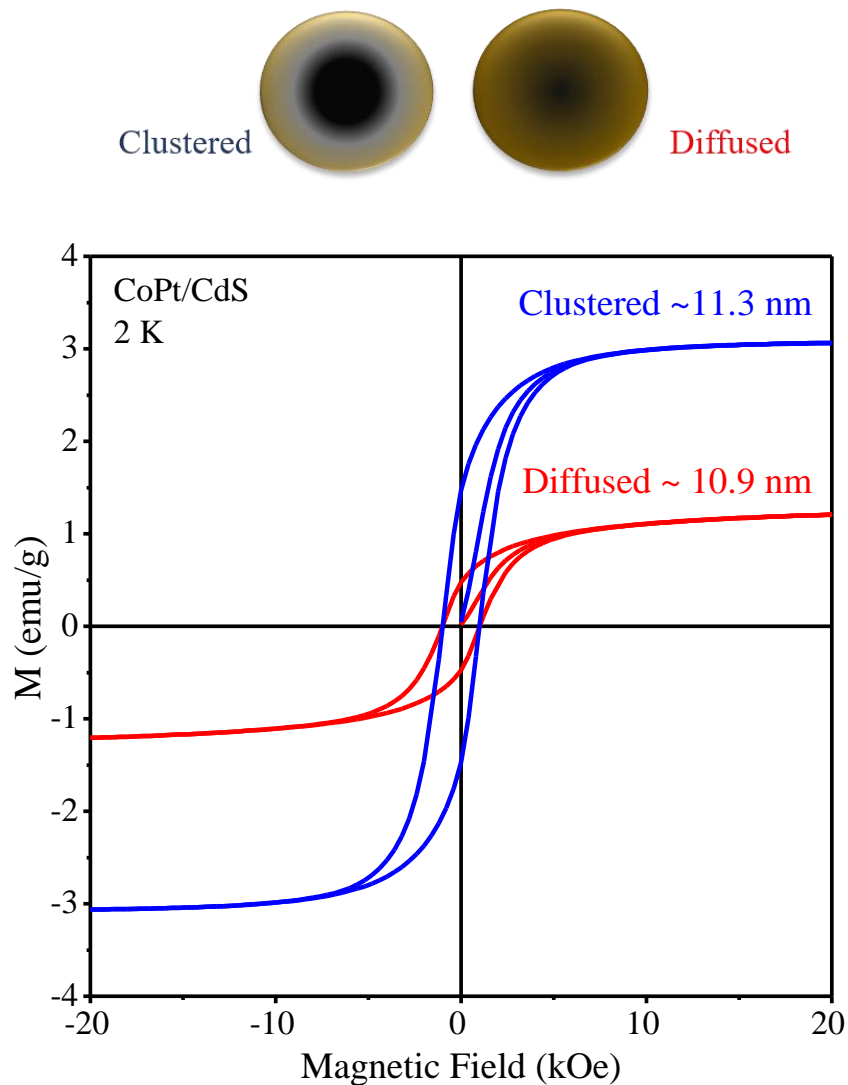


Figure 6.2. A comparison of magnetization vs. field plot for clustered and diffused NCs at 2 K.

Further, the temperature dependence of DC susceptibility was used to determine the blocking temperature by measuring zero-field cooled (ZFC) and field-cooled (FC) magnetization curves as shown in figure 6.3(b). The blocking temperatures (T_B) were determined from the peak of the ZFC curve. The FC and ZFC curves show that the clustered and the diffused NCs get into the blocked state below 50 K and 57 K respectively. The diffused NCs show higher or comparable blocking temperature compared to the clustered counterparts. This suggests that the magnetism arises mainly from the ferromagnetic CoPt core in the clustered NCs while the shell is non-magnetic.

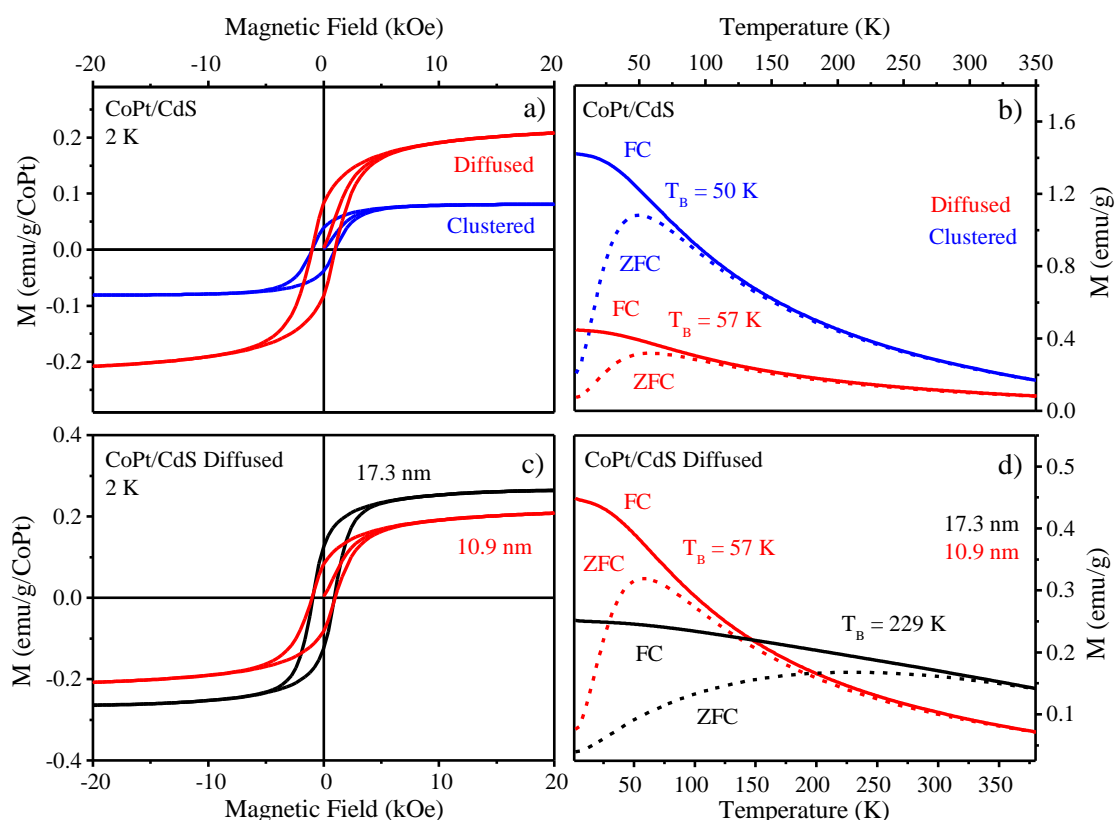


Figure 6.3. (a) A comparison of percentage normalized magnetization vs. magnetic field for clustered and diffused NCs at 2 K. (b) FC (solid line) and ZFC (dotted line) for CoPt/CdS clustered and diffused NCs measured using 200 Oe field. (c) A comparison of magnetization vs. magnetic field as a function of size for diffused NCs at 2 K. (d) FC (solid line) and ZFC (dotted line) plots for CoPt/CdS diffused NCs of different sizes measured using 200 Oe field.

However, in the case of diffused NCs, non-magnetic Cd is assisting in the process with the entire size of the NCs being involved in the magnetic activity and thereby leading to an effective increase in the size of the magnetic domain. To further establish this point,

we prepared diffused NCs of 10.9 nm and 17.3 nm arising from similar cores and the magnetic ion concentration normalized M vs H plots are shown in figure 6.3(c). As expected, we observe that the corresponding saturation magnetization is shown to scale with the size of the NCs consistent with the larger domain size. Similarly, the FC and ZFC measurements show that the larger particles remain in the blocked state up to 229 K as shown in figure 6.3(d), unlike the smaller ones that show a blocking temperature of only 57 K.

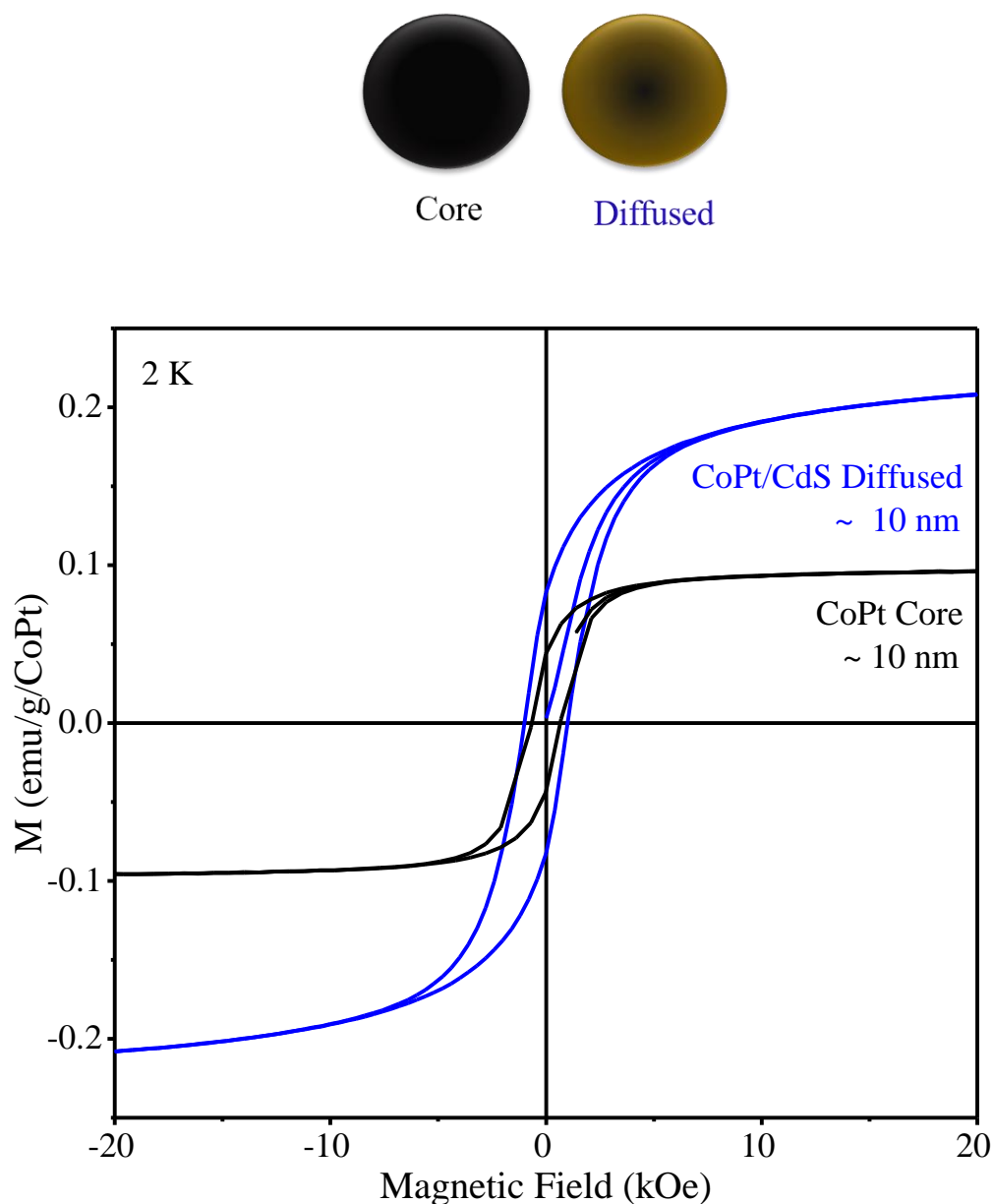


Figure 6.4. A comparison of magnetization vs. field plot for ~10 nm CoPt core, CoPt/CdS diffused NCs at 2 K.

From all these data, it appears that these uniformly diffused NCs behave like complete magnetic domains. The large-sized magnetic domain shows higher saturation magnetization than the smaller ones due to a significant change in domain size with the size of the NCs leading to large changes in magnetization.

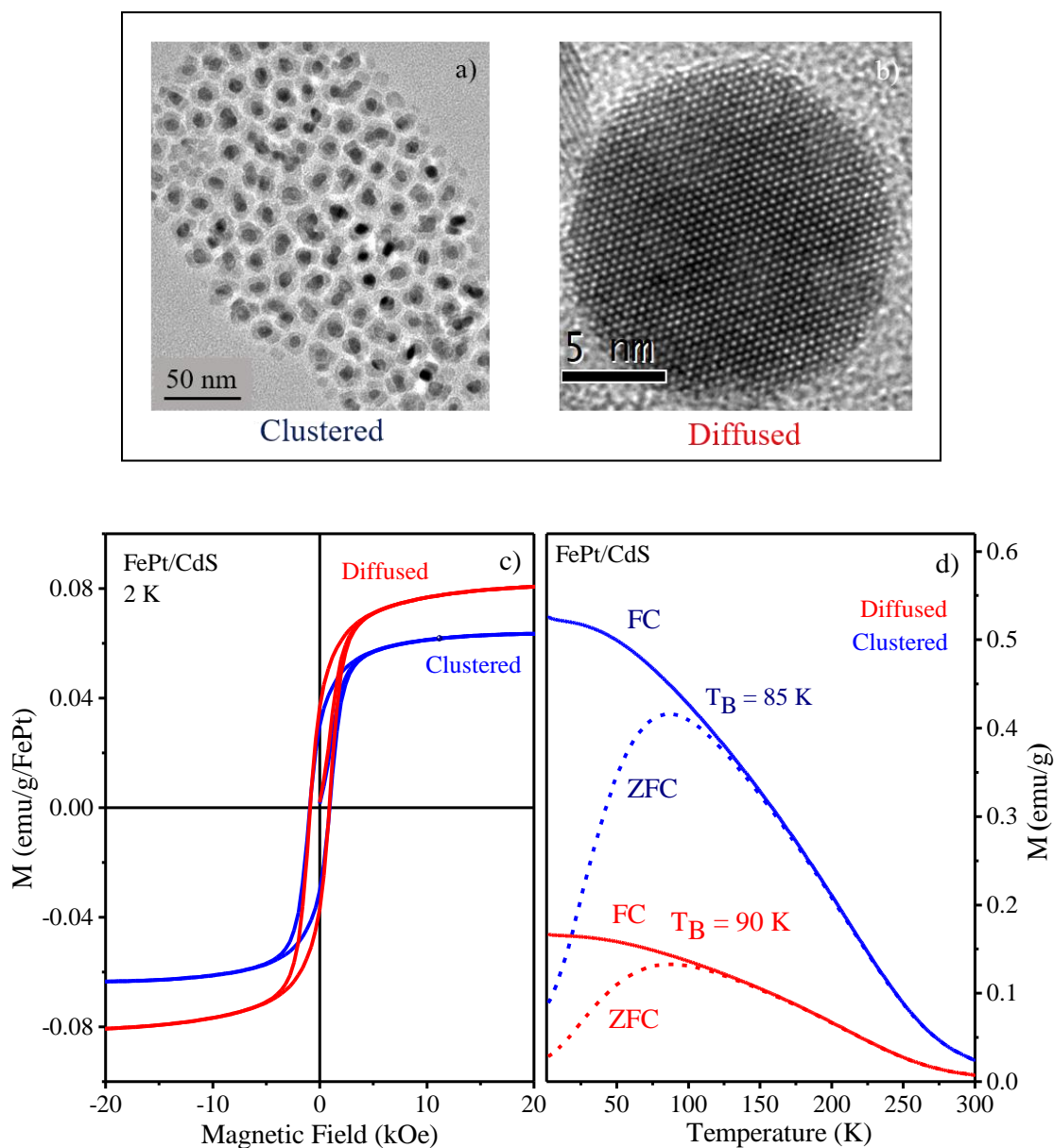


Figure 6.5. TEM image of (a) FePt/CdS clustered, (b) FePt/CdS diffused system. (c) A comparison of magnetization vs. magnetic field for FePt/CdS clustered and diffused NCs at 2 K. (d) FC (solid line) and ZFC (dotted line) for FePt/CdS clustered and diffused NCs measured using 200 Oe field.

These results provide experimental evidence for the involvement of Cd in assisting the magnetic ordering of transition metal dopants confirming the existence of intrinsic ferromagnetism due to doping and not clustering.

Core and diffused NCs. To understand the role of non-magnetic CdS on the magnetic properties, we prepared a large core similar to the size of the diffused NCs. The magnetization of the same in comparison with the diffused NCs of similar size is shown in figure 6.4. It is interesting to note that, M vs. H hysteresis loop for the diffused NCs show higher saturation magnetization than even the core only NCs of similar size at 2 K, suggesting the presence of host-dopant interactions.

FePt/CdS NCs. Similar studies were performed on FePt/CdS NCs to prove the generality and universality of this technique. FePt core was synthesized and overcoated with CdS shell and annealed at high temperature for a long time to get clustered and diffused NCs as discussed previously. Annealing these clustered NCs at high temperature for a long time allows the core to uniformly diffuse inside the CdS host to get a homogeneously doped system. Here, the average particle sizes for clustered and doped NCs are 19.3 and 18 nm respectively as calculated from TEM images (figure 6.5 (a) and (b)), and their respective magnetic ion percentage is found to be 20% and 5% as obtained from ICP-OES.

FePt/CdS NCs show a similar magnetic response as obtained for the CoPt/CdS NCs and is demonstrated in figure 6.5. The M vs H hysteresis curve has been shown in figure 6.5(c) demonstrates that the diffused NCs show a higher value of saturation magnetization (0.08 emu/g/FePt) than the clustered NCs (0.06 emu/g/FePt) at 2 K. The higher magnetization value in the diffused NCs implies the presence of exchange interactions through the non-magnetic CdS lattice, while in the case of clustered NCs, the magnetic contribution comes primarily from the much smaller magnetic core, similar to the CoPt/CdS case. M vs T measurement of the NCs demonstrates the presence of a blocking temperature of 88 K for both clustered and diffused NCs as shown in figure 6.5(d).

6.4.2 Ligand field transitions

Further, we measured the absorption of these samples in highly concentrated dispersions to be able to probe the Co^{2+} ligand field transitions (LFT). No well-defined absorption feature can be observed in the CoPt core or the CoPt/CdS clustered system in the wavelength range between 600 and 850 nm. However, in the diffused case, the expected

signature of ligand field transitions related to Co^{2+} ions tetrahedrally coordinated by S^{2-} anions are present (features between 670 and 750 nm) as shown in figure 6.6. A direct comparison with literature²⁹ shows that the peak maxima observed in diffused case coincide with the literature report for bulk $\text{Co}^{2+}:\text{CdS}$. This allows us to conclude, that Co^{2+} is indeed incorporated into the CdS shell, having $\text{Co}(\mu_4\text{-S})_4$ coordination geometry for the diffused system, unlike the clustered case.

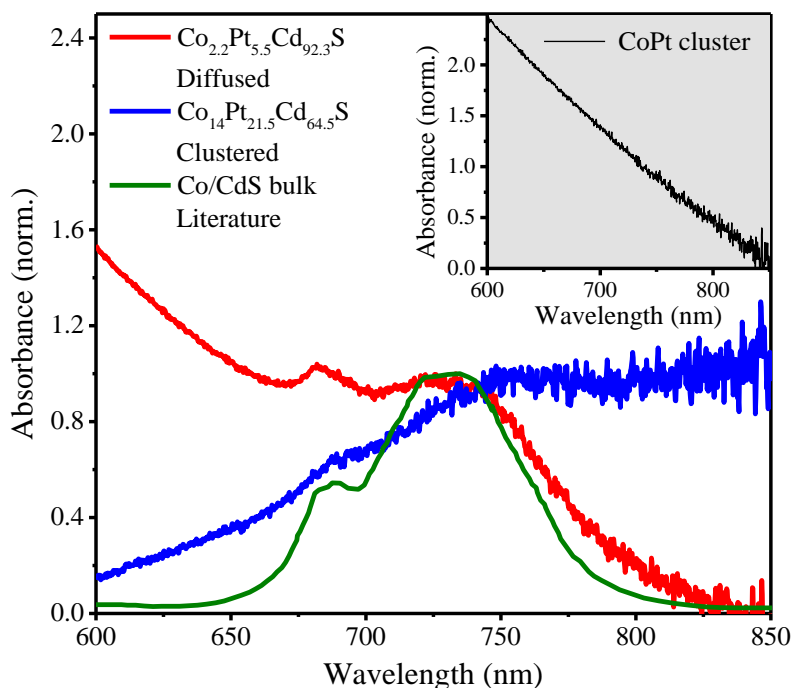


Figure 6.6. Normalized absorption spectra depicting the Co^{2+} ligand field transitions of CoPt cluster, CoPt/CdS clustered and diffused system. Literature data measured on bulk $\text{Co}^{2+}:\text{CdS}$ is included for comparison.

6.4.3 Magneto-optical properties

Since Co and/or Pt are expected to be uniformly diffused inside the CdS matrix, the presence of these magnetic ions in the semiconductor host can lead to several unusual magnetic properties. This may be due to the interaction of the magnetic ions with band electrons and holes as well as to the exchange interaction between individual magnetic ions themselves or between two different dopants. This direct correlation between the architecture of these systems and their magnetic properties gives evidence of magnetic exchange interactions happening in these systems assisted by the local environment. The results presented here show that these diffused NCs can be potential candidates for magneto-optical studies. Thus, we have studied the presence of *sp-d* exchange interactions

between the dopants and the band charge carriers in Co, Pt doped CdS using absorption-based magnetic circular dichroism technique.

Clustered and diffused NCs. Figure 6.7 shows the MCD spectra for the clustered and diffused system measured at 5.5 K and 1.63 T. Two features were observed; namely the excitonic absorption at higher energies ($\lambda < 550$ nm) and Co^{2+} ligand-field transitions at lower energies ($650 \text{ nm} < \lambda < 800 \text{ nm}$).

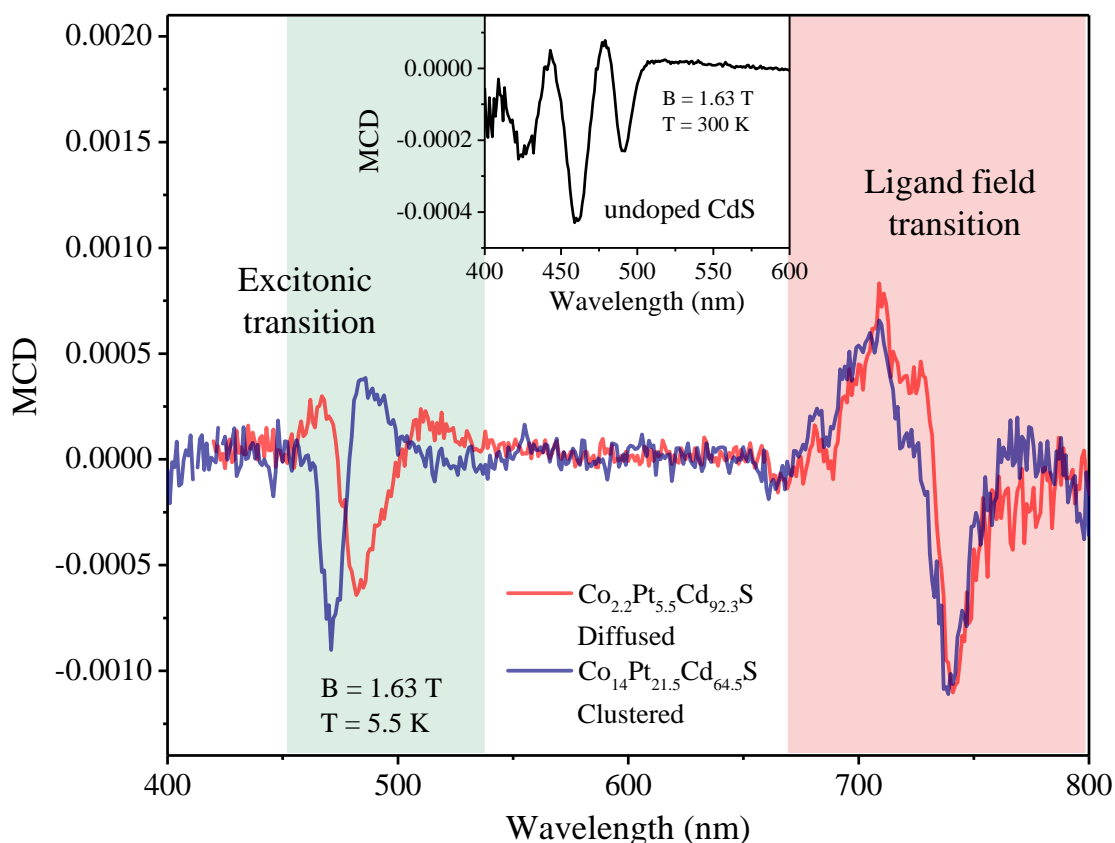


Figure 6.7. MCD spectrum of undoped (inset) measured in dispersion at $T = 300$ K and $B = 1.63$ T. MCD spectra of clustered and diffused system at $T = 5.5$ K and $B = 1.63$ T depicted in blue and red respectively with features related to the excitonic transition (blue) and the Co^{2+} ligand-field transition (red).

The MCD signal of the excitonic transition of lowest energy measured exhibits a positive feature for the undoped CdS as shown in the inset to the figure 6.7 while the sign is reversed for the Co, Pt doped NCs similar to literature reports on Co doped CdS²⁹ suggesting the presence of strong exchange interaction in these systems. Since the intrinsic Zeeman splitting is temperature independent, the undoped system can be directly compared to the results obtained on the clustered and doped systems at low temperatures.

The inverted polarities at the band edge for clustered and diffused NCs relative to undoped NCs observed in the MCD data prove the incorporation of Co and Pt into the CdS lattice.

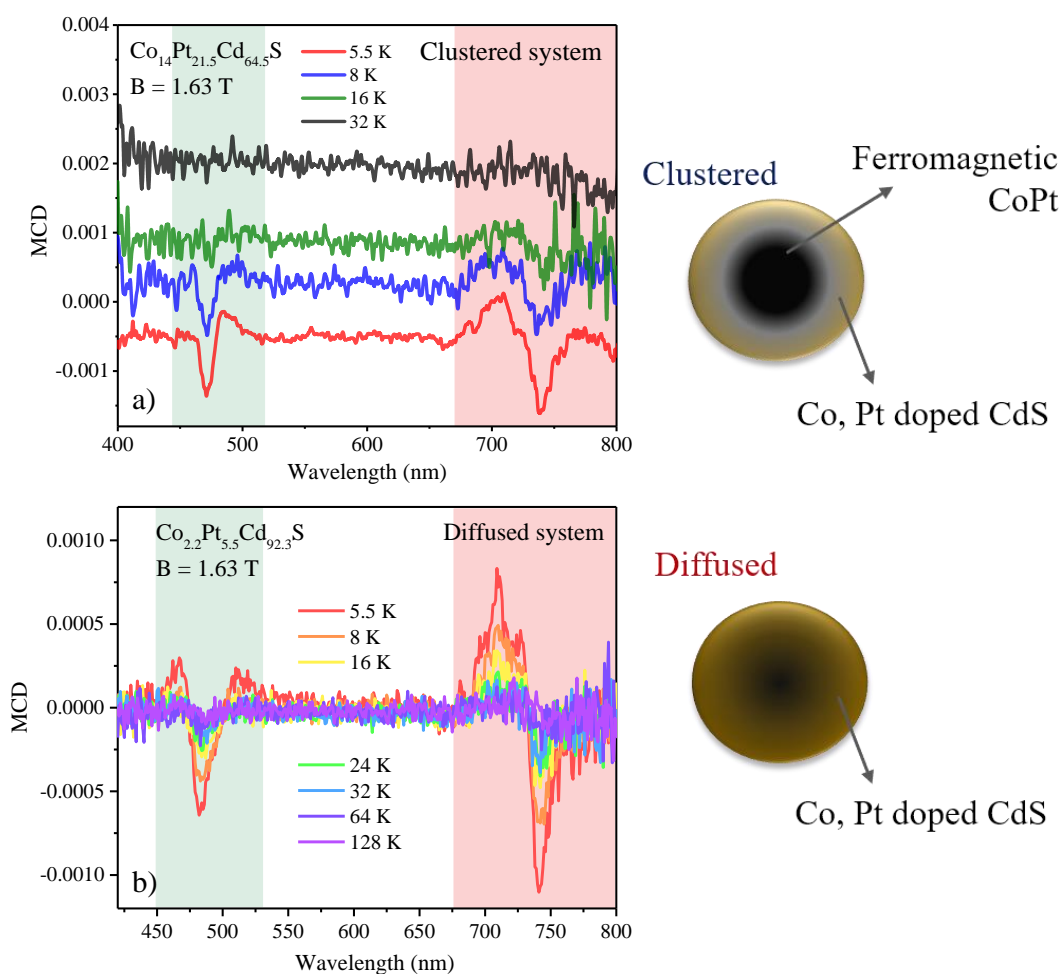


Figure 6.8. a) Temperature-dependent MCD spectra of clustered system measured at $B = 1.63 \text{ T}$. b) Temperature-dependent MCD spectra of Co, Pt diffused CdS measured at $B = 1.63 \text{ T}$.

To get further insight into the magneto-optical response of clustered and diffused system, we performed temperature-dependent MCD experiments. Figure 6.8 depicts the temperature-dependent behavior of the MCD signal. The clustered system shows MCD signal up to 8 K after which the MCD signal fades away (figure 6.8(a)). However, the diffused system shows strong temperature-dependent behavior of the MCD signal (up to 128 K) in figure 6.8(b), probably arising out of the Zeeman splitting within these systems. The clustered system involves some interfacial diffusion of Co and Pt ions into the CdS matrix. Thus, a clustered system ideally constitutes a heterostructure (described in the schematic in figure 6.8(a)) of CoPt that is ferromagnetic at low temperature and a Co, Pt

doped CdS system, where the low-temperature ferromagnetism of CoPt cluster NCs is depicted in figure 6.1 as discussed previously.

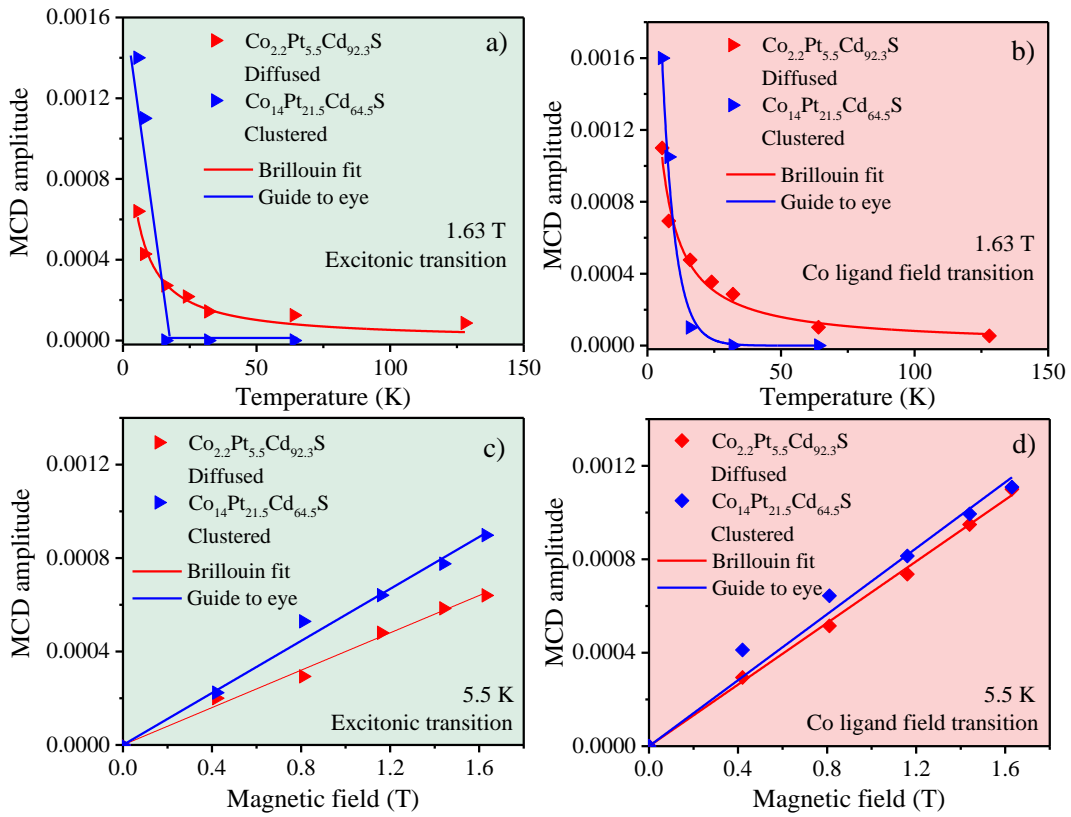


Figure 6.9. MCD amplitude of feature related to the excitonic transition and Co^{2+} ligand-field transition measured at different temperatures in (a) & (b) respectively. MCD amplitude of feature related to excitonic transition and Co^{2+} ligand-field transition measured at different fields in (c) & (d) respectively.

This ferromagnetic CoPt cluster assists the excitonic splitting of the host at low temperatures in this clustered system giving rise to the MCD signal. Further, as we increase the temperature, no features corresponding to excitonic states of the CdS and Co^{2+} ligand-field transitions are observed, confirming the absence of $sp-d$ exchange interactions in the clustered system.

To get further insight into the magneto-optical response of excitonic states and Co^{2+} LF transitions, field and temperature-dependent MCD experiments were performed. The extracted MCD amplitude from the field and temperature-dependent MCD spectra measured for $B = 0$ to 1.63 T and $T = 5.5$ to 128 K are depicted in figure 6.9 for the clustered and diffused system. In the case of $sp-d$ exchange interactions between the host charge carriers and the magnetic dopants, the MCD signal is expected to be proportional

to the magnetization of the Co^{2+} ions, with a temperature dependence according to the Brillouin function.³⁰ Thus, for the diffused system at a constant magnetic field ($B = 1.63$ T) the magnetization decreases as the temperature increases as per the Brillouin function in figure 6.9(a). However, the clustered system shows deviation from the Brillouin fit.

The temperature dependence of the Co^{2+} LF transitions is related to an unequally populated Co^{2+} ground state quartet ($^4\text{A}_2$), which creates a net magnetization. Since the Zeeman splitting of the $^4\text{A}_2$ state (at $B = 1.63$ T) is smaller than the thermal energy $k_B T$ even at the lowest temperature in our experiments, the MCD amplitude is proportional to $g\mu_B B/k_B T$, reflecting the Curie limit of the ground state magnetization of the Co^{2+} ions. Therefore, the MCD amplitude of the Co^{2+} LF transitions is expected to decrease with increasing temperature (wavelength range between 670 and 770 nm), and the extracted MCD amplitude is depicted in figure 6.9(b).

Figure 6.9 (c) and (d) show the variation of MCD amplitude of excitonic feature and Co^{2+} LF transitions as a function of the applied magnetic field. The linear variation of the MCD amplitude with the increasing magnetic field is expected for paramagnetic systems below saturation. The temperature and field dependant data for the diffused case fits well with the Brillouin function. The deviation for the clustered system and the Brillouin fit can be explained by the absence of $sp-d$ exchange interaction in these systems due to the clustering of dopants. The higher MCD amplitude for the clustered case at lower temperatures arises due to the assistance provided by the ferromagnetic CoPt core cluster at lower temperatures as discussed previously in figure 6.8. The relative amplitude of the Co^{2+} ligand-field (LF) transition in figure 6.9 (b) and (d) is higher than its excitonic counterpart in figure 6.9 (a) and (c), indicating that a small amount of Co^{2+} ions have been incorporated, as also seen from ICP-OES data. Extracting MCD amplitudes, we find the classic signatures of $sp-d$ exchange interactions in the diffused case.

6.5 Conclusion

Thus, the effect of clustering of dopants on magnetic and magneto-optical properties was studied by explicitly synthesizing similar-sized clustered and diffused magnetic semiconductors with Co and Pt dopants as microscopic probes to demonstrate the effect of clustering in the CdS lattice. The presence and absence of clustering or phase separation were studied and magnetic/magneto-optical response as a function of clustering has been studied. The Co^{2+} ligand field absorption bands were used to investigate the diffusion

process. Magnetic circular dichroism studies were used to probe the exchange coupling between magnetic dopants with the band charge carriers in the host NCs. The temperature and field dependence of the MCD signal indicates the absence of Co and Pt clusters in the diffused case, showing the homogeneity of the doping process via diffusion doping of the Kirkendall pair.

Part B: Effect of Pt co-doping on Magnetic and Magneto-Optical Properties of Co, Pt doped CdS Nanocrystals.

6.6 Summary

In part B, we present a comparative study of the magnetic and magneto-optical activity of singly and dual doped CdS NCs with only Co doping and Co and Pt co-doping. Strong *sp-d* exchange interactions are observed in both systems, however, the role of Pt has been studied in the absence and uniform presence of Pt spacer. Temperature and field-dependent magnetic studies have been performed to get more insights into the role of Pt in these NCs. The magnetic and magneto-optical properties of cobalt doped CdS with a diamagnetic platinum spacer are shown to be better than that of cobalt-only dopants suggesting the role of the local environment around the magnetic dopant ion.

6.7 Results and discussion

As discussed in the experimental section we have synthesized CoS and CoPt core and have overcoated these core NCs with non-magnetic CdS layers to get a Co doped CdS and Co, Pt co-doped CdS system after the annealing process. Further, we have investigated the magnetic and magneto-optical properties of Co doped CdS and Co, Pt co-doped CdS systems.

6.7.1 Magnetic properties

To study the role of diamagnetic Pt spacer between the ferromagnetic Co dopants, similar-sized diffused NCs of Co doped CdS were considered for the comparative study of magnetism with Co, Pt co-doped NCs. Figure 6.10 shows the magnetization (*M*) vs. applied field (*H*) at 2 K for Co, Pt co-doped CdS along with only Co doped CdS. As observed in figure 6.10, the magnetic property of Co doped CdS is largely superparamagnetic ($M_s \sim 0.13$ emu/g/Co at 2 T) with zero coercivity compared to 1000 Oe coercivity and a much larger saturation magnetization in the case of Co, Pt co-doped

CdS ($M_s \sim 0.22$ emu/g/CoPt at 2 T) signifying the need for the diamagnetic Pt spacer between ferromagnetic Co ions.

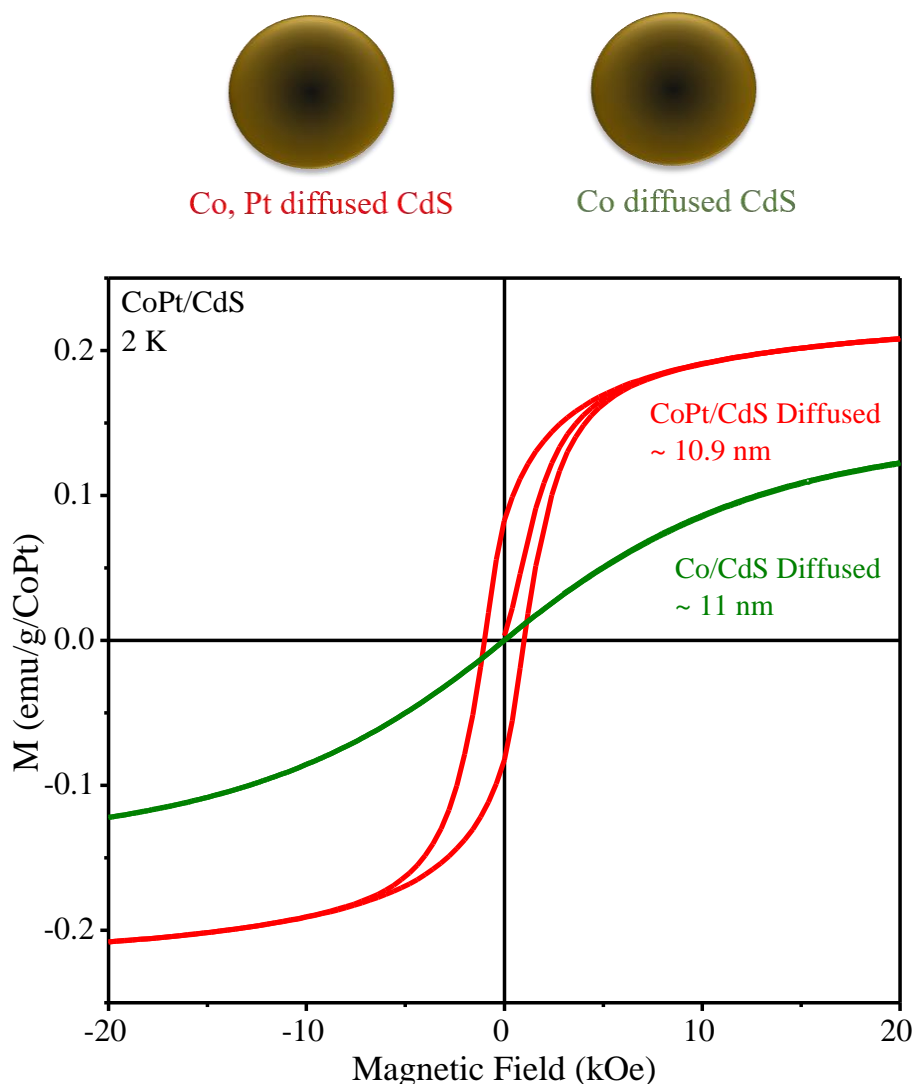


Figure 6.10. A comparison of magnetization vs. field plot for Co, Pt doped CdS and Co doped CdS NCs at 2 K.

This can be explained by the relativistic spin-orbit coupling effect of Pt. It is known that alloying of $3d$ elements with heavy $4d$ and $5d$ elements allows tuning of the magnetic anisotropic energy (MAE) which is a relativistic effect promoted by spin-orbit coupling. Here $3d$ metals with large moments like Fe, Co, Ni when coupled with $4d$ and $5d$ heavy elements with high spin-orbit coupling result in high saturation magnetization as well as high magnetic anisotropy. CoPt alloy in $L1_0$ phase³¹ with 1:1 composition in this class is the best-known example of high MAE material. The effect of polarization of spins of Pt in the $5d$ band is utilized to get high exchange interactions in Co, Pt diffused NCs resulting in higher magnetization.

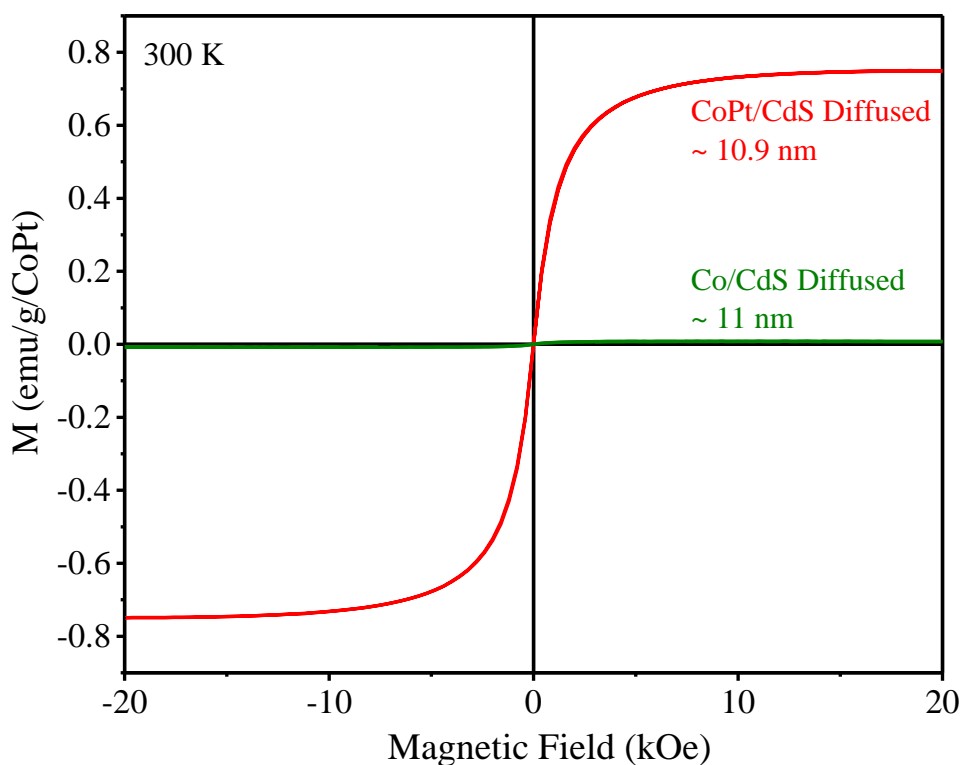


Figure 6.11. A comparison of magnetization vs. field plot for Co, Pt doped CdS and Co doped CdS NCs at 300 K.

This anisotropy in the system induces spin polarisation of Pt atoms, though diamagnetic, followed by ferromagnetic coupling of Co and Pt atoms due to hybridization of Pt $5d$ and Co $3d$ states. This affects the intrinsic anisotropy as well as coercivity of the system and maintains thermal stability of NCs magnetization when alloyed with $3d$ magnetic elements.^{15, 32} Synergistic effect of Pt is expected to have a compound influence on magnetic ordering.

Further, the magnetic field dependence of the magnetization up to 2 T, (hysteresis M-H curves) of nanocrystalline Co, Pt doped CdS and only Co doped CdS were studied at room temperature (300 K) and is presented in figure 6.11. The room temperature magnetic properties exhibit a similar trend like 2 K where higher saturation magnetization is observed for the Co, Pt doped CdS system as compared to only Co doped system. As can be seen in figure 6.11, both the systems exhibit superparamagnetism at room temperature, however, the magnetic properties of Co, Pt doped CdS are better than only Co doped CdS signifying the role of diamagnetic platinum spacer between ferromagnetic cobalt ions. This enhancement is due to platinum assisting the magnetic ordering of cobalt even at room temperature.

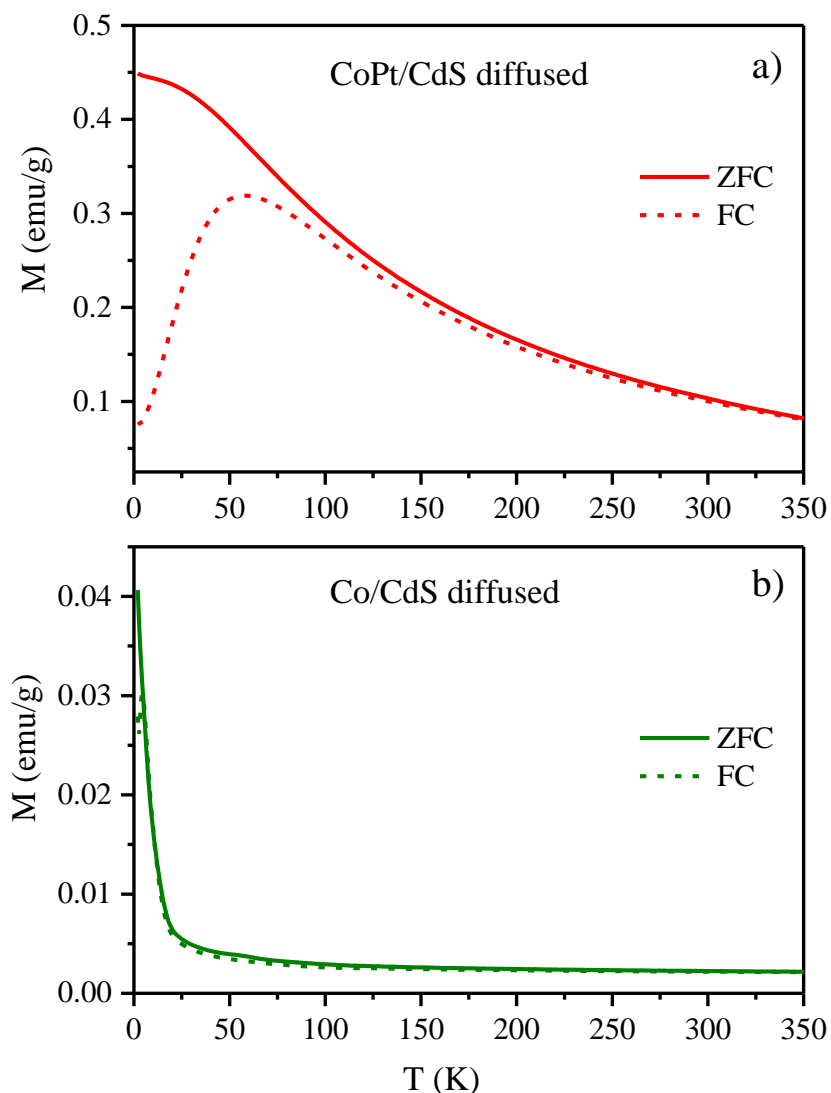


Figure 6.12. Cooling curves, FC and ZFC for for ~ 10 nm CoPt/CdS diffused and Co/CdS diffused NCs.

The field cooled and zero-field cooled curves at 200 Oe in figure 6.12 show that the Co doped CdS and Co, Pt doped CdS get into the blocked state below ~ 10 K and 57 K respectively. The dual doped system shows a higher blocking temperature than the singly doped counterpart. This is consistent with the involvement of Pt in the dual doped case as compared to the singly doped system.

6.7.2 Magneto-optical properties

Further, in order to probe the origin of magnetism in these doped materials and verify it indeed arises from the spin-exchange interaction between d electrons of the dopant with the host semiconductor, we study the magneto-optical response in Co and Co, Pt co-doped CdS NCs using magnetic circular dichroism spectroscopy.

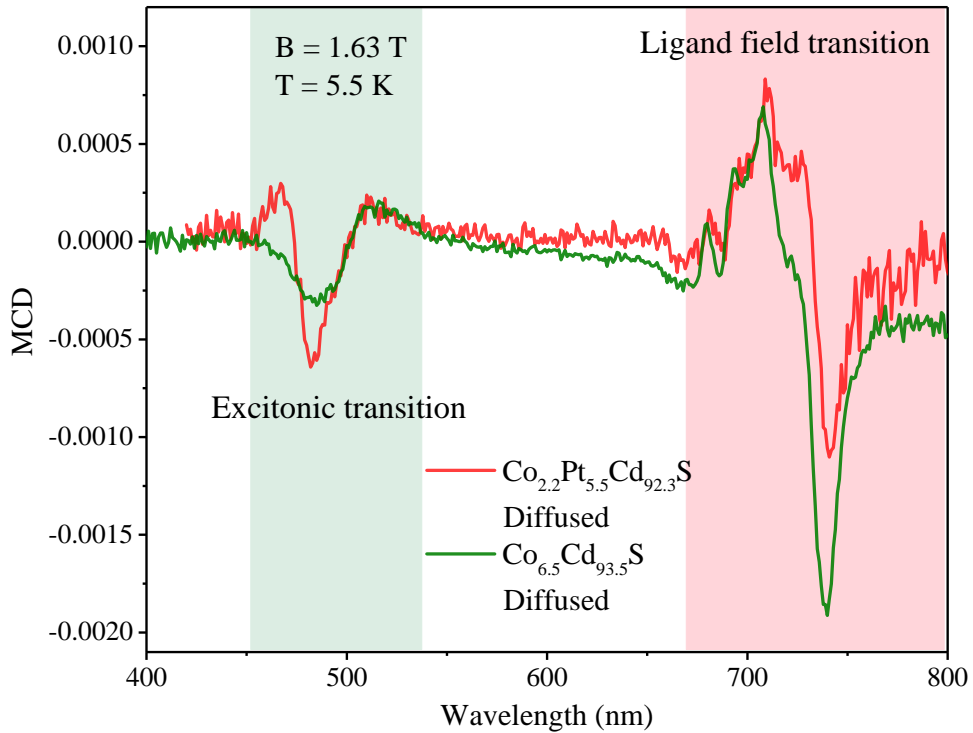


Figure 6.13. MCD spectra of Co, Pt doped CdS and Co doped CdS NCs at $T = 5.5$ K and $B = 1.63$ T depicted in red and green respectively with features related to the excitonic transition (blue) and the Co^{2+} ligand-field transition (red).

Figure 6.13 summarizes MCD data collected for Co doped CdS and Co, Pt doped CdS of similar sizes at 1.63 T and 5.5 K that illustrates the comparison. The MCD amplitude of the excitonic transition is higher for Co, Pt co-doped system than that of the Co doped system even though the percentage of Co is much lower in the co-doped case (Co - 2.2 %, Pt - 5.5 %) than in the singly doped case (Co - 6.5 %) as shown in figure 6.13. This could be attributed to the involvement of Pt assisting the $sp-d$ exchange interactions within the system. However, the MCD amplitude for the Co^{2+} LF transition is higher for the Co doped case because of the higher percentage of Co incorporated into the host lattice.

The temperature and field dependence of the MCD amplitude for the Co doped CdS and Co, Pt co-doped CdS is plotted in figure 6.14. As the temperature increases, the field dependence of MCD amplitude approaches the temperature-independent intrinsic Zeeman splitting also observed in undoped CdS NCs. Thus, the excitonic Zeeman splitting decreases in magnitude as shown in figure 6.14(a).

Even for the Co doped CdS, the excitonic Zeeman splittings are dominated by $sp-d$ exchange interaction. Further, the MCD amplitude for Co^{2+} LF transitions is proportional to $g\mu_B B/k_B T$, reflecting the Curie limit of the ground state magnetization of the Co^{2+} ions.

Therefore, the MCD amplitude of the Co^{2+} LF transitions is expected to decrease with increasing temperature and the extracted MCD amplitude depicted in figure 6.14(b).

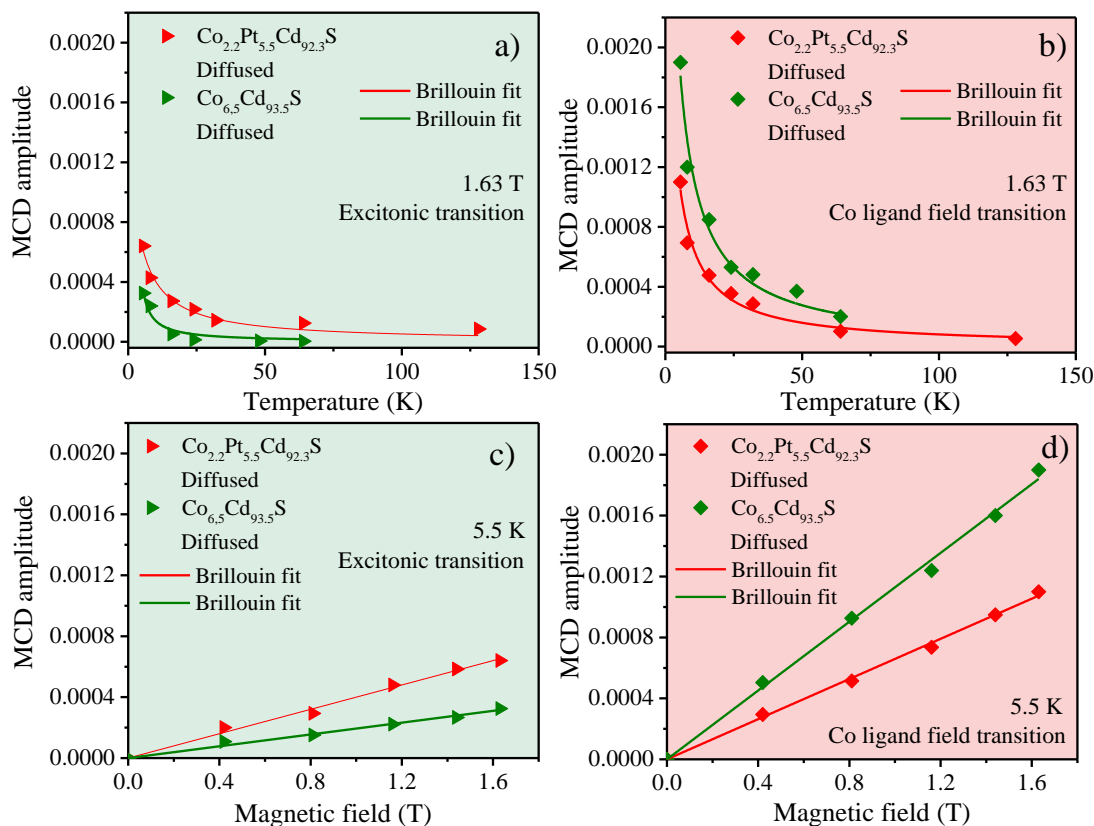


Figure 6.14. MCD amplitude of feature related to the excitonic transition measured at different temperatures and fields in (a) & (c) respectively. MCD amplitude of feature related to the Co^{2+} ligand-field transition measured at different temperatures and fields in (b) & (d) respectively for Co doped CdS and Co, Pt co-doped CdS.

Figure 6.14(c) and (d) show the variation of MCD amplitude of excitonic feature and Co^{2+} LF transitions as a function of the applied magnetic field. The linear variation of the MCD amplitude with the increasing magnetic field is expected for a system with $sp-d$ exchange interaction below saturation. The temperature and field-dependent data for both the doped systems fit well with the Brillouin function signifying the $sp-d$ exchange interaction within these systems. Further from the plots, the MCD amplitude corresponding to the excitonic transition for the temperature and field dependence is higher for the Co, Pt co-doped system where Pt assists the magnetic ordering of Co. However, the amplitude of Co^{2+} LF transition for the temperature and field dependence is higher for the Co doped system implying that a higher amount of Co is substituted into the CdS lattice in the case of Co doped CdS as compared to Co, Pt doped CdS and is also confirmed by ICP-OES data.

6.8 Conclusion

Thus, we have compared the magnetic and magneto-optical properties of Co doped CdS and Co, Pt co-doped CdS NCs. The magnetic and magneto-optical properties give evidence of magnetic exchange interactions happening in these systems assisted by the local environment. The use of diamagnetic ion like Pt in presence of other magnetic ions has shown to display superior magnetic properties in the co-doped materials.

Bibliography

- (1) Andrew, C. C.; Mizuno, M.; Sasaki, Y.; Kondo, H.; Hiraga, K. Structural Characteristics and Magnetic Properties of Chemically Synthesized CoPt Nanoparticles. *Appl. Phys. Lett.* **2002**, *81*, 3768-3770.
- (2) Sui, Y.; Yue, L.; Skomski, R.; Li, X. Z.; Zhou, J.; Sellmyer, D. J. CoPt Hard Magnetic Nanoparticle Films Synthesized by High Temperature Chemical Reduction. *J. Appl. Phys.* **2003**, *93*, 7571-7573.
- (3) Cai, Y.; Wolfkuhler, D.; Myalitsin, A.; Perlich, J.; Meyer, A.; Klinke, C. Tunable Electrical Transport through Annealed Monolayers of Monodisperse Cobalt–Platinum Nanoparticles. *ACS Nano* **2010**, *5*, 67-72.
- (4) Habas, S. E.; Yang, P.; Mokari, T. Selective Growth of Metal and Binary Metal Tips on CdS Nanorods. *J. Am. Chem. Soc.* **2008**, *130*, 3294-3295.
- (5) Gu, H.; Zheng, R.; Zhang, X.; Xu, B. Facile One-Pot Synthesis of Bifunctional Heterodimers of Nanoparticles: A Conjugate of Quantum Dot and Magnetic Nanoparticles. *J. Am. Chem. Soc.* **2004**, *126*, 5664-5665.
- (6) Tian, Z.-Q.; Zhang, Z.-L.; Gao, J.; Huang, B.-H.; Xie, H.-Y.; Xie, M.; Abruña, H. D.; Pang, D.-W. Color-Tunable Fluorescent–Magnetic Core/Shell Multifunctional Nanocrystals. *Chem. Commun.* **2009**, *27*, 4025-4027.
- (7) Lee, J.-S.; Bodnarchuk, M. I.; Shevchenko, E. V.; Talapin, D. V. “Magnet-in-the-Semiconductor” FePt–PbS and FePt–PbSe Nanostructures: Magnetic Properties, Charge Transport, and Magnetoresistance. *J. Am. Chem. Soc.* **2010**, *132*, 6382-6391.
- (8) Saha, A.; Chellappan, K. V.; Narayan, K. S.; Ghatak, J.; Datta, R.; Viswanatha, R. Near-Unity Quantum Yield in Semiconducting Nanostructures: Structural Understanding Leading to Energy Efficient Applications. *J. Phys. Chem. Lett.* **2013**, *4*, 3544-3549.
- (9) Saha, A.; Chattopadhyay, S.; Shibata, T.; Viswanatha, R. The Curious Case of CdTe/CdS: Photoabsorption versus Photoemission. *J. Mater. Chem. C* **2014**, *2*, 3868-3872.
- (10) Saha, A.; Viswanatha, R. Magnetism at the Interface of Magnetic Oxide and Nonmagnetic Semiconductor Quantum Dots. *ACS Nano* **2017**, *11*, 3347-3354.
- (11) García-Santamaría, F.; Brovelli, S.; Viswanatha, R.; Hollingsworth, J. A.; Htoon, H.; Crooker, S. A.; Klimov, V. I. Breakdown of Volume Scaling in Auger Recombination in CdSe/CdS Heteronanocrystals: The Role of the Core–Shell Interface. *Nano Lett.* **2011**, *11*, 687-693.

- (12) Bae, W. K.; Padilha, L. A.; Park, Y.-S.; McDaniel, H.; Robel, I.; Pietryga, J. M.; Klimov, V. I. Controlled Alloying of the Core–Shell Interface in CdSe/CdS Quantum Dots for Suppression of Auger Recombination. *ACS Nano* **2013**, *7*, 3411-3419.
- (13) Fan, Y.; Smith, K. J.; Lüpke, G.; Hanbicki, A. T.; Goswami, R.; Li, C. H.; Zhao, H. B.; Jonker, B. T. Exchange Bias of the Interface Spin System at the Fe/MgO Interface. *Nat. Nanotechnol.* **2013**, *8*, 438-444.
- (14) Yu, J. H.; Liu, X.; Kweon, K. E.; Joo, J.; Park, J.; Ko, K.-T.; Lee, D. W.; Shen, S.; Tivakornsasithorn, K.; Son, J. S.; Park, J.-H.; Kim, Y.-W.; Hwang, G. S.; Dobrowolska, M.; Furdyna, J. K.; Hyeon, T. Giant Zeeman Splitting in Nucleation-Controlled Doped CdSe:Mn²⁺ Quantum Nanoribbons. *Nat. Mater.* **2010**, *9*, 47-53.
- (15) Alloyeau, D.; Ricolleau, C.; Mottet, C.; Oikawa, T.; Langlois, C.; Le Bouar, Y.; Braidy, N.; Loiseau, A. Size and Shape Effects on the Order–Disorder Phase Transition in CoPt Nanoparticles. *Nat. Mater.* **2009**, *8*, 940-946.
- (16) Sellmyer, D. J.; Yu, M.; Kirby, R. D. Nanostructured Magnetic Films for Extremely High Density Recording. *Nanostruct. Mater.* **1999**, *12*, 1021-1026.
- (17) Bonanni, A.; Dietl, T. A Story of High-Temperature Ferromagnetism in Semiconductors. *Chem. Soc. Rev.* **2010**, *39*, 528-539.
- (18) Hanif, K. M.; Meulenberg, R. W.; Strouse, G. F. Magnetic Ordering in Doped Cd_{1-x}Co_xSe Diluted Magnetic Quantum Dots. *J. Am. Chem. Soc.* **2002**, *124*, 11495-11502.
- (19) Makkar, M.; Viswanatha, R. Recent Advances in Magnetic Ion-Doped Semiconductor Quantum Dots. *Curr. Sci.* **2017**, *112*, 1421-1429.
- (20) Sarkar, I.; Sanyal, M. K.; Kar, S.; Biswas, S.; Banerjee, S.; Chaudhuri, S.; Takeyama, S.; Mino, H.; Komori, F. Ferromagnetism in Zinc Sulfide Nanocrystals: Dependence on Manganese Concentration. *Phys. Rev. B.* **2007**, *75*, 224409.
- (21) Norberg, N. S.; Parks, G. L.; Salley, G. M.; Gamelin, D. R. Giant Excitonic Zeeman Splittings in Colloidal Co²⁺-Doped ZnSe Quantum Dots. *J. Am. Chem. Soc.* **2006**, *128*, 13195-13203.
- (22) Cheng, S.-J. Theory of Magnetism in Diluted Magnetic Semiconductor Nanocrystals. *Phys. Rev. B.* **2008**, *77*, 115310.
- (23) Shanker, G. S.; Tandon, B.; Shibata, T.; Chattopadhyay, S.; Nag, A. Doping Controls Plasmonics, Electrical Conductivity, and Carrier-Mediated Magnetic Coupling in Fe and Sn Codoped In₂O₃ Nanocrystals: Local Structure is the Key. *Chem. Mater.* **2015**, *27*, 892-900.

- (24) Gurung, T.; Mackowski, S.; Jackson, H. E.; Smith, L. M.; Heiss, W.; Kossut, J.; Karczewski, G. Optical Studies of Zero-Field Magnetization of CdMnTe Quantum Dots: Influence of Average Size and Composition of Quantum Dots. *J. Appl. Phys.* **2004**, *96*, 7407-7413.
- (25) Saito, H.; Zayets, V.; Yamagata, S.; Ando, K. Magneto-Optical Studies of Ferromagnetism in the II-VI Diluted Magnetic Semiconductor $Zn_{1-x}Cr_xTe$. *Phys. Rev. B.* **2002**, *66*, 081201.
- (26) Sinova, J.; Jungwirth, T.; ČERNE, J. Magneto-Transport and Magneto-Optical Properties of Ferromagnetic (III, Mn)V Semiconductors: A Review. *Int. J. Mod. Phys. B.* **2004**, *18*, 1083-1118.
- (27) van Schilfgaarde, M.; Mryasov, O. N. Anomalous Exchange Interactions in III-V Dilute Magnetic Semiconductors. *Phys. Rev. B.* **2001**, *63*, 233205.
- (28) Sato, K.; Katayama-Yoshida, H.; Dederichs, P. H. High Curie Temperature and Nano-Scale Spinodal Decomposition Phase in Dilute Magnetic Semiconductors. *Jpn. J. Appl. Phys.* **2005**, *44*, L948-L951.
- (29) Radovanovic, P. R.; Gamelin, D. R. In *Magnetic Circular Dichroism Spectroscopy of Co^{2+} : CdS Diluted Magnetic Semiconductor Quantum Dots*, Nanoscale Optics and Applications, International Society for Optics and Photonics: 2002; pp 51-61.
- (30) Gaj, J. A.; Kossut, J. Basic Consequences of sp-d and d-d Interactions in DMS. In *Introduction to the Physics of Diluted Magnetic Semiconductors*, Springer: 2010; pp 1-36.
- (31) Ohtake, M.; Ouchi, S.; Kirino, F.; Futamoto, M. $L1_0$ Ordered Phase Formation in FePt, FePd, CoPt, and CoPd Alloy Thin Films Epitaxially Grown on MgO (001) Single-Crystal Substrates. *J. Appl. Phys.* **2012**, *111*, 07A708.
- (32) Mryasov, O. N.; Nowak, U.; Guslienko, K. Y.; Chantrell, R. W. Temperature-Dependent Magnetic Properties of FePt: Effective Spin Hamiltonian Model. *Europhys. Lett.* **2005**, *69*, 805-811.

CHAPTER 7

Magnetism in Fe, Co Dual-Doped CdS Nanocrystals.

7.1 Summary

In the wide family of transition metal-doped semiconductors, Fe and Co-doped systems in form of bulk samples and nanostructures have attracted much attention in recent years. They have been studied extensively due to their unique properties and perspectives for applications in optoelectronic and spintronic devices. This chapter discusses the magnetic properties of CdS nanocrystals simultaneously doped with Fe and Co with varying Fe/Co compositions. The co-doped nanocrystals show magnetic properties that are different from the singly doped counterparts. Interestingly, co-doped samples show that cobalt is able to assist in the magnetic ordering of ferromagnetic iron in CdS nanocrystals at low temperatures as well as at room temperature.

7.2 Introduction

As already discussed in the previous chapters, doped magnetic semiconductors,¹⁻⁴ formed by substituting a small amount of cations of the host compound semiconductors with magnetic dopants are expected to play an important role in interdisciplinary materials science and future electronics. It is expected that charge and spin degrees of freedom accommodated into a single material can result in interesting magnetic,¹⁻² magneto-optical, and other physical properties.⁵

Among the transition metals, Fe and Co are the dopants that are most widely explored. Several groups have reported on the magnetic properties of iron and cobalt singly doped II-VI semiconductors.⁶⁻¹⁰ Co doped II-VI semiconductors are good candidates for applications such as magneto-optical devices, magnetic field sensors, spintronics,¹¹⁻¹³ magnetic recording¹⁴ and magneto-optical switches.¹³ However, co-doping of iron and cobalt in these materials has never been explored. Doping of the nanocrystals (NCs) is a challenging task¹⁵⁻¹⁷ and these doped and co-doped NCs can give rise to interesting magnetic properties that are absent in singly doped systems.

An ideal doped magnetic semiconductor for practical applications should have a homogeneous distribution of the magnetic dopants. The presence of magnetic precipitates in host semiconductors in the form of clusters or secondary phases⁷ of the magnetic impurities is detrimental to the real applications of doped semiconductors as discussed in chapter 6 and therefore should be avoided. This is because these dopants themselves are intrinsically magnetic. However, clusters of magnetic ions would lead to extremely small

and insignificant magnetism arising out of these clusters rather than the entire lattice. In practice, such precipitates have been directly observed, which affects the magnetic properties of the host.¹⁸⁻²⁰

The present work aims at the synthesis of cobalt and iron doped and co-doped CdS NCs. Generally, soft chemical processing does not assist in dopant substitution in a semiconductor matrix and the dopants are diverted to the surface.²¹ However, using the diffusion doping approach we were able to achieve uniformly doped Fe/Co systems for the first time. The diffusion doping method combined with self purification²²⁻²³ designed to overcome the problems of clustering and phase separation of dopants has been employed to dope and co-dope Fe/Co in CdS NCs. We report the magnetic properties of these CdS nanocrystals doped and co-doped with Fe and Co. Field and temperature-dependent magnetic studies were performed to understand the interactive magnetic ordering in dual and singly doped systems.

We also studied their magnetic properties by varying the concentration ratio of Fe:Co in these systems. Fe and Co singly doped samples show magnetic properties different from the dual doped systems. The presence of another magnetically active ion within the same doped system can contribute to magnetization and magnetic ordering has been investigated. Interestingly, in the systems co-doped with multiple magnetic ions, we observe spin polarization by the existence of other magnetic impurities and communicates the interruption to its neighboring magnetic impurities, thus intervening an indirect magnetic interaction among them. It is expected that in these NCs, cobalt in the co-doped case is assisting the magnetic ordering of iron at low temperatures as well as at room temperature leading to higher coercivity and saturation magnetization in dual doped nanocrystals as compared to the singly doped cases.

7.3 Experimental section

Chemicals used. Cobalt acetylacetonate ($\text{Co}(\text{acac})_2$), iron acetylacetonate ($\text{Fe}(\text{acac})_2$), cadmium oxide (CdO), oleic acid (OA, 90%), 1-octadecene (ODE, 90%), oleylamine (OlAm, technical grade 70%), and sulfur powder (S, 99.5%) were purchased from Sigma Aldrich. All purchased chemicals were used without further purification. Ethanol, acetone and hexane were purchased from Merck (Emparta). All solvents were used without further purification.

Synthesis. CoS NCs. CoS NCs were synthesized using cobalt acetylacetonate (0.05 mmol) and S-powder (0.07 mmol). They were dissolved in 4 mL oleylamine and 1 mL oleic acid in a three-necked round bottom flask. The system was degassed at 80 °C for two hours under constant stirring. The temperature was raised to 200 °C after degassing and kept under constant argon flow. After 10 min the temperature of the reaction mixture was raised to 250 °C gradually (10 °C/3 min). After attaining the temperature, the reaction mixture was kept at 250 °C for 20 min and then cooled down to room temperature. The black precipitate was isolated by centrifuging and was then washed twice by hexane, ethanol and a few drops of acetone. The as-synthesized NCs were then used for further synthesis of doped NCs.

FeS NCs. The FeS core was synthesized using iron acetylacetonate, Fe(acac)₂ (0.05 mmol) and S-powder (0.07 mmol). Oleic Acid and oleylamine were used as coordinating agents and solvents. For the synthesis, Fe(acac)₂ and S-powder were taken in a three-necked round bottom flask. 2 ml of oleic acid and 6 ml of oleylamine were added to it. The system was degassed at 80 °C for two hours with constant stirring. The temperature was raised to 200 °C after degassing and kept under constant argon flow. After 10 min the temperature of the reaction mixture was raised to 300 °C gradually (10 °C/3 min). After attaining the temperature, the reaction mixture was kept at 300 °C for 10 min and then cooled down to room temperature. Then, the as-synthesized nanocrystals were isolated by centrifugation, washed once with ethanol-hexane mixture and a few drops of acetone, and used for further synthesis of doped NCs.

Co_{0.5}Fe_{1.5}S₂ NCs. Co_{0.5}Fe_{1.5}S₂ NCs were synthesized via co-reduction of metal salts cobalt acetylacetonate (0.05 mmol) and iron acetylacetonate (0.15 mmol). Metal salts along with S-powder (0.25 mmol) were dissolved in 4 mL oleylamine and 1 mL oleic acid in a three-neck flask. The system was degassed at 80 °C for two hours under constant stirring. The temperature was raised to 200 °C after degassing and kept under constant argon flow. After 10 min the temperature of the reaction mixture was raised to 300 °C gradually (10 °C/3 min). After attaining the temperature, the reaction mixture was kept at 300 °C for 20 min and then cooled down to room temperature. The black precipitated particles were isolated by centrifuging and were then washed twice by hexane-ethanol mixture and a few drops of acetone. The as-synthesized NCs were then used for further synthesis of doped NCs.

Co_{1.5}Fe_{0.5}S₂ NCs. Co_{1.5}Fe_{0.5}S₂ NCs were synthesized via co-reduction of metal salts cobalt acetylacetonate (0.15 mmol) and iron acetylacetonate (0.05 mmol). Metal salts along with

S-powder (0.25 mmol) were dissolved in 4 mL oleylamine and 1 mL oleic acid in a three-neck flask. The system was degassed at 80 °C for two hours under constant stirring. The temperature was raised to 200 °C after degassing and kept under constant argon flow. After 10 min the temperature of the reaction mixture was raised to 300 °C gradually (10 °C/3 min). After attaining the temperature, the reaction mixture was kept at 300 °C for 20 min and then cooled down to room temperature. The black precipitated particles were isolated by centrifuging and were then washed twice by hexane, ethanol and a few drops of acetone. The as-synthesized NCs were then used for further synthesis of doped systems.

Synthesis of precursors

0.2 M Cadmium oleate. Cadmium oleate, a precursor for the synthesis of doped nanocrystals, was synthesized using cadmium oxide (CdO). Oleic Acid and oleylamine were used as coordinating solvents. For the synthesis of 0.2 M cadmium oleate, 0.3204 g cadmium oxide (CdO), 9 mL of octadecene (ODE) and 7 mL of oleic acid (OA) were taken in a three-necked round bottom flask. System was degassed at 80 °C for two hours under constant stirring. The temperature was raised to 250 °C after degassing and kept under argon flow. System was kept for some time till the red colour disappeared and a clear solution was obtained. It was then cooled down to room temperature.

Synthesis of 0.2 M S-ODE. S-ODE, S-precursor for the synthesis of doped nanocrystals, was synthesized using sulfur powder. For the synthesis of S-ODE, 65 mg of sulfur powder and 10 mL of octadecene (ODE) was taken in a vial. System was degassed at room temperature for 15-20 minutes. Argon was purged. Sonication and heating were performed to get a clear solution.

Fe or Co doped NCs. For the synthesis of Fe or Co-doped CdS NCs, the successive ionic layer adsorption and reaction (SILAR) technique was followed. Approximately 20 mg of presynthesized FeS or CoS NCs dissolved in 3 mL oleylamine, were taken in a three-necked round bottom flask and 6 mL of ODE was added to it. System was degassed at 80 °C for 2 hours under constant stirring. After degassing, the reaction temperature was raised to 250 °C under argon flow. Overcoating was started with the addition of the stoichiometric amount of S-precursor i.e. S-ODE and was kept for 20 min. After 20 min the same amount of Cd precursor, cadmium oleate was injected into the system and annealed for 30 min. The cyclic addition of S precursor followed by Cd precursor was continued until an ultra-thick shell of CdS was formed over the core NCs. The system was

annealed at 250 °C to diffuse the core into the CdS lattice. The reaction was stopped at the required thickness of the CdS shell. Aliquots were collected in between. The samples were washed by centrifugation using hexane-ethanol mixture and a few drops of acetone.

Fe and Co co-doped NCs. For the synthesis of the co-doped system, the same procedure was followed as in the case of singly doped NCs. Here $\text{Co}_{0.5}\text{Fe}_{1.5}\text{S}_2$ and $\text{Co}_{1.5}\text{Fe}_{0.5}\text{S}_2$ were taken and overcoated by CdS. The system was degassed at 80 °C for 2 hours under constant stirring. After degassing, the reaction temperature was raised to 250 °C under argon flow. Overcoating was started with the addition of stoichiometric amount of S-precursor i.e. S-ODE and was kept for 20 min. After 20 min the same amount of Cd precursor, $\text{Cd}(\text{Ol})_2$ was injected into the system and annealed for 30 min. The cyclic addition of S precursor followed by Cd precursor was continued until an ultra-thick shell of CdS was formed over the core NCs. The system was annealed at 250 °C to diffuse the core into the CdS lattice. The reaction was stopped at the required thickness of the CdS shell. Aliquots were collected in between. The samples were washed by centrifugation using hexane-ethanol mixture and a few drops of acetone.

Structural characterization & magnetic properties

The as-synthesized samples were characterized and studied through various techniques. Nanocrystal size and shape identification was carried out using transmission electron microscopy (TEM). TEM was performed on a Tecnai F30 UHR version electron microscope, using a field emission gun (FEG) operating at an accelerating voltage of 200 kV in bright field mode using Cu coated holey carbon TEM grids. Samples for TEM were prepared by adding a solution of the NCs dissolved in hexane dropwise on a carbon-coated Cu grid. The solution was allowed to evaporate leaving behind the NCs. Crystal structure identification of the particles was carried out using x-ray diffraction, recorded on Bruker D8 Advance diffractometer using $\text{Cu K}\alpha$ radiation. Since the diffracted intensities from these NCs are generally weak, all patterns were recorded at a slow scan rate to get a high signal to noise ratio. The 2θ ranges from 20 to 70 degrees. Perkin Elmer inductively coupled plasma-optical emission spectroscopy (ICP-OES) was used to obtain the elemental percentages present in the NCs. To determine the Cd, Fe, Co ratio, elemental analysis was carried out and samples were dissolved in 2-5% of HNO_3 and HCl. The Fe, Co and Cd concentrations were measured against known Fe, Co and Cd standards of high purity. X-ray absorption fine structure (XAFS) spectroscopy was employed to probe the local structure around Co, Fe and Cd atoms for the Fe/Co cores and co-doped CdS

nanocrystals. Data collected was processed using Athena and Artemis software. Measurements were carried out at PETRA III, P-64 beamline, Hamburg, Germany. DC magnetization measurements were carried out in a Superconducting Quantum Interference Device that employs the technique of vibrating sample magnetometer (SQUID-VSM) (Magnetic Property Measurements System MPMS-3, Quantum Design, U.S.). A few milligram of sample was packed in a piece of Teflon for the measurement. M vs. H measurements were carried out at 2 K and room temperature (300 K). Field cooled and zero field cooled measurements were performed for the temperature range of 2 K to 300 K at 200 Oe. The sample was first cooled to 2 K in the absence of an external magnetic field. With heating, magnetization data was recorded in the field strength of 200 Oe (ZFC measurement). In the FC measurement, the sample was cooled in the presence of a magnetic field of 200 Oe. The magnetization was then recorded with temperature up to 300 K in the applied field.

Combining TEM, XRD, XAFS and SQUID measurements, we characterize and study the magnetic response of singly and dual Fe/Co doped nanocrystals.

7.4 Results and discussion

FeS, CoS, CoFeS cores were synthesized and overcoated with non-magnetic CdS layers using the SILAR method followed by high-temperature annealing to get uniformly diffused singly and dual-doped systems. Magnetic core diffuses out into the CdS lattice as growth of a thick CdS shell causes a strain and annealing it at higher temperatures allows self-purification of dopant ions. The annealing temperature and time of growth are maintained such that the rate of diffusion of the magnetic core is slower than the growth of the shell by SILAR technique. This controlled diffusion allows us to have control over percentage and uniformity of doping and size of the NCs.

For dual doping, two sets of samples of CoFeS core with varying Co:Fe ratios have been synthesized. Stoichiometrically calculated, different amounts of Co:Fe were added and the amount of Co:Fe that got incorporated in the CoFeS NCs was measured through ICP-OES.

TEM. Figure 7.1 shows the representative bright-field TEM images of the doped NCs. It can be seen from the figure that the particles are spherical and have a fairly uniform size distribution signifying a uniform growth of NCs.

XRD. Further, the presence of impurity phases of the doped systems can be studied from the XRD of these materials. To explore the composition and crystal structure of these NCs, XRD measurements were carried out. Since XRD is sensitive to the particle size, the occurrence of broad diffraction peaks suggests the presence of small size particles.

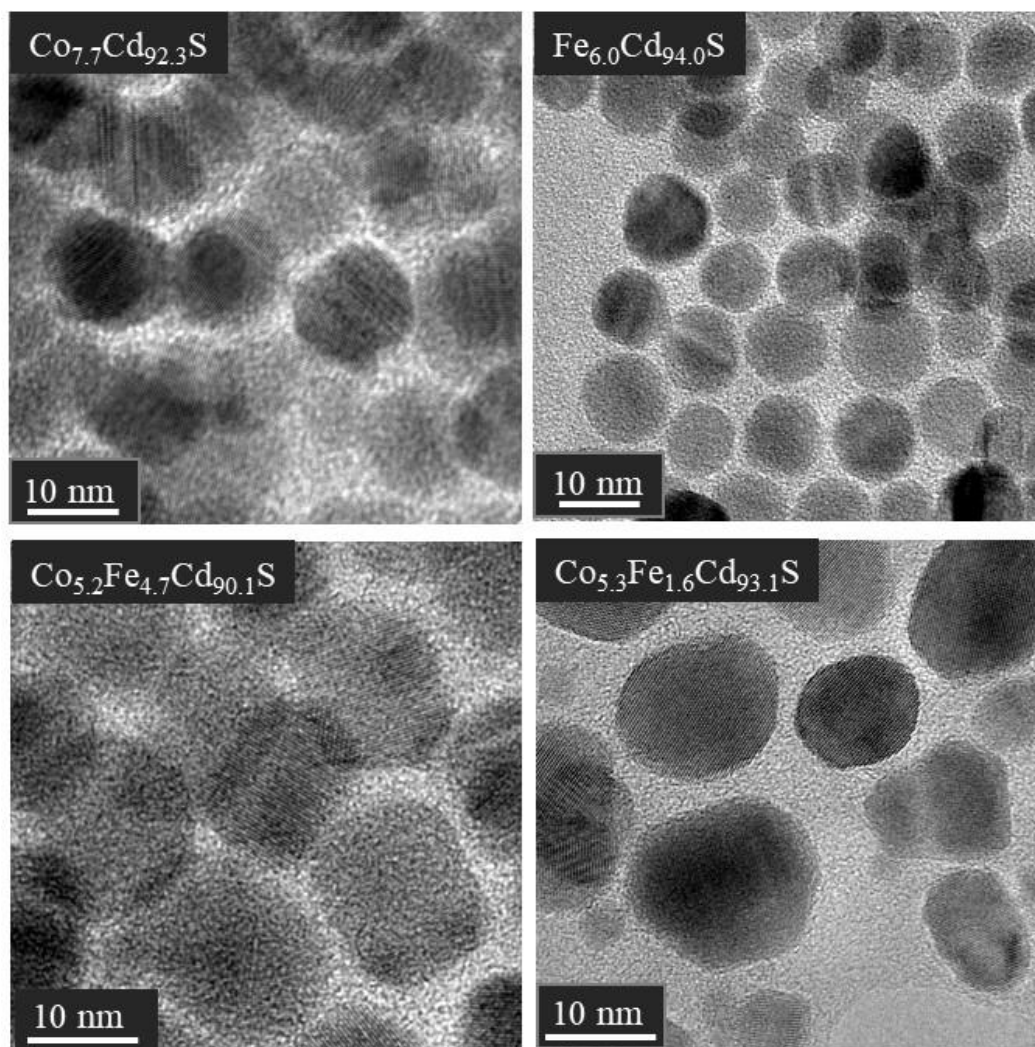


Figure 7.1. TEM image showing (a) $\text{Fe}_{0.02}\text{Cd}_{0.98}\text{S}$, (b) $\text{Co}_{0.015}\text{Fe}_{0.031}\text{Cd}_{0.954}\text{S}$, (c) $\text{Co}_{0.041}\text{Fe}_{0.014}\text{Cd}_{0.945}\text{S}$ (d) $\text{Co}_{0.015}\text{Cd}_{0.985}\text{S}$ NCs.

The XRD patterns in figure 7.2 show that all the doped systems crystallizes in a hexagonal structure similar to that of the bulk (also shown in the figure) CdS as observed from the inorganic crystal structure database. Eventually, in presence of a sufficiently thick shell of CdS and adequately long annealing time, signatures of core structure of CoS/FeS/FeCoS are completely absent. The absence of core features in XRD is indicative of the diffusion of dopants from the core to the CdS matrix. PXRD pattern of the overcoated systems shows prominent CdS features only which is due to the formation of doped CdS NCs. No

other secondary phases were detected. A comparison of the nanocrystal XRD pattern with that of the bulk confirms the existence of a single-phase nature in the doped CdS sample with a hexagonal wurtzite type structure. However, it is still possible to have small clusters that are beyond the resolution of XRD, comprised of 3-10 atoms and hence cannot be conclusive proof for the absence of clustering.

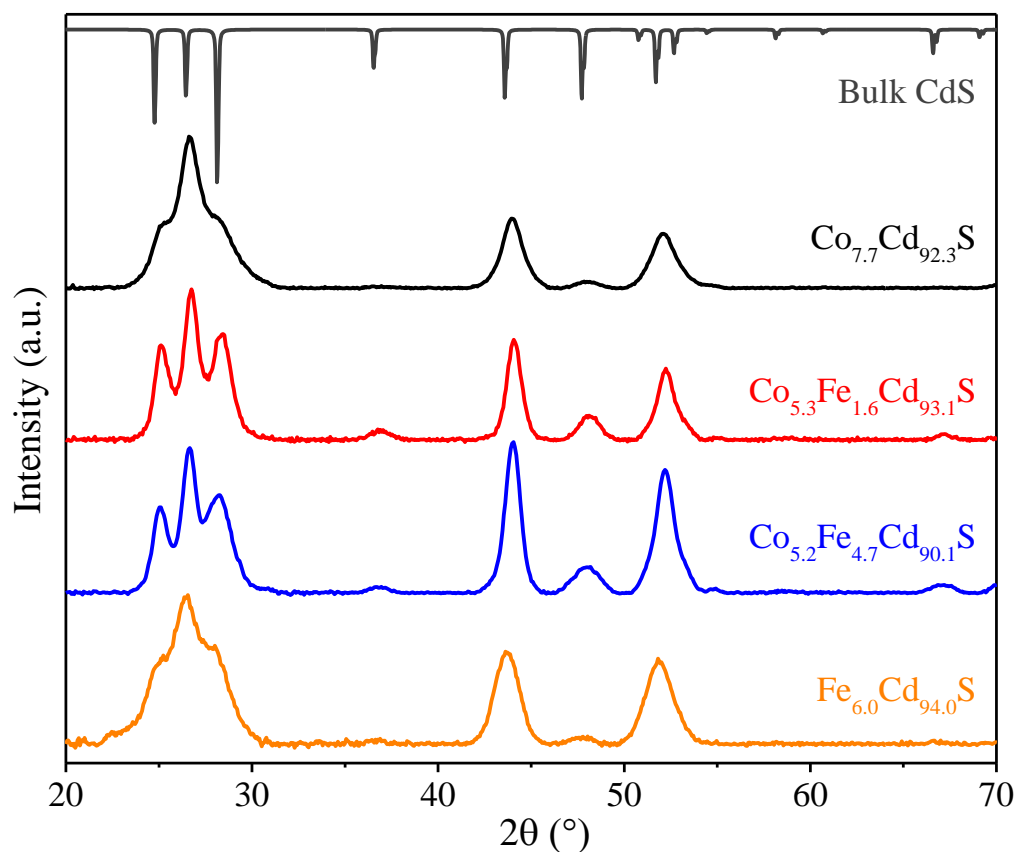


Figure 7.2. X-ray diffraction pattern for Fe/Co doped NCs along with CdS bulk pattern.

XAFS. To obtain more insight into the local structure around the dopant atom, we carried out XAFS measurements on Cd, Co, Fe edges in fluorescence mode for the core and doped systems. XAFS can reveal the local bonding around the atom of interest by measuring the absorption coefficient below, at and above the absorption edge of the element. The data was processed using ATHENA²⁴ and the Fourier transform of Co, Fe and Cd K-edge EXAFS spectra in real (R) space for the doped systems are shown in figure 7.3 for singly doped CdS and figure 7.4 for dual doped CdS. The structure around the Cd atom in singly doped systems is very similar to that of Fe and Co as shown in figure 7.3. Further verification of the absence of the clusters of the core was obtained by the complete absence of the second nearest neighbour contribution.

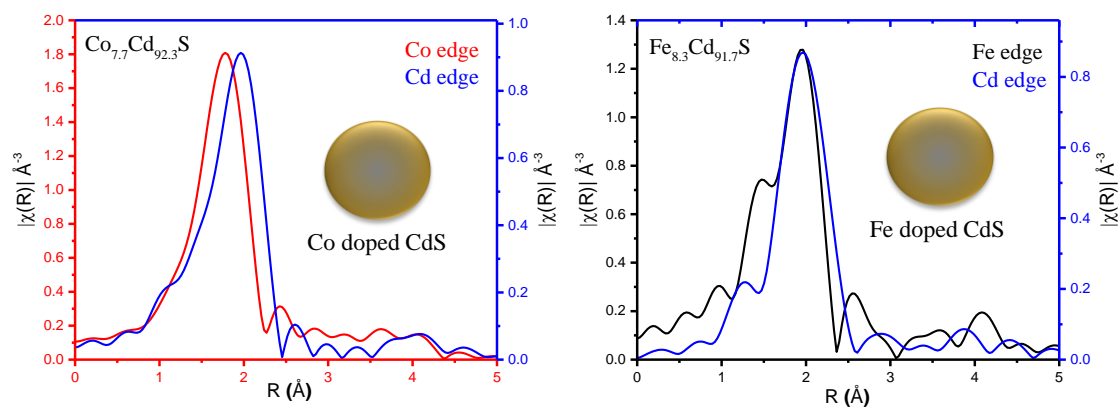


Figure 7.3. Magnitude of Fourier-transformed Co-K edge and Cd-K edge for Co doped CdS and Fe-K edge and Cd-K edge EXAFS spectra for Fe doped CdS.

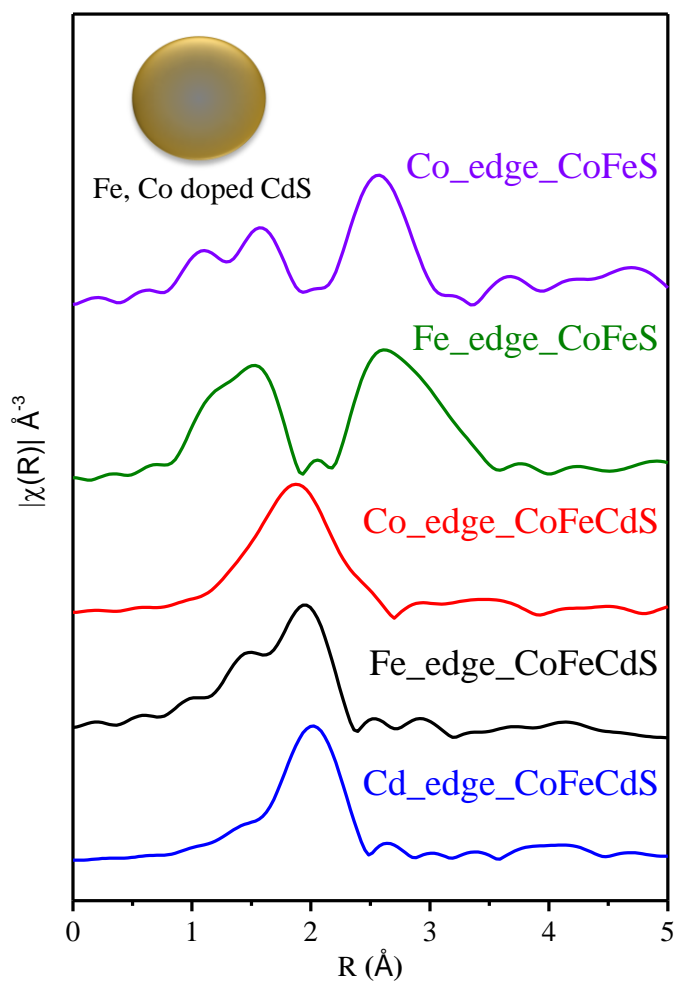


Figure 7.4. Magnitude of Fourier-transformed Fe-K edge, Co-K edge EXAFS spectra for FeCoS core and the Fe, Co co-doped CdS and a comparison with Cd-K edge for Fe, Co co-doped CdS.

Further, for the dual-doped case, the visual inspection of the plots makes it evident that the local structure around Co/Fe in the cores is very different than that of Co/Fe in doped samples as shown in figure 7.4. The Co and Fe-edge for the FeCoS core show the presence of second nearest neighbour contribution in the EXAFS pattern as shown in figure 7.4. However, EXAFS data for Fe and Co K-edge in the doped system shows a dissimilar pattern to that of the cores. Upon analyzing the similar data for the Cd edge, also shown in figure 7.4, it is apparent that the structure around the Cd atom in doped systems is very similar to that of Fe and Co in the doped case. Further verification of the absence of the clusters of FeCoS core was obtained by the complete absence of the second nearest neighbour contributions. After the structural, morphological, compositional and local structure analysis, these systems were taken for magnetic studies.

Magnetic properties. Magnetic properties in doped semiconductors are influenced by the exchange coupling of $3d$ orbital electrons of transition elements with the host semiconductor's electronic levels.²⁵ While long-range magnetic ordering cannot be created by conventional double exchange or superexchange in case of dilute doping limit inside the semiconductors by transition metal dopants,²⁶ $sp-d$ exchange interaction usually mediates this through the formation of magnetic bound polarons in these systems. There have been quite a few studies in the literature²⁷⁻²⁸ on $sp-d$ exchange interaction in semiconductor NCs. However, these doped systems in the past have shown several inconsistencies in the magnetic properties due to the inhomogeneous distribution of dopants inside the semiconductor NCs. For instance, Mn^{2+} doped $ZnSe$ ²⁹ shows enhanced excitonic Zeeman splitting, however, reduced splitting is observed in Mn^{2+} doped CdS QDs³⁰ and Co^{2+} doped $ZnSe$.³¹ Inhomogeneous doping of magnetic ions inside doped NCs results in these discrepancies. In most of the cases, it has been extensively seen that spins within these magnetic islands couple anti-ferromagnetically resulting in reduced magnetic moments.³² Thus, homogeneous doping of magnetic impurities is essential to study the origin of magnetic properties within these systems. Thus far, there have been many studies on doped semiconductors and room temperature ferromagnetism has been observed.^{8, 33-34} However, the development is plagued with the reproducibility of these materials in terms of synthesis. Furthermore, there are almost no reports on the systematic study of dual doping in NCs and magnetic and magneto-optical properties associated with them because of the challenges associated with doping two different species in a strained environment of a NC.

Here we have shown a uniform distribution of Fe/Co dual dopants with control over size and dopant concentration using the diffusion-based technique. This can open up new horizons to study the origin of magnetic interaction in dual doped semiconductor NCs. Here, we have performed magnetic studies on uniformly (singly/dual) Fe/Co-doped CdS NCs.

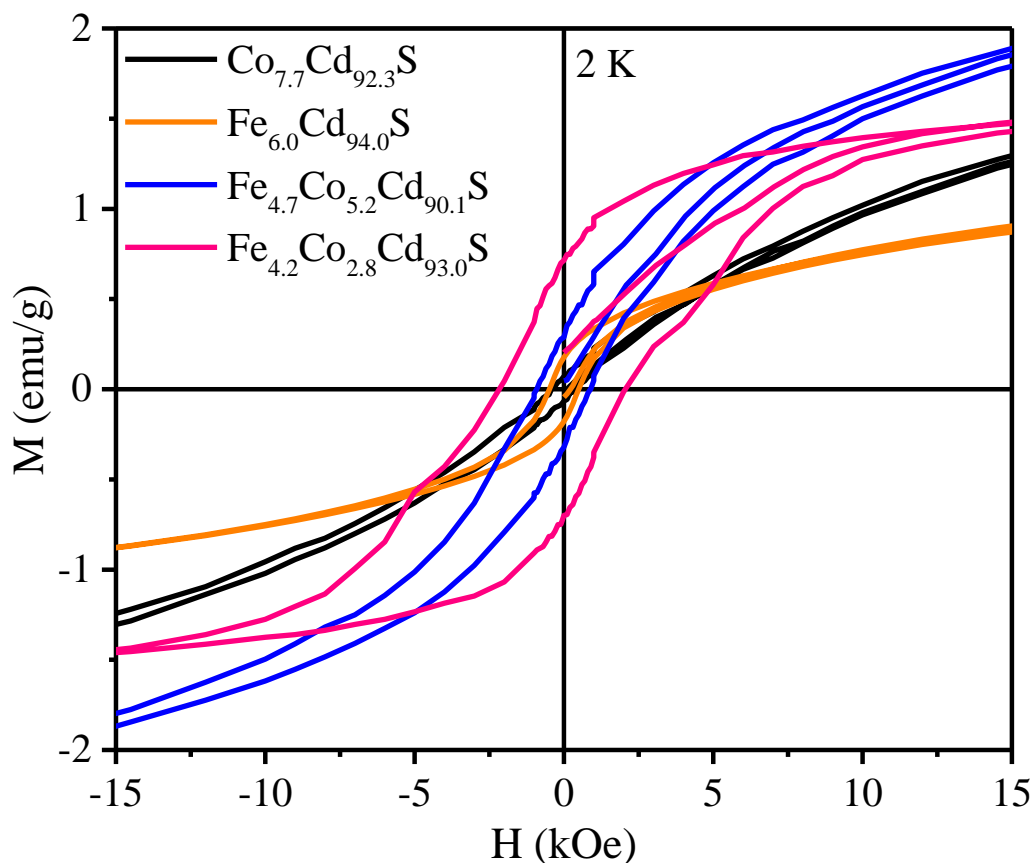


Figure 7.5. Magnetization vs. field plot at 2 K for $\text{Co}_{7.7}\text{Cd}_{92.3}\text{S}$ (black), $\text{Fe}_{6.0}\text{Cd}_{94.0}\text{S}$ (gold), $\text{Co}_{5.2}\text{Fe}_{4.7}\text{Cd}_{90.1}\text{S}$ (blue), $\text{Co}_{2.8}\text{Fe}_{4.2}\text{Cd}_{93.0}\text{S}$ (pink) singly and dual doped systems.

Table 7.1. Saturation magnetization and coercivity values for Fe and/or Co doped CdS NCs at 2 K.

M^{2+} doped	M^{2+} % (ICP)	M_s (emu/g)	Coercivity (KOe)
		2 K	2 K
CdS			
Co-CdS	7.7	Paramagnetic	0.41
CoFe-CdS	5.2, 4.7	3.6	0.9
FeCo-CdS	4.2, 2.8	1.9	2.16
Fe-CdS	6.0	1.5	0.49

To understand the magnetic behavior, DC magnetic measurements were performed at 2 K and room temperature for the doped systems. Figure 7.5 shows magnetization (M) vs. applied magnetic field (H) curves for $\text{Co}_{7.7}\text{Cd}_{92.3}\text{S}$, $\text{Fe}_{6.0}\text{Cd}_{94.0}\text{S}$, $\text{Co}_{2.8}\text{Fe}_{4.2}\text{Cd}_{93.0}\text{S}$, $\text{Co}_{5.2}\text{Fe}_{4.7}\text{Cd}_{90.1}\text{S}$ nanocrystals at 2 K. There is a change in magnetization behavior of the NCs going from singly to dual doped case as can be seen from the shape of the magnetization curves. The data for Co doped system (singly doped) shows a straight line in M vs. H curve suggestive of a paramagnetic behavior along with weak hysteresis behavior at 2 K. Further, $\text{Fe}_{6.0}\text{Cd}_{94.0}\text{S}$ exhibits weak ferromagnetism as evident from the figure. However, the co-doped samples at 2 K where both iron and cobalt are present as dopants in the structure show higher saturation magnetization as compared to the case of singly doped systems. Moreover, in the dual doped case, the coercivity has been found to increase with an increase in the relative Fe content. Thus, dual doped systems show ferromagnetic hysteresis with enhancement in saturation magnetization and coercivity values in M-H curves as reported in table 7.1. From the table, it is evident that the magnetization increases with dual doping.

We have further studied the DC magnetic properties at room temperature. Only Co doped system shows paramagnetic behaviour with a straight line in M vs. H curve. Fe doped system is majorly superparamagnetic. However, the dual-doped systems exhibit ferromagnetic hysteresis.

At room temperature when the entropy of the magnetic system increases, an overall reduction in DC magnetic properties is observed. Similar to 2 K, at room temperature, dual doped systems show higher saturation magnetization and coercivity than the singly doped counterparts as tabulated in table 7.2. The coercivity increases with an increase in the Fe content at 300 K as well. Interestingly the dual-doped systems exhibit, ferromagnetic ordering even at room temperature as is evident from the hysteresis curve in figure 7.6.

Finally, magnetic properties were studied using DC magnetic susceptibility by measuring zero-field cooled (ZFC) and field cooled (FC) magnetization curves. It is observed in figure 7.7 that the dual doped systems show a higher blocking temperature than singly doped systems and is tabulated in table 7.3.

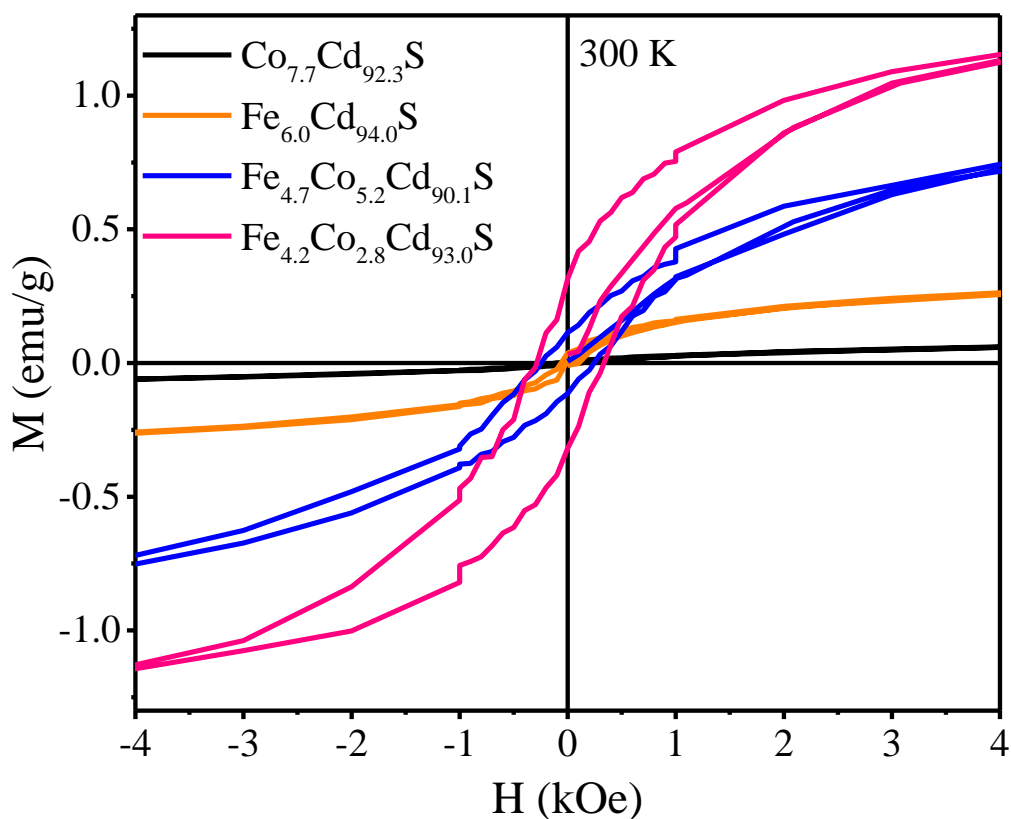


Figure 7.6. Magnetization vs. field plot at room temperature for $\text{Co}_{7.7}\text{Cd}_{92.3}\text{S}$ (black), $\text{Fe}_{6.0}\text{Cd}_{94.0}\text{S}$, (gold) $\text{Co}_{2.8}\text{Fe}_{4.2}\text{Cd}_{93.0}\text{S}$ (pink), $\text{Co}_{5.2}\text{Fe}_{4.7}\text{Cd}_{90.1}\text{S}$ (blue) singly and dual doped systems.

Table 7.2. Saturation magnetization and coercivity values for Fe and/or doped CdS NCs at 300 K.

M^{2+} doped CdS	M^{2+} % (ICP)	M_s (emu/g)	Coercivity (KOe)
		300 K	300 K
Co-CdS	7.7	Paramagnetic	-
CoFe-CdS	5.2, 4.7	1.35	0.25
FeCo-CdS	4.2, 2.8	1.49	0.34
Fe-CdS	6.0	0.45	-

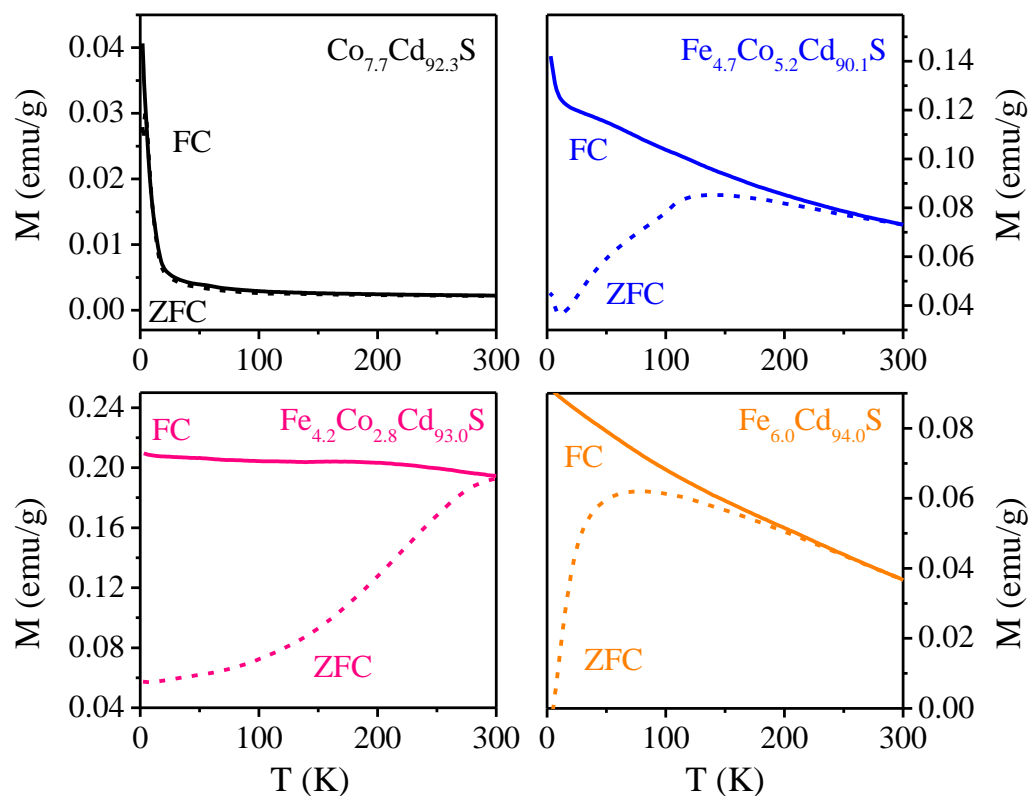


Figure 7.7. FC/ZFC magnetization curve for Fe and/or Co doped CdS NCs using a field of 200 Oe.

Table 7.3. Blocking temperature of Fe and/or Co doped NCs.

M ²⁺ doped CdS	M ²⁺ % (ICP)	Blocking Temp (T _b) K
Co-CdS	7.7	4.4
CoFe-CdS	5.2, 4.7	140
FeCo-CdS	4.2, 2.8	300
Fe-CdS	6.0	67

Therefore, analyzing the temperature and field-dependent magnetic behavior for all the doped systems, we have come up with a possible explanation for the observed behavior for these NCs. It was seen that the co-doped samples at 2 K where both iron and cobalt are present as dopants in the structure show higher saturation magnetization and coercivity as compared to the case of singly doped NCs. Moreover, in the dual doped case, the

coercivity and blocking temperature have been found to increase with a relative increase in the Fe content. At room temperature when the entropy of the magnetic system increases, dual doped systems still show higher saturation magnetization. Moreover, similar to 2 K, in the dual doped case, the saturation magnetic moment, coercivity and blocking temperature increase with an increase in the Fe content at 300 K also. Thus, co-doping with cobalt assists the magnetic ordering of iron at 2 K and 300 K.

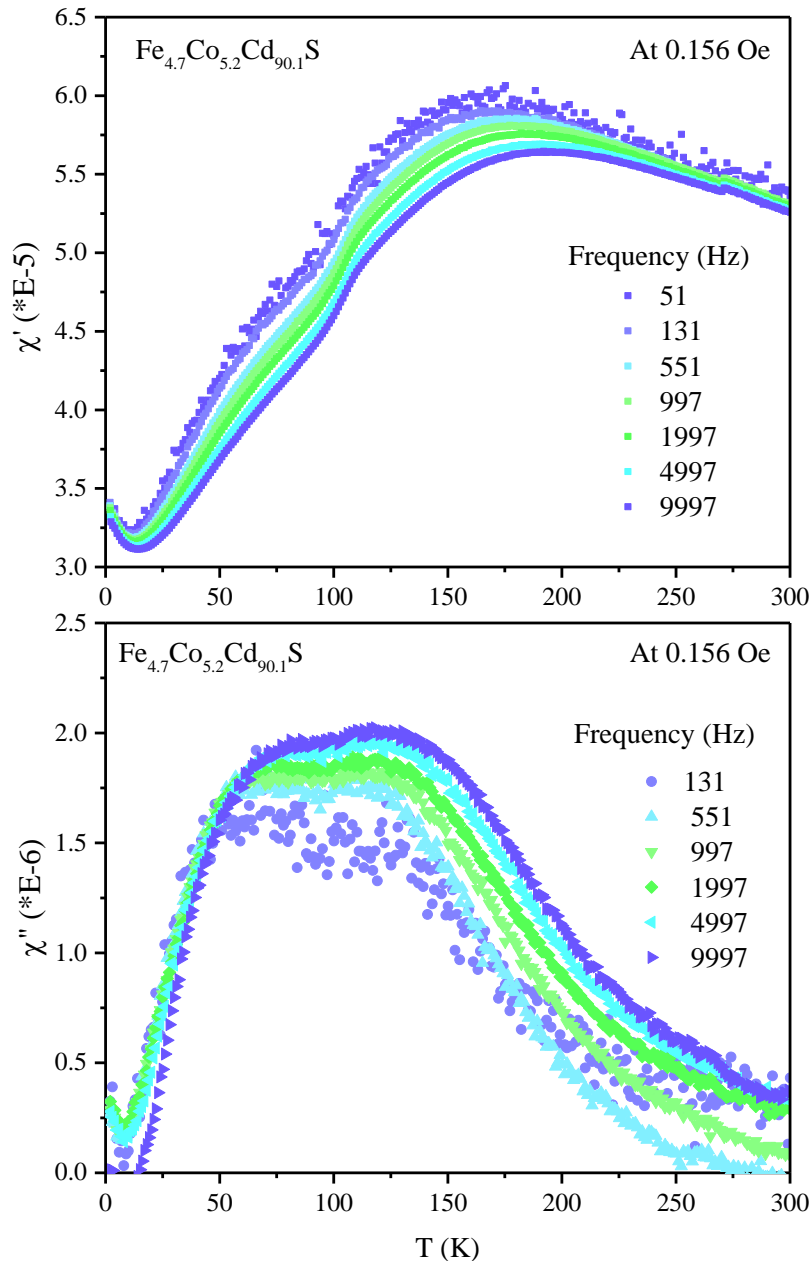


Figure 7.8. AC-susceptibility (a) in-phase, and (b) out-of-phase plots for the Fe, Co co-doped CdS NCs.

Further, the magnetism obtained in these NCs arising out of magnetic ion doping overrides the defect-related magnetism³⁵ by several orders of magnitude. This enhancement can be

related to the magnetic exchange interactions³⁶ between band carriers of the host CdS and magnetic ions or between two magnetic ions.

AC susceptibility. Further, frequency-dependent AC susceptibility measurements were performed to understand the trace of clustering of dopants within the host lattice if any. The absence of clustering is confirmed by measuring the frequency-dependent AC magnetic susceptibility data at 0.156 Oe as shown in figure 7.8(a) and (b). In the AC-susceptibility data, an out-of-phase component χ'' with a frequency-independent (0-60 K) and a frequency-dependent (60-300 K) feature is observed. This might be the result of multiple ordered spin sublattices of Co doped CdS and Fe doped CdS that are magnetically coupled within the system. A nearly frequency-independent feature is observed for χ' in the AC-susceptibility measurement with no different feature arising out of the magnetic clusters. This further confirms that the magnetism in the doped systems is due to the dopant host interactions and not due to the clustering effects.

7.5 Conclusion

In this chapter, we have discussed the synthesis and magnetic properties of Fe and/or Co doped CdS nanocrystals. We have used XAFS and XRD to prove the absence of magnetic islands in these NCs. Our results show that the magnetic properties of singly doped systems are different from the dual-doped case. Here we expect cobalt to be assisting the magnetic ability of iron leading to higher magnetic ordering in dual doped cases as compared to the singly doped counterparts. Such behaviour is also observed at room temperature. Moreover, enhancement in saturation magnetization, coercivity and blocking temperature was observed with a relative increase in iron content in these samples. This opens up a new possibility to understand the impact of dual doping on magnetism in semiconductor NCs. These findings will have far-reaching consequences in the potential application of these materials for future spintronic devices.

Bibliography

- (1) Hanif, K. M.; Meulenberg, R. W.; Strouse, G. F. Magnetic Ordering in Doped Cd_{1-x}Co_xSe Diluted Magnetic Quantum Dots. *J. Am. Chem. Soc.* **2002**, *124*, 11495-11502.
- (2) Bonanni, A.; Dietl, T. A Story of High-Temperature Ferromagnetism in Semiconductors. *Chem. Soc. Rev.* **2010**, *39*, 528-539.
- (3) Habas, S. E.; Yang, P.; Mokari, T. Selective Growth of Metal and Binary Metal Tips on CdS Nanorods. *J. Am. Chem. Soc.* **2008**, *130*, 3294-3295.
- (4) Dietl, T. A Ten-Year Perspective on Dilute Magnetic Semiconductors and Oxides. *Nat. Mater.* **2010**, *9*, 965-974.
- (5) Archer, P. I.; Santangelo, S. A.; Gamelin, D. R. Inorganic Cluster Syntheses of TM²⁺-Doped Quantum Dots (CdSe, CdS, CdSe/CdS): Physical Property Dependence on Dopant Locale. *J. Am. Chem. Soc.* **2007**, *129*, 9808-9818.
- (6) El-Hagary, M.; Soltan, S. Magnetic Behaviour of Fe-Doped CdS Diluted Magnetic Semiconducting Nanocrystalline Thin Films. *J. Appl. Phys.* **2012**, *112*, 043907.
- (7) Murali, G.; Reddy, D. A.; PoornaPrakash, B.; Vijayalakshmi, R. P.; Reddy, B. K.; Venugopal, R. Room Temperature Magnetism of Fe Doped CdS Nanocrystals. *Physica B: Condens. Matter* **2012**, *407*, 2084-2088.
- (8) Singh, S. B.; Limaye, M. V.; Date, S. K.; Gokhale, S.; Kulkarni, S. K. Iron Substitution in CdSe Nanoparticles: Magnetic and Optical Properties. *Phys. Rev. B* **2009**, *80*, 235421.
- (9) Bogle, K. A.; Ghosh, S.; Dhole, S. D.; Bhoraskar, V. N.; Fu, L.-f.; Chi, M.-f.; Browning, N. D.; Kundaliya, D.; Das, G. P.; Ogale, S. B. Co: CdS Diluted Magnetic Semiconductor Nanoparticles: Radiation Synthesis, Dopant– Defect Complex Formation, and Unexpected Magnetism. *Chem. Mater.* **2007**, *20*, 440-446.
- (10) Giribabu, G.; Murali, G.; Reddy, D. A.; Liu, C.; Vijayalakshmi, R. P. Structural, Optical and Magnetic Properties of Co Doped CdS Nanoparticles. *J. Alloys Compd.* **2013**, *581*, 363-368.
- (11) Sarma, S. D. Ferromagnetic Semiconductors: A Giant Appears In Spintronics. *Nat. Mater.* **2003**, *2*, 292-294.
- (12) Felser, C.; Fecher, G. H.; Balke, B. Spintronics: A Challenge for Materials Science and Solid-State Chemistry. *Angew. Chem. Int. Ed.* **2007**, *46*, 668-699.
- (13) Wolf, S. A.; Awschalom, D. D.; Buhrman, R. A.; Daughton, J. M.; Von Molnar, S.; Roukes, M. L.; Chtchelkanova, A. Y.; Treger, D. M. Spintronics: A Spin-Based Electronics Vision for the Future. *Science* **2001**, *294*, 1488-1495.

- (14) Chappert, C.; Fert, A.; Van Dau, F. N. The Emergence of Spin Electronics in Data Storage. *Nat. Mater.* **2007**, *6*, 813-823.
- (15) Chelikowsky, J. R.; Alemany, M. M. G.; Chan, T. L.; Dalpian, G. M. Computational Studies of Doped Nanostructures. *Rep. Prog. Phys.* **2011**, *74*, 046501.
- (16) Viswanatha, R.; Sapra, S.; Sen Gupta, S.; Satpati, B.; Satyam, P. V.; Dev, B. N.; Sarma, D. D. Synthesis and Characterization of Mn-Doped ZnO Nanocrystals. *J. Phys. Chem. B* **2004**, *108*, 6303-6310.
- (17) Pradhan, N.; Sarma, D. D. Advances In Light-Emitting Doped Semiconductor Nanocrystals. *J. Phys. Chem. Lett.* **2011**, *2*, 2818-2826.
- (18) Yuhas, B. D.; Fakra, S.; Marcus, M. A.; Yang, P. Probing the Local Coordination Environment for Transition Metal Dopants in Zinc Oxide Nanowires. *Nano Lett.* **2007**, *7*, 905-909.
- (19) Segura-Ruiz, J.; Martinez-Criado, G.; Chu, M. H.; Geburt, S.; Ronning, C. Nano-X-Ray Absorption Spectroscopy of Single Co-Implanted ZnO Nanowires. *Nano Lett.* **2011**, *11*, 5322-5326.
- (20) Keavney, D. J.; Cheung, S. H.; King, S. T.; Weinert, M.; Li, L. Role of Defect Sites and Ga Polarization in the Magnetism of Mn-Doped GaN. *Phys. Rev. Lett.* **2005**, *95*, 257201.
- (21) Radovanovic, P. V.; Gamelin, D. R. Electronic Absorption Spectroscopy of Cobalt Ions In Diluted Magnetic Semiconductor Quantum Dots: Demonstration of an Isocrystalline Core/Shell Synthetic Method. *J. Am. Chem. Soc.* **2001**, *123*, 12207-12214.
- (22) Erwin, S. C.; Zu, L.; Haftel, M. I.; Efros, A. L.; Kennedy, T. A.; Norris, D. J. Doping Semiconductor Nanocrystals. *Nature* **2005**, *436*, 91-94.
- (23) Dalpian, G. M.; Chelikowsky, J. R. Self-Purification in Semiconductor Nanocrystals. *Phys. Rev. Lett.* **2006**, *96*, 226802.
- (24) Newville, M. IFEFFIT : Interactive XAFS Analysis and FEFF Fitting. *J. Synchrotron Rad.* **2001**, *8*, 322-324.
- (25) Frost, J. M.; Harriman, K. L. M.; Murugesu, M. The Rise of 3d Single-Ion Magnets in Molecular Magnetism: Towards Materials from Molecules? *Chem. Sci.* **2016**, *7*, 2470-2491.
- (26) Coey, J. M. D.; Venkatesan, M.; Fitzgerald, C. B. Donor Impurity Band Exchange in Dilute Ferromagnetic Oxides. *Nat. Mater.* **2005**, *4*, 173-179.

- (27) Beaulac, R.; Schneider, L.; Archer, P. I.; Bacher, G.; Gamelin, D. R. Light-Induced Spontaneous Magnetization in Doped Colloidal Quantum Dots. *Science* **2009**, *325*, 973-976.
- (28) Viswanatha, R.; Pietryga, J. M.; Klimov, V. I.; Crooker, S. A. Spin-Polarized Mn^{2+} Emission from Mn-Doped Colloidal Nanocrystals. *Phys. Rev. Lett.* **2011**, *107*, 067402.
- (29) Norris, D. J.; Yao, N.; Charnock, F. T.; Kennedy, T. A. High-Quality Manganese-Doped ZnSe Nanocrystals. *Nano Lett.* **2001**, *1*, 3-7.
- (30) Hoffman, D. M.; Meyer, B. K.; Ekimov, A. I.; Merkulov, I. A.; Efros, A. L.; Rosen, M.; Couino, G.; Gacoin, T.; Boilot, J. P. Giant Internal Magnetic Fields in Mn Doped Nanocrystal Quantum Dots. *Solid State Commun.* **2000**, *114*, 547-550.
- (31) Norberg, N. S.; Parks, G. L.; Salley, G. M.; Gamelin, D. R. Giant Excitonic Zeeman Splittings in Colloidal Co^{2+} -Doped ZnSe Quantum Dots. *J. Am. Chem. Soc.* **2006**, *128*, 13195-13203.
- (32) Ghosh, A.; Paul, S.; Raj, S. Understanding of Ferromagnetism in Thiol Capped Mn Doped CdS Nanocrystals. *J. Appl. Phys.* **2013**, *114*, 094304.
- (33) Xiong, S.-J.; Du, Y. W. Effect of Impurity Clustering on Ferromagnetism in Dilute Magnetic Semiconductors. *Phys. Lett. A* **2008**, *372*, 2114-2117.
- (34) Huang, J. C. A.; Hsu, H. S.; Hu, Y. M.; Lee, C. H.; Huang, Y. H.; Lin, M. Z. Origin of Ferromagnetism in ZnO/CoFe Multilayers: Diluted Magnetic Semiconductor or Clustering Effect? *App. Phys. Lett.* **2004**, *85*, 3815-3817.
- (35) Madhu, C.; Sundaresan, A.; Rao, C. N. R. Room-Temperature Ferromagnetism in Undoped GaN and CdS Semiconductor Nanoparticles. *Phys. Rev. B* **2008**, *77*, 201306.
- (36) Yan, W.; Liu, Q.; Wang, C.; Yang, X.; Yao, T.; He, J.; Sun, Z.; Pan, Z.; Hu, F.; Wu, Z.; Xie, Z.; Wei, S. Realizing Ferromagnetic Coupling in Diluted Magnetic Semiconductor Quantum Dots. *J. Am. Chem. Soc.* **2014**, *136*, 1150-1155.

APPENDIX

AWSAR STORY

Nature's Play in Dual Doping of Quantum Dots



The following article related to dual doping has been published as a story:

AWSAR Best Popular Science Story 2019 - AW/2019/4313.

“The law of nature” is that no two different species can co-exist in a “confined environment” if you just bring them together one day. The most foreseeable outcome would be - one species will try not to put up in that confined space with the other, either it will walk out or it will not allow the other species to set foot in. Considering this instability we perceive that it is onerous or rather not practicable to keep different species together in a small space or a confined environment.

Still and all, the question remains, is it possible to defy nature’s law?

We all would have heard or read the famous story of “The Jungle Book” in our juvenescence. It’s a story of Mowgli (a human) raised in a jungle with other animals. Isn't it strange? However, even this fictitious story highlights an important point that it was “baby Mowgli” that was raised by a family of wolves. I recommend the readers to keep these particulars at the focal point while reading the story of our research.

So, this is what we are addressing in Quantum Dot Lab at Jawaharlal Nehru Centre for Advanced Scientific Research, Bangalore. We are trying to position two different species (elements/dopants) with dissimilar properties in a very small system (quantum dots) of around 10 nanometers (nm). Quantum dots are tiny semiconductor particles with all three dimensions in less than 10 nm size regime where a nanometer is 1 over 1000 times the thickness of a human hair.

In continuance, over here, we are trying to replace some 2 to 3 atoms with two different dopants from a system of 100 atoms of the host. This process of putting two dissimilar elements in a confined system of nanometer size regime is known as “Dual doping of Quantum Dots”. We have addressed this issue in our manuscript entitled “Thermodynamics of Dual Doping in Quantum Dots” in the “Journal of Physical Chemistry Letters” in April 2019.

However, if we talk about the challenges associated with dual doping in quantum dots till date, it has not been viable to dual dope quantum dots deftly with reproducibility. In a general approach, the quantum dots are synthesized in the first step and different impurity dopants are added to the host thereafter. Already space is confined, on that adding a single impurity element comes at a cost of energy. Adding two dissimilar elements with different nature (chemical and physical properties) is virtually unfeasible. They stand in need of non-identical growth conditions. These dissimilar dopants either phase-segregate or come together and form clusters or they remain at the surface resulting in surface doping as

shown in the first part of the scheme. Further, when we apply temperature for the growth of these quantum dots, the impurity elements try to diffuse out of the system. This is known as “self-purification”. This is analogous to what happens when we add on stress or apply perturbation to different species staying in a confined environment. They try to withdraw from the taxing situation and walk out. And I kept cudgeling my brain on how to make dual doping attainable? Yes, it appears to be arduous owing to the fact that it is energetically unfavorable.

Can we play with the energy barrier by some physical or chemical means? Is there a way out to put them in conjunction? That’s when I looked at nature and started wondering how can we prevail over all these barriers and bring two species together? And there it clicked, it is indeed feasible if we grow these species together. If we grow them together, the plausibility of conflict reduces and it is easier to administer them at the same level.

Here, we concentrate on the dual doping of cobalt (Co) and platinum (Pt) in cadmium sulfide (CdS) semiconductor host. Co has excellent magnetic properties and Pt helps to extend and enhance its properties by holding a connection between Co atoms. So in order to put together Co and Pt in the host CdS, we started with only Co and Pt. We synthesized an alloy of CoPt. Dissimilar to the traditional way of doping, wherein, we add these impurities to the already synthesized host, here we start to build a CdS structure around the CoPt core. This is known as a core-shell structure. Increasing the shell thickness escalated the strain on the CoPt core that starts to diffuse out into the CdS shell. Further, high-temperature annealing assists the diffusion process. Thus, CoPt lattice disintegrates and Co and Pt uniformly walk out into the semiconducting shell.

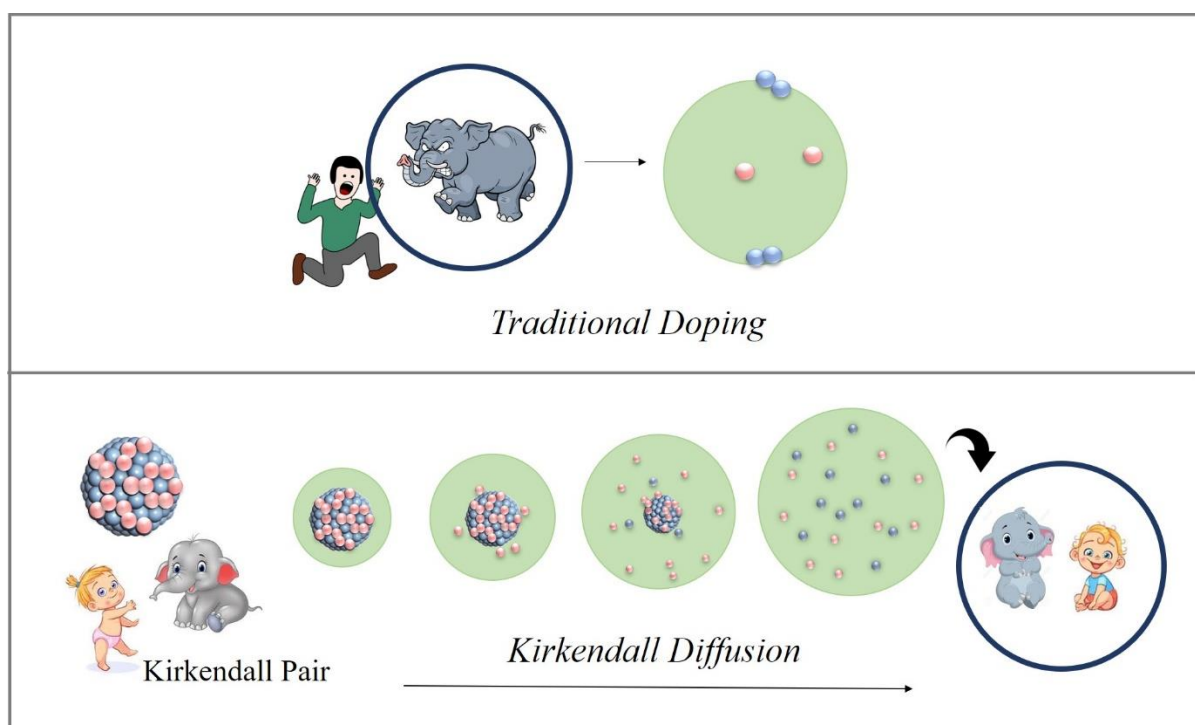
Now both Co and Pt unfold to trace the path of CdS. Based on their individual character and properties, we perceive that Co walks out faster as compared to Pt. This effect is known as the Kirkendall effect that is a sequel of the difference in the diffusion rates of Co and Pt. So based on the ratio of Co and Pt atoms in the starting CoPt, we can modulate the amount of Co and Pt remaining in the CdS after dual-doping. This is how we have achieved dual-doping (coexistence of different species) that is reproducible and consistent and it can further be extended to different Kirkendall pairs.

Now, what is the need of doing this? By doing dual doping we are able to tailor the properties of these CdS semiconductor hosts as a result of the interaction between different dopants and dopants with the host. This is technically important for introducing properties

that are otherwise not present in the CdS host. Over and above that, these materials have applications in light-emitting diodes, photodetectors, optoelectronics, photovoltaics, etc.

Now, the readers who are attending to this research story of dual doping, please cast your mind back to the story of “The Jungle Book”, the tale of baby Mowgli being raised by the family of wolves. The point to put down here is though different species were together in the same environment, even so, it all commenced when Mowgli was a “baby”. They have grown together and survived together in a constrained environment of a jungle. And that is what we have understood for our systems as well! The dual doping was successful when we started with the CoPt core, overcoated it with a thick CdS matrix and allowed the CoPt core to disintegrate and diffuse out into the CdS shell under the influence of lattice strain and high-temperature annealing as shown in the second part of the scheme.

Cartoon depicting traditional doping and diffusion doping using Kirkendall effect....



The way Mowgli and other animals used their expertise to assist each other and for the betterment of the jungle, in like manner dual doping results in riveting synergistic properties in the host that cannot be achieved in any of the individually doped systems. Thus, our objective was to address this fundamental issue of dual doping in quantum dots in a prevailing way that has seldom been explored in view of the challenges that it constitutes in administering different species at the same level.

The fundamental research may not have a linear impact on our lives but it ensues its rewards in its properties and applications that we make use of in our day-to-day life! Thus, Science is fundamentally optimistic and this was our laboratory venture of achieving dual doping in quantum dots pursuing ideas from “Nature” as broached by the title.

And then Co and Pt lived happily thereafter...

List of Publications

1. “Magneto-optical Stark effect in Fe doped CdS nanocrystals” **Mahima Makkar**, Lakshay Dheer, Anjali Singh, Luca Moretti, Margherita Maiuri, Giulio Cerullo, Umesh V Waghmare, Ranjani Viswanatha. *Nano Lett.* **2021**, 21, 9, 3798–3804.
2. “Ultrafast electron-hole relaxation dynamics in CdS nanocrystals” **Mahima Makkar**, Luca Moretti, Margherita Maiuri, Giulio Cerullo, Ranjani Viswanatha. *J. Phys. Mater.* **2021**, 4, 034005.
3. “Crystal facet engineering of CoPt quantum dots for diverse colloidal heterostructures” **Mahima Makkar**, Goutam Prakash, and Ranjani Viswanatha. *J. Phys. Chem. Lett.* **2020**, 11, 6742–6748.
4. “Thermodynamics of dual doping in quantum dots” **Mahima Makkar**, Avijit Saha, Syed Khalid, and Ranjani Viswanatha. *J. Phys. Chem. Lett.* **2019**, 10, 1992–1998.
5. “Frontier challenges in doping quantum dots: synthesis and characterization” **Mahima Makkar** and Ranjani Viswanatha. *RSC Adv.* **2018**, 8, 22103-22112.
6. “Recent advances in magnetic ion-doped semiconductor quantum dots” **Mahima Makkar** and Ranjani Viswanatha. *Curr. Sci.* **2017**, 112, 1421-1429.
7. “Exciton separation in CdS supraparticles upon conjugation with graphene sheets” Kasinath Ojha, Tushar Debnath, Partha Maity, **Mahima Makkar**, Siamak Nejati, Kandalam V. Ramanujachary, Pramit Kumar Chowdhury, Hirendra N. Ghosh, and Ashok Kumar Ganguli. *J. Phys. Chem. C.* **2017**, 121, 6581–6588.
8. “Diffusion doping in quantum dots: bond strength and diffusivity” Avijit Saha, **Mahima Makkar**, Amitha Shetty, Kushagra Gahlot, Pavan A.R. and Ranjani Viswanatha. *Nanoscale* **2017**, 9, 2806-2813.
9. “Ligand assisted digestion and formation of monodisperse FeCoS₂ nanocrystals” Amitha Shetty, Avijit Saha, **Mahima Makkar**, and Ranjani Viswanatha. *Phys. Chem. Chem. Phys.* **2016**, 18, 25887-25892.

10. “Probing the effect of clustering of dopants on magnetic and magneto-optical properties of nanocrystals” **Mahima Makkar**, Rachel Fainblat, Ranjani Viswanatha. (manuscript under preparation).
11. “Magnetism in Fe, Co co-doped nanocrystals” **Mahima Makkar**, Saveena Goyal, Suvankar Chakraverty, Ranjani Viswanatha. (manuscript under preparation).

AWSAR Best Research Story

1. Nature’s play in dual doping of quantum dots” **Mahima Makkar**.
<https://www.awsar-dst.in/result2019>, AW/2019/4313.

